Periodic SIW lines with degenerate band edge for the excitation of giant resonances

Tianyu Zheng

Sorbonne Université

Ecole doctorale : Science Mécanique Acoustique Electronique et Robotique (SMAER)

Laboratoire Génie électrique et électronique de Paris

Periodic SIW Lines with Degenerate Band Edge for the Excitation of Giant Resonances

Par Tianyu ZHENG

Thèse de doctorat d'Électronique

Présentée et soutenue publiquement le

Devant un jury composé de :

M. Boris GRALAK, Directeur de recherche au CNRS, Institut Fresnel	Rapporteur
M. Shah NAWAZ BUROKUR, Maitre des Conférences HDR, Université Paris Nanterre	Rapporteur
M. Philippe FERRARI, Professeur des Universités, Université Grenoble Alpes	Examinateur
M. Florent JANGAL, Chercheur HDR, DGA	Examinateur
Mme Thi-Quynh-Van HOANG, Ingénieur de Recherche, Thalès R&T	Examinatrice
Mme Hélène ROUSSEL, Professeur des Universités, Sorbonne Université	Examinatrice
M. Zhuoxiang REN, Professeur des Universités, Sorbonne Université	Directeur de thèse
M. Guido VALERIO, Maitre des Conférences HDR, Sorbonne Université	Co-directeur de thèse
M. Massimiliano CASALETTI, Maitre des Conférences HDR, Sorbonne Université	Invité

ABSTRACT

In this thesis, we describe the synthesis of periodic substrate-integrated waveguide supporting degenerate band edge (DBE) points. The DBE is a special fourth-order degenerate point encountered at the edge of the stopband in a periodic structure, which leads to field enhancement and high-Q resonances. First DBE realizations have been proposed in optics (with anisotropic dielectrics) and in the low microwave frequencies (with microstrips and waveguides). The choice of SIW technology can lead to the use of the DBE concept in microwave and millimeter-wave integrated circuits, given the easy fabrication, low profile and low-cost features of this technology. Applications of this concept will be oscillators having low threshold currents and being robust to external loading, and sensors with high directivity and sensitivity.

Here a multimodal transfer-matrix method is used to analyse the 4-port unit cell composing the periodic lines which supports a DBE. Conditions for the design of a unit cell providing a DBE point are given after an analysis of several kinds of unit cells, classified according to their S-parameter properties. Based on these guidelines, several SIWs-DBE designs are presented. In each case, a full dispersion analysis including both phase and attenuation constants of each Bloch mode is performed. A distance among all the Bloch-mode eigenvectors is computed to confirm the coalescence of four modes and the existence of a DBE. The influence of losses, of geometrical perturbations, and of truncation are considered. Typical DBE characteristics, such as field enhancement and a steep increase of Q factor and group delay vs. the number of cell in a truncated resonator are observed in lossless and lossy situations. Three low-loss designs are proposed, based on either a low-loss substrate or air-filled SIW solutions. These designs are capable to maintain strong DBE resonances even in the presence of losses. Feeding transitions are designed to feed the SIWs-DBE lines and to perform measurements which fully validate the theoretical analyses. Finally, the design procedure is also applied to a multilayer integrated waveguide, particularly suitable for integrated millimeter-wave applications, showing the versatility of the proposed methodology.

Keywords: *Degenerate band edge*, *dispersive analyses*, *transmission matrix*, *high-Q resonators*, *periodic structures*, *substrate-integrated waveguides*.

ACKNOWLEDGEMENT

I sincerely thank professor Boris GRALAK and professor Shah NAWAZ BUROKUR for reviewing my thesis and giving me suggestions to ensure the quality of this thesis. I would also like to thank my jury members, professor Philippe FERRARI, professor Florent JANGAL, Dr. Thi-Quynh-Van HOANG, and professor Hélène ROUSSEL for examining my thesis and my defence.

I wish to express my sincere thanks to my co-supervisor professor Guido Valerio who gave me a lot of suggestions and encouragement. Without his guidance, this research would not have been successfully completed. I also want to thank my supervisor professor Zhuoxiang REN who gave me the chance to do my PhD and supported me when I met difficulties.

I want to thank my colleagues and professors who helped me during my PhD work. professor Filipo Capolino gave me valuable suggestions for my work and my papers. M. Yves CHATELON, Oussama MOUDDA-AZZEM and Faouzi ARMI helped me a lot with my experimental work.

I want to thank Rudy, Michael, Oussama, Soroush, Matthieu, Ulises, Faouzi, Benjamin, Tuan-Anh, Joanna, Kevin, Yi and Pengfei. It is a honer to work with you in the lab and we had a great time together.

I want to thank my parents for their love and support. Also, I want to thank my wife for being there in my life. We came to France together to do our PhD and you gave me a lot of support and encouragement.

Finally, I want to express my thankfulness to my funding which comes from China Scholarship Council (CSC).

TABLE OF CONTENTS

LIST OF FIGURES

LIST OF TABLES

CHAPTER 1

Introduction

Electromagnetic propagation properties of metamaterials are characterized by the frequency dependence of the various modal wavenumbers supported by the material, defining the series of pass-bands and stop-bands and their features. This information is visualized by means of the well-known Brillouin diagram of the structure. Degenerate points in this diagram occur when two or more wavenumbers meet together with their relevant eigenmodal vectors. At these meeting points, new modes with different propagating features are usually originating. From a physical point of view, this corresponds to the coupling between different modes or harmonics, and can be a quite trivial phenomenon in periodic structures. For example, common degeneracies occur at each band edge of the Brillouin diagram, where two real harmonics (a forward and a backward one) meet to originate two complex conjugate modes. This is indeed the mechanism describing the transition from a pass-band to a stop-band.

Other kinds of degeneracies are less frequent and have received attentions in the last years. Namely, degenerate band edge (DBE) points have recently been investigated and have attracted considerable interest, because they introduce strong dispersive behaviors in periodic structures. The implementation of DBE leads to so-called "giant resonances" characterized by enhanced field magnitudes and then high Q-factors in relatively short lengths, which provides insights into the design of new high Q-factor resonators in a compact size.

These features are particular attractive for the realization of printed circuits in standard PCB technology. For this reason, we aim at studying the possibility to support and excite DBE in an efficient way in substrate integrated waveguides (SIW). These are particularly interesting for low-cost and easy-fabricated microwave circuits, and can pave the way to apply this new DBE concept to other kinds high-performance microwave and millimeter-wave circuits.

In this chapter, the research background and key terms on DBE are introduced. In Section 1, typical dispersion behaviors of one-dimensional (1-D) periodic structures are discussed. In Section 2, we briefly introduce the definition of degenerate band edge (DBE), the giant DBE resonances, and review several existing DBE structures in the

microwave area. After that, a compact, low-cost, and easy-fabricated waveguide called substrate-integrated waveguide (SIW) is presented in Section 3. At last, we describe the research objectives of this work and the outline of the thesis.

1.1 Dispersive properties of periodic structures

Let us assume an electromagnetic structure periodic along one direction (z) with period length d, whose period is called in the following a "unit cell" (Fig. 1.1(a)). A monochromatic regime of angular frequency $\omega = 2\pi f$ is also assumed in the following, where the time-dependence $e^{j\omega t}$ is suppressed. A Bloch mode supported by the structure is a solution of Maxwell equations verifying the boundary conditions enforced by the structure. By virtue of the periodicity, a Bloch mode verifies Floquet-Bloch boundary conditions at the edge of the cell. If we imagine the periodic structure as a series of scatterers embedded in an uniform waveguide, the Bloch mode will be a superposition of forward and backward waves originated by the multiple reflections from the scatterers. If V is a field component only dependent on the z dimension, its eigenvalue function is explicitly given by [1],

$$V(z+d) = e^{-jkd}V(z) \tag{1.1}$$

where k is the complex modal wavenumber. When decomposed in real and imaginary parts $k = \beta - j\alpha$, the two quantities have different physical meanings. β is the propagation constant, which describes the phase variation of the field along the structure (together with its phase and group velocity). α is the attenuation constant of the mode, which is responsible for a possible exponential attenuation along the structure.

We will refer to the dispersive properties of the periodic structure as the properties related to the frequency dependence of the modes supported by the structure (Bloch modes). These properties are simply visualized in the Brillouin diagram, which is a plot of the curve $\mathrm{Re}(k) = \beta$ as a function of ω. This diagram is periodic of $2\pi/d$ as shown in Fig. 1.1(b), and can be thus restricted to the so-called first zone ($-\pi \leq \beta d \leq \pi$) with no loss of generality [1]. Since the Bloch wavenumber is in general complex, it is possible to plot also the attenuation constant as a function of the frequency. If this is done close to the Brillouin diagram, the two curves give complete information on the propagation regimes supported by the structure (Fig. 1.1(b)).

One of the most typical dispersive features of periodic structures is the alternating frequency intervals of different Bloch-mode regimes: pass-bands and stop-bands. A pass-band is a frequency range where a Bloch mode can propagate without a significant attenuation (apart from possible loss effects). A mode in this regime can carry real power and it is visualized in the Brillouin diagram as a real wavenumber (in the absence of losses). A stop-band is a frequency range where the Bloch mode is attenuated and can-

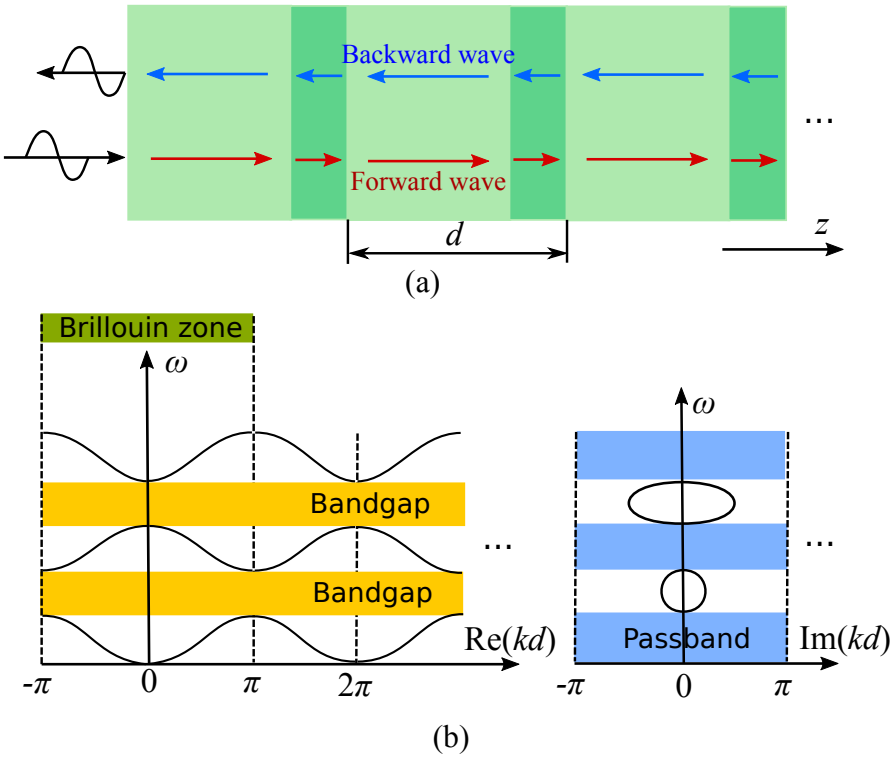

Fig. 1.1 1-D EBG structure [1]: (a) Schematic of 1-D EBG structure, where d is the period. (b) Dispersion diagram of 1-D EBG structure. The Brillouin diagram (on the left) shows the frequency variations of the phase constant $\mathrm{Re}(k) = \beta$. It is periodic of 2π if the normalized constant $\mathrm{Re}(kd)$ is plotted. The diagram on the right shows the attenuation constant $\mathrm{Im}(k)$ and completes the description of the dispersion properties of the structure.

not carry real power along the structure. This is visualized in the Brillouin diagram as a complex mode with a fixed phase constant not varying with frequency (either $\beta = 0$ or $\beta = \pi/p$ in the first zone, but most often not even plotted). In a stop-band regime, the Bloch mode attenuation constant changes with frequency, and its knowledge helps to evaluate the stop-band attenuation and to clarify the regime under study.

This rich dispersive behavior has been one of the reasons of intensive research on periodic structures in the past decades. They can provide frequency-filtering properties or prevent completely wave propagation in the frequency range of interest. In the latter case, and especially in the case of periodicity along two directions, the structure is commonly referred to an electromagnetic band-gap (EBG). After seminal papers such as the one by E. Yablonovitch [17] proposing laser applications of artificial photonic band-gap (PBG), blocking the propagation of light in a specific frequency band, the concept of EBG has been introduced into the electromagnetic field [18]. As the increasing demand of compact and high performance devices, EBG structures have been widely used in electromagnetic applications, including filters [19, 20], resonators [21], waveguides [22], antennas [23], etc.

Most studies of the EBG structures focus on the bandgap behaviors to confine the wave in a waveguide or a cavity surrounded by EBG walls. So far, however, very little attention has been paid to the band edge to achieve interesting wave propagation behaviors. A well-known behavior of waves at the edge of a stopband is the fact that the group velocity $\partial\omega/\partial\beta = 0$ at the band edge, which means that the energy propagation slows down as the transition to a reactive regime is approached (in stopbands, no active power is carried along the structure). Therefore, the band-edge point has been used to design resonators and slow-wave structures [24].
In this thesis, we are interested into the synthesis of an exceptional band edge condition called degenerate band edge (DBE) in 1-D EBG structures, whose definition and properties are discussed in the following sections.

1.2 Degenerate Band Edge (DBE)

A new dispersion phenomenon called degenerate band edge (DBE) was observed and studied by Figotin and Vitebisky [25] in the context of slow-light propagation in photonic crystals. It was pointed out that a series of anisotropic layers having principal axes suitably misaligned leads to a new DBE dispersion relation characterized by a dramatic field enhancement in the structure. In this section, we will review this phenomenon and show several applications.

1.2.1 Exceptional points and degenerate band edges

The DBE is a particular example of the more general concept of "exceptional point" (EP). An EP is a solution in the Floquet eigenvalue problem (1.1) (or another eigenvalue problem in different domains of physics) where several eigenvalues coalesce together with their eigenvectors [26]. The requirement of a degeneracy of both eigenvalues and eigenvectors exclude the modal crossing due to simple symmetric configuration inside each unit cell (such as glide-symmetry [16]). Since EPs are related to modal coupling, the relevant Hamiltonian can be formulated as perturbation of uncoupled Hamiltonians, where the perturbation coefficient describes the coupling between different systems. EPs arise when this coupling coefficient is analytically continued in a complex domain for specific values of this coefficients, corresponding to branch-point singularities in this complex plane [27]. After these first theoretical analyses, several experimental results revealed the physical importance of EP [28]. Since EPs can occur in any eigenvalue problem, these results can be applied and observed in a wide variety of physical systems, such as microwave cavity [29], parity-time-symmetric systems [30] (where periodic losses and gains balance each other), optical systems [31], quantum phase transitions [32].
Trivial degeneracies of second-order occur at each stop-band edge frequency, where two

different real harmonics (a forward and a backward) coalesce and originate two complex conjugate modes. These are called regular band edges (RBE). The phase constants of the real harmonics is quadratic in the neighborhood of the RBE [2]

$$f \approx f_g + \frac{f_g''}{2}(\beta - k_g)^2 \tag{1.2}$$

where $f_g'' = \frac{\partial^2 f}{\partial k^2} < 0$, f_g is the frequency at RBE and k_g is the wavenumber at RBE (see Fig. 1.2(a)).

While RBE occur in any periodic structure, this work focuses on DBE, which are fourth-order EP occurring at a frequency-edge of a stop-band. The phase constants of the real harmonics in the neighborhood of the DBE is this time of fourth order:

$$f \approx f_d + \frac{f_d''''}{24}(\beta - k_d)^4 \tag{1.3}$$

where $f_d'''' = \frac{\partial^4 f}{\partial k^4} < 0$, f_d is the frequency at DBE and k_d is the wavenumber at the DBE. The different behaviour of a DBE with respect to a RBE can be visualized in Fig. 1.2.

A first study of DBE was proposed by Figotin and Vitebsky in the context of slow-light propagation in photonic crystals [33]. They show the possibility to obtain an DBE by cascading a series of dielectric anisotropic slabs, whose principal axes are properly misaligned.

The behavior (1.3) leads to different dispersive features in wave propagation close to the band edge. As observed in the dispersion diagrams in Fig. 1.2(a) and (d) [2], near the band edge the DBE dispersion curve is flatter, because the phase constant β near DBE increases much slower than the k near RBE. At the DBE point, not only the group velocity vanishes, i.e., $v_g = \partial\omega/\partial k = 0$, but also the first and second derivative of group velocity reach zeros, i.e., $\partial v_g/\partial k = \partial^2\omega/\partial k^2 = 0$ and $\partial v_g^2/\partial k^2 = \partial^3\omega/\partial k^3 = 0$ [6]. On the contrary, at the RBE point only the group velocity vanishes, while its derivatives are different from zero. This leads to much lower group velocities at frequency sufficiently close to the DBE. For this reason, higher-order degeneracy are often referred to as “frozen modes”.

1.2.2 Requirements to achieve the DBE

While RBEs are encountered in all periodic waveguides, specific conditions should be designed in order to support a DBE. No general formulas are known in order to obtain such a result without a trial-and-error design procedure. Here we describe previous works providing guidelines for a correct design by analogy. In Chapter 2 we will study in detail the problem of the design of periodic coupled waveguides which can synthesize

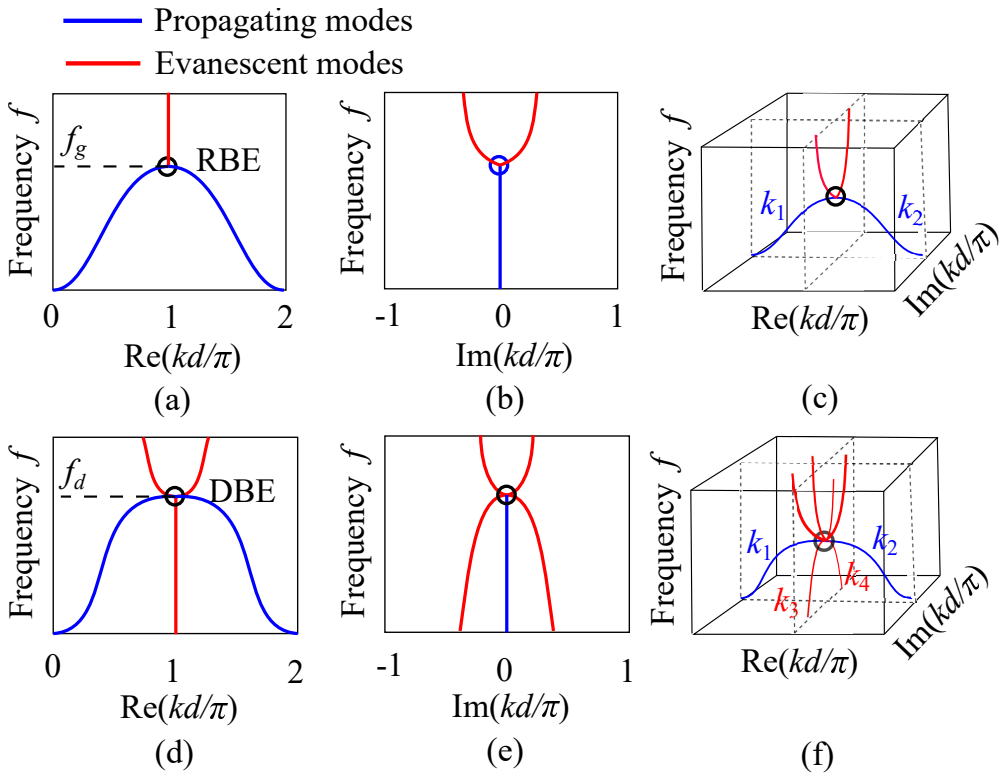

Fig. 1.2 Dispersion relation comparison between RBE and DBE. (a-b) Dispersion relation of RBE in (a) phase constant and (b) attenuation constant. (c) Demonstration of RBE modes in the complex space: with the increasing of the frequency, two propagating modes (k_1, k_2) coalesce at the RBE point. (e-f) Dispersion relation of DBE: (e) phase constant, (f) attenuation constant. (f) Demonstration of DBE in complex space: at DBE point, four modes coalesce (two propagating modes (k_1, k_2), two evanescent modes (k_3, k_4)).

a DBE.

The configuration studied in [2] is a periodic stack of photonic layers. As shown in Fig. 1.3(a), if the unit cell consists of two isotropic layers (A and B), RBEs are obtained. In contrast, when the unit cell of Fig. 1.3(b) includes two anisotropic layers (A_1 and A_2) together with an isotropic layer (B), a DBE condition can be reached. Necessary conditions are that layers A_1 and A_2 have different orientations of their principal axes: φ_1 and φ_2, and the misalignment angle between the axes is $\varphi = \varphi_1 - \varphi_2$, which can be varied between 0 and $\pi/2$ [34] to obtain the DBE. The role of the anisotropy misalignment is to assure the effective coupling between plane waves with different polarization propagating in the isotropic layer. In [2], the following important constrains to obtain a DBE in this configuration are reached:

- The periodic stack should include anisotropic layers.
- At least two of these anisotropic layers should provide in-plane anisotropy not aligned or perpendicular to each other, but with a proper misalignment angle.

- The presence of an isotropic layer is also necessary if the anisotropic layers are identical apart a rotation.

Other structures proposed in the last years confirm the need of the coupling between two different waveguide modes in order to achieve DBE. In [6], two elliptic rings are placed in a circular waveguide, providing a coupling between two TE_{11} with orthogonal polarization. While one ring only is not capable to achieve a DBE condition, by modifying the distance and the misalignment between the rings in a unit cell, a DBE can be obtained. In [35], a DBE is obtained by modulating the coupling between microstrip lines along a unit cell. In [36], a double-ladder topology circuit was used to obtain the DBE with a lumped-element circuit. Models for DBE in transmission lines are discussed in [37] and [38] where analytic constraints on the characteristic impedances of multiconductor transmission lines are derived to fulfill the DBE condition. These studies can give useful guidelines to achieve a DBE in specific structures by showing the need of a coupling mechanism between modes to achieve a DBE. However, no general results are available to design a periodic array whose unit cell is made of a coupler having suitable parameters capable to assure a DBE.

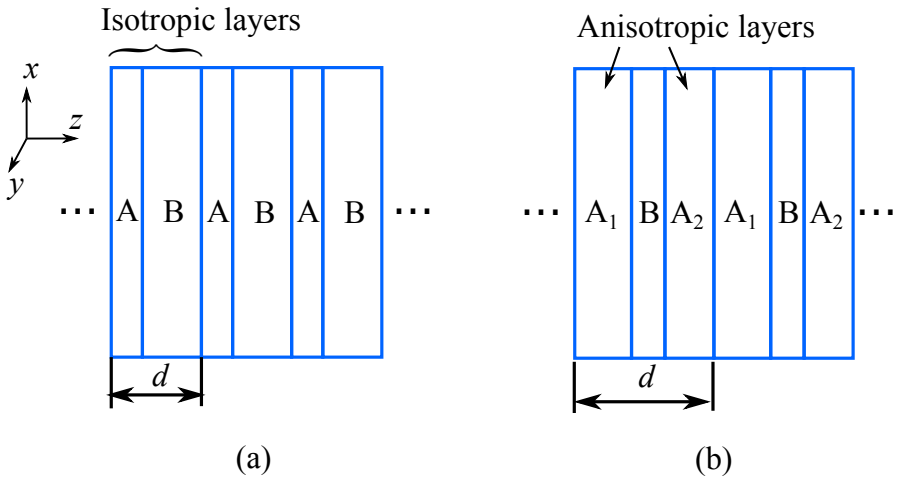

Fig. 1.3 Stacks of periodic layers to develop RBE and DBE [2]. (a) Stacks of isotropic periodic layers A and B. (b) Stacks of anisotropic periodic layers to develop DBE. Layer A_1 and A_2 are anisotropic and their in-plane axes have a proper misalignment angle. Layer B is isotropic.

1.2.3 Truncated Structures based on DBE Resonances

Any practical application of structures supporting DBE points always require the truncation of the periodic structures, i.e. the use of a finite number of unit cells. It is then of interest to know how the field excited in a truncated waveguide behaves, if the original periodic structure supported a DBE condition. It has been shown that, if compared to RBE, DBE resonances lead to an enhancement of the field amplitude, and then to a

higher quality factor Q, which scales differently vs. the number of cells in DBE than in RBE [2].

By truncating a periodic structure which develops RBE or DBE, a Fabry-Pérot resonator is obtained [1]. If this resonator is accessible through two ports at its ends, a typical transmission spectrum through the cavity is shown in Fig. 1.4 [2], where N is the number of cells retained in the truncation.

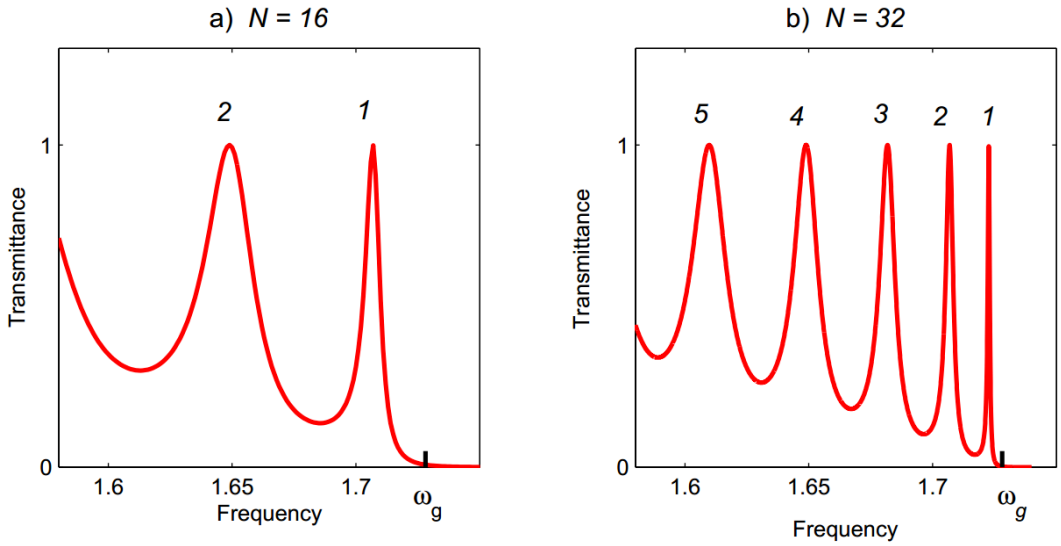

Fig. 1.4 Typical transmission spectrum of Fabry-Pérot resonator [2]. The peaks below the band edge frequency ω_g represent the resonances. (a) The length of resonator $N = 16$. (b) The length $N = 32$. The resonances are narrower when the length increases and their angular frequency positions are closer to the RBE angular frequency ω_g.

When N increases, the finite-length structure is approaching the ideal periodic configuration. The transmission peaks at frequencies lower than the band edge ω_g become sharper and their frequencies approach ω_g. These transmission peaks under ω_g approximately correspond to stationary waves inside the stack, approximately composed by a forward and a backward Bloch mode of similar amplitude, which cancel each other on the boundaries of the structure. It is easy to verify that the waves capable to fulfill this conditions have the following phase constants

$$\beta_s(N) \approx \beta_g \pm \frac{\pi}{Nd}s, \quad s = 1, 2, \ldots \tag{1.4}$$

where $\beta_g = \pi/d$ is the band-edge wavenumber, the $\pm$ sign depends on the forward or backward wave, and the index s selects the resonances shown in Fig. 1.4.

Once the dispersion equation (1.2) is taken into account, the resonant angular frequencies close to an RBE are [2]

$$\omega_s(N) \approx \omega_g + \frac{\omega_g''}{2}\left(\frac{\pi}{Nd}s\right)^2, \quad s = 1, 2, \ldots \tag{1.5}$$

Here and in the following we only consider the first resonance closest to the RBE ($s = 1$), which has the narrowest resonance among the different peaks. Its angular frequency is then

$$\omega_1^{RBE}(N) \approx \omega_g + \frac{\omega_g''}{2}\left(\frac{\pi}{Nd}\right)^2 \tag{1.6}$$

If a periodic structure supporting a DBE is truncated, the different (fourth-order) dispersion curve of the kind (1.3) leads to the angular frequency of a DBE resonance

$$\omega_1^{DBE}(N) \approx \omega_d + \frac{\omega_d''''}{24}\left(\frac{\pi}{Nd}\right)^4 \tag{1.7}$$

where a fourth-order dependence on the number of cells N is recovered.
A different scaling with respect to N is also found when observing the field density in the finite stack of cells. The electromagnetic field distribution inside the Fabry-Pérot cavity of RBE resonances is shown in Fig. 1.5. As we can see, the maximum field density is found in the middle of the resonator (as expected in a stationary wave with only one maximum), and it increases when the length of the cavity increases. The relationship between the maximum field density $|\Psi(z)|^2$, the incident wave amplitude Ψ_I, the number of cells N and the order number of RBE resonance peak s is

$$\max|\Psi(z)|^2 \propto |\Psi_I|^2\left(\frac{N}{s}\right)^2 \tag{1.8}$$

As shown in Fig. 1.5(c), (d), the DBE generates a stronger field enhancement compared to RBE. In fact, the relationship between maximum field density and N of DBE structures scales with a fourth power with respect to N

$$\max|\Psi(z)|^2 \propto |\Psi_I|^2\left(\frac{N}{s}\right)^4 \tag{1.9}$$

While more challenging to achieve, the DBE provides a field enhancement proportional to N^4, whereas the RBE field enhancement is only proportional to N^2. It indicates that the DBE structures can use a smaller number of periods to achieve the same performance as RBE structures, which can be attractive for compact design. Furthermore, fewer cells may suffer less of losses and imperfections.
The difference in formulas (1.8)-(1.9) can be explained by recurring to the composition of a RBE vs. a DBE point. The RBE resonance field is composed of two propagating Bloch modes (forward and backward modes) with close phase constant. In a periodic structure, these two modes eventually coalesce into one at the band edge frequency. In the truncated structure, the squared amplitude of the two Bloch components of the RBE resonance field $\Psi_T(z)$ is shown in Fig 1.6, where numbers 1 and 2 represent the forward and backward Bloch components. Higher-order evanescent fields are also depicted with

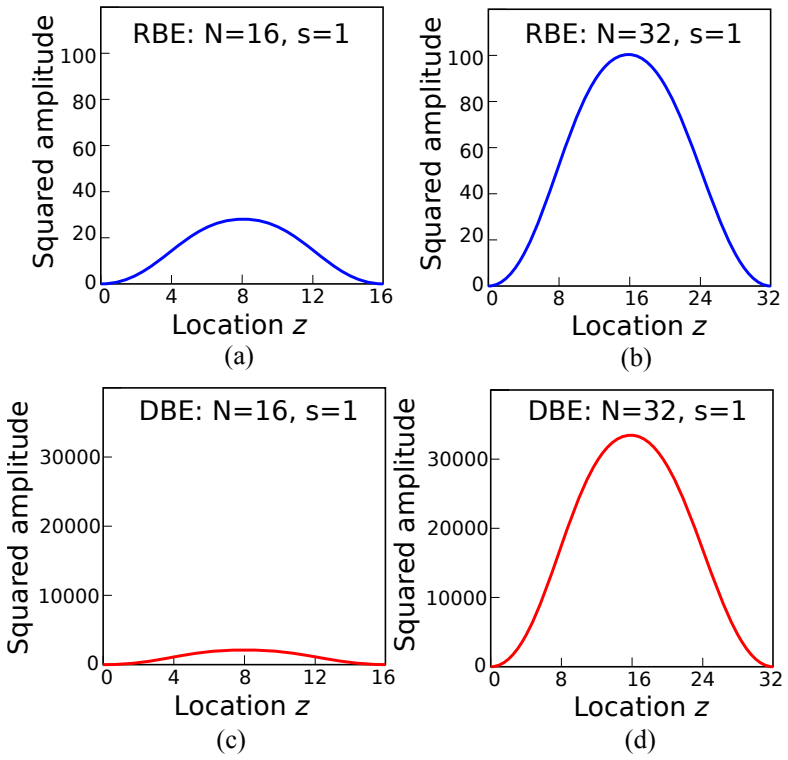

Fig. 1.5 The field intensity of RBE and DBE structures with different lengths [2]. (a) 16-cell RBE structure field distribution. (b) 32-cell RBE structure field distribution. (c) 16-cell DBE structure field distribution. (d) 32-cell DBE structure field distribution.

numbers 3 and 4, but their amplitude is negligible with respect to the main propagating modes. The squared amplitude of the overall propagating and evanescent fields are respectively

$$|\Psi_{pr}(z)|^2 = |\Psi_1(z) + \Psi_2(z)|^2, \qquad |\Psi_{ev}(z)|^2 = |\Psi_3(z) + \Psi_4(z)|^2 \tag{1.10}$$

Since the evanescent components are negligible, the overall field is determined by the propagating components as

$$\Psi_{total}(z) \approx \Psi_{pr}(z) \tag{1.11}$$

We also notice that the amplitudes of the two propagating modes have similar magnitude and opposite phase at the endpoints of the resonator. This allows an approximated standing wave with small amplitudes on the endpoints to be excited, as explained at the beginning of this paragraph.

By contrast, the field composition is different in the DBE situation. It is important to recall that a DBE is the coalescence point of four different modes, two real and two evanescent ones. Therefore, at frequencies close to the DBE, the amplitudes of all four modes are relevant in the total DBE resonance of the truncated structure. This is shown in Fig. 1.7 [2]. The two propagating modes are again labeled as 1 and 2, while the evanescent modes are 3 (forward, attenuating for increasing z values) and 4 (backward,

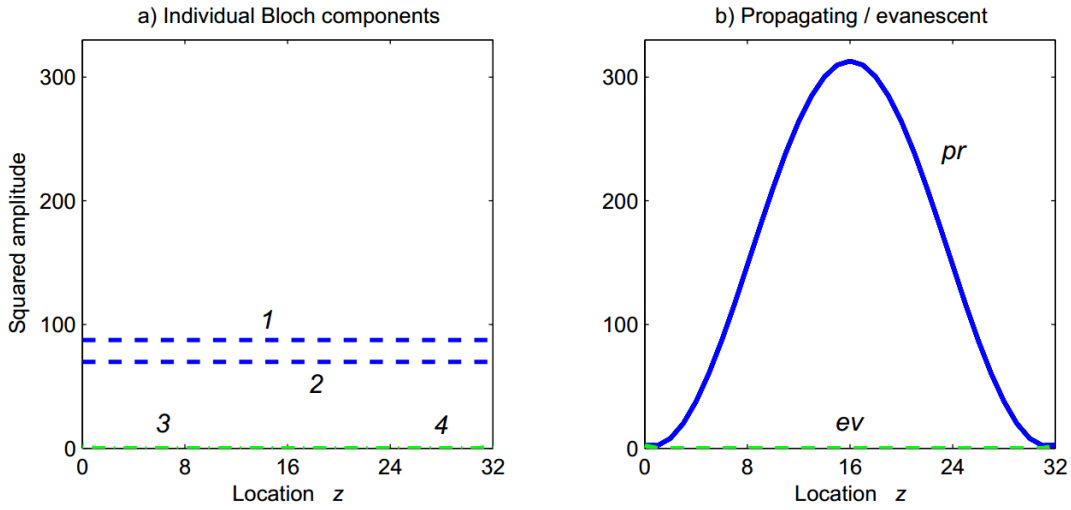

Fig. 1.6 Bloch components of RBE resonance [2]. (a) Individual Bloch components: forward/backward propagating Bloch modes, forward/backward evanescent Bloch modes. (b) Overall propagating and evanescent modes.

attenuating for decreasing z values). At the boundaries at $z = 0$ and $z = Nd$, both the propagating and evanescent components are large, and the four of them cancel together to fit standing-wave boundary conditions. Inside the resonator, the evanescent modes decay fast away from the interfaces, but the propagating modes remain large. This shows that the evanescent components play an important role in forming large field enhancement in the middle of truncated structures at DBE resonances. The presence of evanescent modes helps matching the slowly propagating mode to a fast mode across the interface [39].

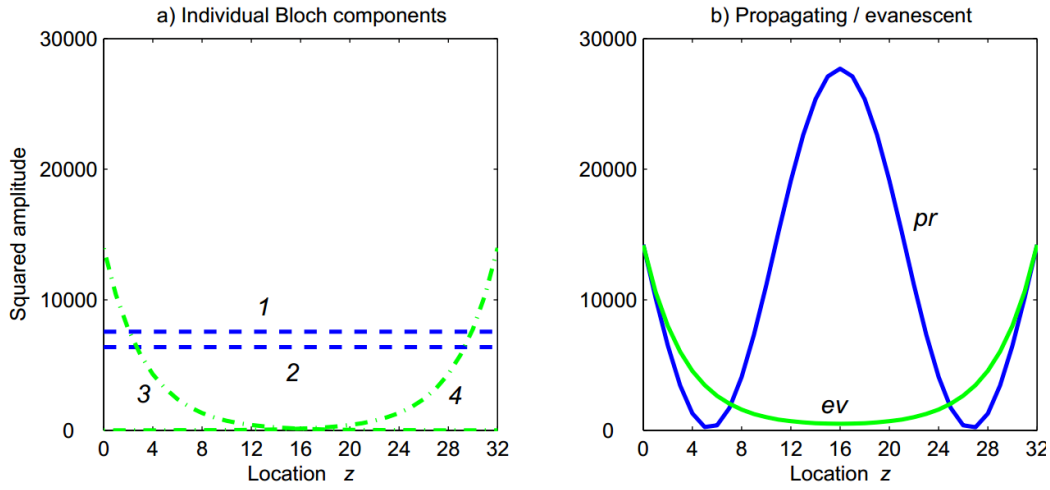

Fig. 1.7 Bloch components of DBE resonances [2]. The evanescent modes are essential for the enhancement of field amplitudes. (a) Four individual Bloch modes: forward and backward propagating modes, forward and backward evanescent modes. (b) Overall propagating and evanescent modes.

The enhancement of the amplitude levels of DBE resonant fields with respect to RBE fields leads to an important consequence in Q factors of truncated resonators. In fact, Q-factors of DBE structures are proportional to N^5, while RBE structures' Q-factors are proportional to N^3 [40]. In [3], the higher Q-factors related to DBE is verified in a double-ladder-circuit resonators and the increase of Q-factors vs. the number of cells is studied in both RBE and DBE resonators. The results are shown in Fig. 1.8. The sharp increase of Q-factors in DBE structures is particularly attractive for the design of high Q-factor resonators of compact size. This field enhancement and the increase of the loaded Q factor confirms the possibility to develop integrated circuits for interesting applications. These include sensors very sensitive to geometrical or physical changes close to the periodic line, oscillators having lower starting current with respect to ordinary oscillators [41], and directive and sensitive antennas if the Fabry-Perot cavity is open with slots, for example. In this view, the development of DBE conditions in integrated technology such as SIW is then important for the design of this new class of circuits and antennas. Of course, resonant phenomena in SIW can suffer from the presence of dielectric and metallic losses, and require a careful design in terms of circuit topology and to the materials to use.

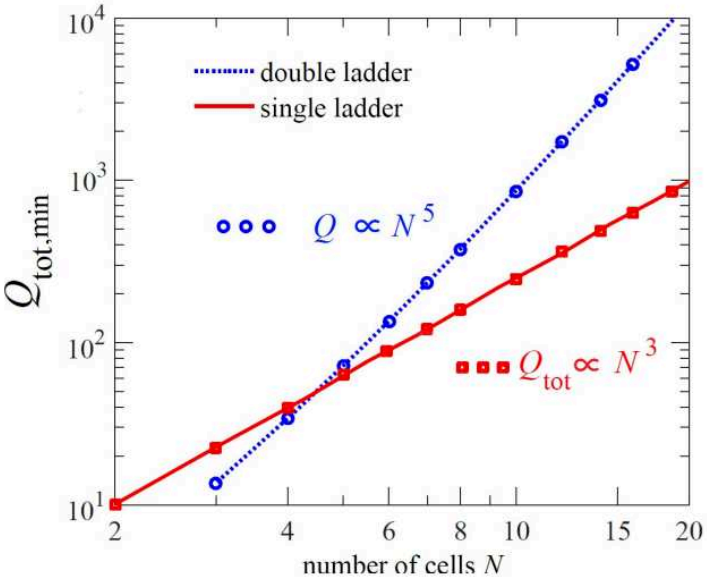

Fig. 1.8 The comparison of Q-factor trends in single ladder circuit with RBE and double ladder circuit with DBE [3]. The red line represents the Q-factor of the single ladder circuit with RBE resonances and it is proportional to N^3. The blue line represents the Q-factor of double ladder circuit with DBE resonances, which is proportional to N^5

.

1.2.4 Effect of Losses on DBE Structures

One of the attractive characteristics of RBE and DBE structures is their slow-wave features. As discussed earlier in this section, in an ideal situation the group velocity vanishes at the band edge frequency [39]. However, in reality, the group velocity reaches a minimum attainable limit because of the losses of material, fabrication tolerances, and finite-length truncation [4]. A few theoretical and experimental researches have dealt with losses influences on DBE synthesis [4] and Q-factors [5, 42].

Losses can be classified as dielectric, conductivity, and radiation losses. Dielectric losses are particularly simple to model, since they can be taken into account by using a complex dielectric constant, whose imaginary part is related to the loss tangent of the material $\epsilon = \epsilon' - j\epsilon''$ [14] where ϵ is the complex permittivity, ϵ' is the real part of dielectric permittivity and ϵ'' represents the dielectric loss. The knowledge of the loss tangent of a material leads to a straightforward estimation of losses of plane waves propagating inside the material. However, loss analysis is more complicated in waveguide structures, and specifically in DBE structures, since the impact of losses depends on the field configuration and is therefore strongly dependent on the structure under analysis.

A few theoretical works are available for a theoretical estimate of group velocity at band edge of photonic crystals. In [43], Pedersen *et al.* proposed a lower bound of the group velocity of RBE structures. Laude *et al.* used a perturbation method to analyze the influence of losses on a dispersion relation close to a band edge, and gave a general analytical expression of the lower limit of the group velocity of complex band structures [4]

$$D(\omega, k, \mu + \delta\mu) = \omega - \omega_0 - \delta\omega - \alpha(k - k_0)^n = 0 \tag{1.12}$$

where $D(\omega, k, \mu + \sigma\mu)$ is the general dispersion relation, μ is a small perturbation of the material constant, α is the constant determined by the shape of the unperturbed dispersion curve near the point (ω_0, k_0), and n is the degenerate order of the band edge (If $n = 2$, it is a RBE; if $n = 4$, it is a DBE).

Fig.1.9 from [4] shows a typical comparison between lossless and lossy dispersion curves near DBE. In the lossy case, the degeneracy is lost, and the group velocity at the DBE does not reach zero as expected in the lossless case. The minimum limit of group velocity given by [4] is

$$v_g^L = n \cdot 2^{-\frac{n-1}{n}} \cos\frac{(n-1)\pi}{2n} |\alpha|^{\frac{1}{n}} (\omega \cdot FL)^{\frac{n-1}{n}} \tag{1.13}$$

where v_g^L is the minimum bound of the real part of the group velocity, which is $v_g^L = \min|\operatorname{Re}(v_g)|$. F is the filling fraction representing the ratio of energy inside the dielectric to the total energy. L is the loss factor. The detailed definitions of F and L are given in [4].

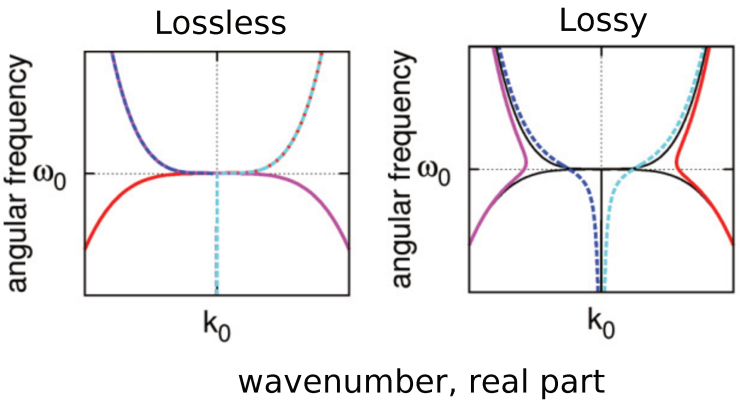

Fig. 1.9 Comparison of dispersion relations in lossless and lossy cases [4]. The dispersion relation is 'curved' because of the losses and the group velocity can't reach zero at the DBE point.

Even if the previously reported results are quite general and have the benefit to show how losses prevent degeneracy points, their use is not easy if applied to a general microwave artificial structure. In this case, full-wave simulations before the fabrication and experimental measurements are the easiest way to quantify different types of losses. Experimental results have been for example shown in [5], in lossy coupled transmission lines. Measurement results are shown in Fig. 1.10(a).

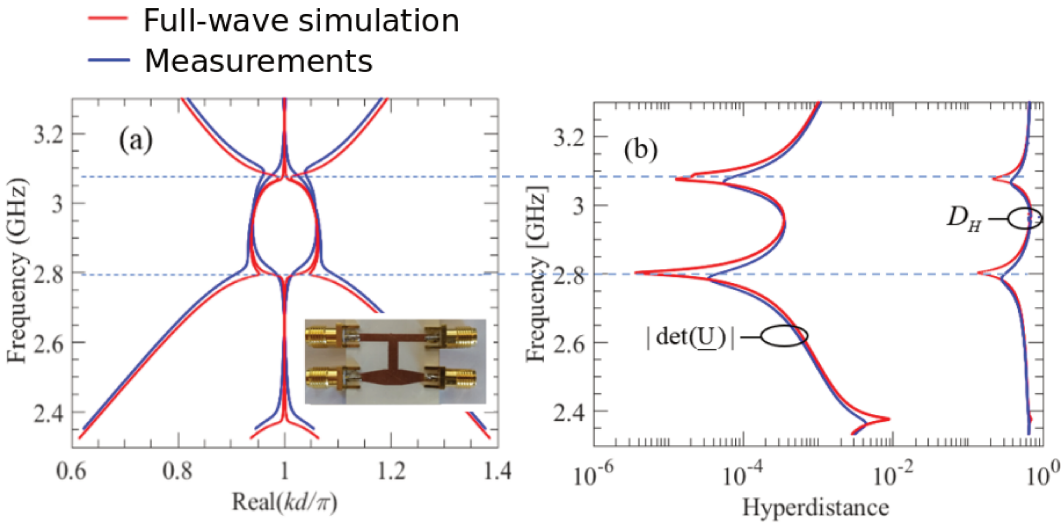

Fig. 1.10 Losses influence in coupled microstrip line with DBE [5]. (a) Dispersion relation in lossless and lossy cases, where the red line represents the full-wave simulation results, the blue line represents the measurements. (b) Hyperdistance calculated from the dispersion relation results, which represents the degenerate degree of four complex Bloch vectors.

Since a perfect degeneracy is certainly removed by introducing losses, a simple tool to evaluate the "quality" of an approximate lossy DBE and compare different implementations is beneficial. This can be done by remembering that the DBE is characterized

by the coalescence of four eigenvectors of the Floquet eigenproblem. A measure of the "hyperdistance" D_H among these vectors can thus quantify how far a point on dispersion relation curve is to an ideal DBE [5]. This hyperdistance can be defined as the sum of the six distances between each pair of the four eigenvectors:

$$D_H = \frac{1}{6} \sum_{\substack{m,n=1 \\ m \neq n}}^{4} \sin \theta_{mn}, \qquad \cos \theta_{mn} = \frac{\mathrm{Re}(\Psi_m, \Psi_n)}{||\Psi_m|| \cdot ||\Psi_n||} \tag{1.14}$$

where Ψ_m are complex Bloch-mode vectors in a four-dimensional complex vector space [44]. (Ψ_m, Ψ_n) is the hermitian inner product between Ψ_m and Ψ_n, $\|\Psi_m\|$ is the norm of Ψ_m, and θ_{mn} is the angle between Φ_m and Φ_n, defined by means of the standard hermitian product between the vectors. In equation (1.14), a perfect DBE corresponds to $D_H = 0$. The lower D_H is, the nearer the point is to an ideal DBE condition.
Losses also limit the expected Q-factor variation when the number of cells in truncated structure is increased. As the length of truncated DBE resonator increases, the influences of the loss is higher [42]. In general, loss tends to limit DBE unique features, especially for long structures, so minimizing losses is an essential task in designing DBE structures.

1.2.5 Review of Existing DBE Structures

Given the interesting characteristics previously described, DBE have been recently synthesized in different technologies, both in photonic and at microwave frequencies, such as double ladder lumped circuit [3, 36, 45], coupled microstrip lines [5, 38, 46–50], circular waveguide [6, 42], silicon ridge waveguides [51, 52], coupled resonator optical waveguide [24, 31, 53], multilayer dielectric resonator [35, 54–56], multilayer dielectric antenna [7, 8, 57–62], coupled transmission line array antenna [63], high power oscillator [64–69], pulse compression device [70], low threshold switching [71], laser [72]. In the following, we show three representative structures for microwave applications, which will be helpful to develop the designs proposed in the following chapters.

1.2.5.1 Circular Waveguide with DBE

In [6], a DBE is obtained in a circular waveguide by introducing two elliptical irises with a proper misalignment angle. The unit cell of the metallic circular waveguide is shown in Fig. 1.11 [6, Fig. 1]. Two forward $90°$-rotated degenerate TE_{11} modes travel along the circular waveguide as well as other two backward modes. The misaligned irises mix the four modes, thus forming the DBE. In [42] the structure is fabricated (Fig. 1.12) and successfully validated by an experiment. Furthermore, as shown in Fig. 1.13, the scaling of the quality factor Q fits with a N^5 law as expected in DBE

resonances. The results show that losses do not impact considerably the structure. This structure can be used in many applications, such as, high power microwave tubes having a strong interaction with an electron beam [73].

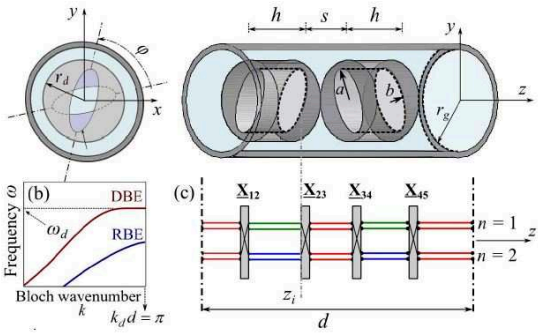

Fig. 1.11 The unit cell for a lossless air-filled circular waveguide with DBE [6]. Two discs with elliptical irises are placed in the waveguide with a proper misalignment angle.

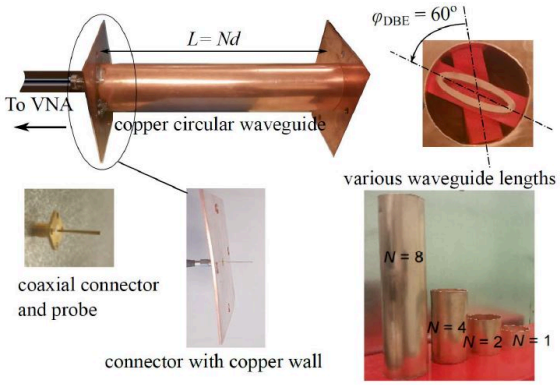

Fig. 1.12 The fabrication of the circular waveguide with DBE. The elliptic rings are supported by low-index foam and different lengths of the structure are considered.

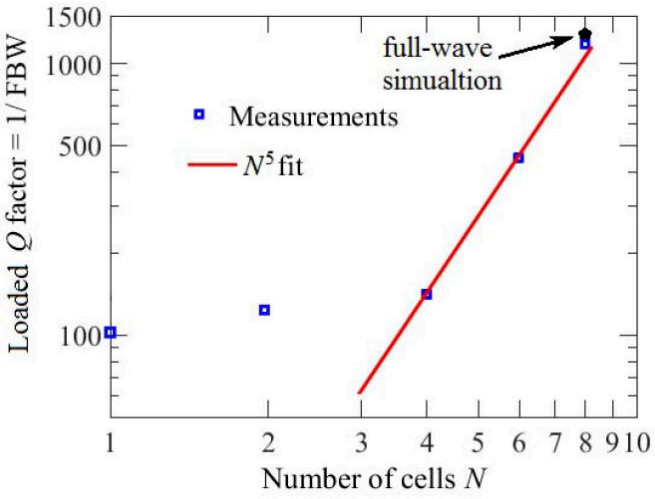

Fig. 1.13 The scaling of the Q factor to the number of the cells fits N^5.

1.2.5.2 Coupled Microstrip Lines with DBE

A pair of coupled microstrip lines is proposed in [35], where coupled and uncoupled line sections are alternated inside each unit cell to obtain the effect given in photonic crystals by anisotropic layers. The geometry is shown in Fig. 1.14 [7]. In the unit cell, the first part A_1 can be modeled by two uncoupled lines. In a parallel with the photonic crystal of Fig. 1.3, they play the role of one anisotropic layer. The second part A_2 couples the lines and emulates the unaligned anisotropic layer. The DBE condition is developed by adjusting the distance between lines and the length of the A_2 section.
This coupled-microstrip-lines DBE structure is the first DBE synthesized in PCB technology, and it can be used for microwave and antenna designs. One of the applications is the microstrip antenna in [7]. The slow-wave condition close to the DBE allows to miniaturize the size of the antenna to $\lambda_0/9 \times \lambda_0/9$.

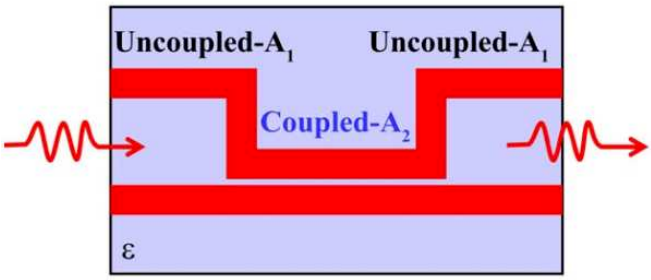

Fig. 1.14 Geometry of Coupled microstrip lines with DBE [7]. Two sections of the coupled lines emulate the anisotropic layers used in [2].

1.2.5.3 Multilayer Dielectric Resonator with DBE

In [61], the DBE condition is obtained at microwave frequencies by introducing artificial anisotropic dielectric layers, in an approach very similar to Figotin's seminal paper [2]. The schematic diagram and the 6-cell length fabricated structure are shown in Fig. 1.15 [8]. The strong slow-wave characteristic of DBE modes contributes to the miniaturization of the resonator. Another advantage is the easy fabrication of the structure.

Beyond the resonator development, this structure was also used to design the dielectric planar antennas in Fig. 1.16 [8]. The DBE enhances the antenna directivity and allows the use of a smaller number of unit cells than normal structures. As we can see, the particular resonance characteristics of DBE gives more flexibility in designing resonators and antennas, and can be used in more applications.

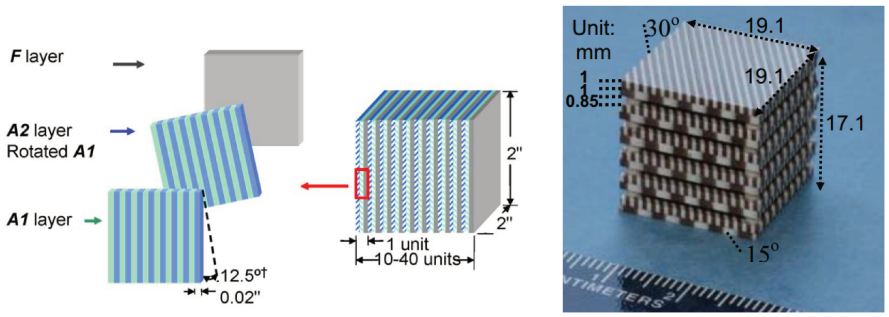

(a) (b)

Fig. 1.15 Multilayer dielectric resonator with DBE [8] (a) Artificial anisotropic dielectric layers to develop DBE. (b) Fabricated 6-cell multilayer resonator with DBE.

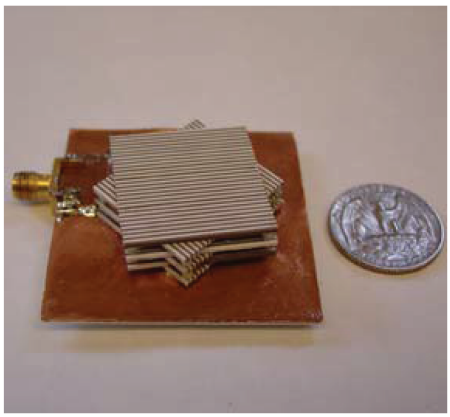

Fig. 1.16 The multilayer dielectric resonator antenna [8]. Each layer is an artificial uniaxial anisotropic dielectric stack. The printed metallic strips on the dielectric stack provide the uniaxial anisotropic characteristics. A proper misalignment angle between adjacent layers leads to DBE.

1.3 Substrate-integrated Waveguide (SIW)

In this section some fundamental concepts are recalled for the definition and design of substrate-integrated waveguide (SIW), together with existing SIW transitions, SIW filter technology, and air-filled SIW. These concepts will be useful in the following chapters for the design of SIW presenting DBE conditions.

1.3.1 Fundamental Properties of SIW

Substrate-integrated waveguides (SIW) [74] have attracted a lot of interest in the last decades and have become a common solution for integrated circuits at microwave and millimeter-wave frequencies. They are low cost, easy to fabricate, and have a good trade-off between high power-handling capability and the compact size compared to microstrip lines (low power-handling ability but compact) and metallic waveguide (high power density but bulk and not integrated). They have been proved to be able to address several issues for applications in high-frequency, high-performance circuits, such as resonators, filters, antennas.

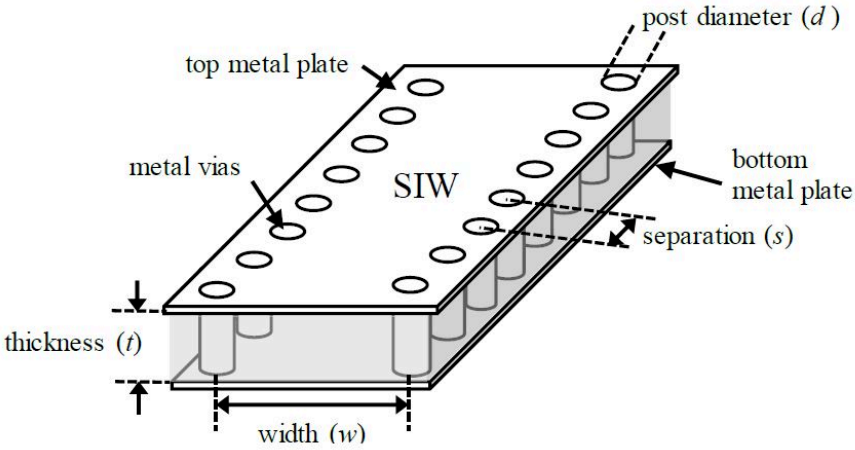

Fig. 1.17 Schematic of SIW structure [9]

A schematic of SIW is shown in Fig. 1.17 [9]. A substrate-integrated waveguide (SIW) consists of two ground planes, a dielectric substrate, and parallel lines of metallic vias. The tightly spaced vias act as sidewalls, to confine the wave inside the SIW, which therefore simulates a rectangular waveguide in a fully integrated technology. Therefore, the SIW can be equivalent to a dielectric rectangular waveguide whose width is given by [75]

$$w_{eff} = w - \frac{d^2}{0.95s}, \tag{1.15}$$

where w is the width of SIW, w_{eff} is the width of the equivalent rectangular waveguide, s is the distance between vias. The cut-off frequency of SIW for the dominant TE_{10}

mode is therefore

$$f_c = \frac{c}{2w_{eff}\sqrt{\epsilon_r}}, \tag{1.16}$$

where c is the light speed, ϵ_r is the relative permittivity of the substrate. In order to prevent lateral power leakage, the rules for via's diameter d and via's separation s are [76]

$$s \leqslant 2d, \qquad s/\lambda_c < 0.35 \tag{1.17}$$

where λ_c is the wavelength in the substrate, i.e., $1/f_c\sqrt{\epsilon_r\epsilon_0\mu_0}$. Once the desired cutoff frequency f_c is determined, we can use equations 1.15 to 1.17 to design the SIW.

1.3.2 SIW Transitions

In order to connect SIW to other parts of integrated circuits realized in different technology, or to perform measurements, suitable transitions are required. Several types of transitions have been used, such as microstrip line [10], conductor-backed coplanar-waveguide (CBCPW) [11], SMA-SIW launcher [12], as shown in Fig. 1.18.

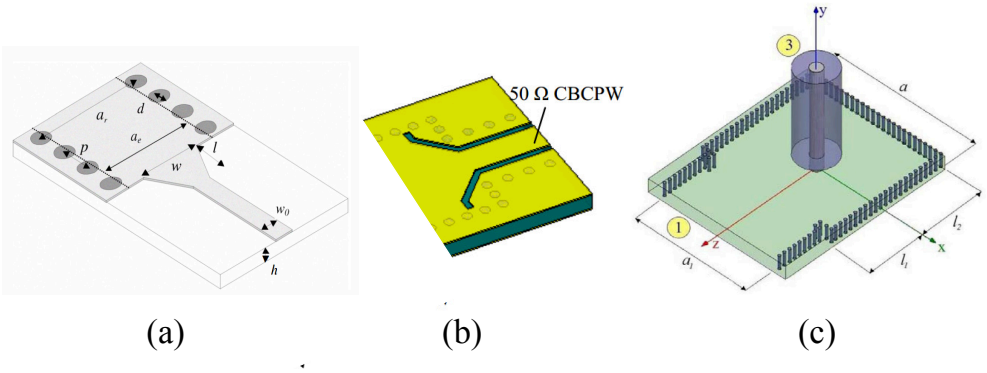

Fig. 1.18 Three common types of SIW transitions. (a) Tapered microstrip to SIW transition [10]. (b) CBCPW to SIW transition [11]. (c) SMA-SIW transition [12].

Microstrip transitions are commonly used and easy to design, according to rules proposed for example in [10]. Only two parameters, the width and length of taper need to be adjusted, and a good performance can be achieved. The transition of CBCPW, whose design details are discussed in [11], is preferable for its low-loss and wide-banded characteristics. The transition between an SMA connector and the SIW is effective to prevent energy leakage, and its design is proposed in [12].

1.3.3 SIW Filters

SIW has been widely applied in compact, high-Q, and cost effective filters for the millimeter-wave applications. A great deal of topologies have been reported, such as

ridge SIW filters [77], half-mode SIW filters [78], SIW filters with modified complementary split ring resonators [79], SIW filters with finite transmission zeros (FTZs) [80–85], etc.

The SIW filters with FTZs are designed by optimizing the FTZs position in the complex frequency plane. There are two methods to produce FTZs [86]. One method introduces a controlled coupling to generate different signal paths. When two signal paths cancel each other out, i.e. they have the same amplitude but opposite phase, an FTZ is introduced. Another method uses stopband resonators to introduce FTZs. Many topologies have been reported capable to grant a proper placement of FTZs. In [87], inductive posts are suitably placed to building the bandpass filter. In [88], a magnetic iris coupling is introduced in a half-wavelength SIW resonator. The most common topologies have multiple paths connecting different resonators. In [80], two bandstop resonators were used to locate FTZs on the imaginary axis. Another four resonators provide FTZs on the real axis and the whole filter was designed using an extracted-pole method [89]. In [81–85], a "negative coupling" was introduced, consisting of a magnetic iris providing an additional 180° phase change to the resonant mode. Furthermore, cross-coupling can be realized by introducing a spurious resonant mode: in [90], the main resonance and the spurious resonance generate together the FTZs. This topology gives the possibility to locate the FTZs near the passband region and thus obtain a high selectivity.

Besides single-mode SIW filters, dual-mode SIW filters aim to decrease the filter's size by more than 50% compared to the cascaded SIW filters, lowering at the same time transmission losses. The first dual-band SIW was proposed in [91]. After that, many dual-band SIW filters were realized in SIW circular cavity as shown in [92–94].

SIW have also been used to implement wideband filters [95–97], multiband filters [98–102], and reconfigurable filters [103, 104]. In [95], a zigzag topology provides a wide bandwidth from 6 GHz to 8.5 GHz. By structuring the ground plane as a periodic structure, a compact and wideband SIW filter is designed in [96]. An ultra-wideband response can also be achieved by cascading lowpass filters, as shown in [97]. Multiband (dual-band) SIW filters are proposed by cascading two passband filters with different center frequencies in [98]. To include reconfigurability, tunable resonators are used to adjust the frequency response. In [103], the vertical posts are used to configure the filter. By short-circuiting the posts to the ground plane, the frequency response can be configured. Another method uses pin diode switching elements to control the filter [104]. The diodes determine if the vias connect to the top layer of the cavity or not. By connecting or disconnecting the vias, the filter's center frequency is reconfigured.

1.3.4 Air-filled SIW

Dielectric losses are one of the main loss contributions in SIW lines [105], and could be of course avoided if the substrate is replaced by air. In [13], an air-filled SIW is proposed. It consists of three substrate layers as shown in Fig. 1.19. The top and bottom layers have metallized lower and upper faces, respectively, in order to act as copper planes for the middle layer. The metallic vias are in the middle layer, and the inner substrate (where vias are not present) is removed before stacking the layers. Measurements show that the air-filled SIW reduces the loss and increases the power-handling capability compared to the normal SIW [13].

Transitions between air-filled SIW and standard SIW are also proposed in [13], and a broadband air-filled SIW to waveguide transition is designed in [106]. Several applications have used air-filled SIWs. Here we cite bandpass filters with inductive posts [107], a fifth-order air-filled SIW filter with iris windows [108], a dual-mode air-filled SIW [109], and an air-filled SIW with FTZs [110].

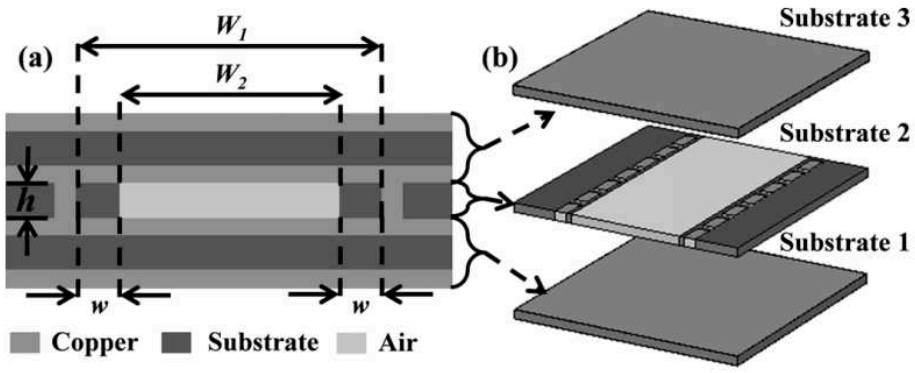

Fig. 1.19 The demonstration of an air-filled SIW [13]. (a) Cross-section diagram. (b) Geometry

1.4 Research Objectives and Outline

The goal of this thesis is to obtain guidlines for the design of DBE in periodic waveguides, propose SIW periodic structures supporting DBE, and to study the effect of truncation in DBE giant resonances presenting the expected Q-factor growth described in the previous sections. The objectives of this thesis are summarized below:

- Develop a mathematical model to find guidelines to achieve the DBE in SIW. By considering the scattering parameters of unit cells providing modal coupling between waveguides, sufficient conditions are sought to design the geometrical shape of couplers capable to grant the existence of DBE.
- Study several unit cell designs of periodic SIW lines with DBE and discuss their optimized designs in terms of losses, robustness to parameter variations, cost, and fabrication aspects.
- Study the effect of truncation of the proposed periodic SIW lines together with the suitable feeding to observe experimentally the giant resonances.
- Fabricate and measure the designed prototypes. The S-parameters and Q-factors of the prototypes are measured and compared with the results of numerical simulations. A discussion is given about challenges encountered and solved during the manufacturing process.

The outline of the remaining chapters of this thesis is as follows:

– **Chapter 2: Guidelines for the Synthesis of SIW-DBE Periodic Structures and Unit-Cell Design.** In this chapter, the Bloch analysis of one-dimensional (1D) periodic structures is presented, by assuming different ideal scattering parameters to describe the unit cell as a four-port network. With the help of transmission line analysis, we look for guidelines for the design of unit cells capable to grant a DBE condition. The results lead to the proposal of several SIW unit-cell designs with DBE. We also compare the size of these unit cells, the impact of losses, and the robustness to parametric variations.

– **Chapter 3: Design of Truncated SIW DBE Structures.** In this chapter, we consider truncated SIW composed of unit cells described in Chapter 2 and study the excitation of DBE resonances and their properties. Low-loss solutions are proposed based on low-loss substrates and air-filled SIW. These structures are fabricated and measured. The distinctive features of DBE resonances are observed in the experiments.

– **Chapter 4 Conclusions and Future Works:** We conclude the thesis and offer the prospect of future work.

CHAPTER 2

Guidelines for the Synthesis of SIW-DBE Periodic Structures and Unit-Cell Designs

2.1 Introduction

In this chapter, we present the tools used to analyze and design SIW periodic structures providing a DBE conditions, we study different types of unit cells with the aim of synthesizing a DBE response, and we propose several periodic SIWs capable to achieve this response.

It should be remarked that the detection of a DBE condition requires the computation of a full Brillouin diagram including both phase and attenuation constants. In fact, the coalescence of four modes (two propagating and two evanescent, the latter ones having a complex propagation constant) must be verified. Together with the eigenvalues in the Brillouin diagram, the calculation of the Bloch eigenvectors is also required. They are needed to compute the hyperdistance (1.14) to understand if the DBE is met or if further adjustment to the structure should (and can) be done. All these quantities cannot be easily computed with ordinary simulation software. The available commercial numerical tools performing dispersion analyses are in fact limited to real-mode computation only. For this reason, the Floquet eigenvalue problem must be solved with an *ad-hoc* method.

We first give in Section 2.1 a brief review of the Bloch analysis of 1-D periodic structures using the well-known transfer-matrix method. Then we generalize the analysis by means of a multimodal transfer matrix which can take into account several modes at each side of the unit cell. This is particularly interesting to study DBEs, which arise from a coupling between different lines. In Section 2.2, we assume a unit cell composed by two identical transmission lines coupled with a coupler characterized by certain scattering parameters. We study different kinds of couplers and we address the study of constraints on these parameters to achieve the DBE. Based on these conclusions, we proceed proposing several SIW-DBE unit cell designs in Section 3.

2.2 Multimode Analysis of 1-D Periodic Structures with DBE

2.2.1 Bloch Analysis of a Cascade of 2-port Networks

The Bloch analysis of a periodic line whose unit cell can be modeled as a 2-port network is well-established as described in [14]. We give a brief review here to show the general idea, and then we extend it into the analysis of periodic structures formed by cascading 4-port networks in the next subsection.

A 1-D periodically loaded transmission line is shown in Fig. 2.1. To fix the ideas as in [14], each unit cell is composed of a shunt susceptance and a transmission line. The length of the unit cell is the period d, and the periodic shunt susceptance is b. A transfer matrix or T matrix can be computed, relating the total voltages and currents on two sides of the 2-port unit cell:

$$\begin{bmatrix} V_{n+1} \\ I_{n+1} \end{bmatrix} = \underline{\mathbf{T}} \begin{bmatrix} V_n \\ I_n \end{bmatrix} \tag{2.1}$$

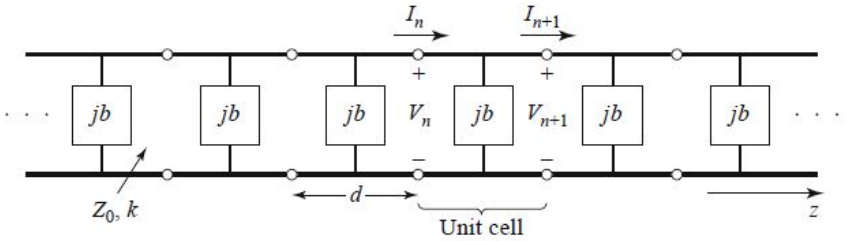

Fig. 2.1 Equivalent circuit of a periodically loaded transmission line [14]

The transfer matrix is particularly useful since the transfer matrix of a cascade of elements is simply the matrix product of the transfer matrices of the elements (in the right order). It is important to note that the definition of transfer matrix or transmission matrix may differ according to the author, but these definitions are basically the same concept. In [5, 6, 111], the transfer matrix is the inverse of the transmission matrix defined in [14]. Other transfer matrices can be defined on the basis of incident and reflected waves, instead of total fields as here (e.g. in [112]). However, the analyses performed under these definitions are equivalent (apart from an unessential exchange between forward and backward modes if the inverse matrix is considered). To prevent any ambiguity, we use in the following the definition of transfer matrix in (2.1). The unit cell of Fig. 2.1 can be divided into a cascade of three parts: a $d/2$-length transmission line, a shunt susceptance b, and another $d/2$-length transmission line. Due to the definition of the matrix, the T matrix of the cascade of different elements along a line is given by the ordered product of the individual T matrices. Therefore, the normalized T matrix of a unit cell of Fig. 2.1 can be expanded as the product of three matrices [14]:

$$\underline{\mathbf{T}} = \begin{bmatrix} \cos\frac{\theta}{2} & -j\sin\frac{\theta}{2} \\ -j\sin\frac{\theta}{2} & \cos\frac{\theta}{2} \end{bmatrix} \begin{bmatrix} 1 & 0 \\ -jb & 1 \end{bmatrix} \begin{bmatrix} \cos\frac{\theta}{2} & -j\sin\frac{\theta}{2} \\ -j\sin\frac{\theta}{2} & \cos\frac{\theta}{2} \end{bmatrix} \tag{2.2}$$

where $\theta = kd$ and impedances are normalized to the same characteristic impedance of the line. Equation (2.1) leads to a simple way to enforce Floquet boundary conditions at the border of the unit cell (1.1). For a Bloch-mode propagating in the z direction, the voltage and current at the n th terminals differ from the voltage and current at $(n+1)$ th terminals by a propagation factor e^{-jkd}, where $k = \beta + j\alpha$ is the complex propagation constant. Thus, the relation (1.1) can be written as:

$$\begin{bmatrix} V_{n+1} \\ I_{n+1} \end{bmatrix} = e^{-jkd} \begin{bmatrix} V_n \\ I_n \end{bmatrix} \tag{2.3}$$

Comparing equation (2.1) and (2.3), the forward and backward propagation constants k_1 and k_2 are related to the eigenvalues of the T matrix of the unit cell λ_1, λ_2. The electromagnetic problem is then equivalent to an eigenvalue problem of a 2×2 matrix

$$k_i = -\frac{1}{jd}\ln(\lambda_i), \quad i = 1, 2 \tag{2.4}$$

When $\alpha = 0, \beta \neq 0$, the wave propagate along the structure without attenuation. Otherwise, the wave is evanescent. The decay due to α can be due to material losses, radiation losses, or to the presence of a stopband preventing the transport of real power, as explained in the previous chapter.

2.2.2 Bloch Analysis of a Cascade of 4-port Networks

As seen in the previous chapter, the DBE condition arises from the mutual coupling of two lines or modes in a guiding structure. For this reason, the approach of the simple T matrix outlined in the previous section is not suitable for the analysis to be performed here.

Already in [5, 6, 111], a generalization of the transfer matrix approach is proposed, by describing the unit cell of a pair of 1-D periodic coupled transmission lines (CTL) as a *four-port network*. With this approach, a unit cell for CTLs (Fig. 2.2) is accessible from two ports on one Floquet boundary (labeled here ports 1 and 2) and other two ports on the other Floquet boundary (labeled here port 3 and 4). On each port an equivalent transmission line is defined, so that two scalar quantities (a voltage and a current) are defined. Accordingly, $V_n(z)$, $I_n(z)$ are interpreted as CTLs voltages and currents, namely, $\mathbf{V}(z) = [V_1(z) \quad V_2(z)]^T$ and $\mathbf{I}(z) = [I_1(z) \quad I_2(z)]^T$. A four-dimensional state

vector is defined as

$$\mathbf{\Psi}(z) = [V_1(z) \quad V_2(z) \quad I_1(z) \quad I_2(z)]^T \tag{2.5}$$

Thanks to the linearity of the system, we can define a new 4×4 transfer matrix relating the state vector from one side of the unit cell $\mathbf{\Psi}(z)$ to the state vector to the opposite side $\mathbf{\Psi}(z+d)$:

$$\underline{\mathbf{T}} \cdot \mathbf{\Psi}(z) = \mathbf{\Psi}(z+d) \tag{2.6}$$

Floquet boundary conditions are still enforced as in (2.3) on the four-dimensional state vector:

$$\underline{\mathbf{T}} \cdot \mathbf{\Psi}(z) = e^{-jkd}\mathbf{\Psi}(z) \tag{2.7}$$

The Bloch wavenumbers are therefore related to the eigenvalues of the transfer matrix $\underline{\mathbf{T}}$ as in the single transmission-line approach.
Unfortunately commercial software do not compute directly transmission matrices. Despite some interest in the last years for the study of periodic structures where multimodal coupling is particularly relevant, to the best of the author's knowledge general formulas for the practical calculation of this matrix are usually omitted in the literature. Note also that, due to the presence of total fields, the calculations are slightly lengthier than those for the matrix used in [112]. Here we propose a method employing the 4×4 impedance (or Z) matrix of the four-port unit cell, easily obtained with *ad-hoc* codes or with commercial software, to be converted to a transfer matrix.

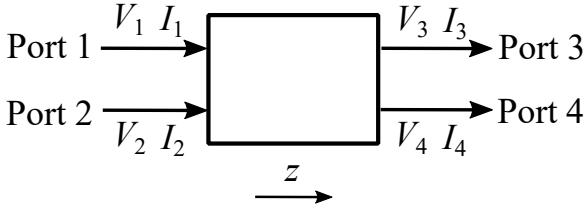

Fig. 2.2 The port numbering of the 4-port network.

The port numbering of the 4-port unit cell is shown in Fig. 2.2. According to the microwave network analysis [14], the impedance relates the voltages and currents are

$$\begin{bmatrix} V_1 \\ V_2 \\ V_3 \\ V_4 \end{bmatrix} = \begin{bmatrix} \underline{\mathbf{Z}}_{aa} & \underline{\mathbf{Z}}_{ab} \\ \underline{\mathbf{Z}}_{ba} & \underline{\mathbf{Z}}_{bb} \end{bmatrix} \cdot \begin{bmatrix} I_1 \\ I_2 \\ -I_3 \\ -I_4 \end{bmatrix} \tag{2.8}$$

where the minus signs of I_3 and I_4 depend on the direction chosen in 2.2 for these currents.

$$\underline{\mathbf{Z}}_{aa} = \begin{bmatrix} Z_{11} & Z_{12} \\ Z_{21} & Z_{22} \end{bmatrix}, \qquad \underline{\mathbf{Z}}_{ab} = \begin{bmatrix} Z_{13} & Z_{14} \\ Z_{23} & Z_{24} \end{bmatrix} \tag{2.9}$$

$$\underline{\mathbf{Z}}_{ba} = \begin{bmatrix} Z_{31} & Z_{32} \\ Z_{41} & Z_{42} \end{bmatrix}, \qquad \underline{\mathbf{Z}}_{bb} = \begin{bmatrix} Z_{33} & Z_{34} \\ Z_{43} & Z_{44} \end{bmatrix} \tag{2.10}$$

We can rewrite (2.8) into two different matrix equations as

$$-\begin{bmatrix} I_3 \\ I_4 \end{bmatrix} = \underline{\mathbf{Z}}_{ab}^{-1} \cdot \begin{bmatrix} V_1 \\ V_2 \end{bmatrix} - \underline{\mathbf{Z}}_{ab}^{-1} \cdot \underline{\mathbf{Z}}_{aa} \begin{bmatrix} I_1 \\ I_2 \end{bmatrix} \tag{2.11}$$

$$\begin{bmatrix} V_3 \\ V_4 \end{bmatrix} = \underline{\mathbf{Z}}_{bb} \cdot \underline{\mathbf{Z}}_{ab}^{-1} \begin{bmatrix} V_1 \\ V_2 \end{bmatrix} + (\underline{\mathbf{Z}}_{ba} - \underline{\mathbf{Z}}_{bb} \cdot \underline{\mathbf{Z}}_{ab}^{-1} \cdot \underline{\mathbf{Z}}_{aa}) \begin{bmatrix} I_1 \\ I_2 \end{bmatrix} \tag{2.12}$$

If we combine (2.11) and (2.12) together, we obtain

$$\begin{bmatrix} V_3 \\ V_4 \\ I_3 \\ I_4 \end{bmatrix} = \begin{bmatrix} \underline{\mathbf{Z}}_{bb} \cdot \underline{\mathbf{Z}}_{ab}^{-1} & \underline{\mathbf{Z}}_{ba} - \underline{\mathbf{Z}}_{bb} \cdot \underline{\mathbf{Z}}_{ab}^{-1} \cdot \underline{\mathbf{Z}}_{aa} \\ -\underline{\mathbf{Z}}_{ab}^{-1} & \underline{\mathbf{Z}}_{ab}^{-1} \cdot \underline{\mathbf{Z}}_{aa} \end{bmatrix} \begin{bmatrix} V_1 \\ V_2 \\ I_1 \\ I_2 \end{bmatrix} \tag{2.13}$$

Thus, the four-port transfer matrix is expressed as a function of the impedance matrix with the following expression

$$\underline{\mathbf{T}} = \begin{bmatrix} \underline{\mathbf{Z}}_{bb} \cdot \underline{\mathbf{Z}}_{ab}^{-1} & \underline{\mathbf{Z}}_{ba} - \underline{\mathbf{Z}}_{bb} \cdot \underline{\mathbf{Z}}_{ab}^{-1} \cdot \underline{\mathbf{Z}}_{aa} \\ -\underline{\mathbf{Z}}_{ab}^{-1} & \underline{\mathbf{Z}}_{ab}^{-1} \cdot \underline{\mathbf{Z}}_{aa} \end{bmatrix} \tag{2.14}$$

2.2.3 Conversion between S-parameters and Transfer Matrix

The formula (2.14) is useful to convert an impedance matrix to a transfer matrix, but very often microwave components are characterized with scattering parameters. Therefore, in this subsection we give formulas to convert S matrix to T matrices.
A 4×4 scattering matrix $\underline{\mathbf{S}}$ can be partitioned into four 2×2 blocks

$$\underline{\mathbf{S}} = \begin{pmatrix} s_{11} & s_{12} & s_{13} & s_{14} \\ s_{21} & s_{22} & s_{23} & s_{24} \\ s_{31} & s_{32} & s_{33} & s_{34} \\ s_{41} & s_{42} & s_{43} & s_{44} \end{pmatrix} = \begin{pmatrix} \underline{\mathbf{S}}_{ii} & \underline{\mathbf{S}}_{io} \\ \underline{\mathbf{S}}_{oi} & \underline{\mathbf{S}}_{oo} \end{pmatrix} \tag{2.15}$$

where the four block matrices are

$$\underline{\mathbf{S}}_{ii} = \begin{pmatrix} s_{11} & s_{12} \\ s_{21} & s_{22} \end{pmatrix}, \qquad \underline{\mathbf{S}}_{io} = \begin{pmatrix} s_{13} & s_{14} \\ s_{23} & s_{24} \end{pmatrix} \tag{2.16}$$

$$\underline{\mathbf{S}}_{oi} = \begin{pmatrix} s_{31} & s_{32} \\ s_{41} & s_{42} \end{pmatrix}, \qquad \underline{\mathbf{S}}_{oo} = \begin{pmatrix} s_{33} & s_{34} \\ s_{43} & s_{44} \end{pmatrix} \tag{2.17}$$

Similarly, the transfer matrix can be divided into four 2×2 blocks

$$\underline{\mathbf{T}} \cdot \begin{bmatrix} \mathbf{V} \\ \mathbf{I} \end{bmatrix} = \begin{bmatrix} \underline{\mathbf{T}}_{ii} & \underline{\mathbf{T}}_{io} \\ \underline{\mathbf{T}}_{oi} & \underline{\mathbf{T}}_{oo} \end{bmatrix} \cdot \begin{bmatrix} \mathbf{V} \\ \mathbf{I} \end{bmatrix} \tag{2.18}$$

As reported in [113], the transformation from the scattering matrix to the transfer matrix is

$$\underline{\mathbf{T}}_{ii} = \frac{1}{2}\underline{\mathbf{Z}}_i^{-1} \cdot \left[(\underline{\mathbf{I}} - \underline{\mathbf{S}}_{ii}) \cdot \underline{\mathbf{S}}_{oi}^{-1} \cdot (\underline{\mathbf{I}} + \underline{\mathbf{S}}_{oo}) + \underline{\mathbf{S}}_{io}\right] \cdot \underline{\mathbf{Z}}_o \tag{2.19}$$

$$\underline{\mathbf{T}}_{io} = -\frac{1}{2}\left[(\underline{\mathbf{I}} + \underline{\mathbf{S}}_{ii}) \cdot \underline{\mathbf{S}}_{oi}^{-1} \cdot (\underline{\mathbf{I}} + \underline{\mathbf{S}}_{oo}) - \underline{\mathbf{S}}_{io}\right] \cdot \underline{\mathbf{Z}}_o \tag{2.20}$$

$$\underline{\mathbf{T}}_{oi} = -\frac{1}{2}\underline{\mathbf{Z}}_i^{-1} \cdot \left[(\underline{\mathbf{I}} - \underline{\mathbf{S}}_{ii}) \cdot \underline{\mathbf{S}}_{oi}^{-1} \cdot (\underline{\mathbf{I}} - \underline{\mathbf{S}}_{oo}) - \underline{\mathbf{S}}_{io}\right] \tag{2.21}$$

$$\underline{\mathbf{T}}_{oo} = \frac{1}{2}\left[(\underline{\mathbf{I}} + \underline{\mathbf{S}}_{ii}) \cdot \underline{\mathbf{S}}_{oi}^{-1} \cdot (\underline{\mathbf{I}} - \underline{\mathbf{S}}_{oo}) + \underline{\mathbf{S}}_{io}\right] \tag{2.22}$$

where $\underline{\mathbf{I}}$ is the identity matrix, $\underline{\mathbf{Z}}_i$ and $\underline{\mathbf{Z}}_o$ are diagonal matrices whose diagonal elements are the characteristic impedances of input/output ports.

2.2.4 Choice of equivalent transmission lines at ports

Since we will study unit cells realized in SIW technology, a TE_{10} rectangular-waveguide mode will be defined on each one of their four ports. Equivalent associated transmission lines are required in order to define the voltages and currents of the state vector (2.5). More specifically, the characteristic impedances $\underline{\mathbf{Z}}_i$ and $\underline{\mathbf{Z}}_o$ of these transmission lines depend on the definition of the voltages and currents can be set to arbitrary numbers, by means of a suitable rescaling of the voltages and currents.

However, this is not a limitation of the method. It is easily shown that if the same voltage/current definition is kept for ports on opposite cell sides (which are connected when the cell is placed in a periodic configuration), the identity holds $\underline{\mathbf{Z}}_i = \underline{\mathbf{Z}}_o$. By rewriting (2.19)-(2.22) in a matrix form, we obtain

$$\underline{\mathbf{T}} = \underline{\mathbf{U}}^{-1} \cdot \underline{\mathbf{T}}_0 \cdot \underline{\mathbf{U}} = \begin{bmatrix} \underline{\mathbf{I}} & \underline{\mathbf{0}} \\ \underline{\mathbf{0}} & \underline{\mathbf{Z}}_i \end{bmatrix}^{-1} \cdot \underline{\mathbf{T}}_0 \cdot \begin{bmatrix} \underline{\mathbf{I}} & \underline{\mathbf{0}} \\ \underline{\mathbf{0}} & \underline{\mathbf{Z}}_o \end{bmatrix} \tag{2.23}$$

where the matrix in the middle, $\underline{\mathbf{T}}_0$ corresponds to the choice $\underline{\mathbf{Z}}_i = \underline{\mathbf{Z}}_o = \underline{\mathbf{I}}$. A different choice transforms the transfer matrix into a new matrix similar to $\underline{\mathbf{T}}_0$, as long as $\underline{\mathbf{Z}}_i = \underline{\mathbf{Z}}_o$. The eigenvalues are therefore not modified by modifying the definition of the transmission lines. In a practical implementation with a commercial software, the scattering matrix or the impedance matrix will then be computed by defining identical ports on opposite sides of the unit cell. This will be sufficient to grant a correct dispersion analysis.

It is also important to mention that the two ports on the same side of the unit cell can be defined on the same physical face of the unit cell. This is the case of the circular waveguide in Section 1.2.5.1, where two TE_{11} modes with different polarization are defined on the same face of the waveguide section. More generally, on the same physical face several modes could be defined, by obtaining a transfer matrix of larger dimensions. In several cases, this can enhance the accuracy of the analysis if the periodic unit cells interact among them by means of higher-order modes. In our structures this will not be necessary, so that 4×4 matrices will always be implied in the following.

2.2.5 Formulas for the conversion from scattering matrix to T matrix

The inverse transformations of (2.19)-(2.22) required to obtain the scattering matrix from the knowledge of the transfer matrix of a N-port network can be easily obtained. Since these formulas are not given in the literature, to the best of the author's knowledge, and they will be required later in this chapter, they are reported here.

$$\begin{aligned}
\underline{\mathbf{S}}_{ii} &= (-\underline{\mathbf{Z}}_i\underline{\mathbf{T}}_{ii}\underline{\mathbf{Z}}_o^{-1} - \underline{\mathbf{T}}_{io}\underline{\mathbf{Z}}_o^{-1} + \underline{\mathbf{Z}}_i\underline{\mathbf{T}}_{oi} + \underline{\mathbf{T}}_{oo}) \\
&\quad \cdot (\underline{\mathbf{Z}}_i\underline{\mathbf{T}}_{ii}\underline{\mathbf{Z}}_o^{-1} - \underline{\mathbf{T}}_{io}\underline{\mathbf{Z}}_o^{-1} - \underline{\mathbf{Z}}_i\underline{\mathbf{T}}_{oi} + \underline{\mathbf{T}}_{oo})^{-1} && (2.24) \\
\underline{\mathbf{S}}_{oo} &= (\underline{\mathbf{Z}}_i\underline{\mathbf{T}}_{ii}\underline{\mathbf{Z}}_o^{-1} - \underline{\mathbf{T}}_{io}\underline{\mathbf{Z}}_o^{-1} + \underline{\mathbf{Z}}_i\underline{\mathbf{T}}_{oi} - \underline{\mathbf{T}}_{oo}) \\
&\quad \cdot (\underline{\mathbf{Z}}_i\underline{\mathbf{T}}_{ii}\underline{\mathbf{Z}}_o^{-1} - \underline{\mathbf{T}}_{io}\underline{\mathbf{Z}}_o^{-1} - \underline{\mathbf{Z}}_i\underline{\mathbf{T}}_{oi} + \underline{\mathbf{T}}_{oo})^{-1} && (2.25) \\
\underline{\mathbf{S}}_{oi} &= 2(\underline{\mathbf{Z}}_i\underline{\mathbf{T}}_{oo}\underline{\mathbf{Z}}_o^{-1} - \underline{\mathbf{T}}_{io}\underline{\mathbf{Z}}_o^{-1} - \underline{\mathbf{Z}}_i\underline{\mathbf{T}}_{oi} + \underline{\mathbf{T}}_{oo})^{-1} && (2.26) \\
\underline{\mathbf{S}}_{io} &= 2\underline{\mathbf{T}}_{oo} - (\underline{\mathbf{I}} + \underline{\mathbf{S}}_{ii})\underline{\mathbf{S}}_{oi}^{-1}(\underline{\mathbf{I}} - \underline{\mathbf{S}}_{oo}) && (2.27)
\end{aligned}$$

More details about the inversion of these formulas can be found in the Appendix.

2.3 Modal Couplings for DBE Conditions

As discussed in Chapter 1, the DBE is a degeneracy of four Bloch modes (two propagating modes and two evanescent modes). In order to achieve it, we need a unit cell supporting at least two modes per direction (each described as a transmission line). Furthermore, the unit cell needs to provide a suitable coupling among these modes. We assume here a unit-cell topology (Fig. 2.3) of length d, composed of a two transmission-

line sections of length d_1, connected to a lossless and reciprocal four-port coupler, followed by another pair of transmission-line section of the same length d_1 (with no loss of generality). The two transmission lines are identical, as in the majority of the structures recently proposed to achieve a DBE conditions. As shown in [35], two different lines could also be used in order to obtain a further degree of freedom, but this possibility will not be used in the following analysis. As it will be clear from the results, different coupler topologies can indeed achieve DBE by using identical CTLs.

The two transmission lines are assumed uniform and identical, describing waveguide modes with cutoff frequency $f_c = c\frac{k_c}{2\pi}$, where c is the free-space light velocity and k_c is the modal transverse wavenumber. The propagation constant is therefore [76]

$$k_z = \sqrt{k^2 - k_c^2} \tag{2.28}$$

The transfer matrix of one single line is [14]

$$\underline{\mathbf{T}} = \begin{pmatrix} \cos k_z d_1 & -jZ_0 \sin k_z d_1 \\ -jY_0 \sin k_z d_1 & \cos k_z d_1 \end{pmatrix} \tag{2.29}$$

where $Y_0 = 1/Z_0$, d_1 is the length of the line. The normalized T matrix of the two lines is

$$\begin{pmatrix} V_3 \\ Z_0 I_3 \\ V_4 \\ Z_0 I_4 \end{pmatrix} = \begin{pmatrix} \cos k_z d_1 & -j \sin k_z d_1 & 0 & 0 \\ -j \sin k_z d_1 & \cos k_z d_1 & 0 & 0 \\ 0 & 0 & \cos k_z d_1 & -j \sin k_z d_1 \\ 0 & 0 & -j \sin k_z d_l & \cos k_z d_1 \end{pmatrix} \begin{pmatrix} V_1 \\ Z_0 I_1 \\ V_2 \\ Z_0 I_2 \end{pmatrix} \tag{2.30}$$

The order of the voltage and currents in the state vector is different than in (2.5) in order to highlight the block structure of (2.30). Of course this has no impact on the eigenvalues of the matrices, as long as the same variable ordering is used when multiplying

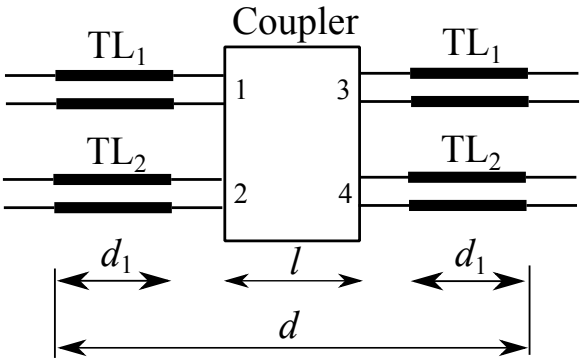

Fig. 2.3 Schematic of unit cell with one coupler.

different T matrices inside the same cell. Also, currents in (2.30) are normalized with respect to the port characteristic impedance, so that this parameter does not appear in the matrix. As seen in (2.23), as long as this normalization is the same on opposite ports, the eigenvalue results are not affected.

In the following sections, we look for conditions on the coupler scattering parameters capable to reach a DBE. These conditions will guide the design of a number of SIW unit-cells exhibiting DBE. The model based on T-matrix computation of ideal components is particularly interesting since it is very general (not limited of course to SIW lines) and very efficient, so that many numerical analysis can be easily carried out. Unfortunately, analytical formulas cannot be obtained with this model, due to the mathematical complexity of the DBE condition (null hyperdistance among the four eigenvectors of the problem (2.7)), so it is more amenable to a numerical than an analytical solution. It is important to note that analytical conditions for DBE synthesis are available for coupled *uniform* transmission lines. However, those analyses rely on the existence of an equivalent circuit-model description of the transmission lines. Therefore, it can be not directly applicable to the design of a cell of the kind of Fig. 2.3. We analyze here three cases where the components of the unit cells are different. By analyzing the three following cases, we find the connections between the S-parameters of couplers and the existence of DBE. The couplers are defined on the basis of their scattering matrix, as usual in microwave four-port structures.

2.3.1 Case 1: Perfectly Matched Directional Coupler

In this first paragraph, the coupler is assumed to be perfectly matched at all its ports, and its schematic is shown in Fig. 2.4 together with its port numbering. p represents the transmission coefficient between ports connecting the same transmission line (Ports 1 and 3, Ports 2 and 4), and q represents the cross-coupling between the diagonal ports connecting different transmission lines (Ports 1 and 4, Ports 2 and 3).

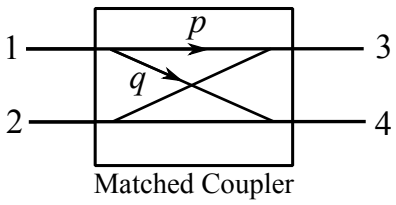

Fig. 2.4 Schematic of a matched coupler. p represents the transmission coefficient between Ports 1 and 3, Ports 2 and 4. q represents the cross-coupling between Ports 1 and 4, Ports 2 and 3.

The S-parameters fulfil the reciprocal conditions $S_{ij} = S_{ji}$ and lossless conditions: $\mathbf{S} \cdot (\mathbf{S}^*)^T = \mathbf{I}$ [14]. This means that two real parameters p and q and a phase ϕ describe the directional coupler. p is magnitude of the direct coupling between ports 1 and 3 and

between ports 2 and 4, while q is the cross coupling between ports 1 and 4 and between ports 2 and 3. ϕ is the phase of the direct coupling. The coupling magnitudes verify the constraint $p^2 + q^2 = 1$, so that only the parameter p is assumed independent in the following analysis. Two choices can be done to verify the constraint, thus obtaining two different couplers:

1. Symmetric Coupler:

$$\underline{\mathbf{S}}_1 = \begin{pmatrix} 0 & 0 & p \cdot e^{j\phi} & jq \cdot e^{j\phi} \\ 0 & 0 & jq \cdot e^{j\phi} & p \cdot e^{j\phi} \\ p \cdot e^{j\phi} & jq \cdot e^{j\phi} & 0 & 0 \\ jq \cdot e^{j\phi} & p \cdot e^{j\phi} & 0 & 0 \end{pmatrix} \tag{2.31}$$

2. Antisymmetric Coupler:

$$\underline{\mathbf{S}}_2 = \begin{pmatrix} 0 & 0 & p \cdot e^{j\phi} & q \cdot e^{j\phi} \\ 0 & 0 & -q \cdot e^{j\phi} & p \cdot e^{j\phi} \\ p \cdot e^{j\phi} & -q \cdot e^{j\phi} & 0 & 0 \\ q \cdot e^{j\phi} & p \cdot e^{j\phi} & 0 & 0 \end{pmatrix} \tag{2.32}$$

The overall T matrix of the unit cell is

$$\underline{\mathbf{T}}_{total} = \underline{\mathbf{T}}_{TL} \cdot \underline{\mathbf{T}}_{coupler} \cdot \underline{\mathbf{T}}_{TL} \tag{2.33}$$

where the transmission matrix of the coupler can be converted from its S-parameters according to (2.19)-(2.22). Then, the unit cell dispersion relation is obtained by solving the eigenvalue problem using the overall T matrix.

To assess if the unit cell in Fig. 2.4 can achieve a DBE condition, we compute the hyperdistance (1.14) among the eigenvectors of (2.33). If the value of the hyperdistance is zero, then a DBE point is met. This computation is performed in the frequency interval from dc to $2f_c$. By referring to a rectangular waveguide configuration (the one used in the SIW designs later in this chapter), beyond the frequency $2f_c$, higher-order modes start propagating and the analysis is no more accurate. These higher-order modes need to be included in the model by adding additional access point to the unit cell and leading to a larger T matrix. However, this possibility is not relevant here: the unit cell would be electrically large at those frequencies, so we aim at a DBE synthesis within this frequency limit.

Another important point should be stressed here. The coupler parameters are here assumed constant with respect to frequency. Obviously, this hypothesis is never verified for real couplers. However, the problem to be solved is narrowband (the eigenvalue is

solved at each frequency). If a DBE condition is met at a frequency $\hat{f}$ with a certain coupler, this means that the required coupler needs to have the selected S parameters at $\hat{f}$, while they will vary at other frequencies. It should be noted that the transmission-line sections at the side of the coupler could be included in the coupler definition. However, their presence is useful to keep a frequency dispersion typical of waveguide modes (cut-off frequency, etc) of the unit cell, while keeping a simple description for the coupler. Of course the design presented later in the second part of this chapter will take into account the correct frequency dispersion of the unit-cell parameters by means of full-wave simulations.

Unfortunately, the eigenvectors of (2.33) cannot be determined in closed form. For this reason, an extensive numerical analysis is performed over the values $p \in [0, 1]$, the phase $\phi \in [0, \pi]$, and the period $d \in [\lambda_c/4, \lambda_c]$, λ_c being the cutoff wavelength. For each combination of parameters we compute the hyperdistance at each frequency point in $f \in [0, 2f_c]$ and we show the minimum of this distance. A zero will reveal that a DBE is met at a frequency point within the considered range. A number different from zero will show that no DBE is achievable with the selected parameters.

In the following, two different sizes are considered for the coupler, as a fraction of the period.

1. The length of the coupler is $d/4$, the length of each transmission-line section is therefore $d_1 = 3d/8$.

   The hyperdistance diagram of the coupler defined by (2.31) is shown in Fig. 2.5a, and the coupler defined by (2.32) is shown in Fig. 2.5b. The color of the point on the plane indicates the hyperdistance value, and the color mapping is showed on the right side of the diagram.

2. The length of the coupler is $d/2$, the length of each transmission-line section is therefore $d_1 = d/4$.

   The hyperdistance diagrams of the coupler defined by (2.31) or by (2.32) are shown in Fig. 2.6a and Fig. 2.6b.

Resuming the results shown in these hyperdistance diagrams, it is seen that it is impossible to achieve a DBE condition with a fully matched coupler. For the coupler whose S-parameters are $\underline{\mathbf{S}}_1$, the hyperdistances are all near 1. For the coupler with S-parameters of $\underline{\mathbf{S}}_2$, the hyperdistances may have lower values, but stay well above 0, so no DBE is obtained. It means that other types of unit-cell models must be explored to obtain DBE points.

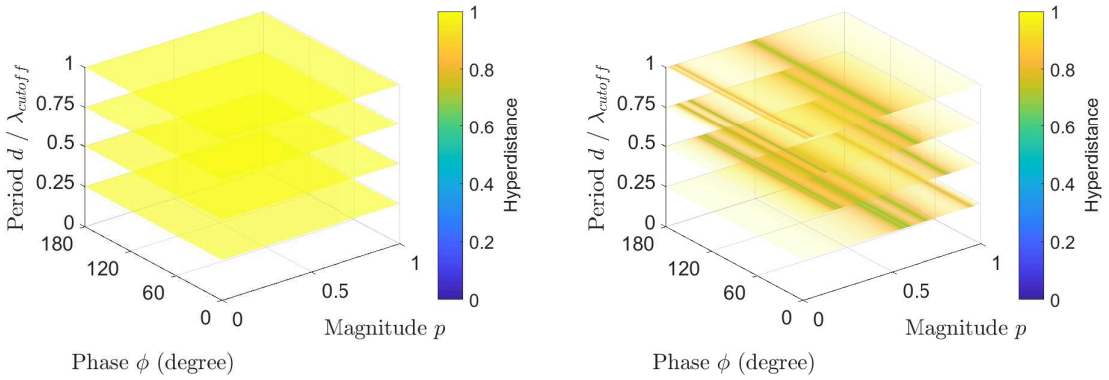

(a) coupler defined by $\underline{\mathbf{S}}_1$ in (2.31) **(b)** coupler defined by $\underline{\mathbf{S}}_2$ in (2.32)

Fig. 2.5 Hyperdistance diagram of the the unit-cell model (Fig. 2.3) with a matched coupler. The coupler's length is $d/4$.

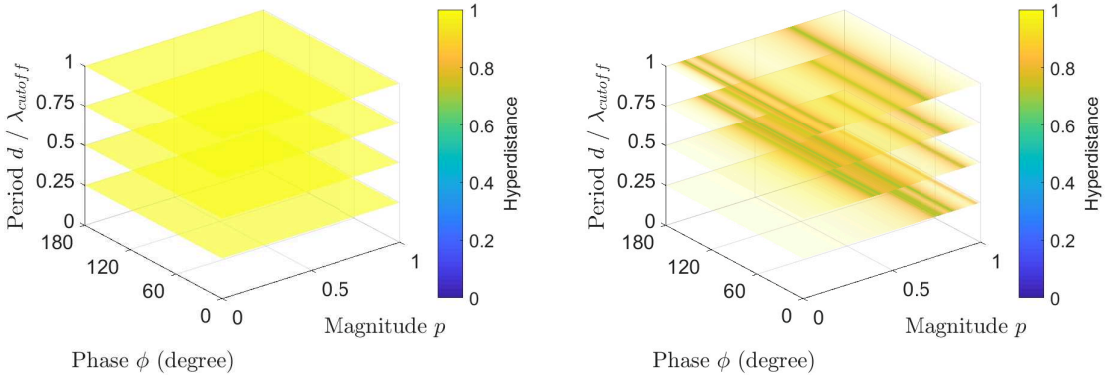

(a) coupler defined by $\underline{\mathbf{S}}_1$ in (2.31) **(b)** coupler defined by $\underline{\mathbf{S}}_2$ in (2.32)

Fig. 2.6 Hyperdistance diagram of the the unit-cell model (Fig. 2.3) with a matched coupler. The coupler's length is $d/2$.

2.3.2 Case 2: The Unit Cell Consists of One Unmatched Symmetric Coupler

Here the complexity of the coupler is increased, by admitting a level of mismatch at the ports. However, we still keep a fully symmetric form of the coupler. This means that $s_{11} = s_{22} = s_{33} = s_{44}$, $s_{12} = s_{34}$, $s_{14} = s_{32}$. The schematic is shown in Fig.2.7.
The scattering matrix of this coupler is

$$\underline{\mathbf{S}}_3 = \begin{pmatrix} h \cdot e^{j\phi_1} & -jg \cdot e^{j\phi_2} & p \cdot e^{j\phi_1} & jq \cdot e^{j\phi_2} \\ -jg \cdot e^{j\phi_2} & h \cdot e^{j\phi_1} & jq \cdot e^{j\phi_2} & p \cdot e^{j\phi_1} \\ p \cdot e^{j\phi_1} & jq \cdot e^{j\phi_2} & h \cdot e^{j\phi_1} & -jg \cdot e^{j\phi_2} \\ jq \cdot e^{j\phi_2} & p \cdot e^{j\phi_1} & -jg \cdot e^{j\phi_2} & h \cdot e^{j\phi_1} \end{pmatrix} \tag{2.34}$$

where the real numbers p, q, g, h are the coupling magnitudes described in Fig. 2.7, and the constraints due to the lossless and reciprocal conditions are: $p^2+q^2+g^2+h^2 = 1$ and $ph = gq$. Among the four parameters p, q, g, h, two of them are therefore independent.

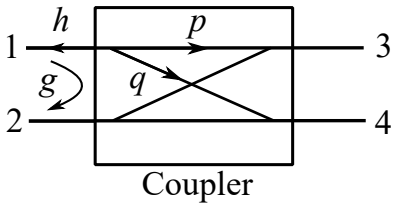

Fig. 2.7 Schematic of signal flow in the mismatched symmetric coupler. h represents the magnitude of the reflection coefficient, g, p, q are the magnitude of transmission coefficients between ports on the same side, aligned on the opposite side, and on the diagonal corners, respectively.

We assume them to be p and q, together with the two phases ϕ_1, ϕ_2 related to these two free parameters.

Due to the large number of parameters to consider, different analyses are performed. For each of the following cases, the minimum hyperdistance in the frequency interval $[0, 2f_c]$ is shown, for couplers whose length is $d/4$ and $d/2$. As in the previous section, different period lengths are considered.

1. We sweep p and q in the intervals $p \in [0, 1]$ and $q \in [0, 1]$. We keep fixed the phases ϕ_1 and ϕ_2 for different values (minimum hyperdistance in Fig. 2.8a).

2. We sweep ϕ_1 and ϕ_2 in the intervals $\phi_1 \in [0, \pi]$ and $\phi_2 \in [0, \pi]$. We keep fixed the magnitude p and q for different values (minimum hyperdistance in Fig. 2.9).

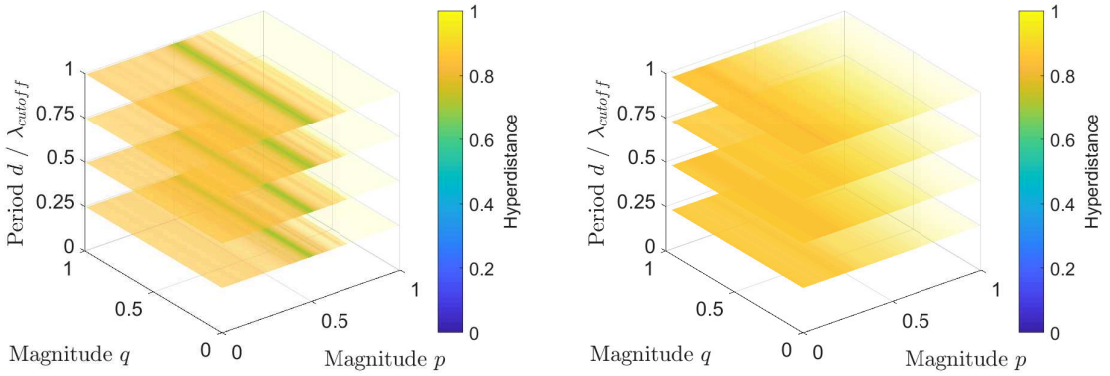

(a) $\phi_1 = \phi_2 = 0$ **(b)** $\phi_1 = \pi/6, \phi_2 = \pi/4$

Fig. 2.8 Hyperdistance diagram of the unit-cell model (Fig. 2.3) with an unmatched coupler. The coupler length is $d/4$.

Again, no DBE is found in these configurations, as the hyperdistance is clearly never even close to a null. The results collected so far show that a symmetric coupling between identical transmission lines is not sufficient to generate a DBE response, but we need also a suitable level of asymmetry in the way we couple the lines: e.g., $s_{14} \neq s_{23}$. This will lead in turn to a fully asymmetric coupler design having for example also $s_{11} \neq s_{22}$.

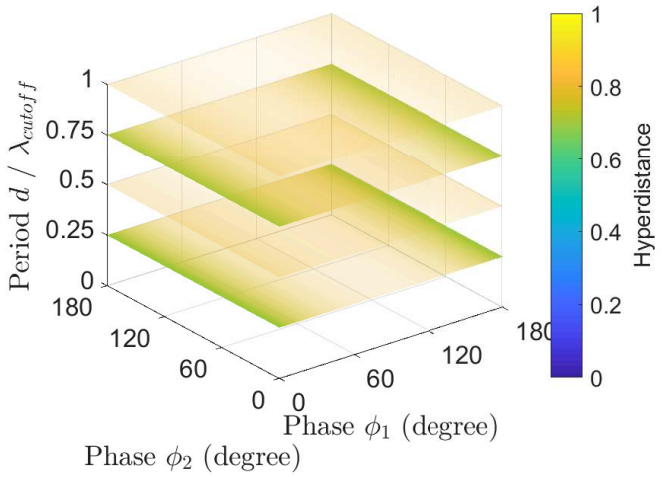

Fig. 2.9 Hyperdistance diagram of the unmatched coupler whose $p = 0.3, q = 0.1$. The coupler length is $d/4$.

2.3.3 Case 3: Asymmetric Coupler Formed with Two Misaligned Symmetric Couplers

In order to visualize the effect of coupling asymmetries capable to produce a DBE, we choose not to perform parametric analyses of general scattering matrices, due to the large number of free parameters and the lack of physical insight that would be gained. Instead, we recur to the basic ideas of the DBE condition achieved in the circular waveguide by means of two rotated rings assuring the coupling of two degenerate orthogonal TE_{11} (Section 1.2.5.1). Simple parametric analyses confirm that one ring only is not sufficient to achieve a DBE condition. The presence of two *rotated* rings introduce the required asymmetry in the unit cell.

Here we investigate the introduction of an asymmetric coupling between identical lines by considering a unit cell analogous to the one in Section 1.2.5.1: a coupler is here composed by the cascade of a symmetric element in (2.34), a transmission-line section, and a second identical element rotated with respect to the previous one. The rotation operation is particular interesting for several reasons. By modifying the rotation angle at a fixed frequency, we transition from a perfectly symmetric coupler to an asymmetric one. If the DBE is met for a suitable angle, the S parameters evolution can be tracked and their values can be used as guidelines to design practical DBE in different waveguide technologies (SIW in our case). The rotation operation is also interesting since it can be described in a simple analytical approach, as it is described later in this paragraph.

The schematic of the unit cell is shown in Fig. 2.10. The unit cell can be divided into three parts: two uncoupled transmission lines touching the two boundaries of the cell, and a coupler between the lines. This coupler in turn is composed of a symmetric

coupler, a transmission-line section and a rotated symmetric coupler.

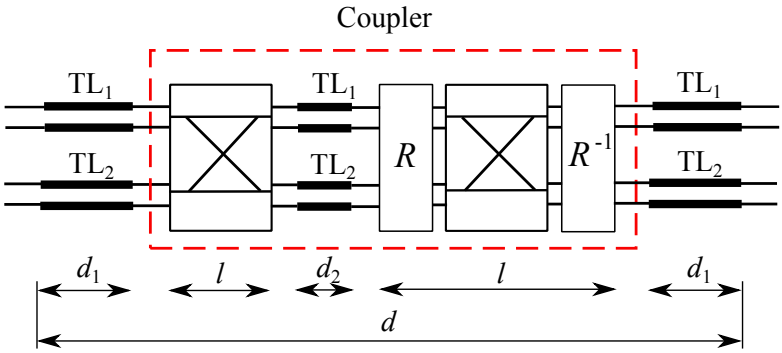

Fig. 2.10 Schematic of unit cell with two misaligned symmetric couplers in a circular waveguide.

The S-parameters of the two symmetric couplers have the same form as $\underline{\mathbf{S_3}}$ in (2.34). In a circular waveguide, the rotation of a scatterer can be performed on its transmission matrix with a simple analytical formulation, as discussed in [114]. Since voltages and currents are associated to transverse fields of waveguide modes, a rotation R_θ of an angle θ on them has the same effect of a rotation of these modal fields. To fix the ideas, let us rotate the tangential electric field of a mode with $m\phi$ angular dependence. Two degenerate modes are present, one with $\cos$ and the other with $\sin$ dependence:

$$E_{mn}^{\cos}(\rho,\phi) = J_m\left(k_{mn}\rho\right)\cos\left(m\phi\right) \tag{2.35}$$

$$E_{mn}^{\sin}(\rho,\phi) = J_m\left(k_{mn}\rho\right)\sin\left(m\phi\right) \tag{2.36}$$

The coordinate rotation of θ of these two modes is

$$R_\theta E_{mn}^{\cos}(\rho,\phi) = \cos(m\theta)E_{mn}^{\cos}(\rho,\phi) - \sin(m\theta)E_{mn}^{\sin}(\rho,\phi) \tag{2.37}$$

$$R_\theta E_{mn}^{\sin}(\rho,\phi) = \sin(m\theta)E_{mn}^{\cos}(\rho,\phi) + \cos(m\theta)E_{mn}^{\sin}(\rho,\phi) \tag{2.38}$$

Once the coordinates are rotated, the original transmission matrix can be used in the rotated coordinates. After the effect of the coupler, the original coordinates should be recovered by means of an opposite rotation $R_{-\theta}$ for the last part of the unit cell.
The transformations (2.37)-(2.38) can be expressed in a matrix form by means of the rotation matrix $\underline{\mathbf{R}}$ acting on the voltages/currents (we suppose the presence of a circular-waveguide TE_{11} modes)

$$\underline{\mathbf{R}}\begin{pmatrix} V_3 \\ Z_0 I_3 \\ V_4 \\ Z_0 I_4 \end{pmatrix} = \begin{pmatrix} \cos\theta & 0 & \sin\theta & 0 \\ 0 & \cos\theta & 0 & \sin\theta \\ -\sin\theta & 0 & \cos\theta & 0 \\ 0 & -\sin\theta & 0 & \cos\theta \end{pmatrix}\begin{pmatrix} V_3 \\ Z_0 I_3 \\ V_4 \\ Z_0 I_4 \end{pmatrix} \tag{2.39}$$

The overall T matrix of the rotated coupler is therefore

$$\underline{\mathbf{T}}_{rotated\,coupler} = \underline{\mathbf{R}} \cdot \underline{\mathbf{T}}_{coupler} \cdot \underline{\mathbf{R}}^{-1} \tag{2.40}$$

and the T matrix of the unit cell is

$$\underline{\mathbf{T}}_{total} = \underline{\mathbf{T}}_{TL1} \cdot \underline{\mathbf{T}}_{coupler} \cdot \underline{\mathbf{T}}_{TL2} \cdot \underline{\mathbf{R}} \cdot \underline{\mathbf{T}}_{coupler} \cdot \underline{\mathbf{R}}^{-1} \underline{\mathbf{T}}_{TL1} \tag{2.41}$$

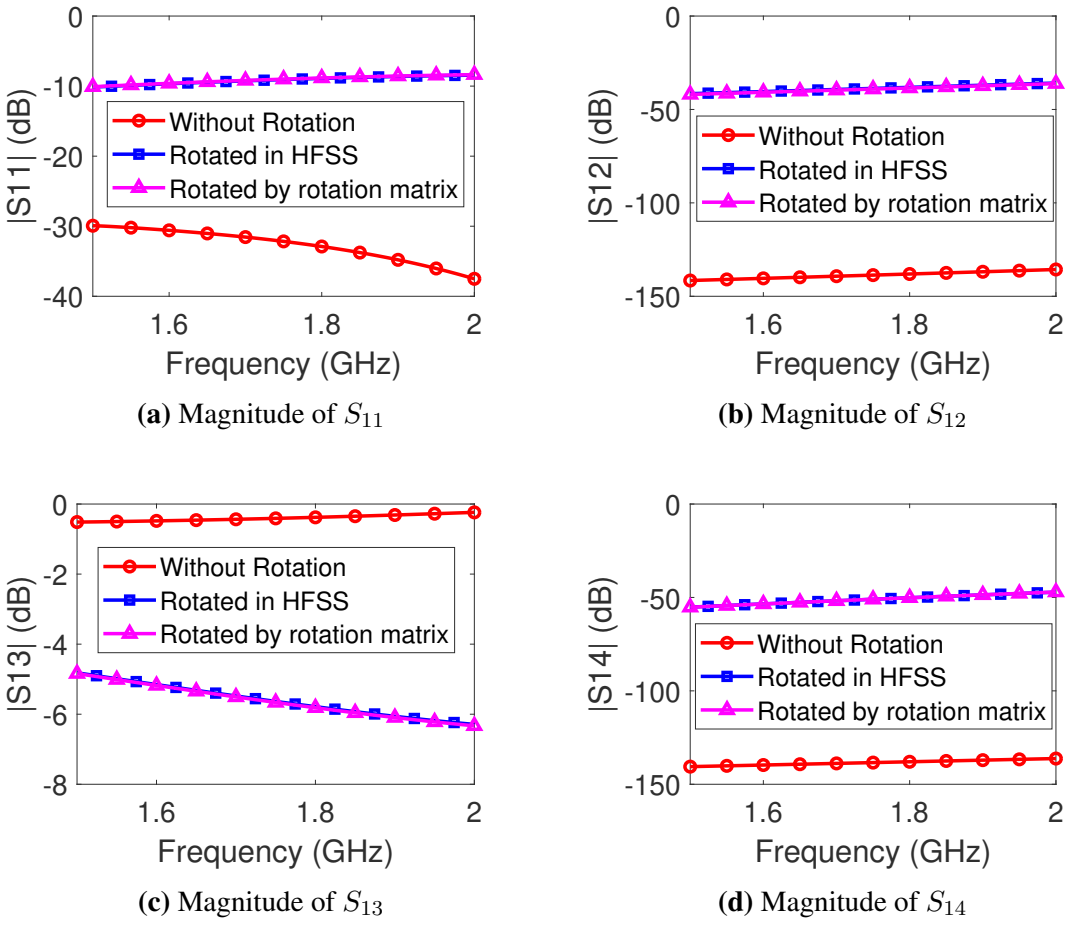

(a) Magnitude of S_{11}

(b) Magnitude of S_{12}

(c) Magnitude of S_{13}

(d) Magnitude of S_{14}

Fig. 2.11 S parameters comparison of circular waveguide's ring rotated in HFSS or rotated using the rotation matrix R

We verify the rotation matrix $\underline{\mathbf{R}}$ method using a ring structure in circular waveguide from [6] (see Fig.1.11). With the commercial software HFSS we simulate the ring scattering parameters with and without rotation where the rotation angle θ is 72°. For the rotation matrix method, we firstly convert the S parameters of ring without rotation to a T matrix and then use (2.40) to get the T matrix of the rotated coupler. At last, we convert back the rotated T matrix to an S matrix and compare with the simulation of the rotated ring results from HFSS. In Fig. 2.11, the magnitudes of S_{11}, S_{12}, S_{13}, and S_{14} from HFSS and from the rotation matrix method fit well with each other, which

verifies the effectiveness of the rotation matrix method. The other S parameters are also compared and fit well, but they are not showed here for brevity.

Here we search for a DBE point with this unit-cell model at a selected frequency of $1.4f_c$. Since there are several variables to be determined, some of them are set to be constant to limit the degrees of freedom. We set $q = 0.2, \phi_1 = \phi_2 = 0$ but keep p and rotation angle θ to be variables. The hyperdistance diagram in Fig. 2.12 shows some regions in the parametric space where nulls of the hyperdistance appear at the chosen frequency, confirming the existence of DBEs.

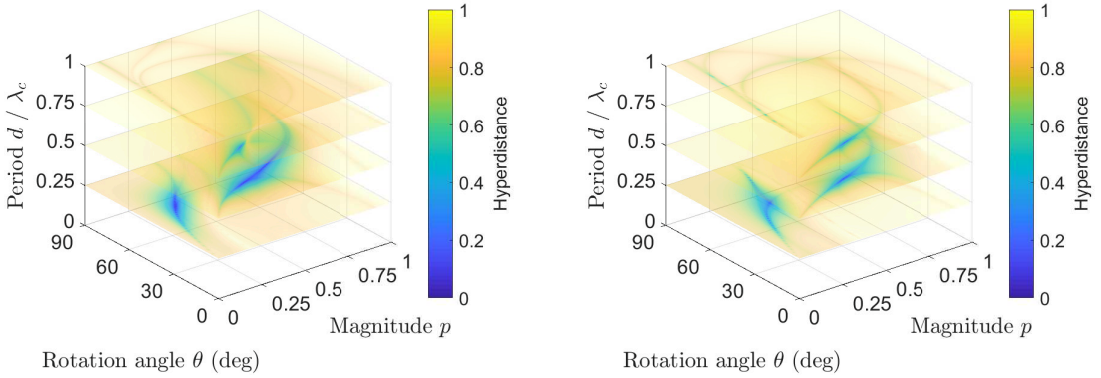

(a) $q = 0.2$ **(b)** $q = 0.4$

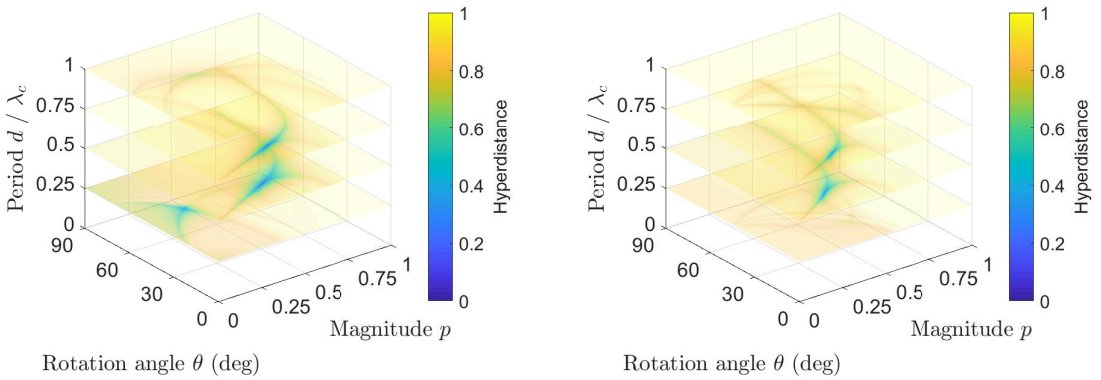

(c) $q = 0.6$ **(d)** $q = 0.8$

Fig. 2.12 Hyperdistance diagram of the unit-cell model in Fig. 2.10. The length of each coupler is $0.375d$, the two transmission-line lengths are $d_1 = 0.05d, d_2 = 0.15d$. We assume $q = 0.2, \phi_1 = \phi_2 = 0$.

To verify the DBE existence using the dispersion relation, we choose the point $p = 0.161, \theta = 47.7°, d = 0.25\lambda_c$ corresponding to a null of the hyperdistance to plot the corresponding dispersion diagram in Fig. 2.13 which fits the typical dispersion curve as shown in Fig. 1.2. This confirms that this unit-cell can achieve a DBE at the chosen frequency. Different frequencies in the range $[f_c, 2f_c]$ would lead to other solutions for the θ, p parameters, but not to remarkable differences.

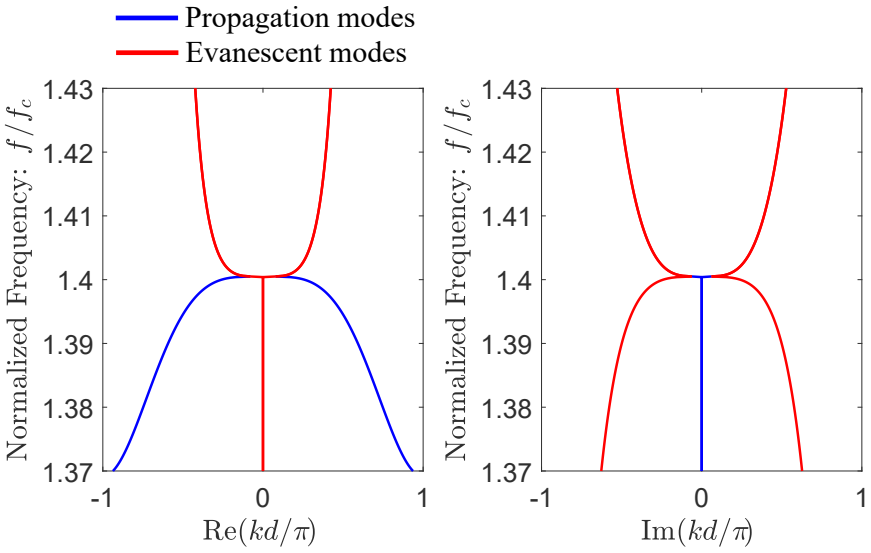

Fig. 2.13 The dispersion diagram to verify the DBE point on the hyperdistance plane. The parameters for the unit cell are: $p = 0.161, q = 0.2, \phi_1 = \phi_2 = 0, \theta = 47.7°, d = 0.25 \cdot \lambda_c$. The DBE frequency is at $1.4 f_c$.

2.3.3.1 Relationship between S-parameters and the Existence of DBE

We have found points in the parameter space of Fig. 2.13 corresponding to dispersion diagram with a DBE point. We study now the scattering parameters of the complete coupler composed of the first coupler and the rotated one. We will track the scattering parameters as the rotation angle varies, from the absence of rotation (symmetric coupler) to the angle leading to the DBE condition. This evolution will give us qualitative information on the kind of coupler required to obtain a DBE condition in a general configuration (not necessarily composed of two misaligned sub-couplers).
For this task we use the formulas (2.42), in order to compute the scattering matrix starting from a 4-port transmission matrix. We first cascade the T matrices of the sub-elements to get the T matrix of the equivalent coupler

$$\underline{\mathbf{T}}_{eq} = \underline{\mathbf{T}}_{coupler} \cdot \underline{\mathbf{T}}_{TL2} \cdot \underline{\mathbf{R}} \cdot \underline{\mathbf{T}}_{coupler} \cdot \underline{\mathbf{R}}^{-1} \underline{\mathbf{T}}_{TL1} \tag{2.42}$$

Then, we use the formulas (2.24)-(2.27) to compute the scattering matrix of the coupler starting from a 4-port transmission matrix. We consider several cases to explore the evolution of the scattering parameters in the complex plane towards the DBE point.
In Fig. 2.14, the S parameters of the complete couplers are shown as the θ angle varies. We notice that the perfectly symmetry for $\theta = 0°$ is broken as the angle starts varying. The DBE is met for couplers characterized by a strong mismatch at least at one or two input ports (s_{ii} coefficients close to unitary magnitude) and a different phase of these coefficients. This was expected, since perfectly matched couplers tend to be symmetric, and they cannot reach a DBE point as shown in Section 2.3.1. Conversely, the introduc-

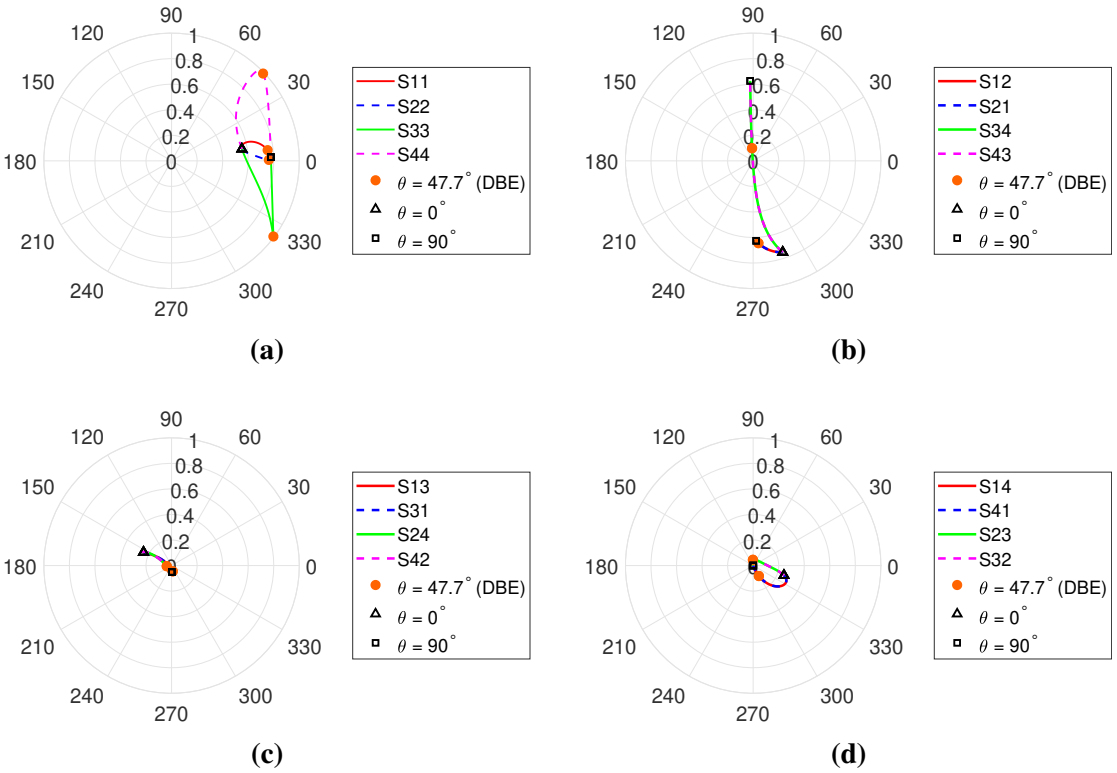

Fig. 2.14 Polar plots of S parameters in coupler of Fig. 2.10, when $p = 0.161$, $q = 0.2$, $d = 0.25\lambda_c$, θ from $0°$ to $90°$

tion of a strong mismatch allows for a significant asymmetry in the cross-coupling.
In addition to this condition, one or two of the other coupling parameters have a much higher level with respect to the other ones. In Figs. 2.14 and 2.16, a strong s_{12} is obtained if compared to the other coefficients. In Figs. 2.15 and 2.17 strong s_{12} and s_{34} are obtained. In Figs. 2.18 and 2.19, higher s_{12} and s_{34} are found, together with higher cross coupling s_{14} and s_{23}, which is associated to a slightly smaller reflection level at the ports.
These qualitative conditions are sufficient in order to obtain a DBE point in a unit cell of the chosen period. As a summary, the ideal unit-cell candidate for a DBE structure, should provide

- a strong reflection at some ports
- a privileged propagation path between two of the four ports.

Even if these are not necessary conditions, they can be useful guidelines in order to design a unit-cell topology as a starting-point to be subsequently fine tuned and provide a DBE.

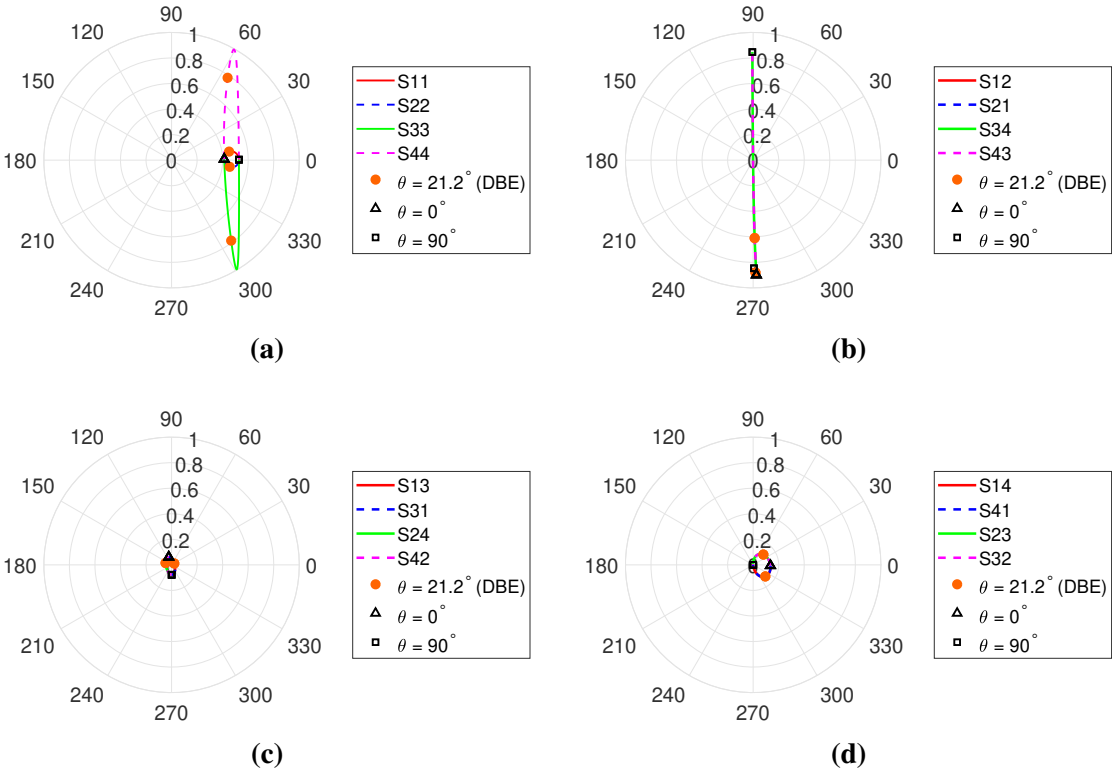

Fig. 2.15 Polar plots of S parameters in coupler of Fig. 2.10, when $p = 0.321$, $q = 0.2$, $d = 0.5\lambda_c$, θ from $0°$ to $90°$

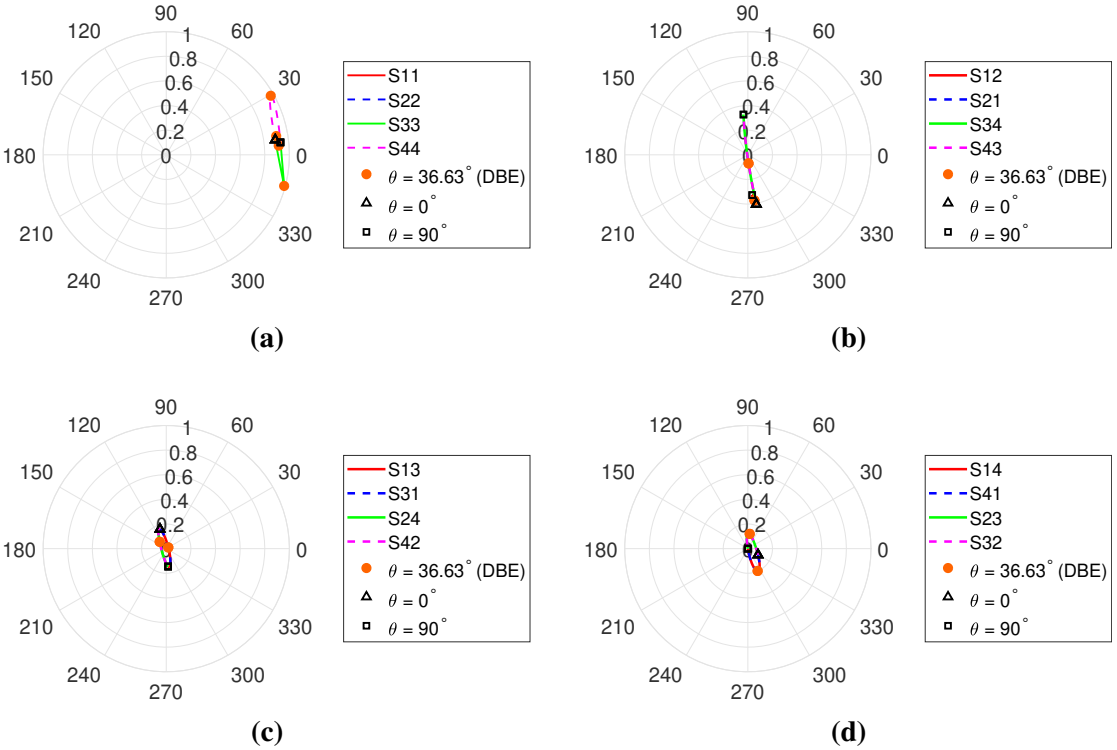

Fig. 2.16 Polar plots of S parameters in coupler of Fig. 2.10, when $p = 0.141$, $q = 0.4$, $d = 0.25\lambda_c$, θ from $0°$ to $90°$.

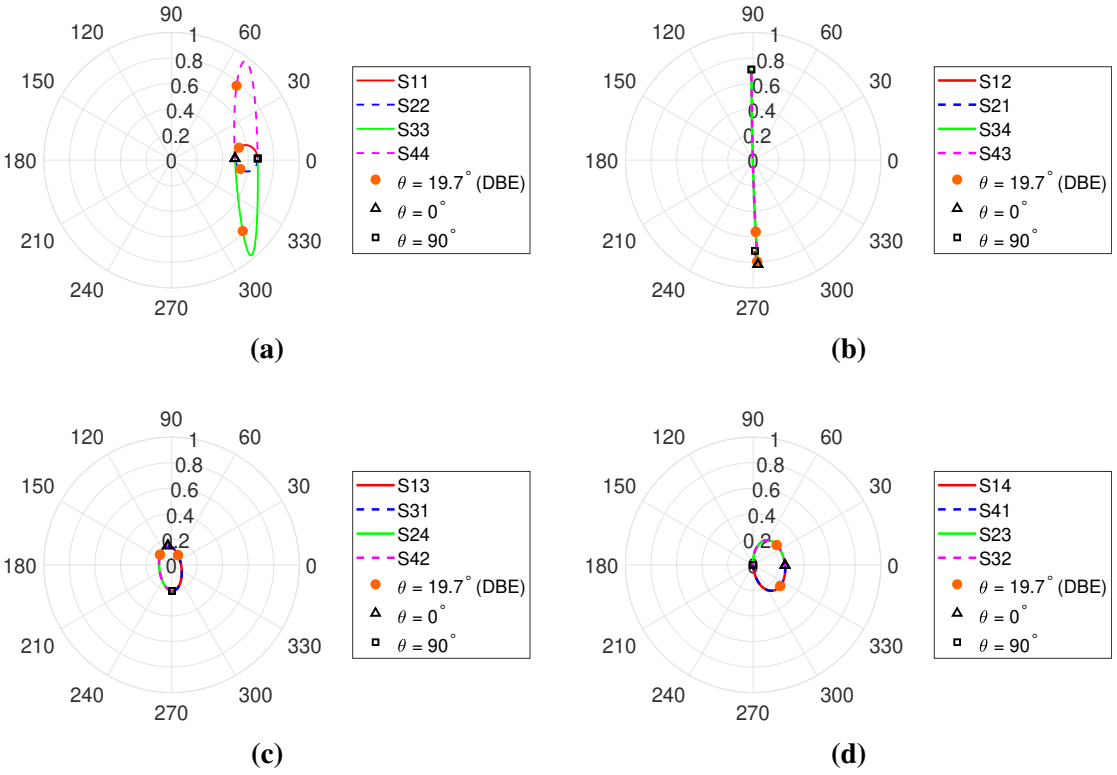

Fig. 2.17 Polar plots of S parameters in coupler of Fig. 2.10, when $p = 0.421$, $q = 0.4$, $d = 0.5\lambda_c$, θ from $0°$ to $90°$

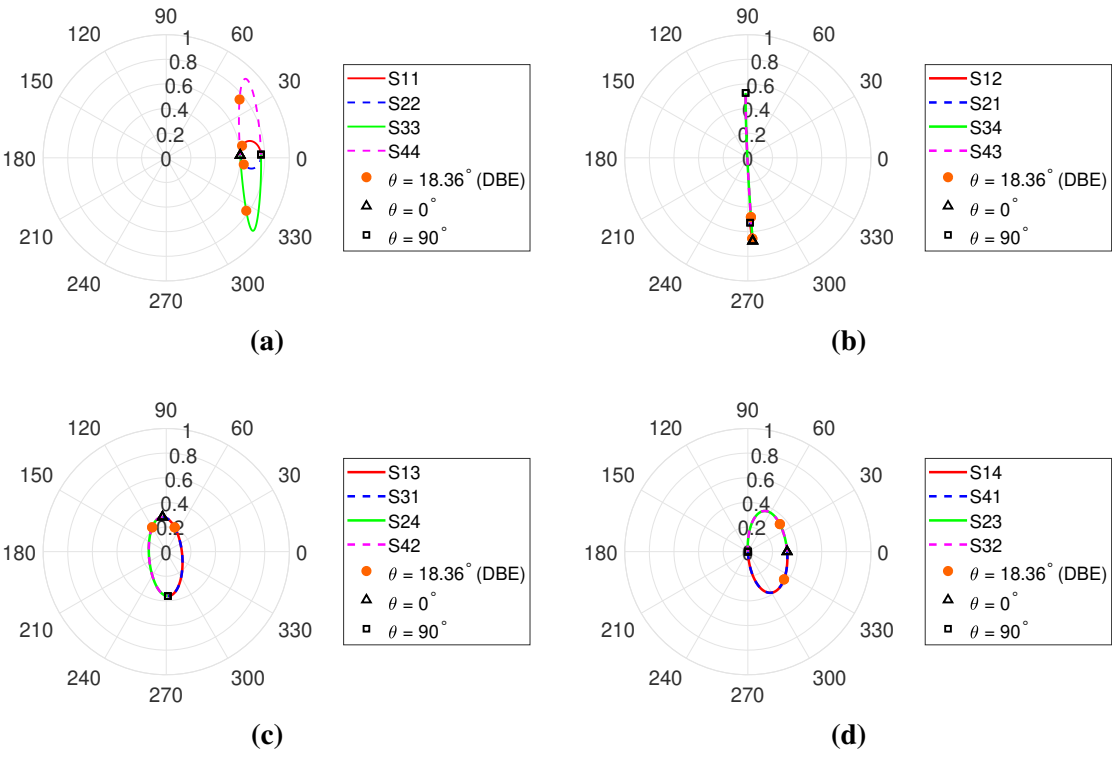

Fig. 2.18 Polar plots of S parameters in coupler of Fig. 2.10, when $p = 0.411$, $q = 0.6$, $d = 0.5\lambda_c$, θ from $0°$ to $90°$.

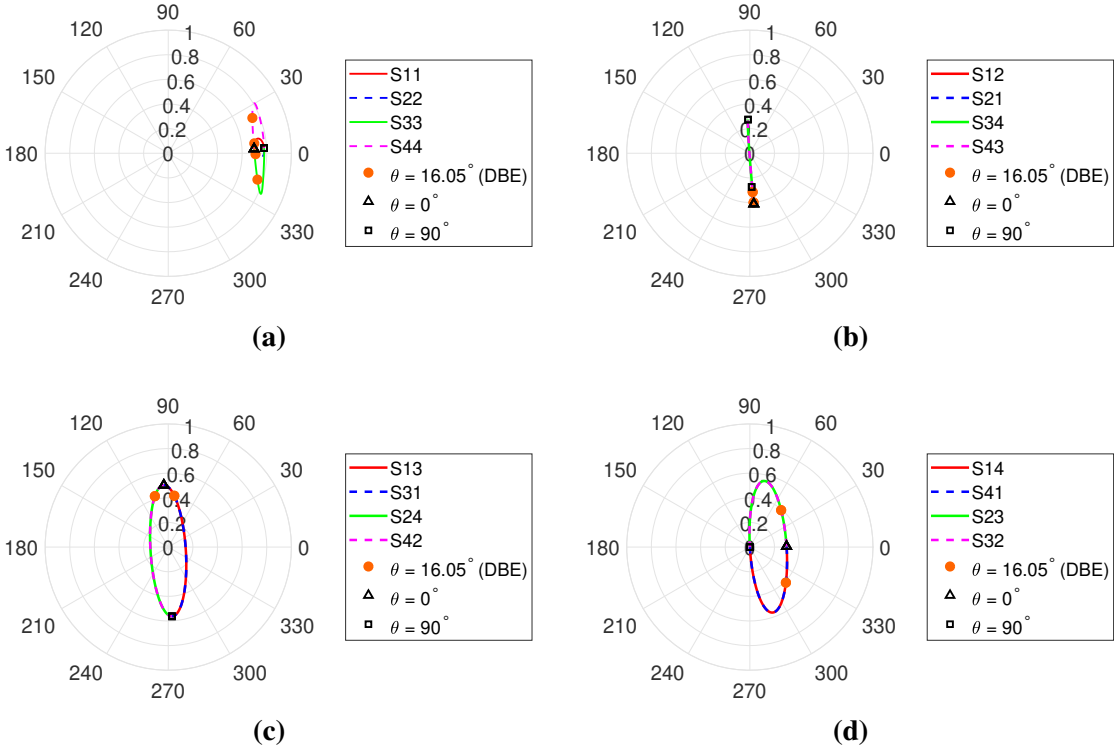

Fig. 2.19 Polar plots of S parameters in coupler of Fig. 2.10, when $p = 0.281$, $q = 0.8$, $d = 0.5\lambda_c$, θ from $0°$ to $90°$

2.4 SIW-DBE Unit Cell Designs

In this section, we will implement a few designs of SIW-DBE unit cells inspired by the conclusions of the previous section. In the first part, we propose a design with a coupler composed of two sub-elements, which can be considered analogous to the circular waveguide with DBE in [6]. In the second part, we will shorten the original coupler by transforming it to a single-element coupler, following the rules in 2.3.3.1. Four different designs are thus proposed. The first design uses two oblique lines of vias and one coupling gap, which can be seen as a simplified version of the two-coupler SIW-DBE cell by removing one coupling gap. The second design uses one oblique line of vias and one coupling gap to explore the simplest way to implement the coupler with DBE. In the third design, we explore if other structures (such as an array of air vias) can also synthesize the proper coupler. In the last design, we further simplify the unit cell by minimizing the presence of vias, which can be beneficial for the practical implementation of the structure in different technologies. Finally, in order to reduce the dielectric losses impact on DBE, we propose three low-loss designs: one employs a low-loss substrate, and other two utilize air-filled SIWs.
For the convenience of comparison, we give these designed structures short names as “long cell”, “double-oblique-line cell”, “single-oblique-line cell”, “air-via cell”, “corner cell”, “low-loss-substrate cell”, “air-filled cell 1”, “air-filled cell 2”, respectively.

2.4.1 Unit Cell with Two Coupling Gaps (“long cell”)

Inspired by the misaligned metal rings introducing DBE in circular waveguide [6], we first try using similar physical structures to demonstrate DBE in SIWs. We use two identical parallel SIWs supporting the same fundamental TE_{10} mode. The two modes are coupled with two oblique lines of vias and coupling gaps inside each unit cell. The coupling gaps are chosen to provide the cross couplings, and the oblique lines of vias provide rotations between coupled models.
The geometry of the “long cell” is shown in Fig. 2.20. The structure of Fig. 2.3 is visible, with two waveguides on the sides of the cell and a central coupler formed here of two oblique lines and two coupling gaps between the SIW waveguides. The topology formed with the via distributions is a very good example of how the guidelines obtained in the study of ideal couplers in the previous sections can help the choice of the geometry. In fact, the unit cell is expected to offer a stronger reflection at the four input ports because of the presence of the oblique lines (stronger at ports 1 and 4 than at ports 2 and 3). This reflection can be tuned by increasing the density of pins along these lines. Also, two different propagation paths exist between ports in the two SIW waveguides. The path joining port 1 to 4 is expected to be privileged by the orientation

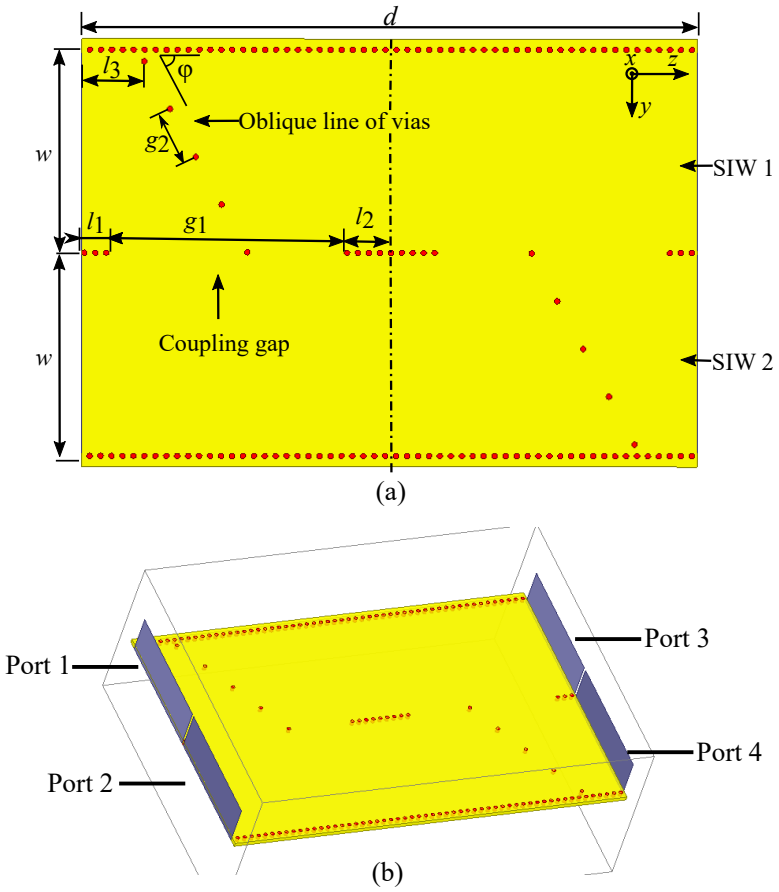

Fig. 2.20 Geometry of the "long cell" SIWs-DBE design. (a) Top view with the definition of the relevant parameters. (b) 3-D view with the definition of the access ports.

of the pin, and again the value of the transmission coefficient (in magnitude and phase) can be tuned by the angle φ of the lines and the density of vias. These properties will be later verified on the optimized geometry.

The width w is 30 mm, the period d is 90 mm and the thickness of the substrate is 1 mm. For the parallel vias of the SIWs, the radius is 0.8 mm and the distance between consecutive via is 1.6 mm. The lengths of the middle via lines $l_1 = 4$ mm and $l_2 = 6.8$ mm, respectively. The length of the coupling gap $g_1 = 34.2$ mm. The length from the starting point of oblique line to the left border $l_3 = 9.1$ mm and the distance between the oblique vias $g_2 = 8$ mm. The material of the substrate is Rogers RO3010, whose relative permittivity is 10.2. The vias and the ground plane are perfect electric conductors (PECs), and, at this stage, the structure is assumed to be lossless.

The mode-coupling parts in the unit cell affect the existence of DBE, and the oblique line's misalignment angle φ and position l_3 are two main parameters in order to perform a fine tuning of the structure and to obtain a DBE. In Fig. 2.21 (a), we report the dispersion diagram for three different misalignment angles, $\varphi = 60°$, $\varphi = 61.7°$ and $\varphi = 63°$, and the oblique line's position is fixed to $l_3 = 9.2$ mm. These simulations have been performed with the frequency-domain finite-element solver of commercial

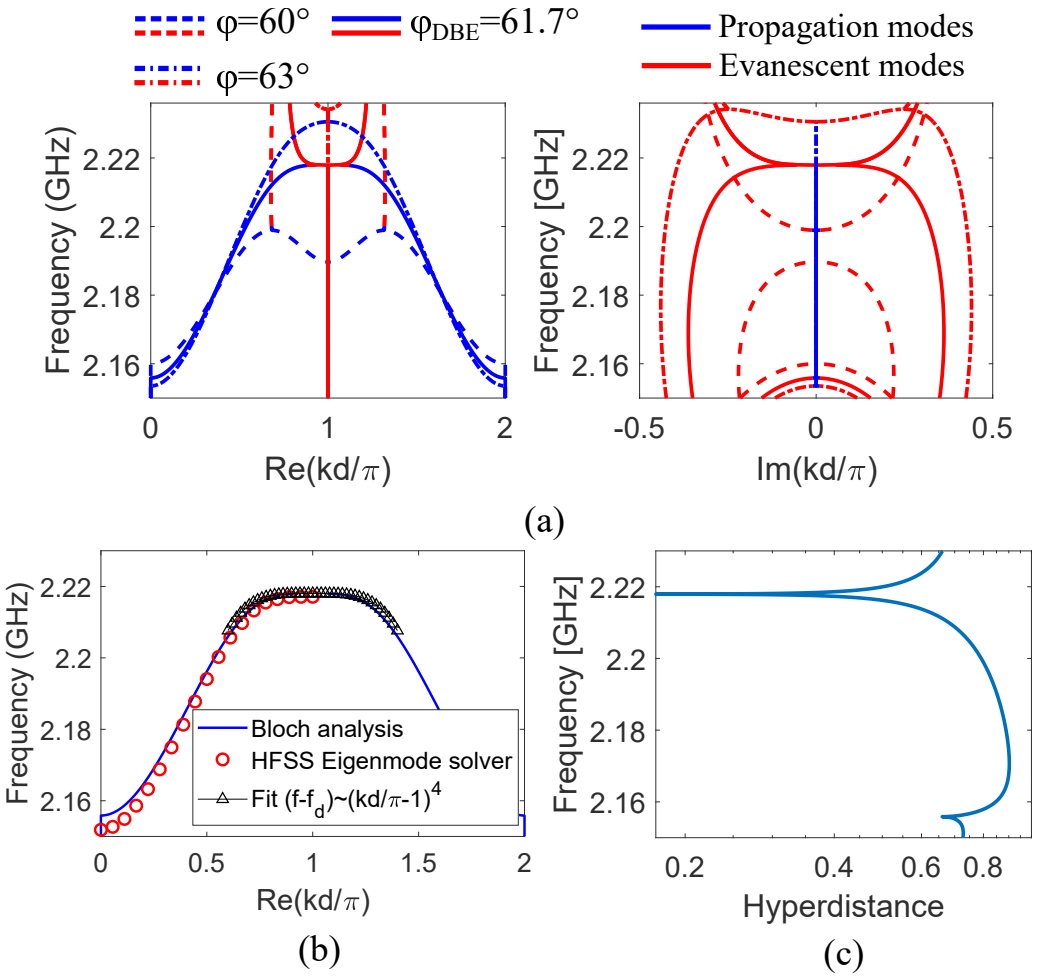

Fig. 2.21 The dispersion diagram of "long cell" design without considering losses. (a) The dispersion relation for different misalignment angles. (blue curves represent the propagation modes, red curves represent the evanescent modes.) (b) The dispersion diagram when DBE is achieved. (c) Hyperdistance of "long cell" design without losses.

software HFSS. The full-wave solver computes the multimodal S parameters of a single cell and the multimodal Z matrix. In each simulation, the excitations at the four ports are defined as 'wave port' with the fundamental TE_{10} mode. The accuracy for the 'maximum delta S' is set as 5×10^{-3}. The Z matrix from HFSS is used to compute the T matrix according to the (2.14). After computing the T matrix, we solve the Floquet eigenvalue problem to obtain dispersion relations, and from the values of the hyperdistance among the four eigenvectors we can verify the presence of a DBE point. Based on the simulation results, we find that, for different misalignment angles, we can always get an RBE point, but the DBE point is more difficult to obtain. When φ increased from $60°$ to $61.7°$, the dispersion curve of propagating modes becomes more flat and the four Bloch modes tend to degenerate together. When the misalignment angle is increased to $63°$, the dispersion curves separate from each other, i.e., the four Bloch modes do not align to each other and it is impossible to achieve a DBE. In conclusion, the DBE point exists for $\varphi_{DBE} = 61.7°$, and the dispersion curve is shown in

Fig. 2.21 (b). As desired, the four modes degenerate into one point in the dispersion diagram, thus meeting the definition of the DBE condition.

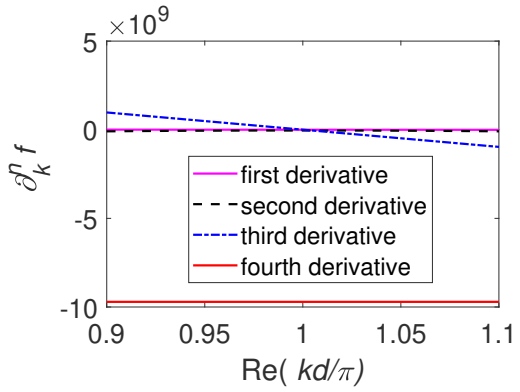

Fig. 2.22 The four derivatives of the dispersion curve near DBE point for the "long cell" design. The first, second and third derivatives are all zero at the Brillouin edge and the fourth derivative is a constant of -9.71×10^9, which meets the definition of the DBE.

According to (1.3), at the DBE point, the first three derivatives $\partial_k^n f \ (n \in \{1,2,3\})$ should be zero at the DBE (namely, the first-order derivative is the group velocity $\partial_k \omega = 0$). Therefore, if these constraints on the first derivatives are satisfied, we can confirm that there is a DBE point. The four derivatives near the DBE point are shown in Fig. 2.22, which satisfies the constraints and proves the existence of the DBE point. The constant α in (1.3) can be computed as $\alpha = \partial_k^4 f/24$. In this case, we obtain $\alpha = -4.05 \times 10^8\,\mathrm{m^4 s^{-1}}$ for a DBE frequency at $f_{DBE} = 2.218$ GHz, as shown in Fig. 2.21 (b). Then, the knowledge of α can lead to plot the fitting curve $f - f_{DBE} = \alpha\,(k - k_d)^4$ in Fig. 2.21 (b). A root-mean-square error (RMSE) is in the order of $\sim 10^{-4}$, indicating that a very good fit is obtained with this fourth-order local approximation, as expected close to DBE points. We also show the hyperdistance plot in Fig. 2.21 (c) to confirm that the four Bloch vectors coalesce. A clear sharp peak of the hyperdistance going to zero is observed close to the DBE frequency as expected.

The S parameters of the coupler used in the optimized unit cell are depicted in Fig. 2.23. As expected, the coupler is of the kind seen in the previous section. All the reflection coefficients s_{ii} are large, two being close to unity magnitude, and only one off-diagonal term (the s_{14}) is dominant with respect to the others. This confirms the results of the analysis discussed at the end of Section 2.3.3.

Moreover, we use the eigensolver tool in HFSS to plot the Brillouin diagram as a validation of the transmission-matrix method. Of course this method does not allow for the computation of the hyperdistance and of the evanescent modes coalescing together with the real modes at DBE. For this reason these results can validate the analysis done by revealing a fourth-order behaviour of the real Bloch-mode, but cannot replace the analysis based on the transmission matrix and its associated eigenvalue problem. The results of

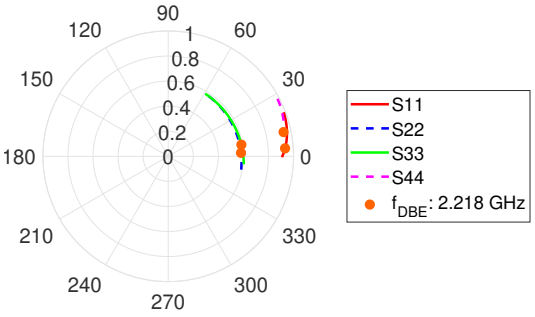

(a) Polar Plot of S_{11}, S_{22}, S_{33}, S_{44}.

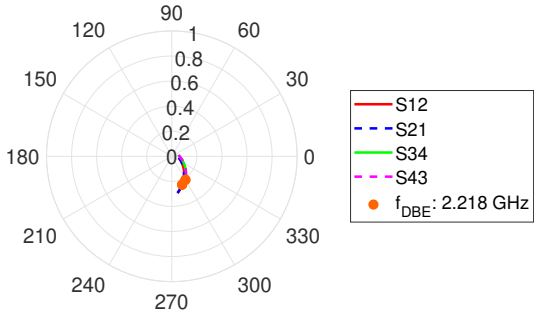

(b) Polar Plot of S_{12}, S_{21}, S_{34}, S_{43}.

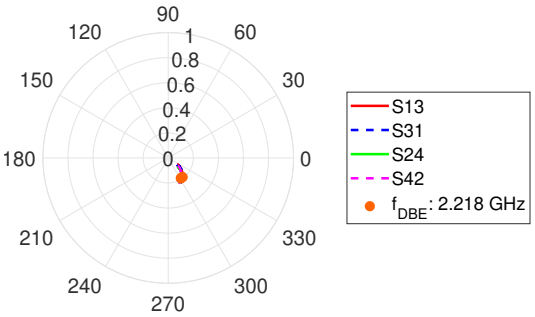

(c) Polar Plot of S_{13}, S_{31}, S_{24}, S_{42}.

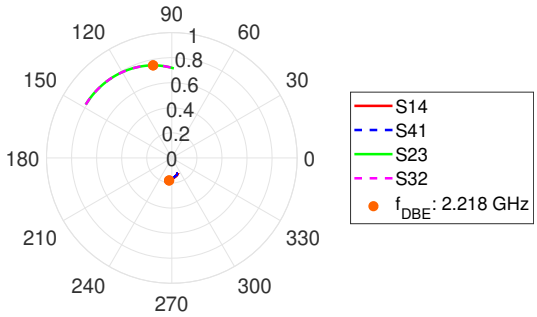

(d) Polar Plot of S_{14}, S_{41}, S_{23}, S_{32}.

Fig. 2.23 Polar plot of scattering parameters of the coupler part of " long cell" design in the frequency range 2.15 GHz - 2.236 GHz.

the eigensolver HFSS tool fit well with Bloch analysis results in Fig 2.21(b). This also confirms that neglecting higher-order modes of SIWs in the transmission matrix (which would have required a matrix of larger dimension than 4×4) was a correct hypothesis: these modes are neglected in the transmission-matrix computation but not in the HFSS eigensolver. The agreement between the methods confirm that higher-order modes do not play a significant role in the coupling among the discontinuities of the waveguides. Using the eigensolver, we also obtain the field distribution inside a unit cell at the DBE frequency, shown in Fig. 2.24. We can see how the oblique lines couple the two modes between the different SIWs.

Since the DBE is achieved in a lossless situation, losses should be considered because they prevent the degeneracy of the Bloch modes, i.e. the existence of the DBE point. Losses in SIW include conductor losses, dielectric losses and leakage through the via wall, but leakage is here negligible when the via wall satisfies the rules in [76]. The dielectric losses are determined by the loss tangent of the substrate (3.5×10^{-3} for Rogers RO3010). In Fig. 2.25a, after considering losses, the dispersion shows a smooth behaviour near the band edge and the DBE point is not perfectly degenerated. Furthermore, if we consider conductor losses and dielectric losses separately, we can see that dielectric losses is the main contribution to total losses. The hyperdistance results confirm this conclusion (Fig. 2.25b): while the hyperdistance of the lossless case is

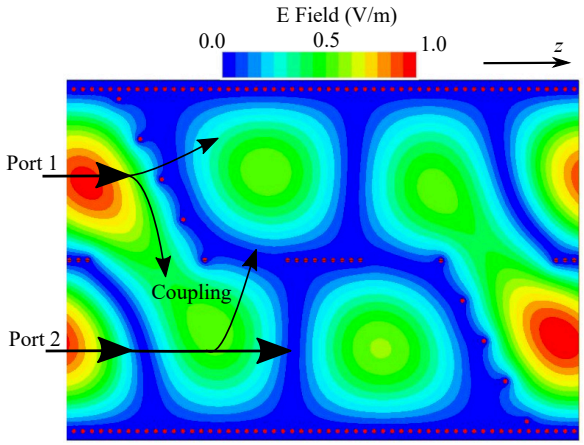

Fig. 2.24 The E-field distribution for the unit cell in Fig. 2.20.

zero, it stays above 0.4 after considering the losses. The hyperdistance invcluding only the dielectric losses is larger than the one only considering the conductor losses, which confirms that the dielectric losses are the main source of losses. Furthermore, we notice that a thicker SIW can reduce the influence of copper losses. In Fig. 2.26 (a) and (b), if we only consider the conductor losses, after increasing the thickness from 0.5 mm to 2 mm, the hyperdistance is decreased from 0.47 to 0.36. As expected, as shown in Fig. 2.26, the thickness does not affect the influence of dielectric losses.

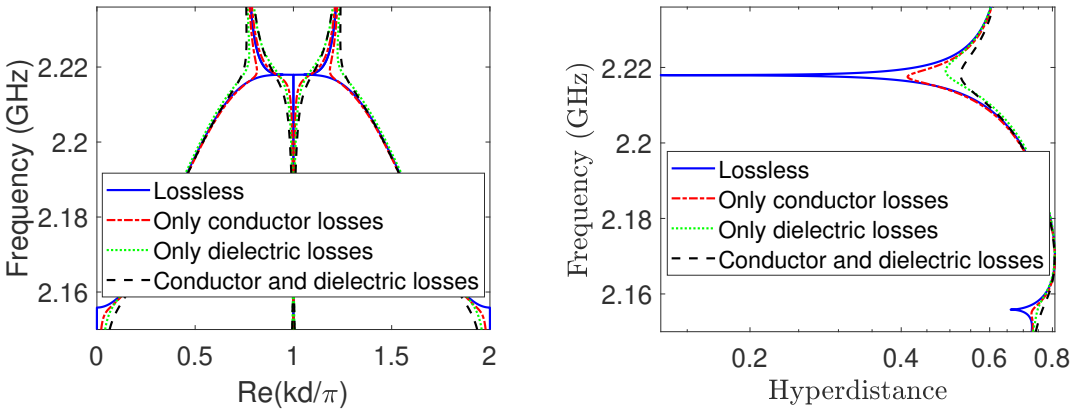

Fig. 2.25 Loss influence on DBE of "long cell" design. (a) Dispersion relation considering different losses influence (only conductor losses, only dielectric losses, and both of them). (b) Hyperdistance considering different losses influence.

In conclusion, the Bloch analysis method is in perfect agreement with independent results. The guidelines developed in the previous sections led to a geometrical configuration which, upon optimization, could successfully develop DBE in a periodic SIWs structure.

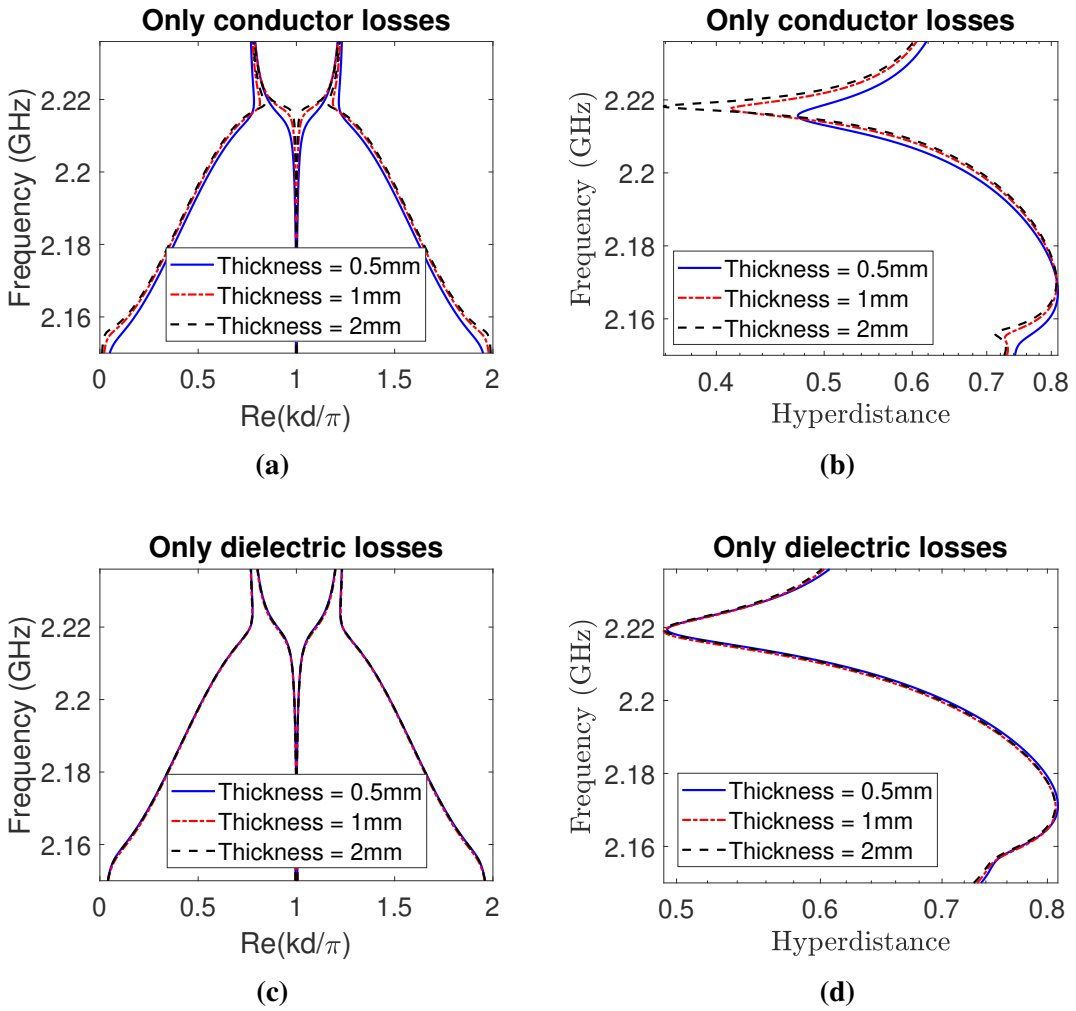

Fig. 2.26 Relationship between thickness and losses in the "long cell" design. (a) Dispersion relation of "long cell" with only conductor losses in different thicknesses (0.5mm, 1mm, 2mm). (b) Hyperdistance of "long cell" with only conductor losses in different thicknesses (0.5mm, 1mm, 2mm). (c) Dispersion relation of "long cell" with only dielectric losses in different thicknesses (0.5mm, 1mm, 2mm). (d) Hyperdistance of "long cell" with only dielectric losses in different thicknesses (0.5mm, 1mm, 2mm).

2.4.2 Compact Unit Cell with Two Oblique Lines of Vias ("double-oblique-line cell")

We design now a coupler with only one coupling gap and two oblique lines of vias to acquire the DBE, in Fig. 2.27.

The two oblique lines of vias are placed in front of ports 1 and 4, which makes ports 2 and 3 have strong reflections. An asymmetric response among different ports is certainly obtained, since the reflection coefficients at ports 2 and 3 are expected to be smaller than those at ports 1 and 3. The two oblique lines also enhance the cross coupling between ports 1 and 4 while suppressing the one between ports 2 and 3. Thus, the oblique line of vias blocks the wave propagation, making the cross coupling between port 1-4 stronger than port 2-3. This is expected to potentially lead again to a DBE response after fine tuning of the unit cell. The S parameters of the unit cell will be computed after the optimization in order to confirm this reasoning.

The distance between the vias in the oblique line is g_2 =9 mm. The oblique line's angle $\varphi_{DBE} = 63.4°$, and its position l_2 =24 mm. The via's diameter, the separation of the parallel vias, and the parameters of the substrate are the same as the "long cell" we proposed above. The width of the SIW follows w =20 mm. The period d =45 mm. The overall size of the unit cell is 40 mm × 45 mm. The length of the gap g_1 =25 mm, and l_1 =10 mm. The substrate material is Rogers RO3010, whose $\epsilon_r = 10.2$ and loss tangent is 3.5×10^{-3}.

The lossless dispersion diagram is shown in Fig. 2.28(a), where the DBE point is achieved at 2.53 GHz. It is verified that the hyperdistance is a null at the DBE point in Fig. 2.28(b), which indicates the existence of DBE.

In Fig. 2.29 the scattering parameters of the optimized unit cell are shown. As expected, a strong asymmetry is obtained on the diagonal elements (s_{22} and s_{33} have high magnitude, while s_{11} and s_{44} are negligible), and only one off-diagonal element (s_{14}) has much larger magnitude than the others.

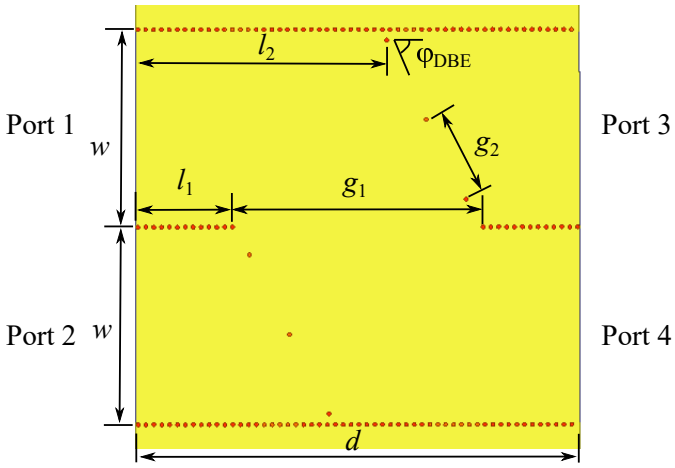

Fig. 2.27 Geometry of the "double-oblique-line cell" design.

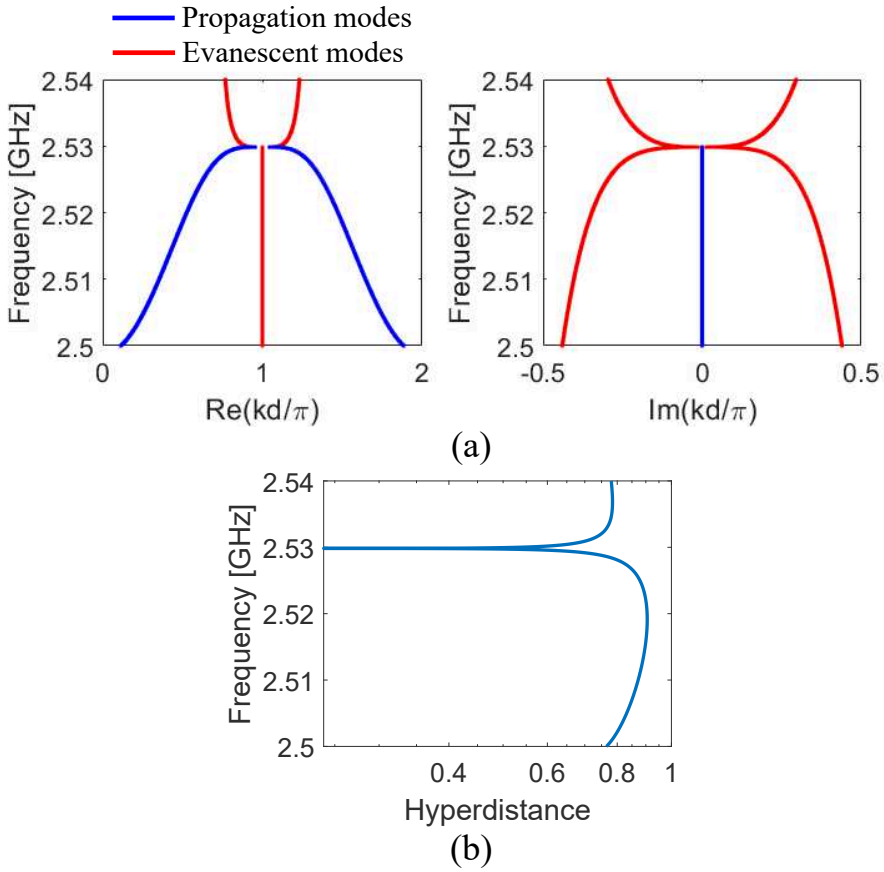

Fig. 2.28 The dispersion relation of lossless "double-oblique-line cell" design. The DBE point locates at 2.53 GHz. (a) Dispersion diagram: propagating modes (blue lines), evanescent modes (red lines). (b) Hyperdistance.

The influence of losses on the dispersion diagram is shown in Fig. 2.30. In this design, the DBE is more sensitive to the losses compared to the previous "long cell" design. When considering the losses, the shape of the dispersion curve is more heavily distorted which can be seen form the hyperdistance in Fig. 2.30(b). After considering the losses, the hyperdistance increased to 0.76, while for "long cell" design, it was around 0.6. However, since the period is smaller with respect to the previous structure, losses are expected to have here a lower impact than when truncating the two structures with the same number of cells. This design indicates that the configuration with one coupling gap with two oblique lines of vias is able to implement a suitable asymmetric coupler to achieve a DBE.

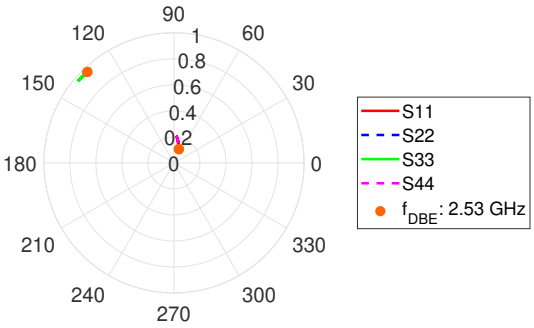

(a) Polar Plot of S_{11}, S_{22}, S_{33}, S_{44}.

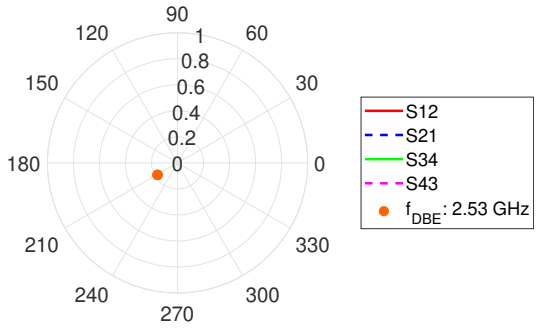

(b) Polar Plot of S_{12}, S_{21}, S_{34}, S_{43}.

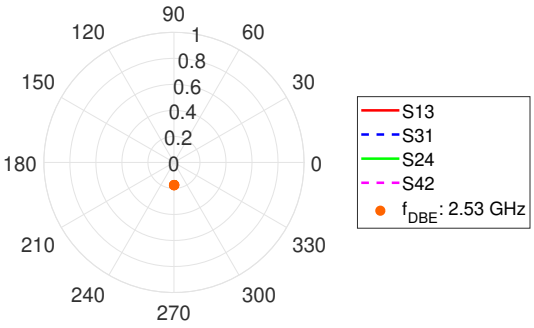

(c) Polar Plot of S_{13}, S_{31}, S_{24}, S_{42}.

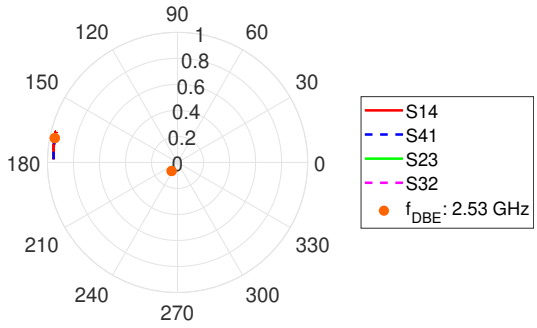

(d) Polar Plot of S_{14}, S_{41}, S_{23}, S_{32}.

Fig. 2.29 Polar plot of coupling part of "double-oblique-line cell". The frequency changes from 2.5 GHz to 2.54 GHz.

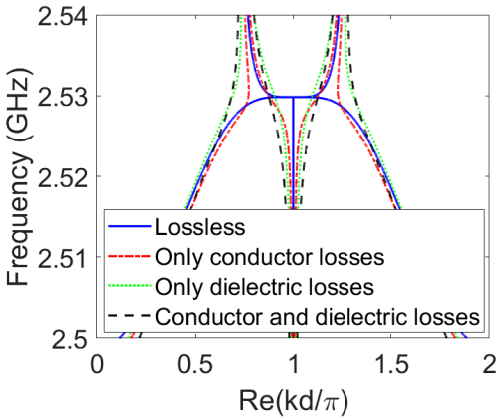

(a)

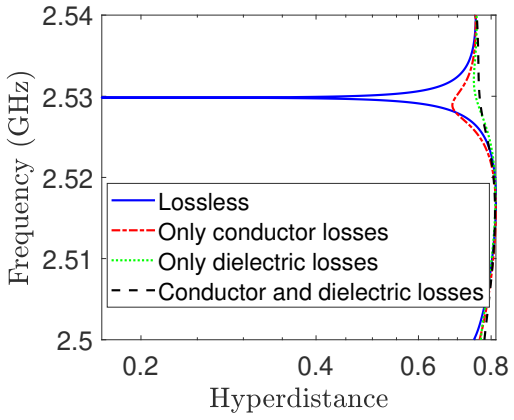

(b)

Fig. 2.30 Influences of losses on the dispersion diagram of "double-oblique-line cell" design in different cases (only conductor losses, only dielectric losses and both of them). (a) Dispersion diagrams. (b) Hyperdistance.

2.4.3 Compact Unit Cell with One Oblique Line of Vias ("single-oblique-line cell")

The previous design gave relatively good results in achieving DBE, but we want to further simplify the unit cell in order to make it more robust with respect to geometrical imperfections and possibly losses. We use here only one coupling gap and only one oblique line of vias to get the asymmetric reflections and couplings. The S matrix of the coupler used here is less simple than the previous cases. Here we expect as before a clear asymmetry in the diagonal terms (s_{11} being higher than the other reflections coefficients). However, no single coupling between ports is clearly dominant. We expect that s_{23}, s_{34} and s_{24} are large due to the absence of vias blocking these paths.

The compact design with only one oblique line of vias is shown in Fig. 2.31. In this design, we only use one coupling gap in each cell, and the the whole size is 40 mm$\times$44.8 mm, i.e., $1.07\lambda_{DBE} \times 1.20\lambda_{DBE}$, where λ_{DBE} is the wavelength in the unit cell at the DBE frequency. The width of the SIW w =20 mm and the period d =44.8 mm. To ignore the leakage losses, the via's diameter is set to 0.4 mm and their separation is 0.8 mm. The thickness of the substrate is 1.28 mm and the material of the substrate is Rogers RO3010, which is the same as the "long cell" design with two coupling gaps. The coupling-gap length is g_c =26.4 mm. The distance between vias in the oblique line g_o =7 mm. After optimization, the angle $\varphi_{DBE} = 71^\circ$ and the length of the line g_d =11.3 mm.

The dispersion diagram is shown in Fig. 2.32(a). The DBE point is at 2.516 GHz and is confirmed to satisfy its definition in (1.3). The hyperdistance null also confirms the DBE requirement in Fig. 2.32(b). The losses influence on the dispersion diagram is shown in Fig. 2.33, which reconfirmed that DBE requires low-loss structures.

In Fig. 2.34, the S parameters of this cell are shown. They confirm what was said at the beginning of the paragraph. The scattering matrix form found in Section 2.3.3.1 is a sufficient requirement to obtain a DBE point, but the optimization of the structure can lead to more complex matrices still compatible with a DBE condition.

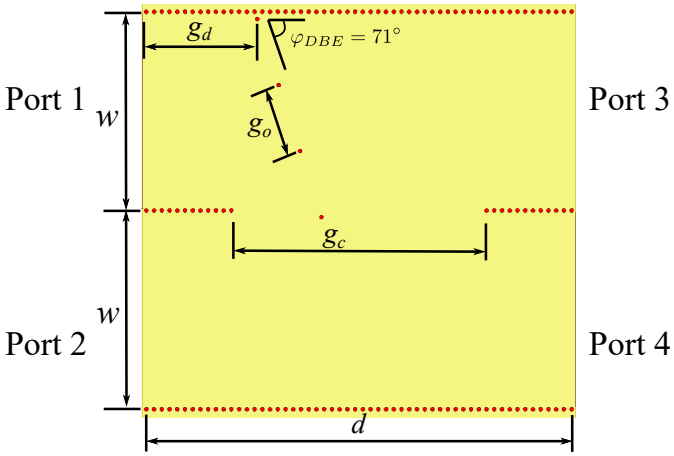

Fig. 2.31 Geometry of "single-oblique-line cell".

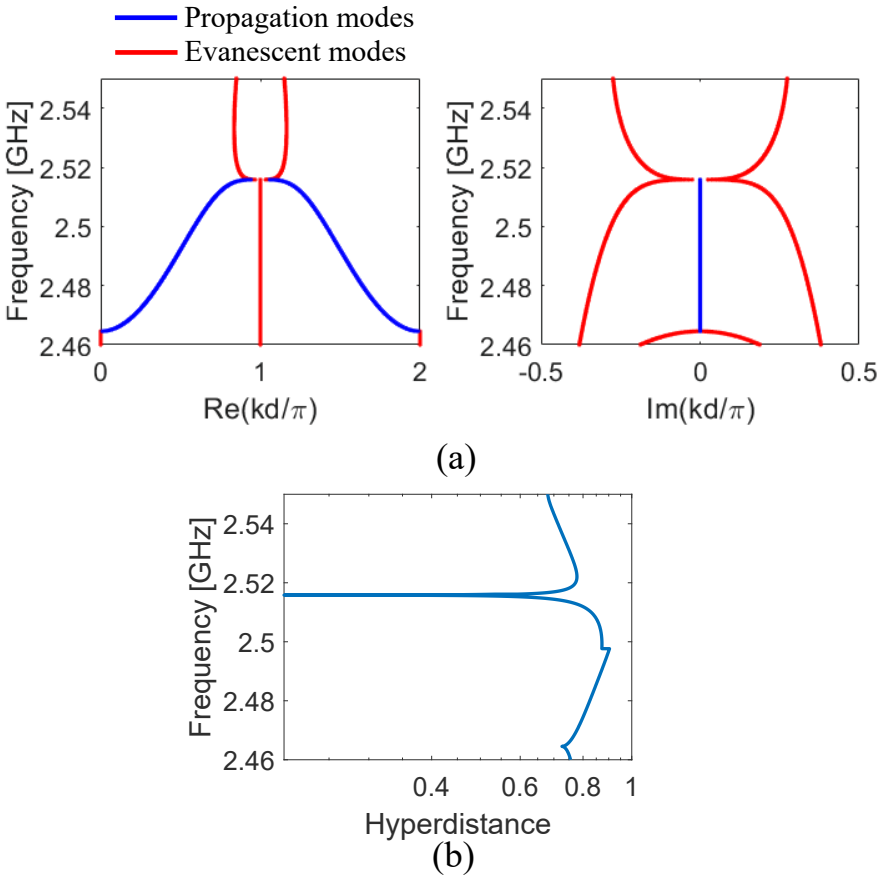

Fig. 2.32 Dispersion relation of "single-oblique-line cell". The DBE locates at 2.516 GHz. (a) Dispersion diagram: propagating modes (blue lines), evanescent modes (red lines). (b) Hyperdistance of lossless cell.

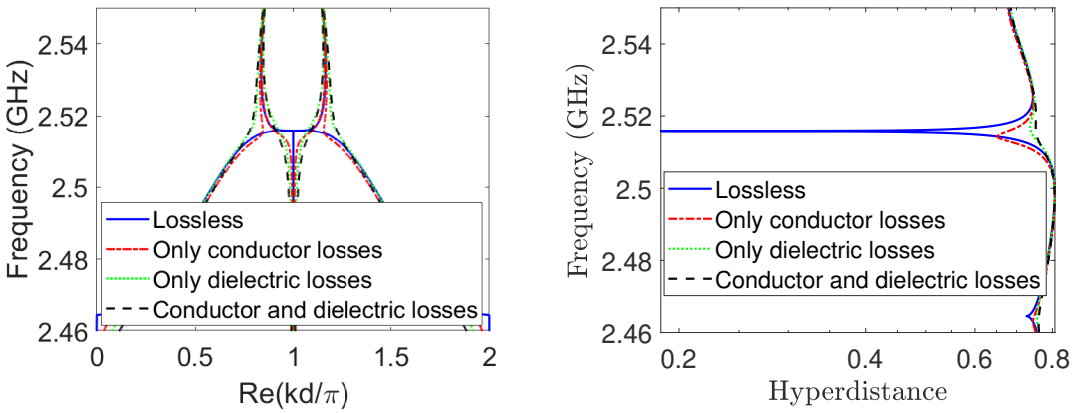

(a) **(b)**

Fig. 2.33 Losses influences to dispersion diagram of "single-oblique-line cell" design in different cases (only conductor losses, only dielectric losses and both of them). (a) Dispersion diagrams. (b) Hyperdistance.

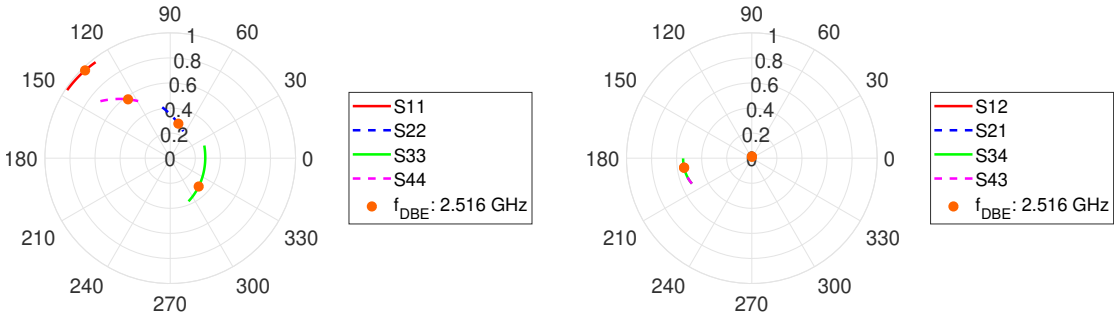

(a) Polar Plot of S_{11}, S_{22}, S_{33}, S_{44}.

(b) Polar Plot of S_{12}, S_{21}, S_{34}, S_{43}.

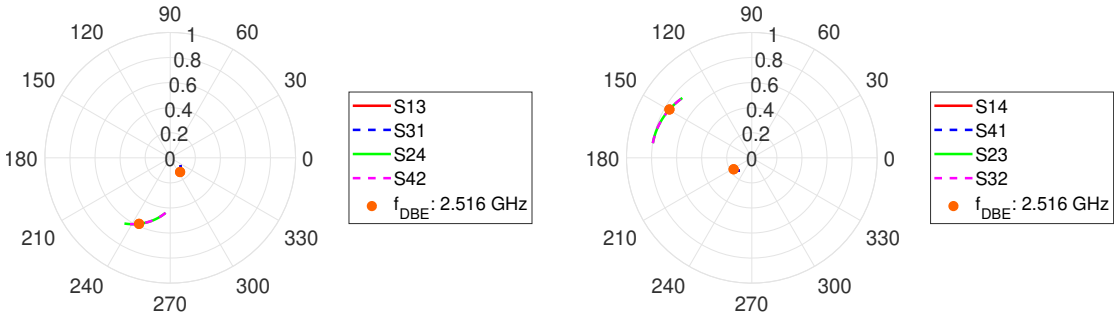

(c) Polar Plot of S_{13}, S_{31}, S_{24}, S_{42}.

(d) Polar Plot of S_{14}, S_{41}, S_{23}, S_{32}.

Fig. 2.34 Polar plot of coupling part of "single-oblique-line cell" design. The frequency changes from 2.46 GHz to 2.55GHz.

2.4.4 Compact Unit Cell with an Array of Air Vias ("air-via cell")

In this section, we want to explore if other types of defect in SIW can also be used to design a proper coupler to achieve a DBE point. This can inspire other ideas to develop the coupler with different geometric and physical solutions. Scatterers in SIW are not only restricted to metallic vias: slots or other possible structures embedded in the substrate can also be used to develop the DBE, which can give more freedom in certain technologies.

In Fig. 2.35, inspired from [115], we use several lines of air holes to create a reflection at port 1 which is not present in the other ports, and leave a gap between the waveguides to couple them. The width of each waveguide is w =30 mm, the period is d =45 mm. The substrate parameters do not change. After optimization of the parameters, the length of the via line is l_1 =9.6 mm and the gap length is g_1 =25.4 mm. The position of air-holes array l_2 =7.5 mm. The length of the air-holes array l_3 =20 mm and the width l_4 =6 mm. The diameter of each air hole is 1 mm and the separation between each hole is 2 mm. The air holes only go through the substrate and are covered by the two copper layers, in order to avoid any leakage through the air holes.

The DBE is obtained at 1.858 GHz as shown in Fig. 2.36(a). The result is verified using the hyperdistance in Fig. 2.36(b).

The scattering parameters of the coupler used here (Fig. 2.37) show that the expected asymmetries in the parameters are mainly concentrated in the phases of the reflection coefficients at each port, while the coupling among ports are quite similar ($s_{12} \approx s_{34}, s_{13} \approx s_{24}, s_{14} \approx s_{24}$). This coupler is therefore not of the kind discussed in Section 2.3.3.1. This should not surprise, since that form is sufficient but not necessary to achieve a DBE.

The dispersion diagram including losses is shown in Fig. 2.38. Even though a DBE condition has been obtained, losses have a huge influence on the dispersion diagram. Even conductor losses alone lead a strong distortion of the dispersion curve near the DBE. This phenomenon is related to the presence of a propagating mode in pass-band close to the DBE, at higher frequencies. In the presence of losses, the pass-band reaching the DBE and the higher-frequency pass-band are joined together and the DBE is lost. So, although this design proves that different topologies could also be used to develop a DBE point, it will not be considered in the following truncated SIWs-DBE designs.

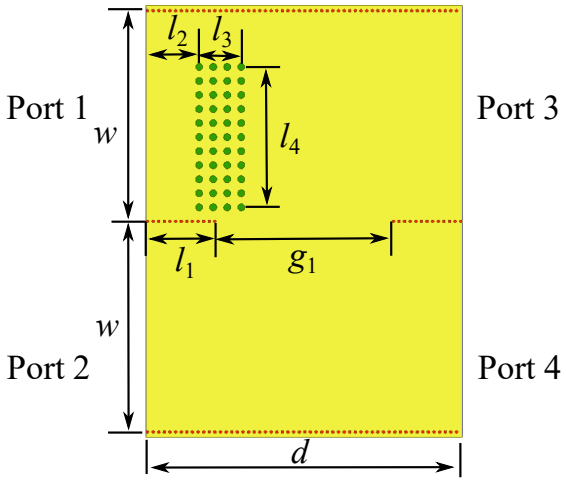

Fig. 2.35 Geometry of the "air-via cell" design.

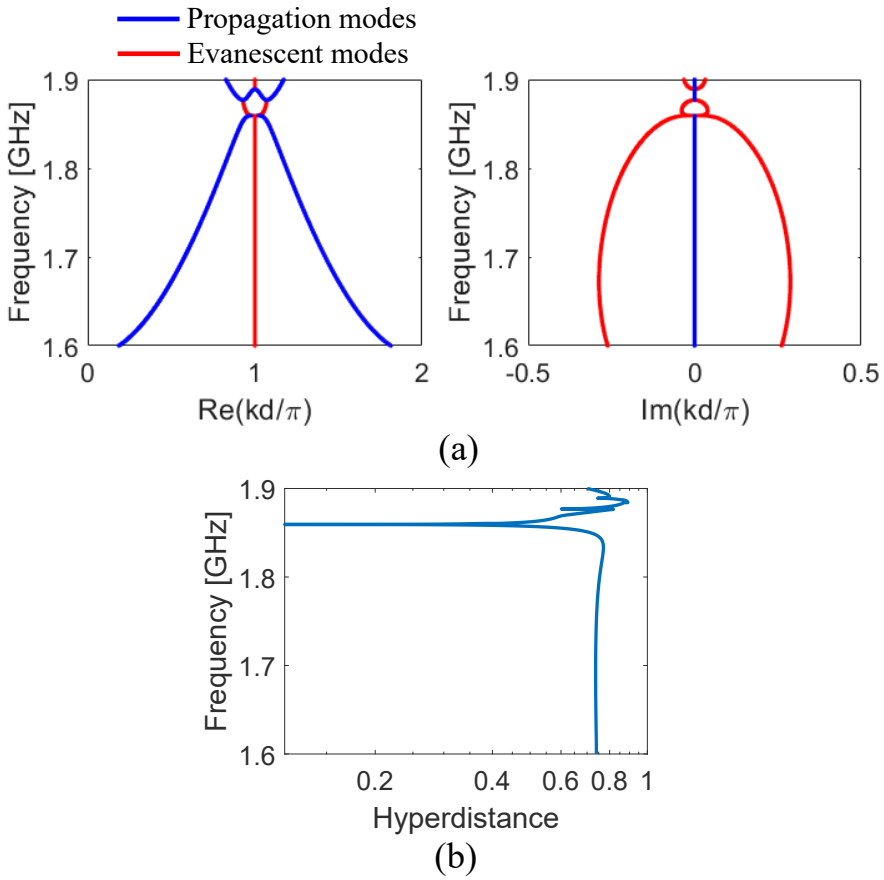

Fig. 2.36 Dispersion diagram of the lossless "air-via cell". The DBE locates at 1.858 GHz. (a) Dispersion diagram: propagating modes (blue lines), evanescent modes (red lines). (b) Hyperdistance.

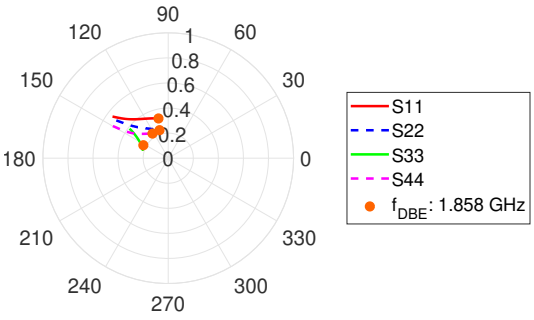

(a) Polar Plot of S_{11}, S_{22}, S_{33}, S_{44}.

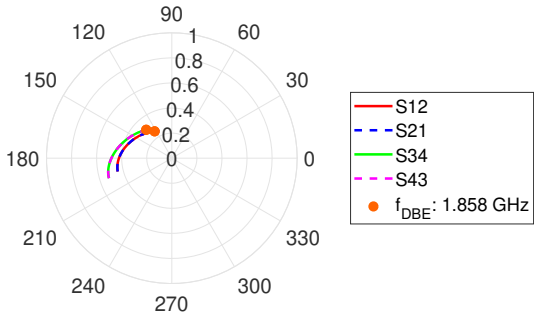

(b) Polar Plot of S_{12}, S_{21}, S_{34}, S_{43}.

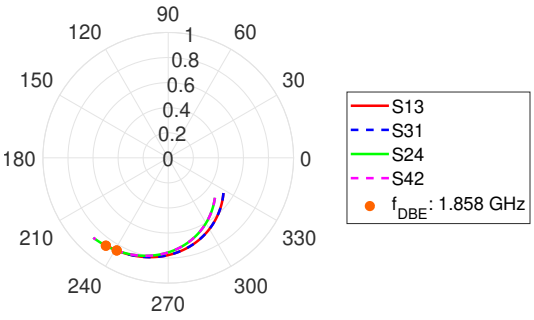

(c) Polar Plot of S_{13}, S_{31}, S_{24}, S_{42}.

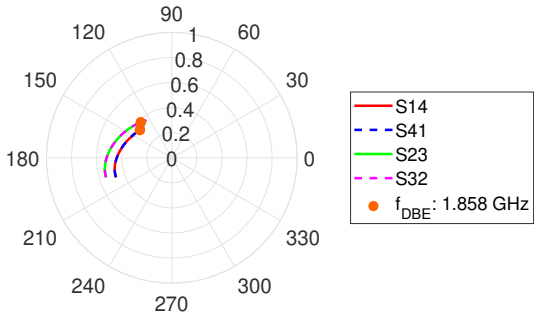

(d) Polar Plot of S_{14}, S_{41}, S_{23}, S_{32}.

Fig. 2.37 Polar plot of coupling part of "air-via cell" design. (1.58 GHz to 1.9 GHz)

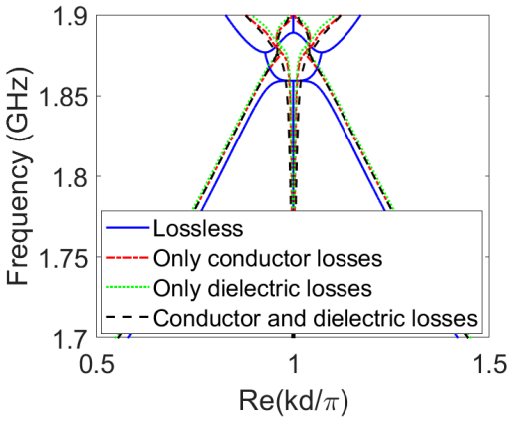

(a)

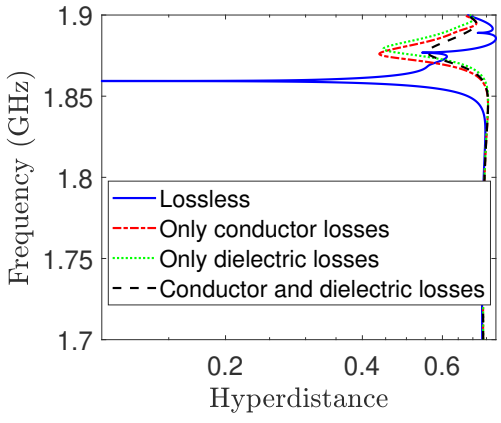

(b)

Fig. 2.38 Losses influence on the dispersion relation of "air-via cell" in different cases (lossless, only conductor losses, only dielectric losses, conductor and dielectric losses). (a) Dispersion diagram. (b) Hyperdistance.

2.4.5 Unit Cell Robust to Perturbations ("corner cell")

Here we propose a last design to make easier the matching of the periodic line once a truncated resonator will be designed in the following. In [36, 116], the truncated DBE resonators are excited from two opposite ports, and the other two ports are shorted. In this design we adopt a geometry such that the two ports which are not shorted are minimally perturbed by the periodic vias assuring the DBE conditions. Even more interestingly, this design is found to be far more robust to the perturbation of the oblique vias position if compared with previous designs.

The new design includes two short oblique lines of vias near port 1 and 3 and a coupling gap as shown in Fig 2.39. The new unit cell is now symmetric with respect to the middle plane orthogonal to both waveguides, and the required asymmetry between the waveguides is due to the two short oblique lines of vias in front of port 1 and 3, which provide different reflections at port 1 (3) and at port 2 (4). Of course the coupling between ports 1-3 and between ports 2-4 are different. The width $w = 21.5$ mm; the period $d = 34.8$ mm; the length $l_1 = 4.5$ mm, $l_2 = 4.5$ mm; the gap's length $g = 25.8$ mm; the angle $\varphi = 76°$. The diameter of the via is 0.6 mm, the separation between vias is 1.2 mm. The substrate is 1.524 mm Rogers RO3010.

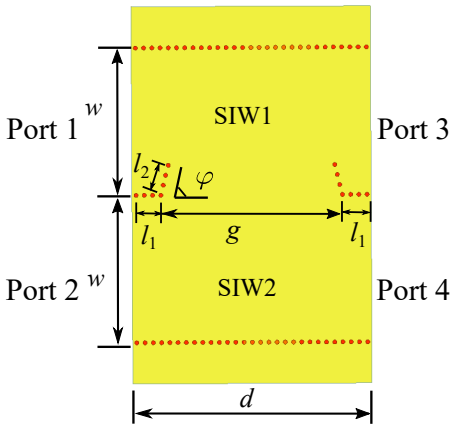

Fig. 2.39 Geometry of "corner cell".

The dispersion diagram for the lossless cell is shown in Fig. 2.40(a) which shows the DBE is achieved at 2.5 GHz (similar as "double-oblique-line cell" and "single-oblique-line cell"). The hyperdistance is zero at DBE in Fig. 2.40(b), which confirms the existence of DBE. The most interesting feature of this new design is its increased robustness to the perturbation of the oblique lines of vias. In Fig. 2.41, we compared the influence of a perturbation (angle ϕ of oblique vias) on DBE of this design and the "single-oblique-line cell". From Fig. 2.41(a) and (c), we can see that, for a wide range of perturbation (from $11.3\,\mathrm{deg}$ to $84\,\mathrm{deg}$), the new compact design can always achieve the DBE with a small frequency shift. On the contrary, the "single-oblique-line cell" loses the DBE even for a small perturbation of $5\,\mathrm{deg}$ (Fig. 2.41(c)). Not only the dispersion

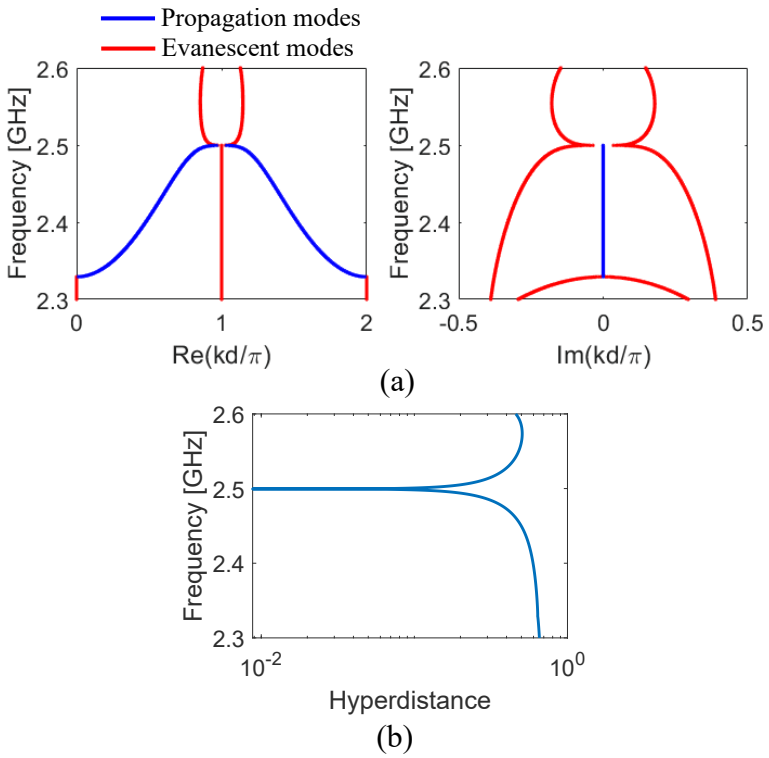

Fig. 2.40 Dispersion diagram of the lossless "corner cell". The DBE frequency is at 2.5 GHz. (a) Dispersion diagram: propagating modes (blue lines), evanescent modes (red lines). (b) Hyperdistance.

diagrams, but also the hyperdistances in Figs. 2.41(b) and (d) confirm this conclusion. The same conclusion can be drawn if this comparison is be performed with the first "long cell" design. In Fig. 2.21, we observed the loss of DBE for small perturbation of $1.7\,\mathrm{deg}$ and $1.3\,\mathrm{deg}$. This robustness is particularly useful, since it allows to move the DBE frequency when changing the φ angle of the oblique lines. This gives an additional degree of freedom in order to place the DBE frequency as far as possible from other stop-band and RBE points. In fact, as shown with the "air-via cell", the presence of higher-order pass-bands close to the DBE point can deteriorate the degeneracy much more when losses or imperfections are introduced (and also when the periodic structure is truncated with a finite number of cells).

The scattering parameters of the coupler (Fig. 2.42) show that the symmetric geometry of "corner cell" lead the same reflections for ports 1 (3) and 2 (4) ($s_{11} = s_{33}, s_{22} = s_{44}$). However, this does not contradicts the conclusions in Section 2.3.3, since asymmetries are still visible ($s_{11} \neq s_{22}, s_{22} \neq s_{44}$). The symmetry also lead the same coupling ($s_{12} = s_{34}, s_{14} = s_{23}$). The coupling between ports 2-4 is strong ($s_{24} \approx 0.9$), while the coupling between ports 1-3 are influenced by the oblique vias but still not negligible ($s_{13} \approx 0.5$).

Finally, the effect of losses is shown in Fig. 2.43. The hyperdistance is the smallest among all the cells presented: a minimum value of 0.2 is reached, while the other cells

reach minimum values larger than 0.5. In conclusion, this new compact "corner cell" design has a similar size of the previous "single-oblique-line cell" design, it is much more robust to the perturbation of oblique vias, and seems to suffer less of losses. For this reason, we select this topology for modifications by using a low-loss substrate and further improve its performance under losses.

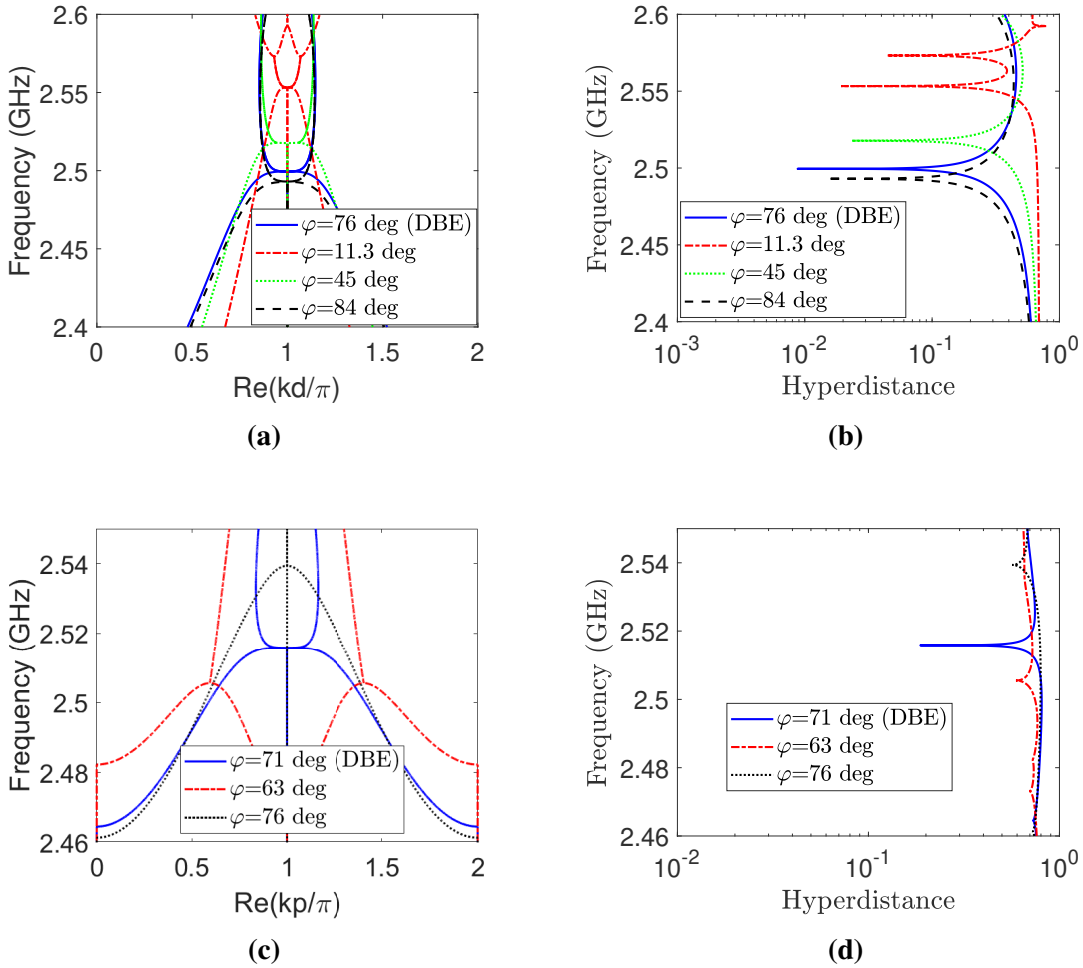

Fig. 2.41 The influence of perturbation (angle φ of oblique vias) to DBE. (a) Dispersion diagram of new compact design with different φ. (b) Hyperdistance of new compact design with different φ. (c) Dispersion diagram of "single-oblique-line cell" with different φ. (d) Hyperdistance of "single-oblique-line cell" with different φ.

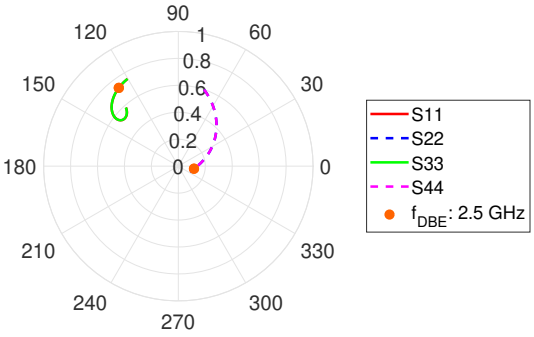

(a) Polar Plot of S_{11}, S_{22}, S_{33}, S_{44}.

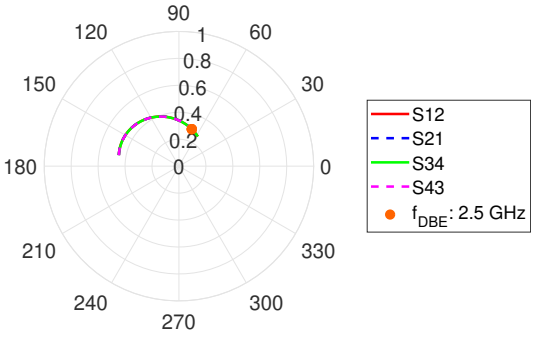

(b) Polar Plot of S_{12}, S_{21}, S_{34}, S_{43}.

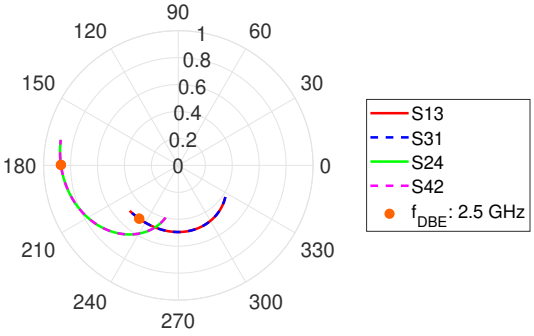

(c) Polar Plot of S_{13}, S_{31}, S_{24}, S_{42}.

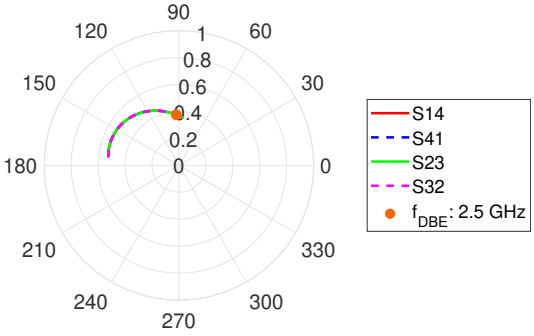

(d) Polar Plot of S_{14}, S_{41}, S_{23}, S_{32}.

Fig. 2.42 Polar plot of coupling part of "corner cell" design. (2.1 GHz to 2.6 GHz)

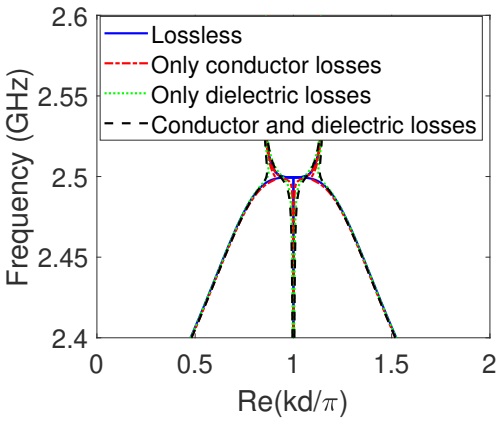

(a)

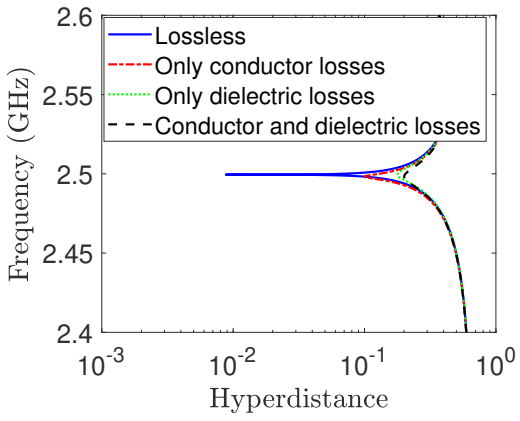

(b)

Fig. 2.43 Losses influence on the dispersion diagram of the "corner cell" in different cases (lossless, only conductor losses, only dielectric losses, both conductor and dielectric losses). (a) Dispersion diagram. (b) Hyperdistance.

2.4.6 Corner-cell using Low-loss Substrate ("low-loss-substrate cell")

As shown in the four previous designs, the DBE sensitivity to losses makes is necessary the development of low-loss designs where the DBE behavior does not change a lot. This is crucial to be able to cascade several SIW-DBE cells to achieve a high Q-factor resonator. Also, this would be helpful to increase the DBE point in higher frequency, where the advantage of SIW over other printed technologies is more relevant.

In all previous designs, dielectric losses are the main contributors to the total losses. For this reason, we propose here a higher-frequency design using a low-loss substrate. We set the DBE frequency to about 6 GHz. We modify slightly the geometry shown in Fig. 2.39. The width of both SIW is $w = 20$ mm; the period $d = 30$ mm; the coupling gap's length $g = 21.6$ mm; the length $l_1 = 4.2$ mm; the length $l_2 = 4$ mm; the angle $\varphi = 45°$. The diameter of the via is 0.6 mm, the separation between two vias is 1.2 mm. The thickness of the substrate is 1.524 mm. The substrate material is Neltec NY9208, whose $\epsilon_r = 2.08$, loss tangent is 6×10^{-4}.

The dispersion relation of "low-loss-substrate cell" is shown in Fig. 2.44(a). The DBE point is at 6.17 GHz and its existence is confirmed by a null of the hyperdistance in Fig. 2.44(b). The loss influences on the dispersion relation of "low-loss-substrate cell" is shown in Fig. 2.45. From Fig. 2.45, we find that the contribution of dielectric losses is now decreased comparable to the conductive losses, indicating that the loss tangent of the new substrate is sufficiently low and even lower loss tangent would not significantly increase the degeneracy.

In order to clearly show the reduction of the losses, we compare the hyperdistance at the DBE point with losses for all the SIW unit cell designs in Table. 2.1. After considering the losses, the first four designs' hyperdistance are all above 0.5, which means the DBE degeneracy is almost lost. In contrast, the hyperdistance of the low-loss design is decreased to less than 20% of the first four designs.

Table 2.1 Hyperdistance of the Lossy SIW Unit Cells at the DBE Frequency

Unit Cell Type	DBE Frequency (GHz)	Hyperdistance
"long cell"	2.218	5.20×10^{-1}
"double-oblique-line cell"	2.530	7.64×10^{-1}
"single-oblique-line cell"	2.516	8.31×10^{-1}
"air-via cell"	1.858	5.72×10^{-1}
"corner cell"	2.500	2.01×10^{-1}
"low-loss-substrate cell"	6.170	1.26×10^{-1}
"air-filled cell 1"	8.830	9.82×10^{-2}
"air-filled cell 2"	9.100	5.40×10^{-2}

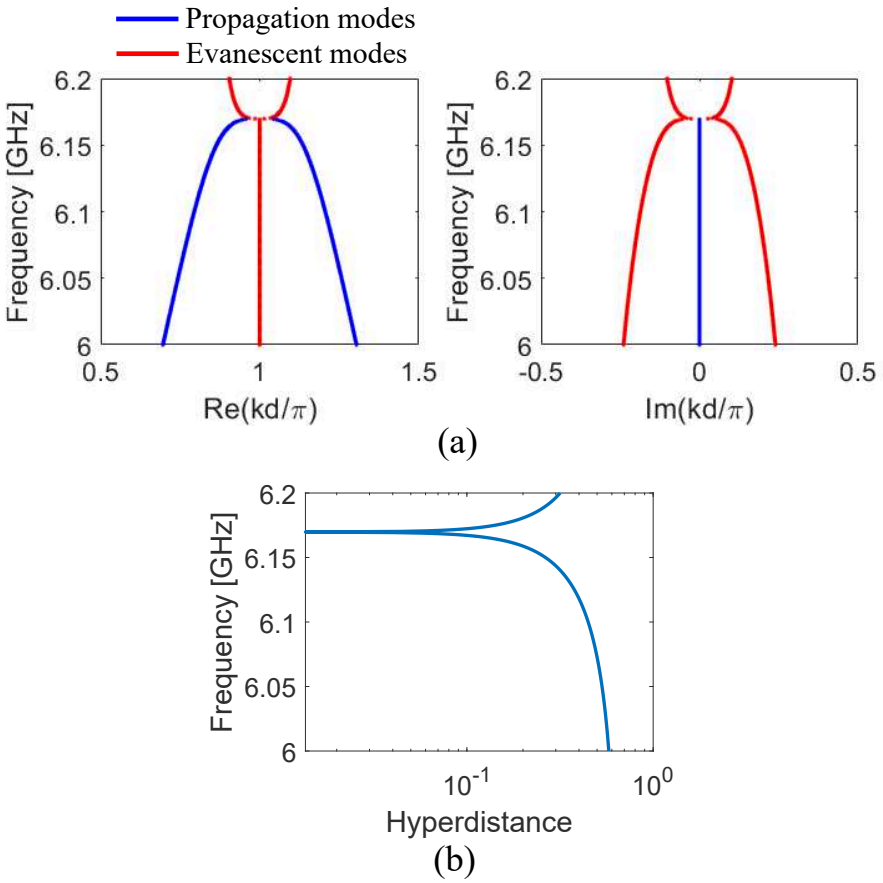

Fig. 2.44 The dispersion diagram of "low-loss-substrate cell" design without considering losses. The DBE frequency is at 6.17 GHz. (a) Dispersion diagram. (b) Hyperdistance.

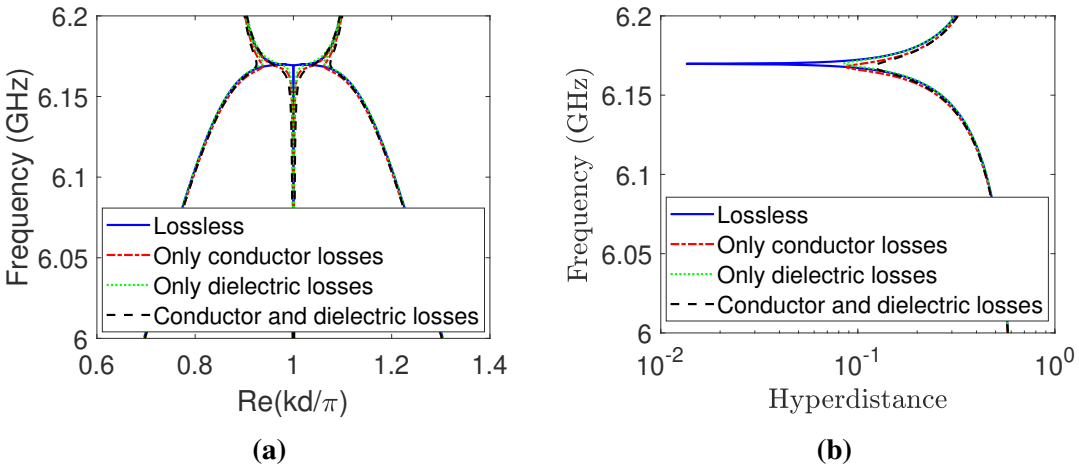

Fig. 2.45 Loss influence on the dispersion diagram of "low-loss-substrate cell" in different cases (lossless, only conductor losses, only dielectric losses, both conductor and dielectric losses). (a) Dispersion diagram. (b) Hyperdistance.

2.4.7 Low-loss Compact Unit Cell using Air-filled SIW Structure ("air-filled cell 1")

As introduced in Section 1.3.4, air-filled SIW structures are reported in many publications to decrease the dielectric losses in SIW. Air-filled SIW can possibly provide then a cost-effective solution to achieve the DBE. Compared to a more expensive design requiring a low-loss substrate, the air-filled SIW only needs low-cost FR-4 substrates to have even lower dielectric losses. In this design, we develop the DBE in an air-filled SIW cell with a similar structure as the previous "low-loss-substrate cell".

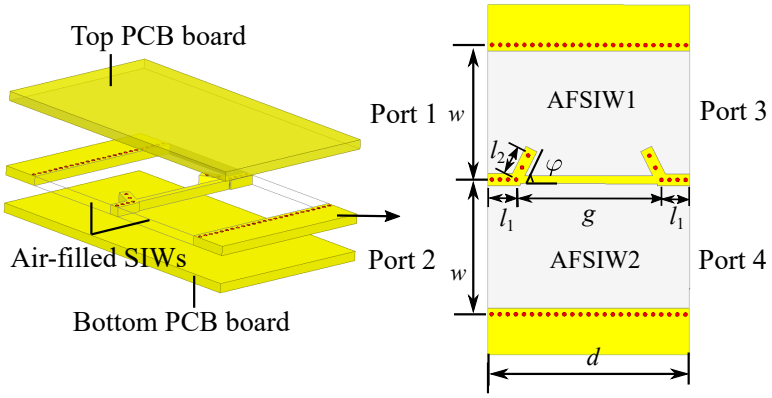

Fig. 2.46 Geometry of the "air-filled cell 1".

The geometry of "air-filled cell 1" is shown in Fig .2.46. The air-filled SIW cell consists of three layers: top PCB board, bottom PCB board and the air-filled middle PCB board. The top and bottom boards provide the copper planes for the air-filled middle PCB board, and the wave propagate in the air-filled part of the middle board, so that dielectric losses are virtually suppressed. The following are the dimensions of the air-filled SIWs in the middle layer: The width $w = 20$ mm, the period $d = 30$ mm, the length $l_1 = 4.2$ mm, $l_2 = 5$ mm, the coupling gap $g = 21.6$ mm, the angle φ is $63.4°$. The substrate is FR-4 whose ϵ_r is 4.4, loss tangent is 0.02. Considering the fabrication limitations, the minimum distance from the via center to the edge of the air-filled part is 0.9 mm. A 1.2 mm-width bar is remained at the coupling gap; otherwise, the middle vias between two air-filled SIWs will drop from the middle layer when fabricating the truncated periodic lines.

The dispersion relation without considering losses is shown in Fig. 2.48(a) where the DBE is achieved at 8.83 GHz. The null hyperdistance in Fig. 2.48(b) confirms the existence of DBE. The dispersion relation considering the losses is shown in Fig. 2.49 where the dielectric losses is decreased to the same level as conductor losses indicating the influence of losses is reduced. The hyperdistance in Fig. 2.49(b) shows that even after considering all the losses (conductor losses and dielectric losses), the hyperdistance still stays in a low value about 0.1.

The scattering parameters of the coupler is shown in Fig. 2.47, which is similar to

"corner cell" design as expected.

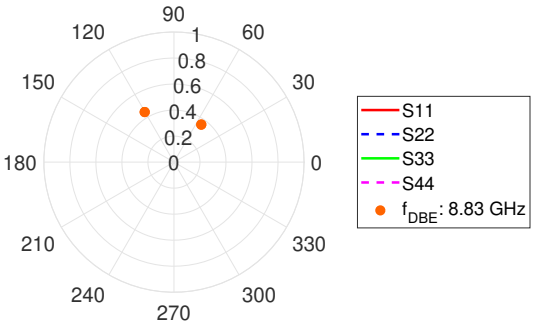

(a) Polar Plot of S_{11}, S_{22}, S_{33}, S_{44}.

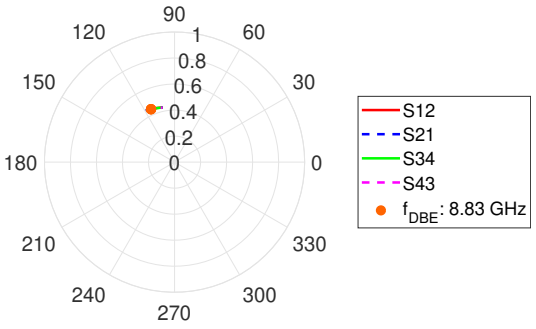

(b) Polar Plot of S_{12}, S_{21}, S_{34}, S_{43}.

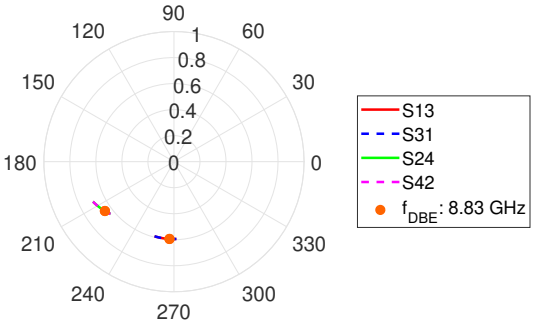

(c) Polar Plot of S_{13}, S_{31}, S_{24}, S_{42}.

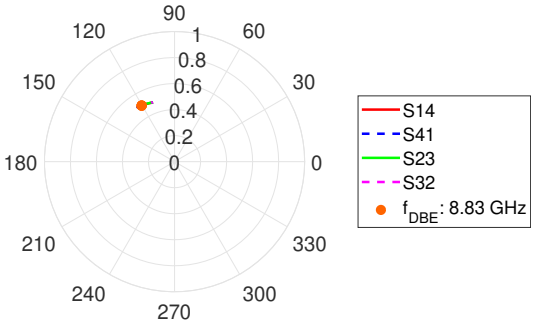

(d) Polar Plot of S_{14}, S_{41}, S_{23}, S_{32}.

Fig. 2.47 Polar plot of the coupling part of "air-filled cell 1". (8.7 GHz to 8.9 GHz)

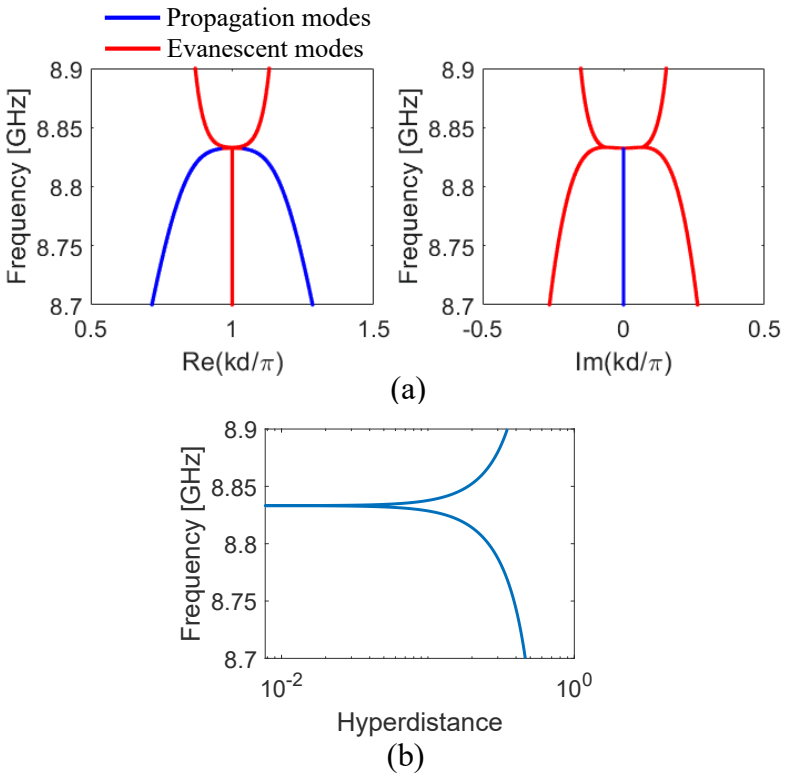

Fig. 2.48 The dispersion diagram of the "air-filled cell 1" without considering losses. The DBE frequency is at 8.83 GHz. (a) Dispersion diagram. (b) Hyperdistance.

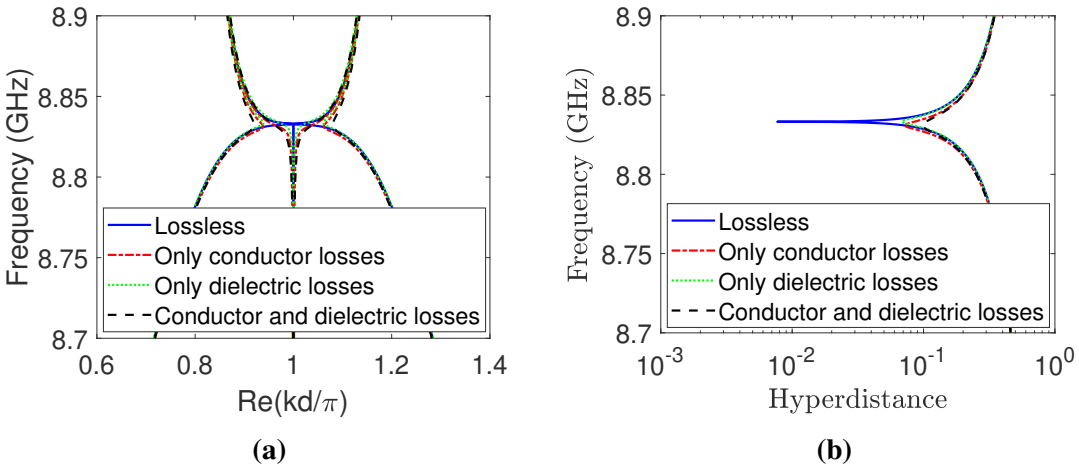

(a) **(b)**

Fig. 2.49 Loss influence on the dispersion diagram of the "air-filled cell 1" in different cases (lossless, only conductor losses, only dielectric losses, conductor losses and dielectric losses). (a) Dispersion diagram. (b) Hyperdistance.

2.4.8 Air-filled SIW Structure using Copper Pillars (“air-filled cell 2”)

The previous “air-filled cell 1” design has to leave a part of substrate at the coupling gap to hold the vias, which is a source of losses and may increase fabrication complexity. A simplified design is shown in Fig. 2.50. In the design, several copper pillars are inserted through the air-filled SIW cell to act as the metallic vias and soldered to the SIW plates. This avoids keeping a dielectric line inside the structure. The dimensions are: $w = 20$ mm, $d = 30$ mm, $l_1 = 3.8$ mm, $l_2 = 5$ mm, $g = 22.4$ mm, $\varphi = 76.6°$. The thickness of the middle FR-4 board is 1.6 mm. The copper pillars penetrate the top and bottom PCB boards.

The scattering parameters of the coupler (Fig. 2.51) show that the copper pillars decrease the coupling between ports 1-3 more than “corner cell” design, while the other characteristics of S parameters stay similar to “corner cell” design.

The lossless dispersion diagram is shown in Fig. 2.48(a) where the DBE is obtained at 9.1 GHz confirmed by the zero hyperdistance in Fig. 2.48(b). The lossy dispersion diagram is shown in Fig. 2.53(a). The dielectric losses are so low in this case that the dispersion curve considering only the dielectric losses almost overlaps the lossless curve. In Fig. 2.53(b), the hyperdistance with only dielectric losses is also almost the same as lossless case. In other words, dielectric losses are negligible and the only source of losses are conductor losses. The hyperdistance at the DBE frequency when considering the losses is presented in Table. 2.1. This is the lowest lossy hyperdistance compared to the other designs, which confirms the fact that this structure is the less affected by losses among the presented ones.

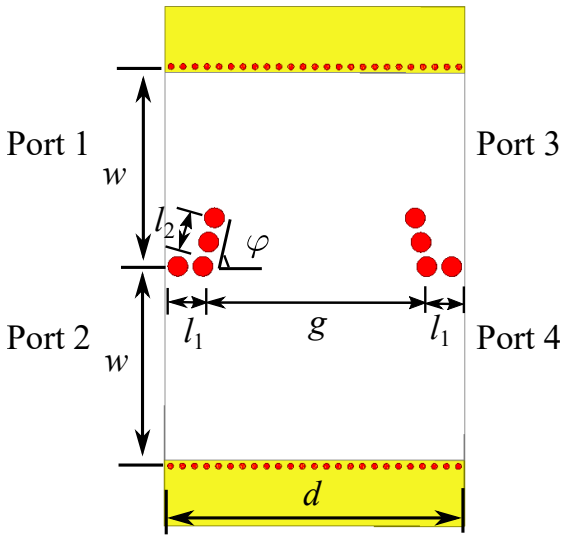

Fig. 2.50 Geometry of the “air-filled cell 2”.

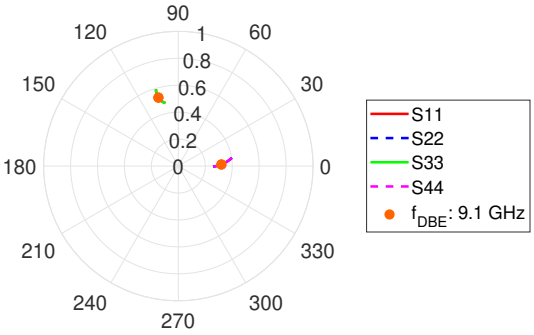

(a) Polar Plot of S_{11}, S_{22}, S_{33}, S_{44}.

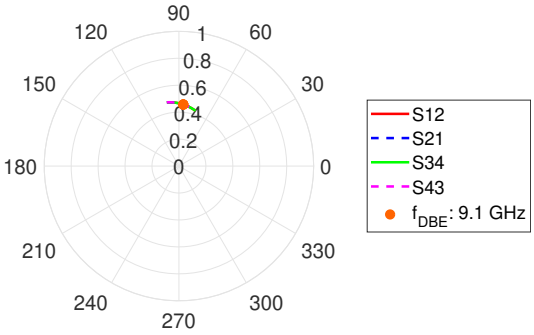

(b) Polar Plot of S_{12}, S_{21}, S_{34}, S_{43}.

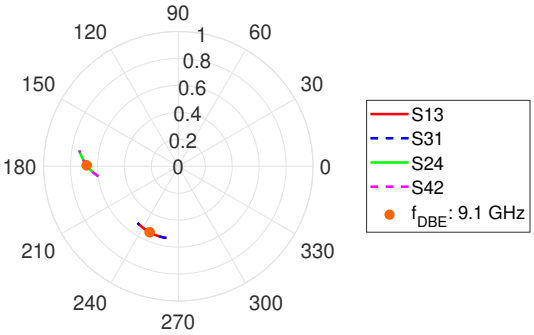

(c) Polar Plot of S_{13}, S_{31}, S_{24}, S_{42}.

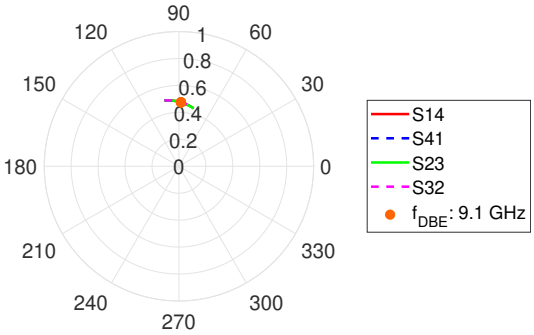

(d) Polar Plot of S_{14}, S_{41}, S_{23}, S_{32}.

Fig. 2.51 Polar plot of "air-filled cell 2" (the whole unit cell). The frequency interval is from 9 GHz to 9.15 GHz.

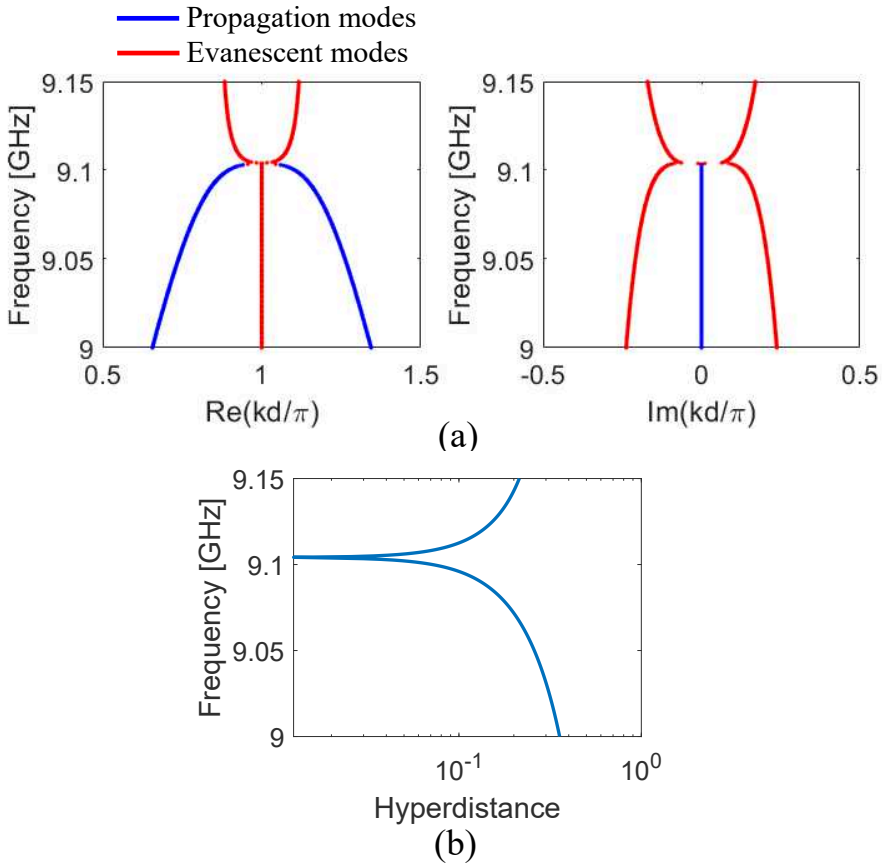

Fig. 2.52 The dispersion diagram of "air-filled cell 2" without considering losses. The DBE frequency locates at 9.1 GHz. (a) Dispersion diagram. (b) Hyperdistance.

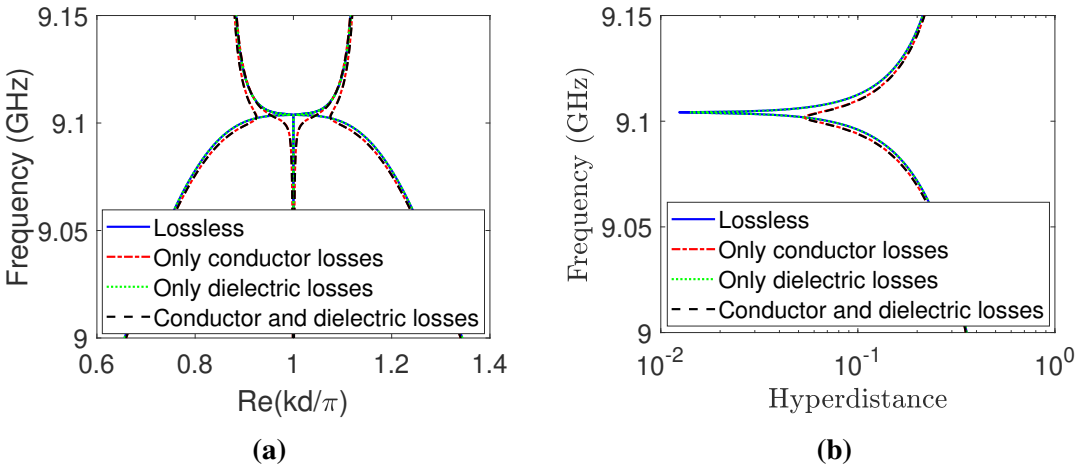

Fig. 2.53 Loss influence on the dispersion diagram of "air-filled cell 2" in four cases (lossless, only conductor losses, only dielectric losses, both conductor and dielectric losses). (a) Dispersion diagram. (b) Hyperdistance.

2.4.9 Comparison of the Normalized Size of the SIW-DBE Designs

One of the advantages of the SIW structures is their low-profile and ease of integration. DBE provides the possibility to obtain high Q-factor values with a small number of unit cells, so the size of each unit cell is an important factor to evaluate, being related to the size of the truncated DBE structure.

The different designs presented in the previous sections have different DBE frequencies and substrate materials. In order to compare their size, we normalize them with respect to the dielectric wavelength at the DBE frequency. The comparison of the SIW-DBE unit cells in normalized size is shown in Table. 2.2. Among all the designs, the "air-via cell", the "corner cell" and the three derived ones (the "low-loss-substrate cell" and the two air-filled designs) have the smallest normalized size, about 1.20 $\times$ 0.90.

Table 2.2 Normalized Size Comparison of Proposed SIW-DBE designs

Unit Cell Type	DBE Frequency (GHz)	Size (mm) (width $\times$ length)	Normalized Size (size / λ_{DBE})
"long cell"	2.218	60×90	1.42×2.13
"double-oblique-line cell"	2.53	40×45	1.08×1.21
"single-oblique-line cell"	2.516	40×44.8	1.07×1.21
"air-via cell"	1.858	60×45	1.19×0.89
"corner cell"	2.5	43×34.8	1.14×0.93
"low-loss-substrate cell"	6.17	40×30	1.19×0.89
"air-filled cell 1"	8.83	40×30	1.17×0.88
"air-filled cell 2"	9.1	40×30	1.21×0.91

2.5 Conclusions

In this chapter, we proposed a multimodal transfer-matrix method to analyse the 4-port DBE unit cell. We modelled a single unit cell as a four-port network formed of two transmission-line sections on both ends of the cell, and a coupler granting the necessary modal coupling responsible for the DBE degeneracy.

Based on this method, we studied different S matrix forms of the couplers to see which couple form can lead to a DBE synthesis. We found that the symmetric couplers (such as the perfectly matched one and the symmetric unmatched one) cannot introduce a DBE. Sufficient qualitative conditions for a coupler to obtain a DBE are: (1) Different reflections at the four ports and strong reflection at some ports; (2) a privileged propagation path between at least two of the four ports.

Following this guidelines, we successfully synthesised a DBE degeneracy in different kinds of SIW cells, including “long cell”, “double-oblique-line cell”, “single-oblique-line cell”, “air-via cell”, “corner cell”, “low-loss-substrate cell”, “air-filled cell 1”, “air-filled cell 2”. For all these unit cells, we explained the rationale behind their design, we gave the key parameters capable to reach a DBE condition, considered the influence of losses, and compared their performance in terms of robustness to the variation of geometrical parameters. The last low-loss designs (“low-loss-substrate cell”, “air-filled cell 1”, “air-filled cell 2”) have a good performance when considering losses and have the smallest normalized size. The impact of losses confirms the difficulty in designing a periodic SIW presenting DBE effects which can be observed, if compared to other structures (empty waveguides, microstrip lines) which either do not present dielectric losses or suffer less of both metallic and dielectric losses. The last three low-loss results show that once dielectric losses are sufficiently reduced, metallic losses seem not to impact significantly the degeneracy. This will be verified in the next chapter by studying the resonances of truncated structures.

CHAPTER 3

Truncated SIWs-DBE Lines

3.1 Introduction

In the previous chapter, five SIWs-DBE unit cell designs have been proposed. The influence of losses has been considered, and their sizes have been compared to show their miniaturization efficiency. By suitably modifying one of the unit cells, three low-loss designs have also been proposed to lower the impacts of losses as much as possible. The last three low-loss unit cells are also relatively compact among the proposed designs.
In this chapter, we study the resonant behavior of truncated SIW lines made with the unit cells described in the previous chapter. We calculate the S parameters, Q-factors and group delays for different length of SIWs-DBE resonators with and without losses. This will lead to the confirmation of the possibility to excite DBE resonances in finite SIW structures. After presenting all the designs, we discuss the choice of the most suitable designs for fabrication, among the three low-loss ones. Experimental validation of these resonances will then be obtained.

3.2 Resonant Behavior of Truncated SIWs-DBE Lines

In order to build practical resonators, the periodic DBE structures have to be truncated into finite-length lines. It is then necessary to check if the exceptional DBE resonant behaviors, as presented in Section 1.2, can be observed after the truncation. In this section, full-wave simulations of six truncated SIWs-DBE lines are presented, which are "long cell" SIWs line, "double-oblique-line cell" SIWs line, "single-oblique-line cell" SIWs line, "corner cell" SIWs line, "low-loss-substrate cell" SIWs line, "air-filled cell 1" SIWs lines and "air-filled cell 2" SIW lines. Among the unit cell discussed in the previous chapter, only the "air-via cell" design is not presented here. In that case, a higher-frequency pass-band is very close to the DBE, which severely affects the DBE shape when losses are added. The same strong perturbation is observed when the structure is truncated: the DBE resonance vanishes even in the absence of losses. For the sake of brevity, the results of the truncation of this structure are not presented here.
For each design, truncated lines with different numbers of cells are considered, where

the number of cell varying from 4 to 8. Both lossless and lossy cases are considered, and the S parameters, Q factors and group delays are calculated to verify the enhanced resonances by DBE.

3.2.1 Truncated "long cell" SIWs Lines

An N-cells truncated "long cell" SIWs line is shown in Fig. 3.1. The feeding of the finite structure needs to be addressed before this truncated structure can be considered. Each unit cell is a four-port structure, and so the entire line can be accessed through four different ports (the two left ports of the first cell, and the two right port of the last cell). However, as in [36], the truncated DBE resonator is here accessed through two ports, a feeding port on the left and an output port on the right. The other two ports are shorted in order to keep the design simpler than a feeder distributed on two ports would require. In Fig. 3.1, we short the up-left and down-right ports by PEC boundaries and connect the other two ports to external waveguide ports. The choice for the excitation ports is dictated by avoiding too strong reflections at the first cell, in order to have a smooth transition from the waveguide to the unit cell. This should assure a good matching to the overall line. As shown in Fig. 2.23, the oblique lines of vias cause strong reflections at the up-left and down-right ports, so we shorted these two ports. Different combinations of excitation ports have also been verified and led to worse performances and will not be considered in the following.

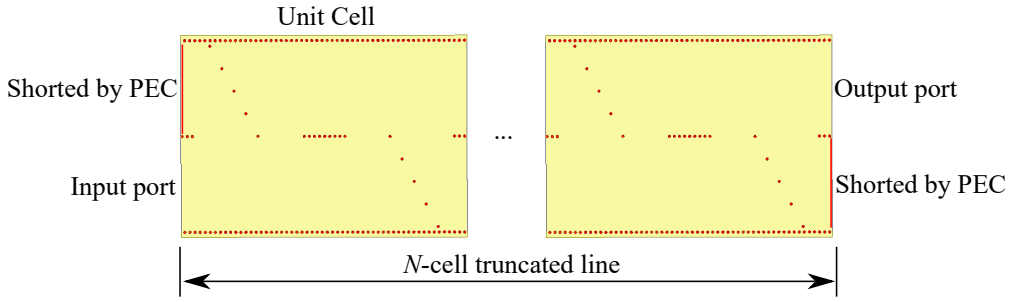

Fig. 3.1 N-cell truncated "long cell" SIWs Lines.

At first, we study the S parameters of truncated lines of different lengths in the pass-band just below the DBE frequency. The simulations are performed with the commercial software HFSS [117]. The simulation relative accuracy is set as 10^{-2} on the S parameter computation. The full-wave simulation results of S parameters of the different truncated lines are shown in Fig. 3.2 considering both lossless and lossy conditions. The DBE resonance occurs at $f_{r,d}$ which is the closest resonance peak to the DBE frequency f_d. To show the DBE resonance peak clearly, we plot all the S_{11} parameters in a narrow frequency range close to the DBE frequency in Fig. 3.4. The DBE resonant frequency is approaching the DBE frequency as the number of cells N increases, which is a characteristic of Fabry-Pérot resonator as explained in Section 1.2. In the

lossless situation, the DBE resonance peaks are clear indicating resonances are increasingly narrow. However, when considering losses, the DBE resonance peaks become flat, indicating that the resonances are strongly affected.

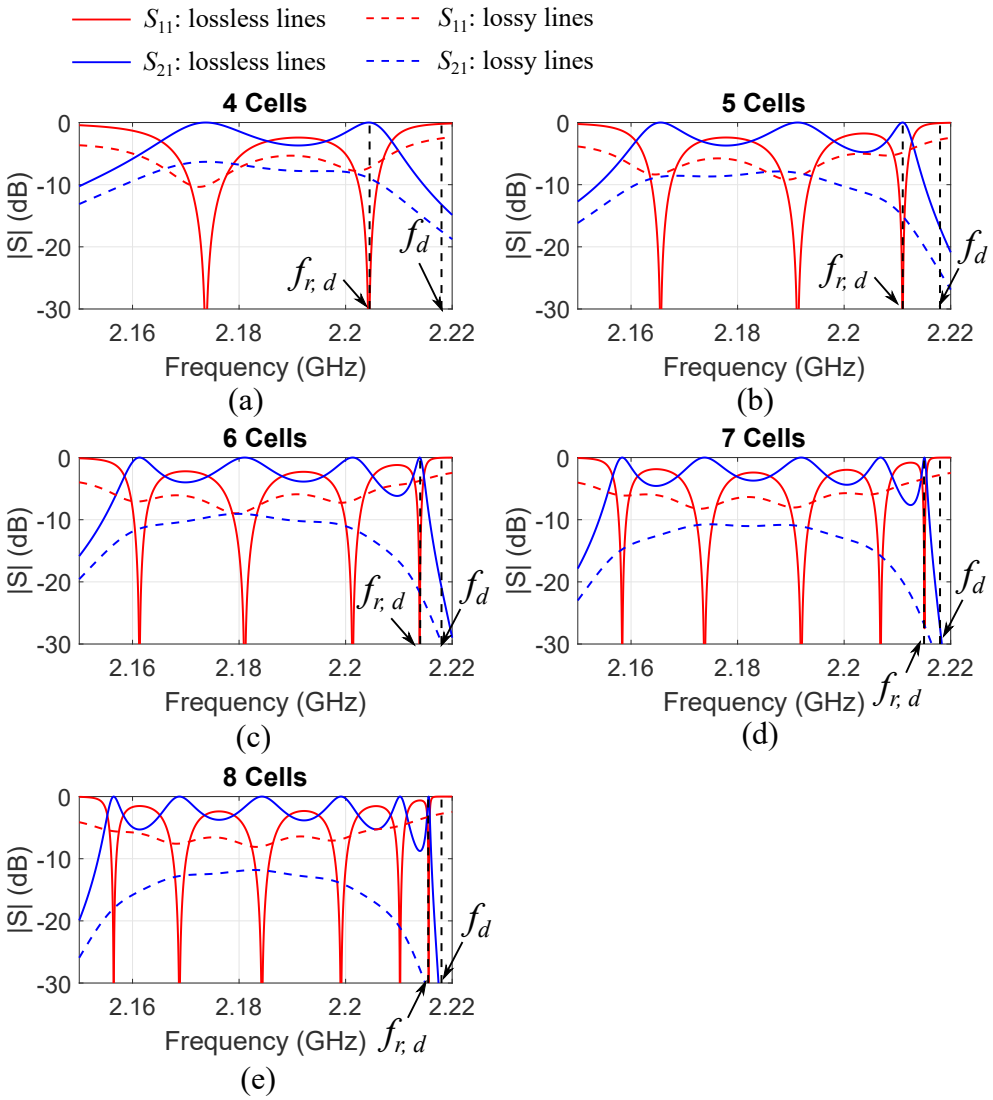

Fig. 3.2 S parameters of "long cell" SIWs lines. (a) 4-cell truncated SIWs line. (b) 5-cell truncated SIWs line. (c) 6-cell truncated SIWs line. (d) 7-cell truncated SIWs line. (e) 8-cell truncated SIWs line.

The DBE condition leads to a stronger field enhancement with the same number of cells compared to RBE as described in Section 1.2. In order to verify this conclusion, we only modify the oblique-line angle φ to break the DBE and form a RBE at 2.242 GHz, which is not far from the DBE frequency of the original line (2.218 GHz). The other parameters of this new RBE structure remain the same in order to get a fair comparison between these structures. By calculating the E-field at the DBE or RBE resonance frequency when both lines are fed on the left with an ideal waveguide port of 1 W, we observe the resonance DBE/RBE field in the 8-cell truncated SIWs line (Fig. 3.4(a) and (b)). As expected, the E-field amplitude is higher at the center and much smaller at the

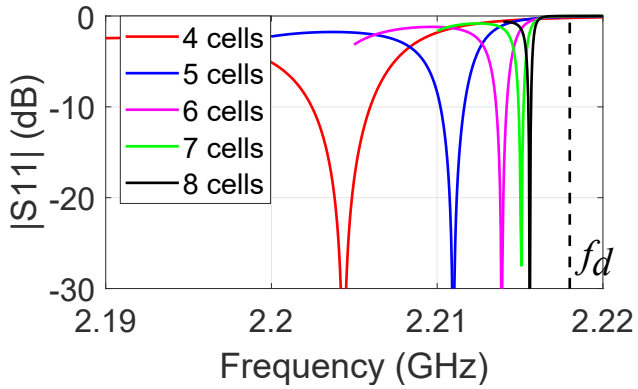

Fig. 3.3 S_{11} magnitude of lossless truncated "long cell" SIWs lines at the DBE resonances.

two ends, as shown in Fig. 1.5. We compare the E-field magnitude of DBE and RBE lines in Fig. 3.4(c). The data is taken along the black dashed lines (middle of the bottom SIW) in Fig. 3.4(a) and Fig. 3.4(b). The results show that, at the center of the resonator, the field is enhanced up to about 60 kV/m for DBE lines, while the maximum E-field of 8-cell RBE line is about 26 kV/m (Fig. 3.4(c)).

Despite the strong impact of losses on this truncated structure, we propose a simple way to verify the DBE nature of the resonances observed so far, i.e., the computation of the Q factors of these filters:

$$Q = \frac{f_{r,d}}{BW} \approx 2\pi f_{r,d} \frac{W_{rad}}{P_{loss}} \tag{3.1}$$

where $f_{r,d}$ is the resonance frequency, BW is the resonance bandwidth defined as the full width at half maximum. If Q is much larger than unity, the two expressions given in (3.1) are approximately equivalent. W_{rad} is the stored energy in the line. In the lossless case, the dissipated power P_{loss} is the power delivered on the output port, while in the lossy case also the dissipated power is considered in the denominator. In any case, the expression of Q given in terms of resonance frequencies will be used. The resonances are defined on the S_{11} parameters of the relevant truncated lines. The same definitions have been used for example in [42].

The loaded Q-factor for SIWs lines is then here computed in order to observe the fast increase of Q-factors with the number of cells N. The loaded Q-factors of different length lossless truncated resonators are shown in Fig. 3.5a, which shows that the Q-factor is proportional to N^5. This is the typical DBE characteristic of fast increasing Q-factor with the length of truncated lines as shown in Section 1.2.

The transmission group delay is also a prove of the existence of DBE, which is defined as $\tau = -\partial\left(\angle S_{21}\right)/\partial\omega$, $\angle S_{21}$ being the phase of the transmission coefficient S_{21}. [6]. In order to compare the group delays between different length truncated lines, the group delay is normalized by the delay in free space Nd/c. The normalized group delay

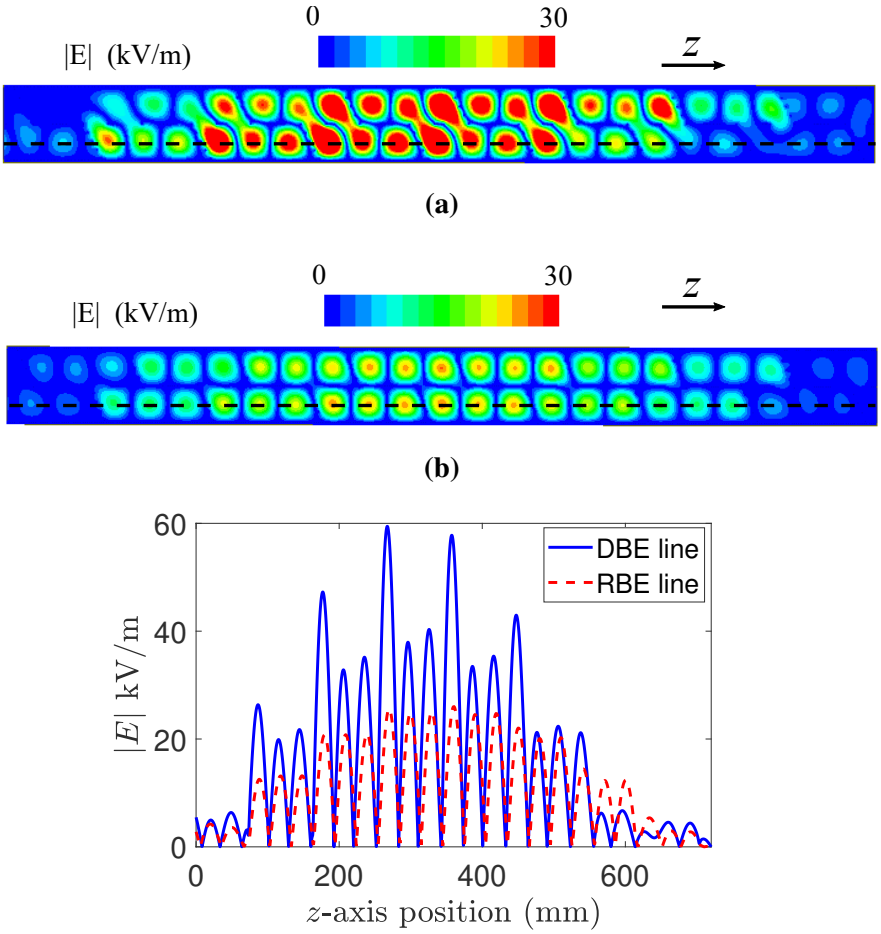

Fig. 3.4 E-field comparison between DBE and RBE 8-cell "long cell" line. (a) E-field distribution of DBE line. (b) E-field distribution of RBE line. (c) E-field magnitude (comparison between DBE and RBE lines) computed along the black dashed lines in the two previous subfigures.

is shown in Fig. 3.5b, where the group delay is proportional to N^4, typical of DBE resonances in [73].

To summarize these first results, for the lossless case, the "long cell" truncated SIW lines support strong DBE resonances, as confirmed by the computed Q factors, group delays, and field amplitude distribution. However, when the losses are considered, the DBE resonances are strongly affected. These results emphasize again the very sensitive behavior of DBE to the loss in SIW structures, with respect to other previous designs such as empty waveguides (where dielectric losses are absent) and microstrip lines (where conducting and dielectric losses are less severe). This confirms the difficulty in designing SIWs-DBE lines, where losses should carefully controlled.

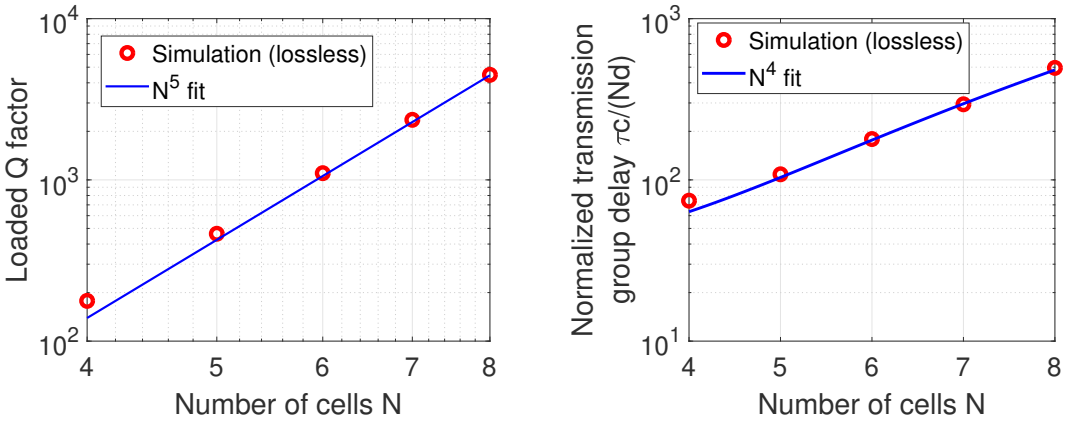

(a) **(b)**

Fig. 3.5 The Q-factor and group delay of different length "long cell" truncated SIWs resonators. (a) Q-factor whose scaling is proportional to N^5. (b) Group delay whose scaling fits to N^4.

3.2.2 Truncated "Double-oblique-line cell" SIWs Lines

The schematic of N-cell truncated SIWs lines of "double-oblique-line" unit cells is shown in Fig. 3.6, where the left-down and right-up ports are shorted by PEC boundaries and the other two ports are excited. Also in this case, the two ports to be shorted have been selected because they have strong reflections according to Fig. 2.29.

The S parameters of 4- to 8-cell SIWs resonators are shown in Fig. 3.7 with and without losses. For the lossy case, the resonance peaks are flat indicating that also in this case the perturbation of the DBE condition is severe. The magnitude of lossless S_{11} at the DBE resonance frequency is shown in Fig. 3.8, which shows more clearly that the resonance frequency is approaching to the DBE frequency as N increases.

The E-field distribution for a 8-cell truncated structure at the DBE resonance frequency is shown in Fig. 3.10(a). We modify this structure by shortening the separation between the oblique vias. This leads to an alternative line having a RBE at 2.507 GHz. The E-field distribution of 8-cell truncated RBE line is shown in Fig. 3.10(b). We plot also the E-field magnitude along the black dashed lines in Fig. 3.10(a) and (b), when the 8-cell DBE and RBE lines are both fed on the upper-left port with an ideal waveguide of 1W. The maximum field density of 8-cell DBE line is 47 kV/m, while for 8-cell RBE line, it is 35 kV/m.

For the lossless situation, the Q-factor according to the number of cells is shown in Fig. 3.9a, confirming the trend proportional to N^5. In Fig. 3.9b, the group delay of the lossless truncated lines fits the N^4 scaling.

As a conclusion, the "double-oblique-line" truncated SIWs lines support strong DBE resonances for the lossless case, but losses weaken considerably these resonances.

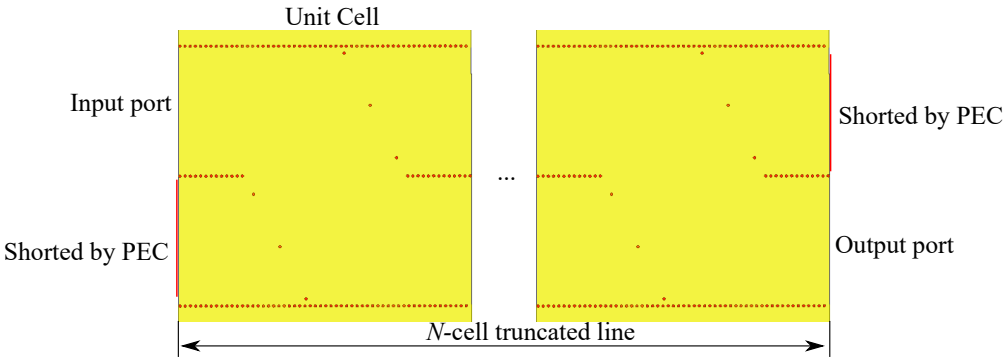

Fig. 3.6 N-cell "double-oblique-line" SIWs line.

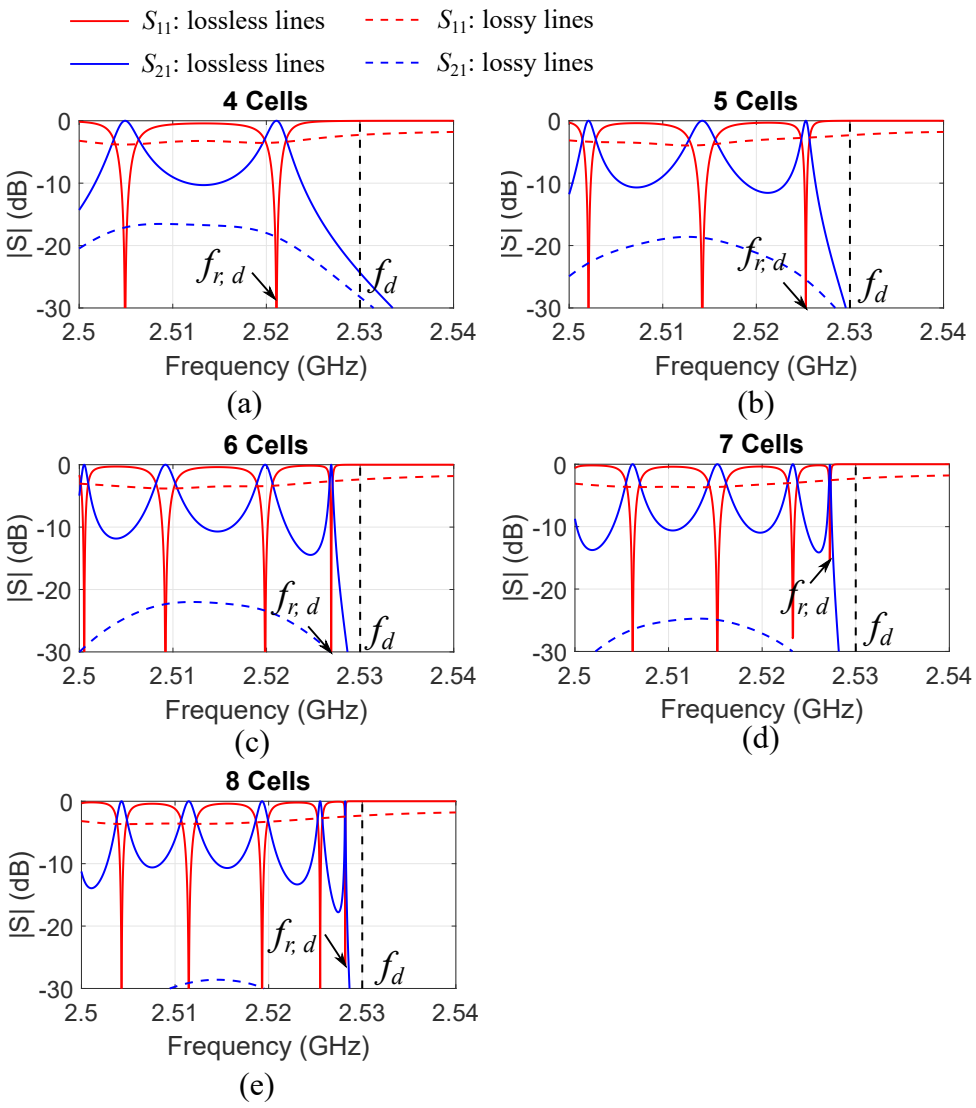

Fig. 3.7 S parameters of the "double-oblique-line" truncated SIWs lines. (a) 4-cell truncated SIWs line. (b) 5-cell truncated SIWs line. (c) 6-cell truncated SIWs line. (d) 7-cell truncated SIWs line. (e) 8-cell truncated SIWs line.

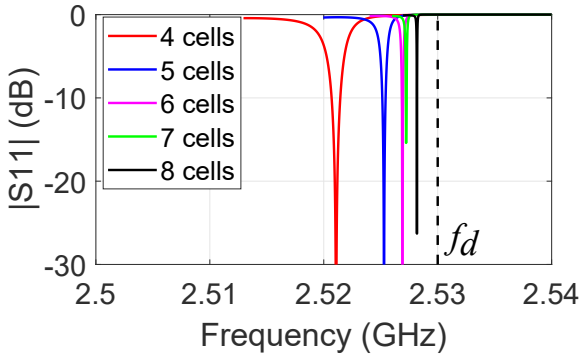

Fig. 3.8 $|S_{11}|$ at the resonance frequency for different length of "double-oblique-line" truncated SIWs lines.

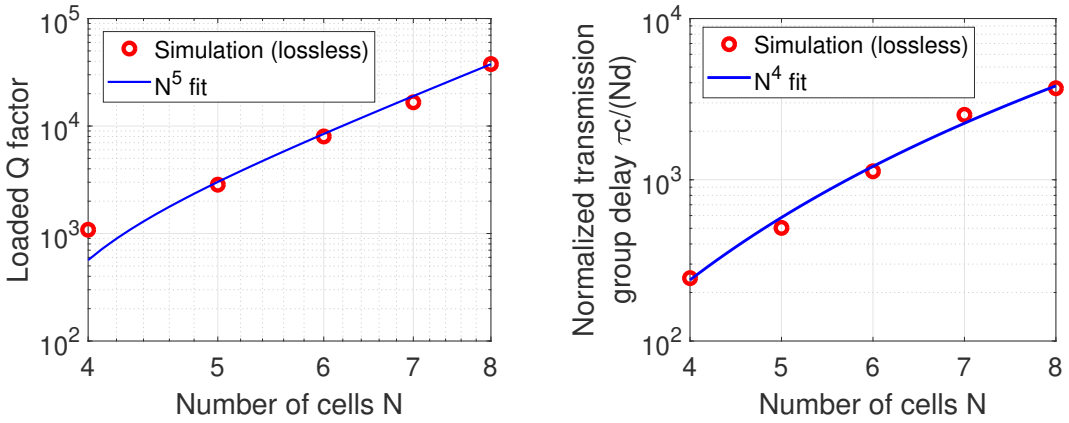

(a) **(b)**

Fig. 3.9 The Q-factor and group delay of different length "double-oblique-line" truncated SIWs resonators. (a) The Q-factor is proportional to N^5. (b) The group delay is proportional to N^4.

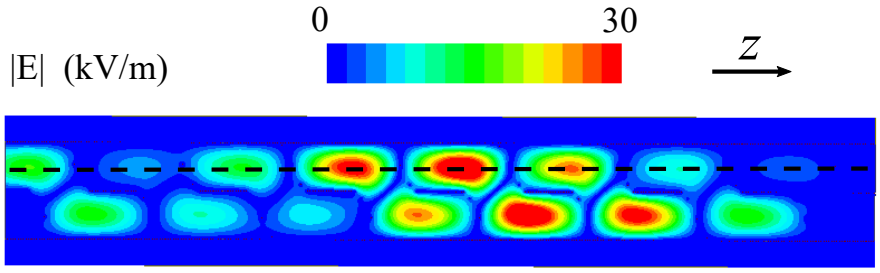

(a)

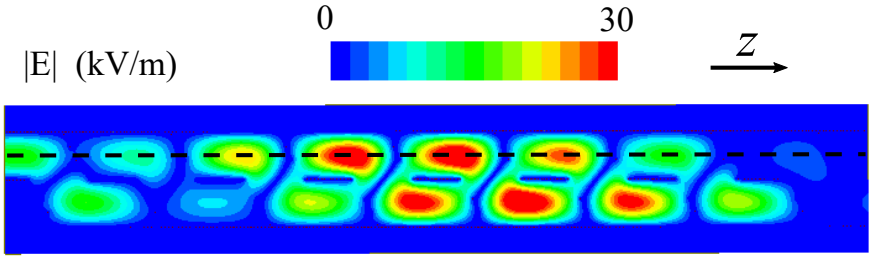

(b)

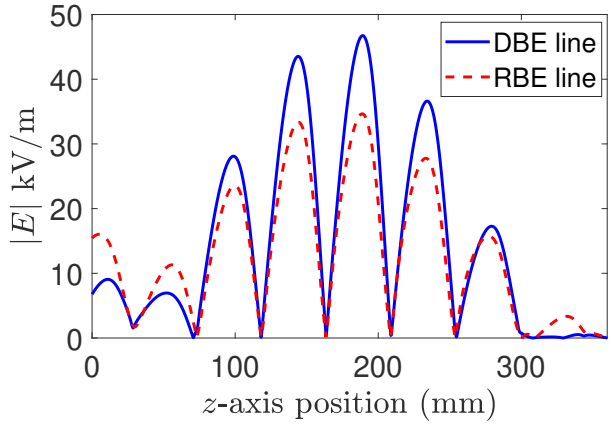

(c)

Fig. 3.10 E-field comparison between DBE and RBE 8-cell "double-oblique-line cell" line. (a) E-field distribution of DBE line. (b) E-field distribution of RBE line. (c) E-field magnitude (comparison between DBE and RBE lines) computed along the black dashed lines in the two previous subfigures.

3.2.3 Truncated "Single-oblique-line cell" SIW Lines

A finite-length SIW line composed of "N single-oblique-line" cells is shown in Fig. 3.11, whose upper-left and lower-right ports are shorted by two PEC boundaries and the other two ports are excited in the simulation.

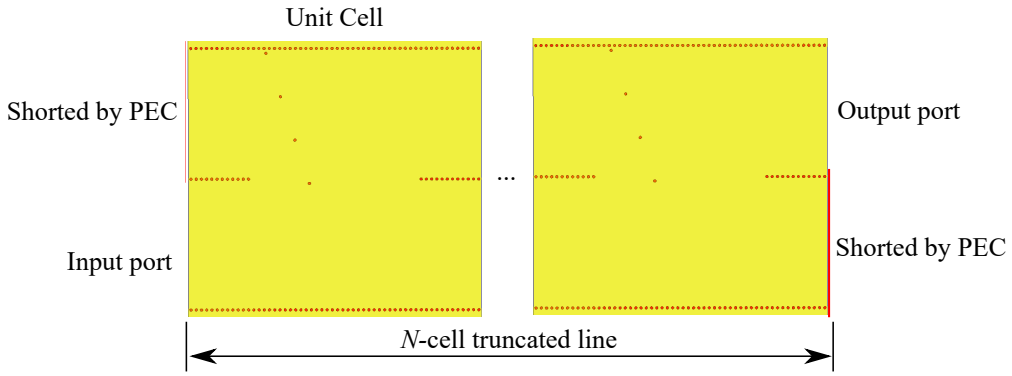

Fig. 3.11 The N-cell truncated simulation model of "single-oblique-line cell".

The magnitude of S parameters for different truncated lines with and without losses are shown in Fig. 3.12. Again, losses have a strong impact on the DBE condition. In this structure, the DBE resonance is still visible with a 4-cell lossy structures, but it is lost as the structures becomes longer. Losses limit then the total length of the structures. When we increase the length from 6 cells to 8 cells, the DBE disappears (the $|S_{11}|$ peak does not drop below -3dB at the resonance frequency). For the lossless case, the coefficient S_{11} has a very narrow peak at the resonance frequency, which means the resonator is well matched and the quality factor Q is very high. The resonance frequency $f_{r,d}$ is approaching to DBE frequency f_d, when the number of cells is increasing, as shown in Fig. 3.13. Also the resonance peak is getting narrower, which means the Q factor is increasing. As the number of cell N increases, the Q factor is in fact again proportional to N^5 (Fig. 3.15a), and the group delay is proportional to N^4 (Fig. 3.15b).
The E-field distribution at the DBE and RBE resonance frequency is shown in Fig. 3.14, where the RBE structure is obtained by adjusting the oblique angle φ to $76\,\mathrm{deg}$. The two 8-cell resonators are excited by an ideal 1W waveguide at bottom-left port. In Fig. 3.14(c), the E-field magnitude along the dashed black lines in Fig. 3.14(a) and (b) shows the maximum field density is enhanced to 60 kV/m in DBE line compared to 25 kV/m in RBE line.
In conclusion, for the lossless truncated N-cell SIW-DBE resonator, as expected, its Q factor is proportional to N^5. The resonance frequency is approaching the DBE frequency when the number of cells is increasing, and a giant field enhancement at the center is obtained. However, we also find that losses strongly impact the robustness of the DBE condition, which may disappear as the length of the structure increases.

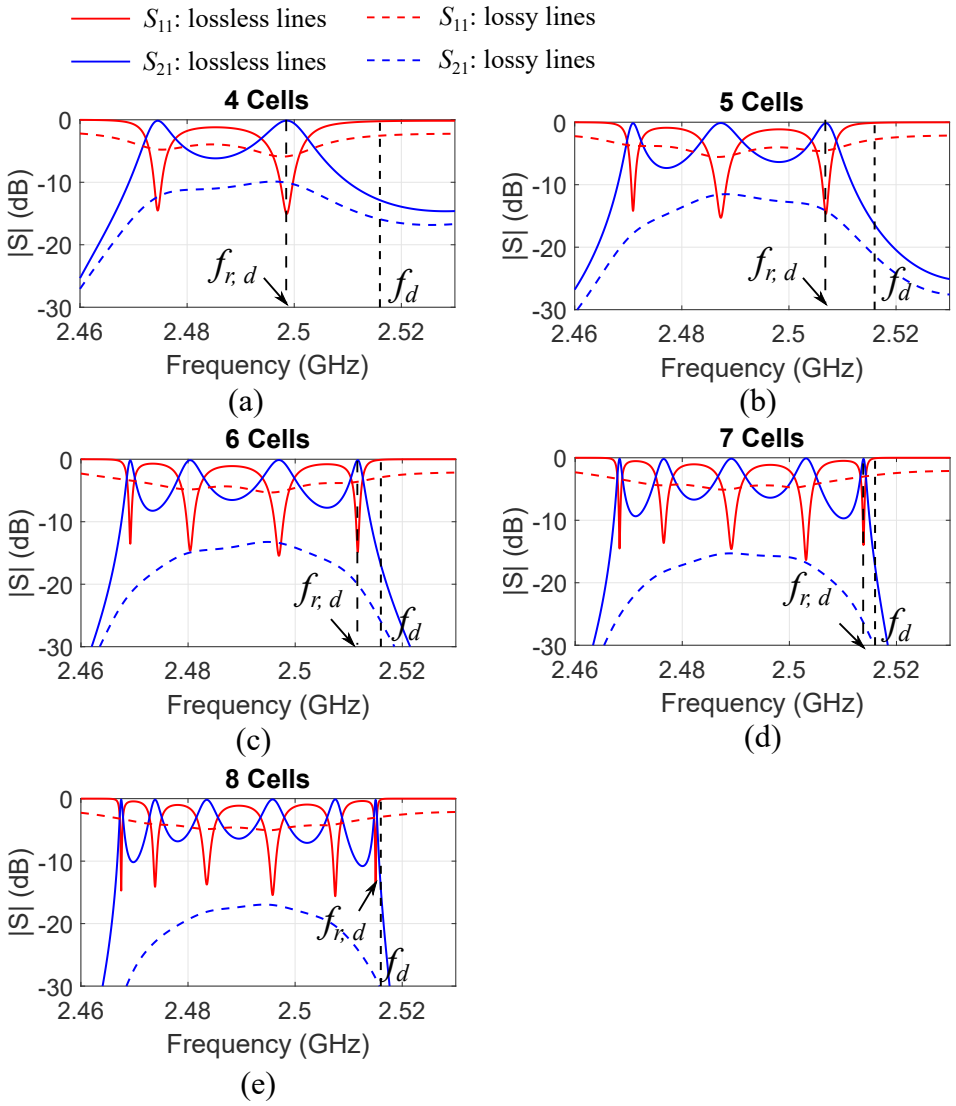

Fig. 3.12 Full-wave simulation results of S parameters of "single-oblique-line cell" SIWs lines considering the influence of losses. (a) 4-cell truncated SIWs line. (b) 5-cell truncated SIWs line. (c) 6-cell truncated SIWs line. (d) 7-cell truncated SIWs line. (e) 8-cell truncated SIWs line.

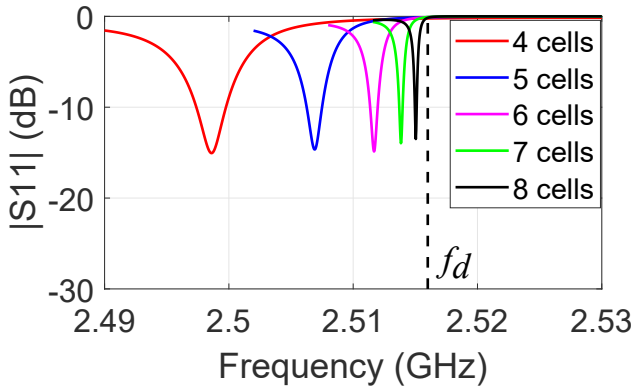

Fig. 3.13 Magnitude of S_{11} of different length "single-oblique-line cell" SIWs lines. When the number of cells increases, the resonance frequency is approaching the DBE frequency and the resonance peak gets narrower.

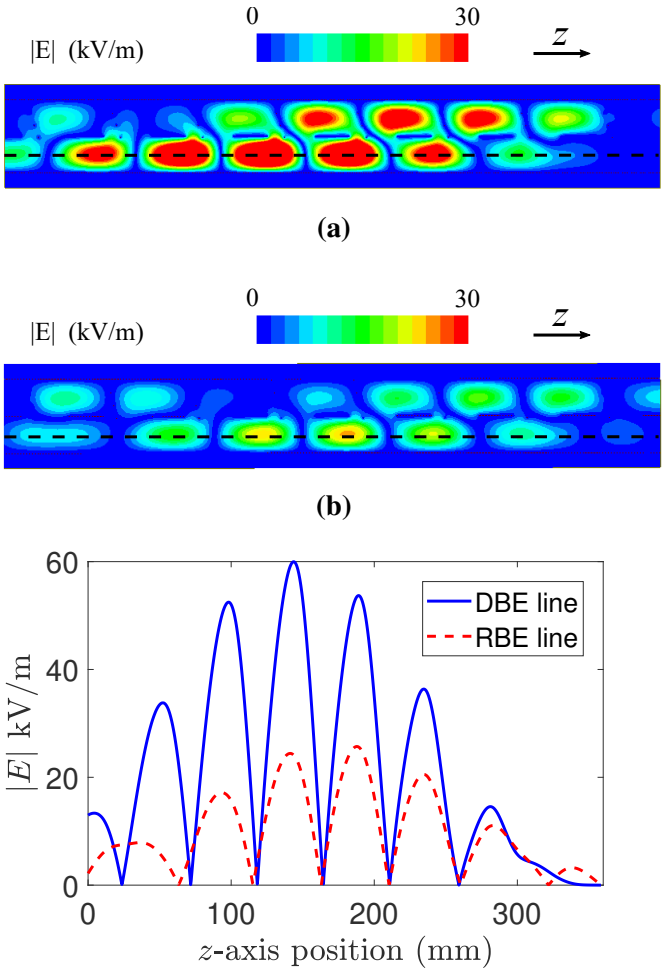

Fig. 3.14 E-field comparison between DBE and RBE 8-cell "single-oblique-line cell" line. (a) E-field distribution of DBE line. (b) E-field distribution of RBE line. (c) E-field magnitude (comparison between DBE and RBE lines) computed along the black dashed lines in the two previous subfigures.

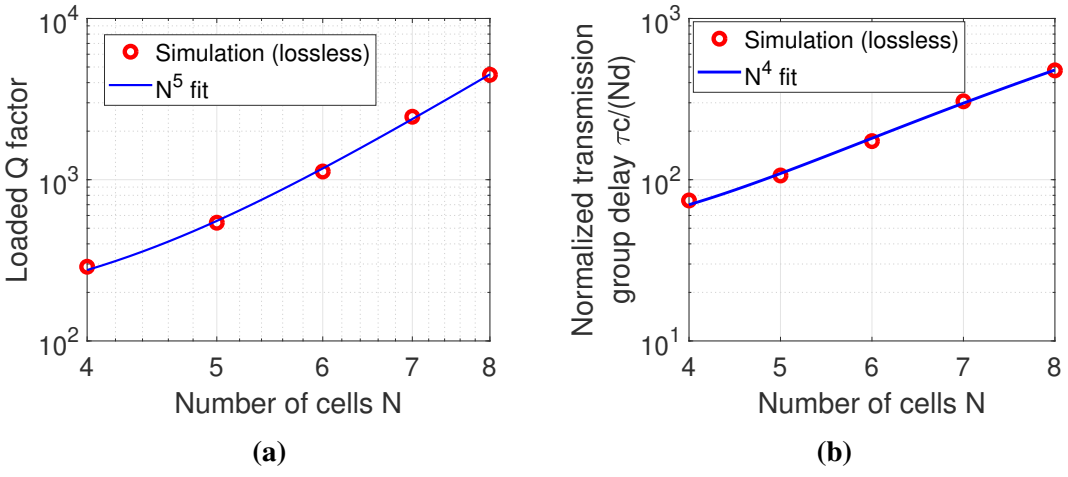

Fig. 3.15 The Q-factor and group delay of "single-oblique-line cell" SIWs lines. (a) The Q-factor is proportional to N^5. (b) The group delay is proportional to N^4.

3.2.4 Truncated "Corner cell" SIWs Lines

The truncated "corner cell" SIWs line is shown in Fig. 3.16. The structure is accessible through the two lower ports, excited in the HFSS simulation with ideal waveguide ports, while the two upper ports are shorted with PEC boundaries, again in order to minimize reflections close to the ports of the truncated line.

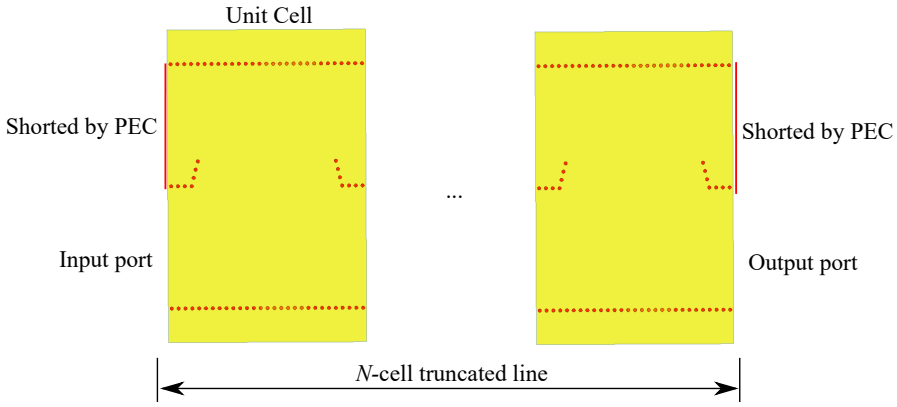

Fig. 3.16 The N-cell truncated SIWs simulation model of "corner cell" and "low-loss-substrate cell" designs.

The magnitude of the S parameters (Fig. 3.17) show the DBE resonances of different length lines with and without losses. In the lossless case, the $|S_{11}|$ and $|S_{21}|$ patterns are the same as in the previous truncated lines (the DBE resonance peak gets narrower and approaches DBE frequency as N increases). Interestingly, the "corner cell" truncated lines are more robust under the losses influence compared to the previous three designs. The shape of the resonance peaks are still recognizable and the magnitude peak of S_{11} is below -3 dB for filters of 4, 5 and 6 cells (Fig. 3.18). This phenomenon confirms the reduced impact of losses as quantified by the hyperdistance in Table. 2.1: the hyperdistance of lossy "corner cell" is 0.2, lower than the one of the lossy "long cell" (0.52), "double-oblique-line cell" (0.76), and "single-oblique-line cell" (0.83). This indicates that the "corner cell" is not only more robust to the perturbations of oblique vias but also to the losses influence, as confirmed by these truncated-line results. The E-field distribution of 8-cell "corner cell" is shown in Fig. 3.19. The distribution of RBE resonator is not shown here for the "corner cell" topology. As explained, this cell is more robust to the geometrical perturbation. Therefore, it is hard to get a structure having a RBE near the DBE frequency of the original structure, by modifying a single geometrical parameter.

The Q-factors and group delays are shown in Fig. 3.20a and Fig. 3.20b. As the lossy 4- and 5-cell truncated lines have recognizable DBE resonance peak, lossy Q factors can be computed and plotted in these cases. In Fig. 3.20a, the lossless Q-factors fit N^5 as observed in previous designs, and the lossy Q-factors have the same trend, but

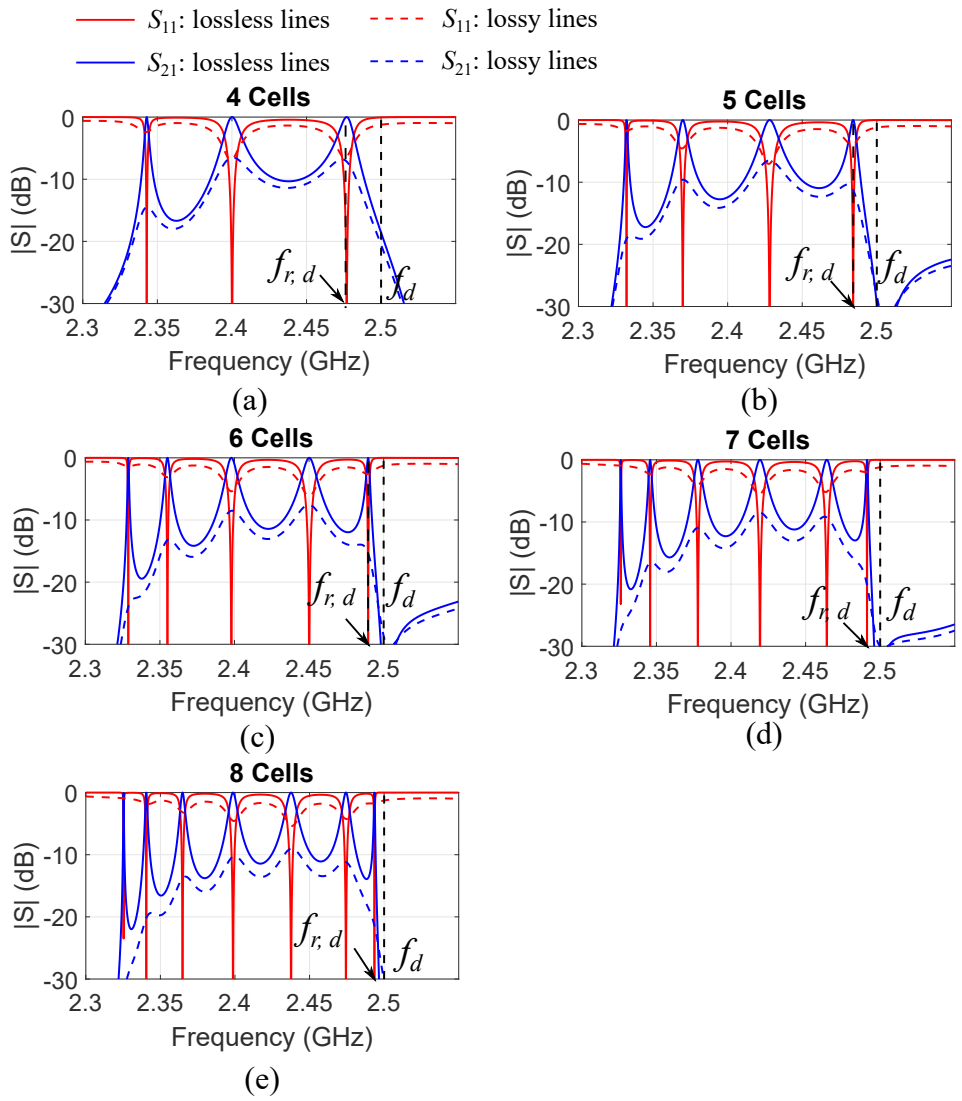

Fig. 3.17 S parameters of "corner cell" SIWs line considering the influence of losses. (a) 4-cell truncated SIWs line. (b) 5-cell truncated SIWs line. (c) 6-cell truncated SIWs line. (d) 7-cell truncated SIWs line. (e) 8-cell truncated SIWs line.

with lower values. The group delay of lossless lines fit N^4 but the two lossy lines group delays do not increase with N, which may be related to weaker resonances under losses.

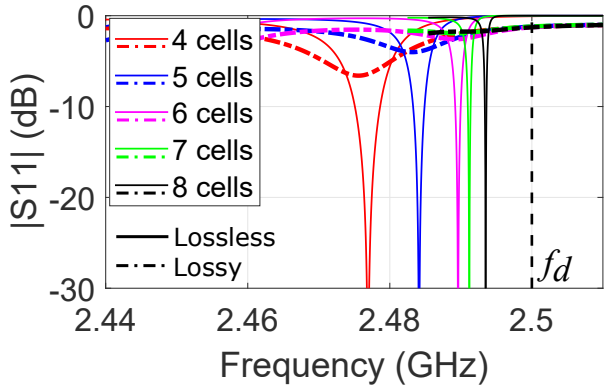

Fig. 3.18 Magnitude of S_{11} for different length "corner cell" SIWs structures.

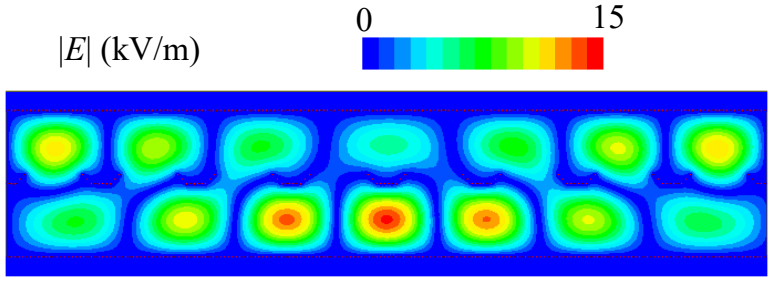

Fig. 3.19 The E-field distribution of 8-cell truncated SIWs of "corner cell".

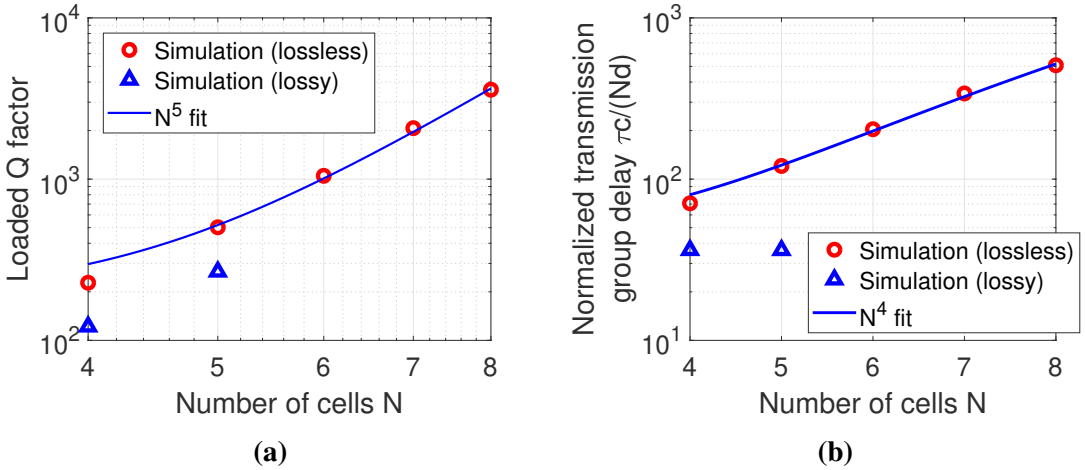

Fig. 3.20 The Q-factor and group delay of "corner cell" SIWs lines. (a) The scaling of Q factor fits a N^5 law. (b) The scaling of group delay fits a N^4 law.

3.3 Truncated Low-loss SIWs Lines

In this section we simulate the truncated lines obtained with the three different low-loss cells proposed in the previous chapter: the "low-loss-substrate cell" employing a low-loss substrate and the two air-filled SIWs.

3.3.1 Truncated "Low-loss-substrate cell" SIWs Lines

The simulation model of N-cell truncated SIW line of "low-loss-substrate cell" having a DBE frequency at around 6 GHz is similar to the "corner cell" of Fig. 3.16, apart from the different values of parameters given in section 2.4.6. In this structure, the upper two ports are shorted and the bottom two ports are connected to waveguide ports.
The S parameters of different truncated lines with and without losses are shown in Fig. 3.21. As expected, the use of a lower-loss substrate considerably reduces the loss impact on the resonances, and it is confirmed to be the main cause for the DBE disappearance in the results of the previous section. Despite the presence of the losses in the copper, the resonance peaks of $|S_{11}|$ are now below -3dB until 8 cells. The $|S_{11}|$ of the DBE resonances in the different structures are shown together in Fig. 3.22, which shows more clearly the influence of the losses as a decrease of the peaks of DBE resonances as N increases. The E-field distribution of 8-cell line at DBE frequency is shown in Fig. 3.23.
The Q-factors and group delay in lossless and lossy conditions are shown in Fig. 3.24a and Fig. 3.24b. Both the Q-factors with and without losses fit the N^5 scaling. The difference between them becomes larger with the increase of N, thus predicting a limitation in the number of cells when observing the DBE. The influence of losses is more significant for group delays. For the lossless SIWs lines, the group delay fits the N^4 scaling. However, for the lossy SIWs lines, the growth rate significantly slows down when the number of cells is more than 6.
To summarize, losses have been significantly reduced in this "low-loss-substrate cell" SIWs design to such a point that the DBE resonances can be observed in 8-cell lines whose $|S_{11}|$ is below -3dB. The Q-factor trend with respect to the number of cells N is not significantly modified by losses, despite lower values, while the group delay of lossy lines indicates that the typical fast increase with N is lost for long truncated lines.

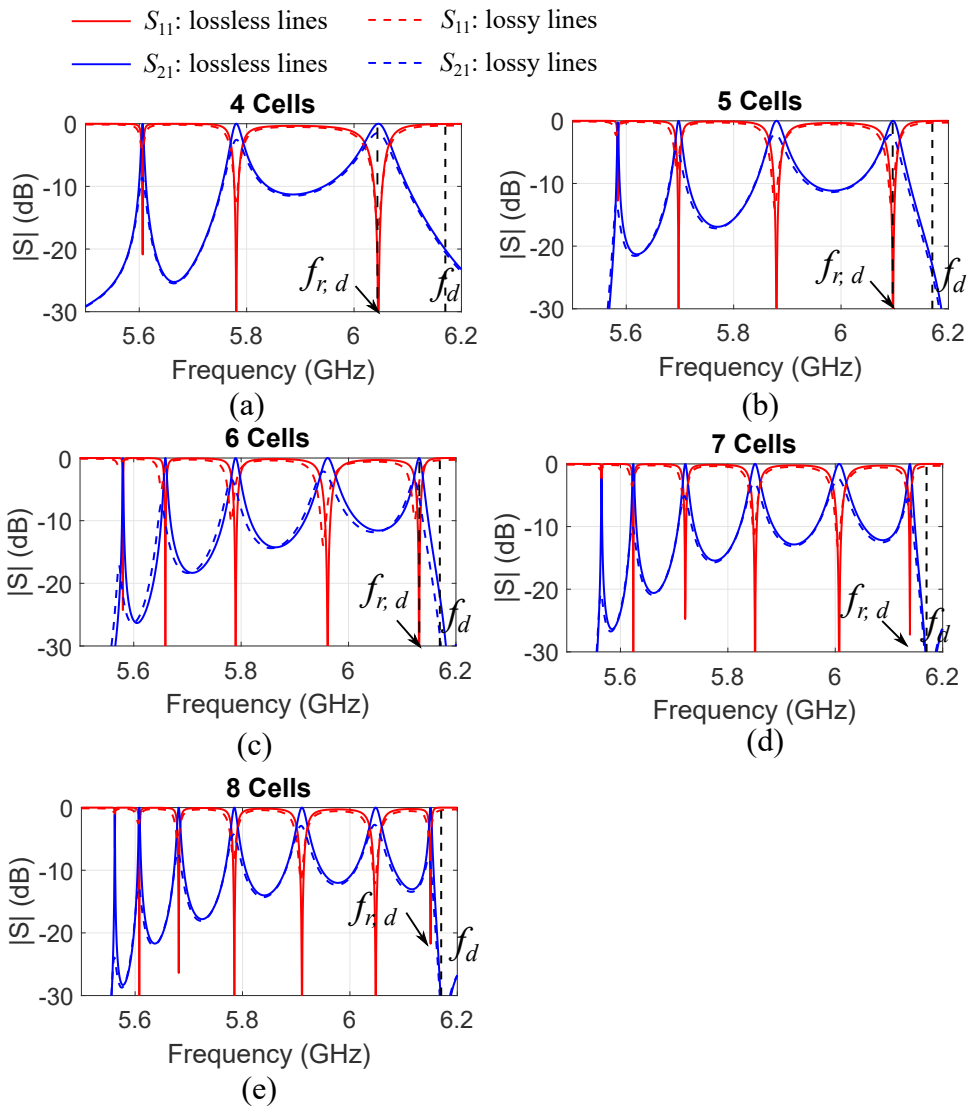

Fig. 3.21 S parameters of "low-loss-substrate cell" SIWs line considering the influence of losses. (a) 4-cell truncated SIWs line. (b) 5-cell truncated SIWs line. (c) 6-cell truncated SIWs line. (d) 7-cell truncated SIWs line. (e) 8-cell truncated SIWs line.

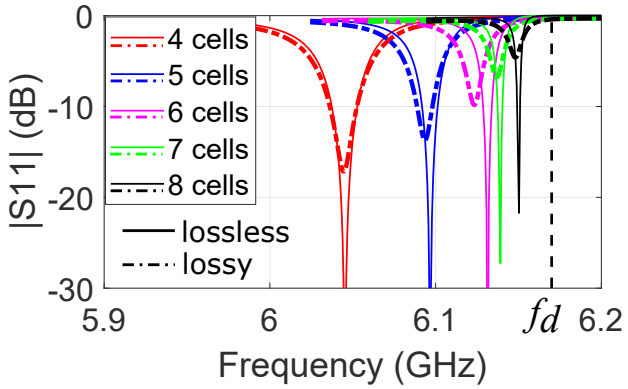

Fig. 3.22 Magnitude of S_{11} for different length "low-loss-substrate cell" SIWs structures.

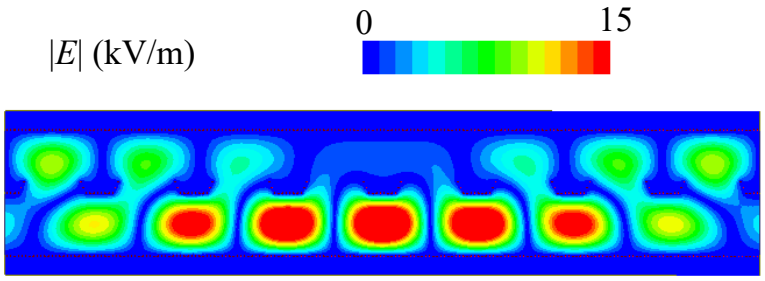

Fig. 3.23 The E-field distribution of 8-cell truncated SIWs of "low-loss-substrate cell".

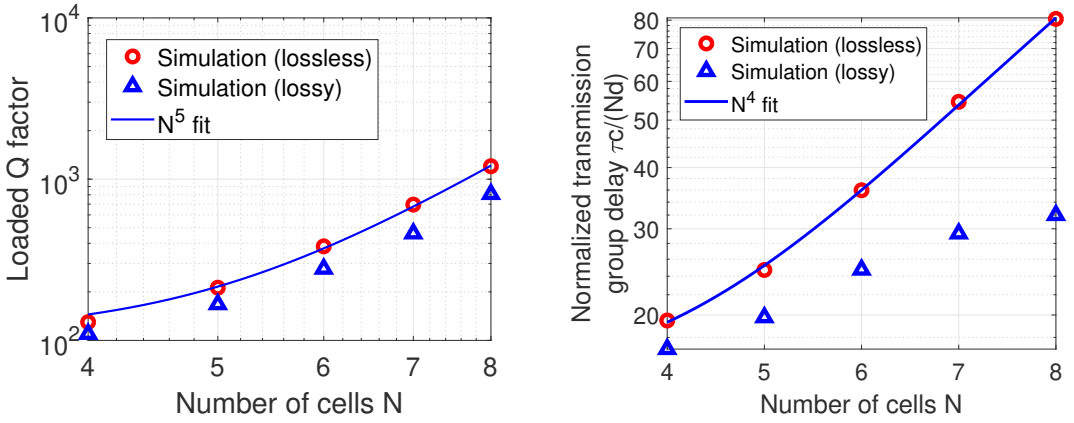

Fig. 3.24 The Q-factor and group delay of "low-loss-substrate cell" SIWs lines. (a) The scaling of Q factor fits a N^5 law. (b) The scaling of group delay fits a N^4 law.

3.3.2 Truncated "Air-filled cell 1" SIWs Lines

Fig. 3.25 shows the middle layer of the simulation model of truncated "air-filled cell 1" SIWs lines (see Section 2.4.7), in which the two ports of the upper SIW line are shorted and the bottom two ports are excited. As explained in the previous chapter, the air-filled SIWs are composed of three layers, where the top and bottom layers act as copper planes and the air-filled part of middle layer provides the propagation path of the wave.

The S parameters of different truncated lines with and without losses are shown in Fig. 3.26. The DBE resonance peaks of $|S_{11}|$ are shown in Fig. 3.27. The loss influence is reduced with respect to the previous low-loss structure, thanks to the absence of dielectric. The DBE resonance peak of $|S_{11}|$ is below -3dB until 7 cells. The E-field distribution of 8-cell truncated SIW lines at the DBE frequency is shown in Fig. 3.28.

The Q-factors and group delays of different truncated SIW lines are shown in Fig. 3.29a, and Fig. 3.29b. The Q-factor of lossy lines also fit the N^5 scaling as the lossless case. However, the group delay of the lossy case does not increase fast with N^4 as lossless case. The group delay of 8-cell line is even lower than 7-cell line, which corresponds to the disappearance of the DBE resonance peak of 8-cell line in $|S_{11}|$ curve.

To resume, the "air-filled cell 1" design also reduced the losses as the previous "low-loss-substrate cell" design. Still, the FR-4 substrate embedded in the air-filled area to realize the central lines of pins may be source of losses. In the next design, we use the second air-filled unit cell of Section 2.4.8, where this middle line is not present, with the aim of further minimizing losses.

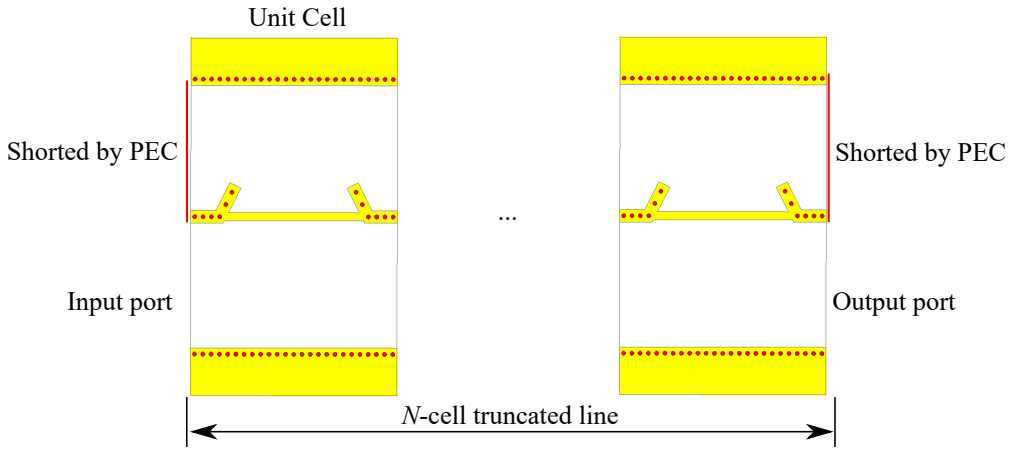

Fig. 3.25 The N-cell truncated simulation model of "air-filled cell 1".

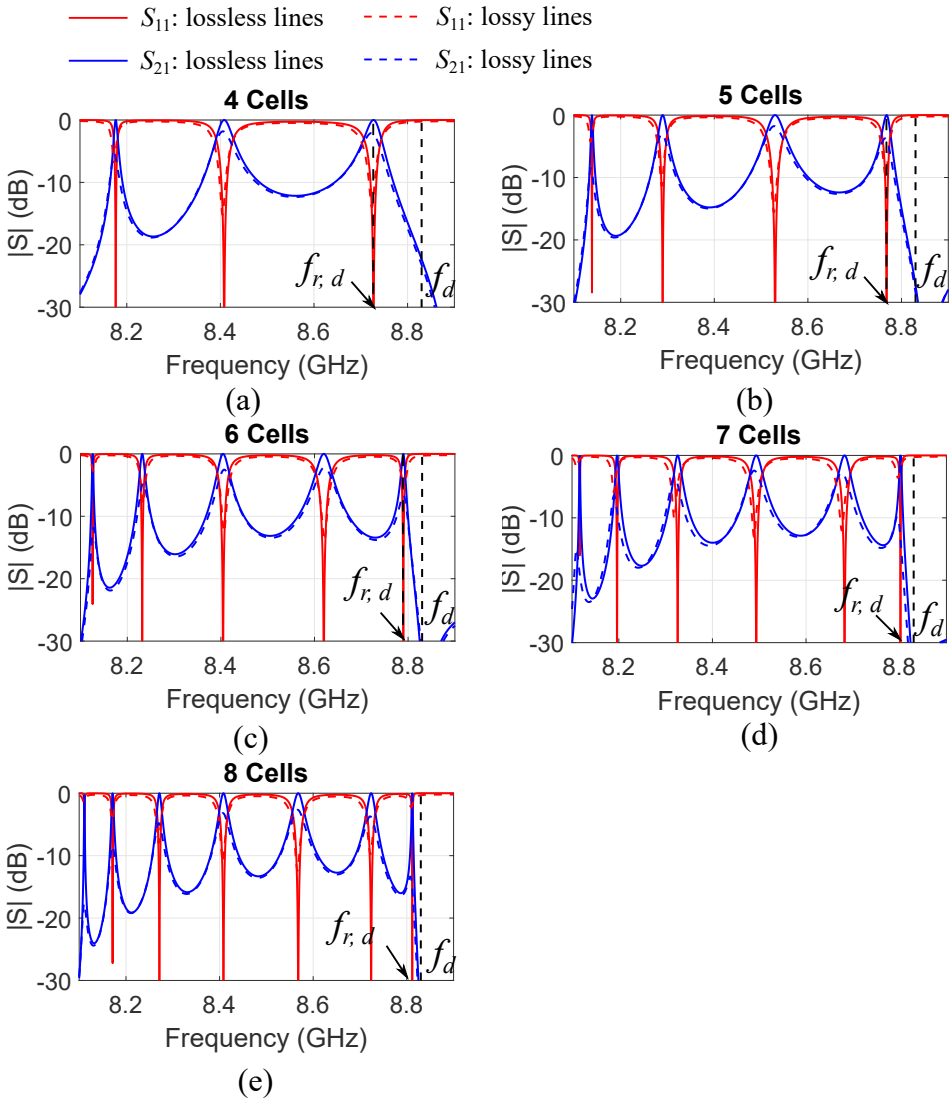

Fig. 3.26 S parameters of "air-filled cell 1" SIWs lines considering the influence of losses. (a) 4-cell truncated SIWs line. (b) 5-cell truncated SIWs line. (c) 6-cell truncated SIWs line. (d) 7-cell truncated SIWs line. (e) 8-cell truncated SIWs line.

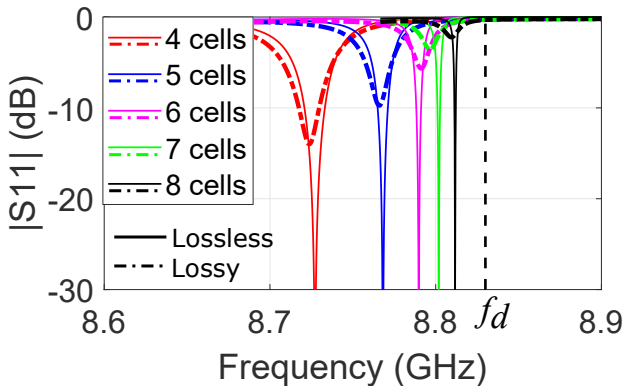

Fig. 3.27 Magnitude of S_{11} of different length "air-filled cell 1" SIWs lines.

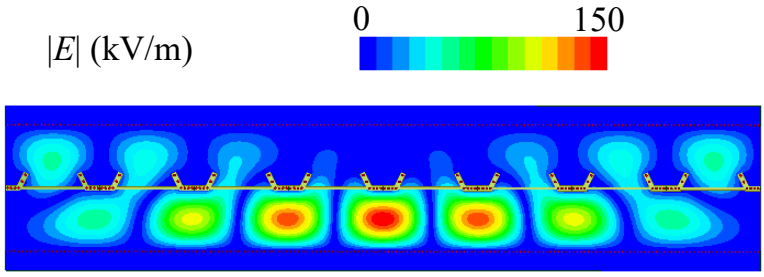

Fig. 3.28 The E-field distribution of 8-cell truncated SIWs of "air-filled cell 1".

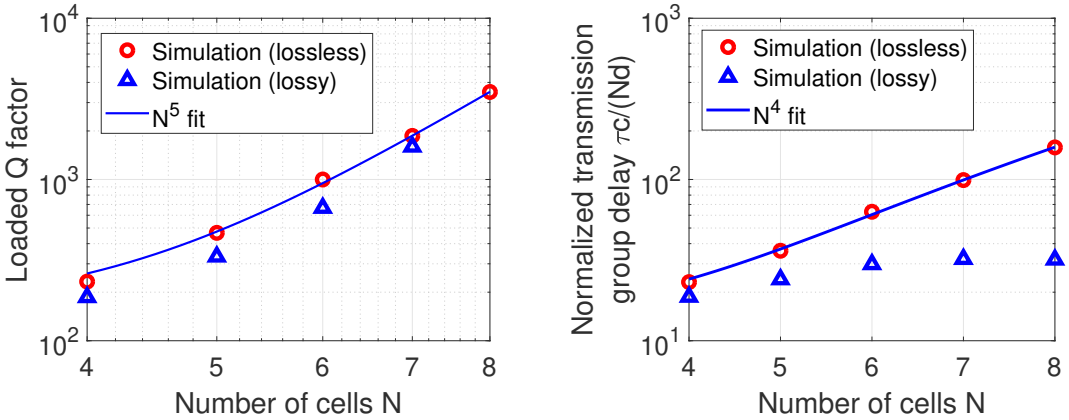

Fig. 3.29 The Q-factor and group delay of "air-filled cell 1" SIWs lines. (a) The scaling of Q factor is 5-th power of N. (b) The scaling of group delay is fit to N^4.

3.3.3 Truncated “air-filled cell 2” SIWs Lines

The simulation model of the truncated SIW lines composed of the “air-filled cell 2” unit cells discussed in Section 2.4.8 is shown in Fig. 3.30. Again the upper two ports are shorted by PEC and the lower ports are excitation ports. As explained in the previous chapter, the “air-filled cell 2” line are made up of three PCB boards, where the top and bottom boards act as copper planes and the middle board is an air-filled SIW line. The copper pillars are soldered to the top and bottom layers, so the substrate middle line used in the previous design to hold the vias is no more needed, which is expected to further reduce the substrate losses.

The S parameters of different truncated lines are shown in Fig. 3.31 with and without losses. And the $|S_{11}|$ of DBE resonance peaks is below -3 dB until 7 cells as shown in Fig. 3.32. In Fig. 3.33, the E-field distribution at the DBE resonance frequency of 8-cell truncated line is presented.

The Q-factor and group delay are shown in Fig, 3.34a and Fig. 3.34b. Similar to the the “air-filled cell 1” SIWs designs, the Q fits N^5 for both lossless and lossy cases. The group delay for lossless case fits N^4 as usual, while, for the lossy case, the group delay decreases if more than 6 cells.

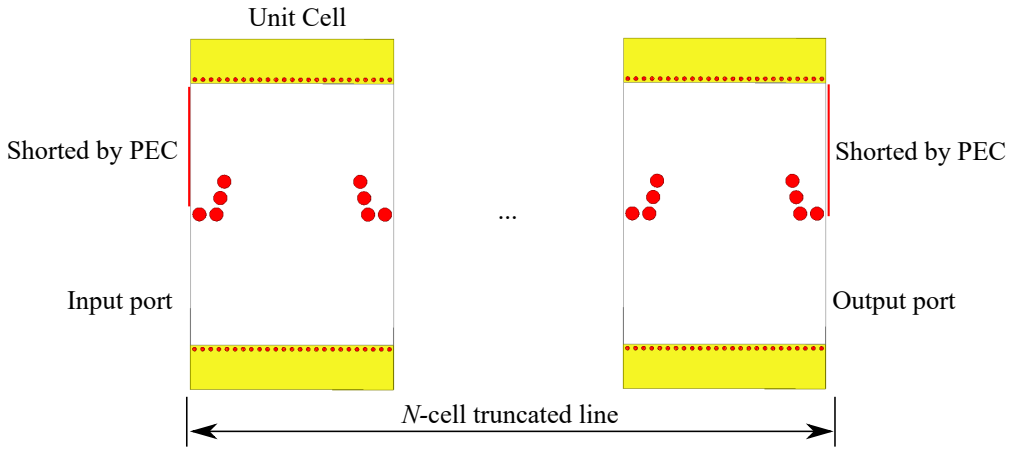

Fig. 3.30 The N-cell truncated simulation model of “air-filled cell 2”.

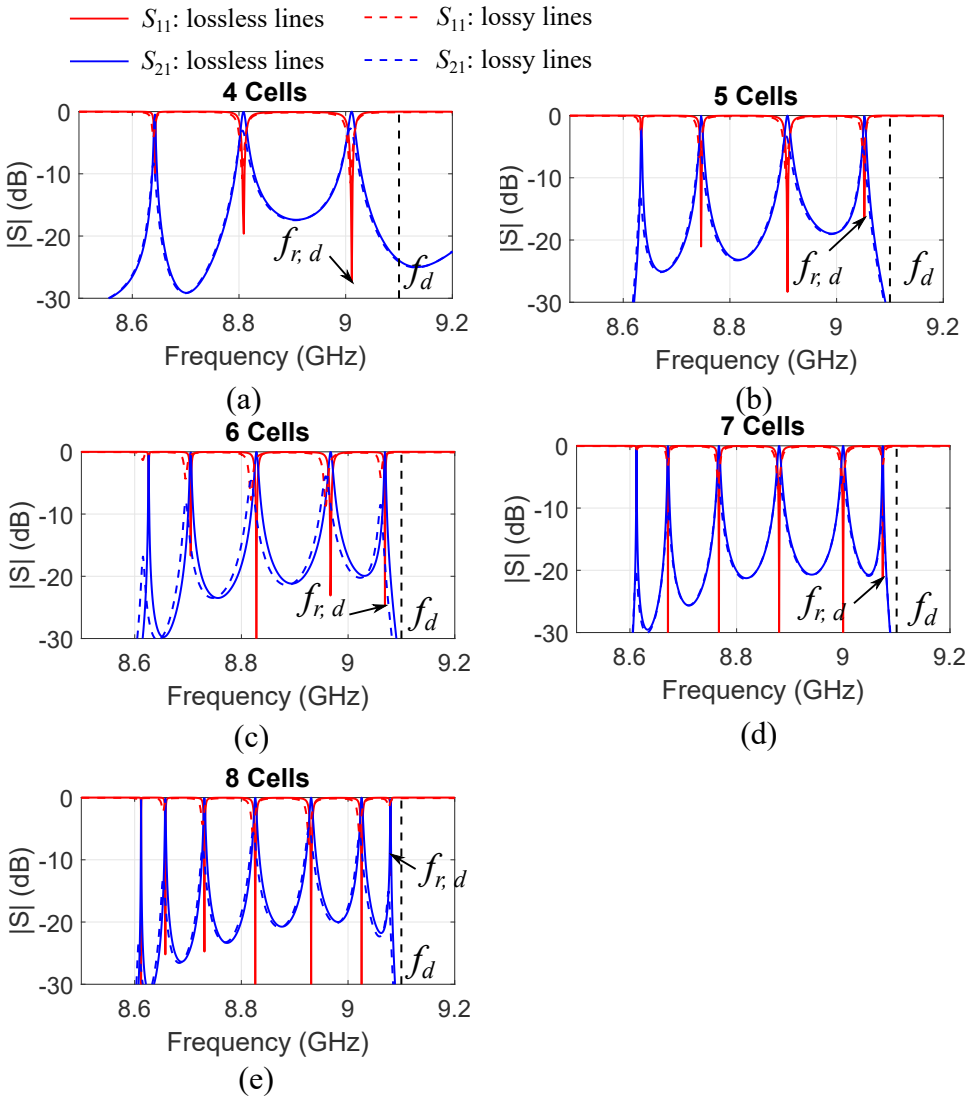

Fig. 3.31 S parameters of "air-filled cell 2" SIWs lines considering the influence of losses. (a) 4-cell truncated SIWs line. (b) 5-cell truncated SIWs line. (c) 6-cell truncated SIWs line. (d) 7-cell truncated SIWs line. (e) 8-cell truncated SIWs line.

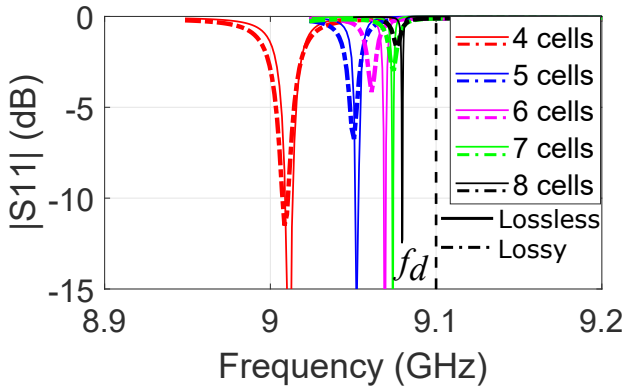

Fig. 3.32 Magnitude of S_{11} of different length "air-filled cell 2" SIWs lines.

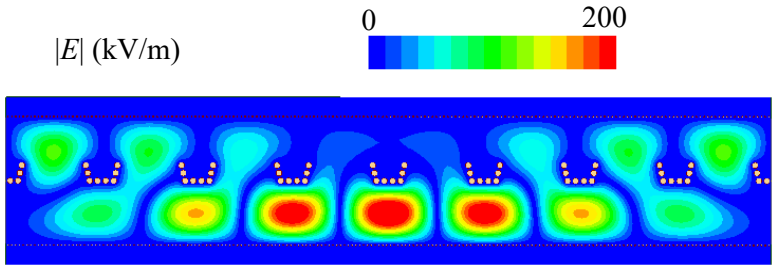

Fig. 3.33 The E-field distribution of 8-cell truncated SIWs of "air-filled cell 2".

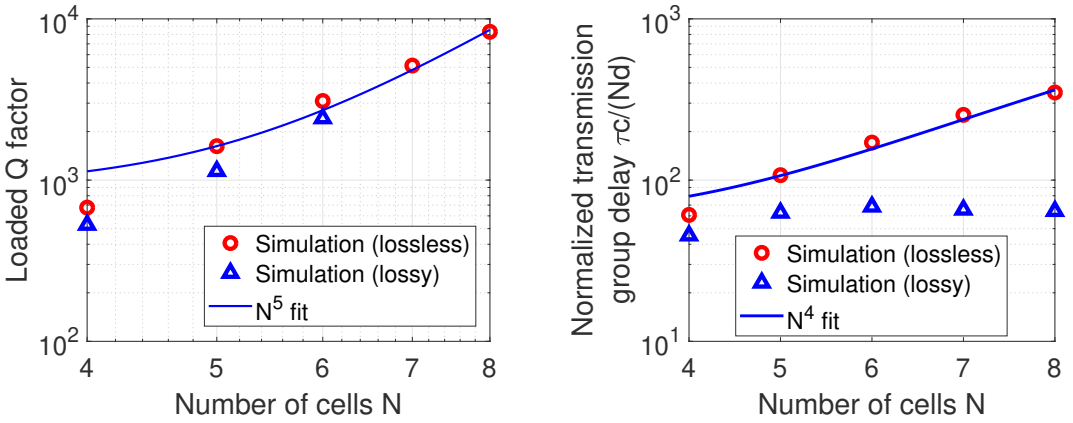

(a) **(b)**

Fig. 3.34 The Q-factor and group delay of "air-filled cell 2" SIWs lines. (a) The scaling of Q factor is 5-th power of N. (b) The scaling of group delay is fit to N^4.

3.3.4 Comparison of Truncated SIWs Designs

In this subsection, we compare the Q-factors and normalized group delays of different SIWs designs. This comparison will also help to select the best candidate for an experimental validation fabrication. The results are shown in Table. 3.1. The three low-loss designs ("low-loss-substrate cell", "air-filled cell 1", and "air-filled cell 2") can lead to measurable DBE resonances considering losses. Among them, we find that although they have similar unit cell size, their loaded Q-factor and group delay have significant differences.

The lossless results of these last three structures are at first analyzed. The Q-factor of "air-filled cell 1" SIWs is more than twice than the one of a "low-loss-substrate cell" SIW. In turn, the Q factor of the "air-filled cell 2" is more than twice than the "air-filled cell 1". The group delay of "low-loss-substrate cell" SIWs lines and "air-filled cell" SIWs lines are similar, but the group delays of "air-filled cell 2" lines are more than doubled.

Other considerations can be added if losses are included in the model. Among these last three designs, the "low-loss-substrate cell" design suffers less from losses for larger values of N. This makes it a good candidate for an experimental validation of the growing trend of Q vs. N. The "air-filled cell 1" and "air-filled cell 2" are also robust to the influence of loss and obtain DBE resonances. Although their DBE resonances disappear for long lines, their load Q-factors of 6 or 7 cells are still larger than the 8-cell "low-loss-substrate cell". This makes them interesting structures to be fabricated as comparison. This is particularly true if the cost factor is also considered, since these structures use low-cost FR-4 dielectrics instead of a more expensive low-loss substrate.

Table 3.1 Comparison of loaded Q-factor and group delay between different truncated SIWs designs

Type of SIWs design	N	Loaded Q-factor		Normalized group delay	
		lossless	lossy	lossless	lossy
"long cell"	4	178	/	74	/
	5	463	/	108	/
	6	1101	/	179	/
	7	2358	/	294	/
	8	4484	/	495	/
"double-oblique-line cell"	4	171	/	33	/
	5	249	/	41	/
	6	467	/	56	/
	7	820	/	78	/
	8	1274	/	103	/
"single-oblique-line cell"	4	289	/	74	/
	5	541	/	106	/
	6	1124	/	174	/
	7	2457	/	306	/
	8	4477	/	479	/
"corner cell"	4	228	122	71	36
	5	503	267	121	36
	6	1048	/	204	/
	7	2071	/	340	/
	8	3588	/	509	/
"low-loss-substrate cell"	4	130	110	20	17
	5	212	168	25	20
	6	383	278	36	25
	7	695	460	55	29
	8	1202	808	81	32
"air-filled cell 1"	4	233	186	24	19
	5	467	333	36	24
	6	1000	667	63	30
	7	1864	1598	99	32
	8	3490	/	158	32
"air-filled cell 2"	4	675	528	61	45
	5	1624	1138	107	63
	6	3096	2416	171	68
	7	5132	/	254	66
	8	8315	/	350	64

3.4 Design of feeding transitions for Truncated SIWs-DBE Lines

In this subsection, we describe the designs of two SIW transitions (a CBCPW transition and an SMA-SIW transition) necessary to connect the truncated SIW-DBE lines (or truncated AFSIW-DBE lines) with a coaxial cable. These transitions will be used for the measurement of the fabricated prototypes. The transitions are designed by means of the full-wave simulator HFSS. The S parameters of the transitions are first given. After, we simulate truncated SIW-DBE lines together with the transitions and SMA connectors in order to show the transitions influence on the DBE resonances.

3.4.0.1 CBCPW Transition for SIW-DBE Lines

Due to the wide use of SIW in microwave and millimeter-wave applications, high performance transitions are a key component to connect SIW and planar transmission lines in the integrated circuit. As presented in Section 1.3.2, both microstrip line and CBCPW transitions have been investigated to connect SIW. For our SIW-DBE structures, a moderate thickness of the substrate was shown capable to reduce losses on the copper plates (Fig. 2.26). This suggests that the CBCPW transition is more suitable than the microstrip transition, which can suffer from leakage in such a configuration. So the CBCPW reported in [11], which works better for the high thickness substrate and has a good performance for high-frequency applications, is here re-designed for the structures presented in the previous section.

We first propose a transition from CBCPW to AFSIW, composed of a first section to match a standard SIW and a second section to transition from an SIW to an AFSIW.

The schematic of a CBCPW-to-SIW transition is shown in the left part of Fig. 3.35 (a) and the relevant dimensions are shown in Fig. 3.35 (b), where w_1=2 mm, l_1=3.7 mm, $\theta = 132°$. Here, the substrate is a FR-4 ($\epsilon_r = 4.4$) with thickness of 2.5 mm, but the CBCPW transition can be applied to other thick substrates by suitably optimizing the parameters w_1, l_1 and θ. The SMA connector is a 50 Ω PCB edge mounting connector, whose working frequency is from dc to 18 GHz, which covers the DBE resonances of the SIW designs. In order to transition to the AFSIW-DBE design, a transition from SIW to AFSIW is also necessary. We implement a similar design as [13], but we accept a reduction in the operational bandwidth in order to make the transition more compact. The second section in Fig. 3.35 shows also the geometry of the SIW-AFSIW transition, where w_2 is 6.4 mm, l_2 is 25 mm, and the width of the connected AFSIW line is 20 mm. The S parameters of CBCPW transition and the complete transition including CBCPW and SIW to AFSIW transitions are shown in Fig. 3.36. The CBCPW transition has a wider bandwidth compared to the overall transition. Its $|S_{11}|$ is below -15 dB from 7.5 GHz and beyond 10 GHz, and it is below -20 dB from 8.5 GHz to 9.7 GHz. By

contrast, for the complete transition $|S_{11}|$ is below -15 dB ranges from 8.1 GHz to 9.2 GHz, and below -20 dB from 8.28 GHz to 8.84 GHz. Since the DBE frequency of the "air-filled cell 1" design is at 8.83 GHz, and the DBE resonance frequencies of the truncated lines are slightly below that frequency, the overall transition $|S_{11}|$ is below -20 dB at frequencies of interest. However, the insertion loss $|S_{21}|$ is low near the DBE frequency, which is -1.1 dB for both the CBCPW and the overall transition. We can see that this return loss is caused by the dielectric losses in FR-4 substrate. If we only consider the conductor losses in CBCPW-SIW-AFSIW transition, the return loss decreases to -0.26 dB.

To summarize, the CBCPW to SIW and the SIW to AFSIW transitions presented provide a $|S_{11}| < -20$ dB and $|S_{21}| = -1.1$ dB matching for the "air-filled" SIWs truncated lines. The $|S_{21}|$ is low because of dielectric losses, so, in the next subsection, we will try another transition design to have a better performance.

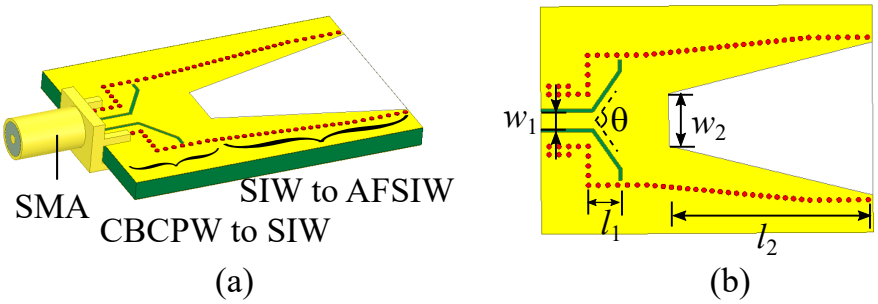

Fig. 3.35 The CBCPW to SIW transition.

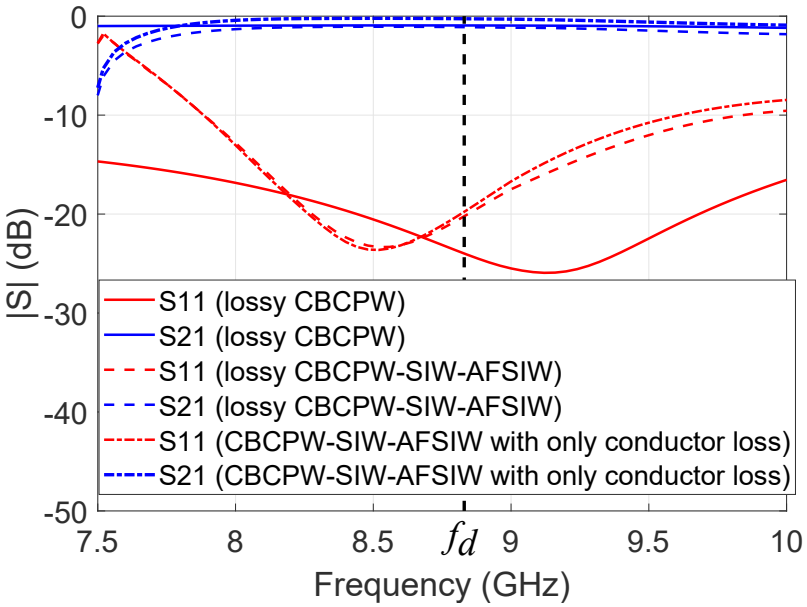

Fig. 3.36 The magnitude of S parameters of CBCPW to AFSIW-DBE lines transition.

3.4.1 SMA-SIW/AFSIW transitions for SIW-DBE Lines

In order to improve the matching of the structures, an SMA-SIW/AFSIW transition is studied to be implemented into SIW/AFSIW-DBE lines which is inspired by the design in [12]. The advantage of these transitions are their compact size. They are also easier to design compared to CBCPW transitions. The SMA transition for SIW is shown in Fig. 3.37 (a). It is designed for the "low-loss-substrate cell" designs, whose substrate is Neltec NY9208 (ϵ_r=2.08), and the substrate thickness is 1.28 mm. The relevant dimensions shown in the figure are w_1=23.6 mm, l_1=25.2 mm, l_2=6.8 mm, l_3=1.8 mm, l_4=11.1 mm. The SMA-AFSIW transition is shown in Fig. 3.37(b), and it is designed for the "air-filled cell 1" design. Its substrate is 2.5 mm FR-4 board. The top and bottom board acting for the copper planes are transparent in the figure, in order to show the details of the middle air-filled layer. After optimization, the relevant dimensions are w_2=26 mm, w_3=22 mm, l_5=20.4 mm, l_6=12 mm, l_7=19.3 mm. Both the SMA-SIW and SMA-AFSIW are connected to the 20 mm width SIW/AFSIW lines.

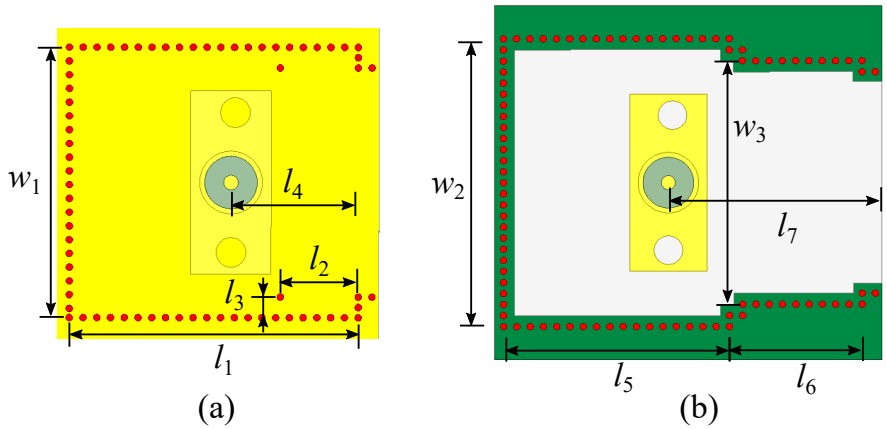

Fig. 3.37 The SMA transition. (a) SMA-SIW transition. (b) SMA-AFSIW transition

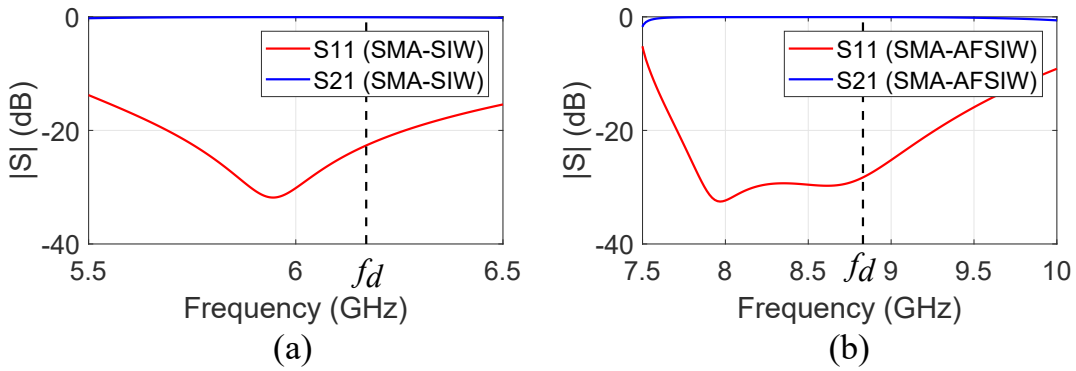

Fig. 3.38 The S parameters of SMA-SIW transition. (a) S parameters of SMA-SIW transition. (b) S parameters of SMA-AFSIW transition.

The S parameters of both the SMA-SIW and SMA-AFSIW transitions are shown in Fig. 3.38. The $|S_{11}|$ is lower than -20 dB from 5.69 GHz to 6.26 GHz for the SMA-SIW

transition, and from 7.71 GHz to 9.24 GHz for the SMA-AFSIW transition. Both of them cover the DBE resonance frequencies of the relevant structures. Good levels of $|S_{21}|$ are obtained for both the transitions, (-0.07 and -0.05 dB respectively).

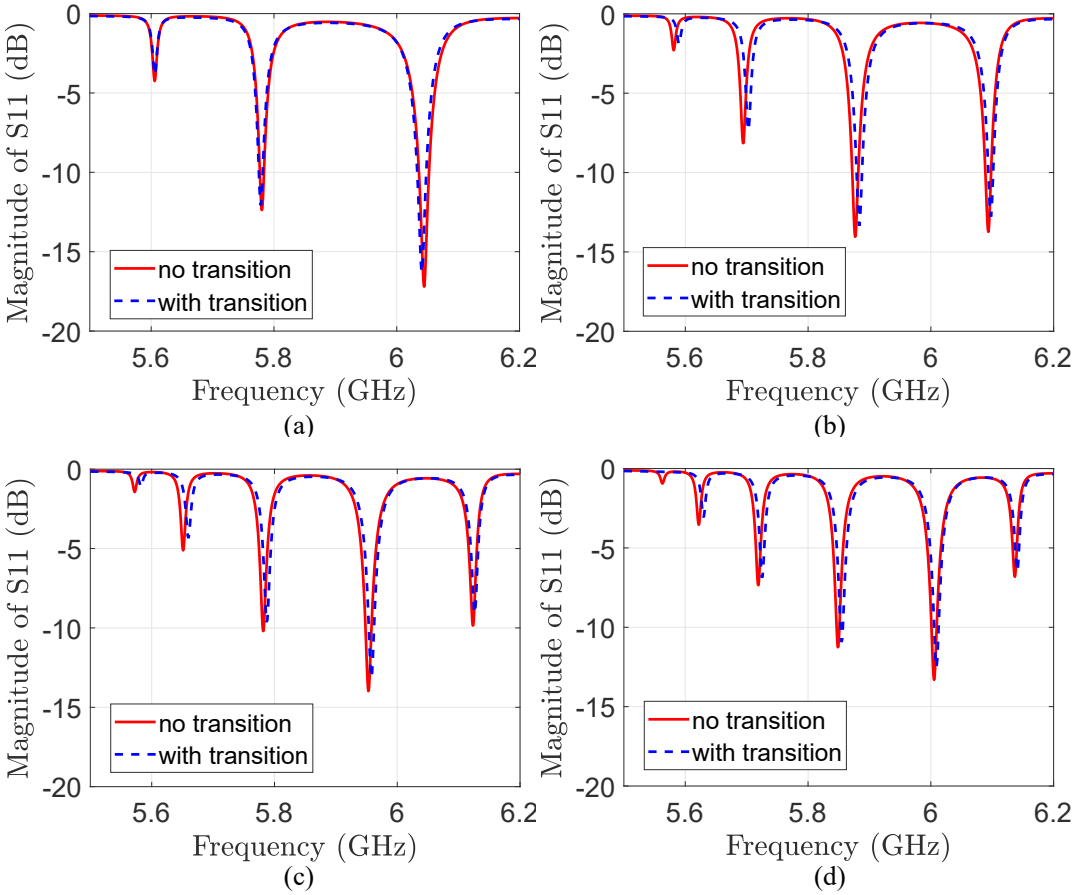

Fig. 3.39 Influence of SMA-SIW transition on $|S_{11}|$ of "low-loss-substrate cell" lines. (a) 4-cell line. (b) 5-cell line. (c) 6-cell line. (d) 7-cell line. The "no transition" results (*red solid lines*) are obtained with ideal waveguide ports. The "with transition" results (*blue dashed lines*) are obtained with the SMA-SIW transition.

The magnitude of S_{11} of the "low-loss-substrate cell" lines with the SMA-SIW transitions and the "air-filled cell 1" lines with the SMA-AFSIW transitions are now shown in Fig. 3.39 and Fig. 3.40 respectively, and show a perfect agreement with the results obtained with the ideal waveguide ports.

In conclusion, SMA-SIW and SMA-AFSIW transition suffers much less from losses if compared to CBCPW-AFSIW transition, which do not involve wave-propagation in lossy dielectric. The shape and frequency of the DBE resonances are not altered by the presence of the transitions.

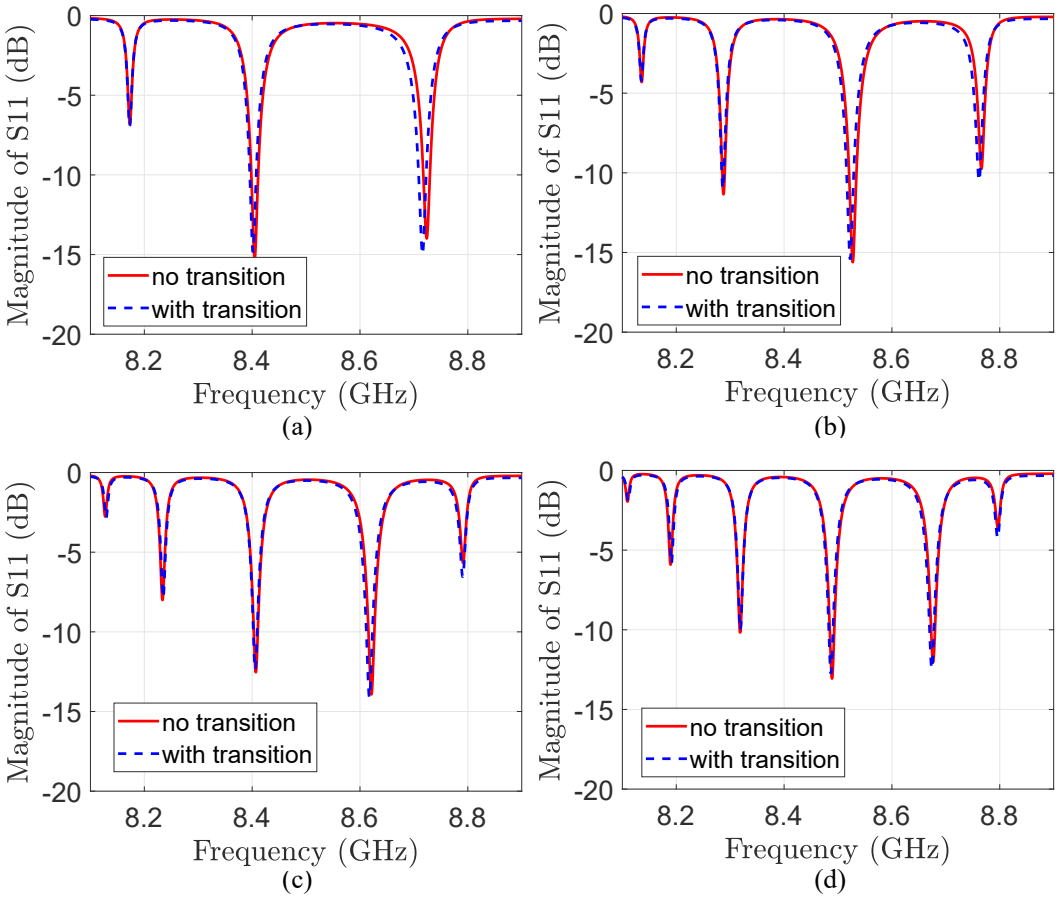

Fig. 3.40 Influence of SMA-AFSIW transition on $|S_{11}|$ of "air-filled cell 1" lines. (a) 4-cell line. (b) 5-cell line. (c) 6-cell line. (d) 7-cell line. The "no transition" results (*red solid lines*) are obtained with ideal waveguide ports. The "with transition" results (*blue dashed lines*) are obtained with the SMA-AFSIW transition.

3.5 Experimental Results

In this section, fabrications and measurements are described of the SIWs-DBE designs chosen from previous section. Two SIWs-DBE designs are fabricated, selected among the ones who are among the less impacted by losses. They are the "low-loss-substrate cell" and "air-filled cell 2". At first, the manufacturing process and the limitations of the fabrications are presented. Then, the S parameters of different truncated lines are measured and compared with the full-wave simulation results. Their Q-factors are calculated and compared with the simulation results to recover the N^5 typical trend in DBE structures.

3.5.1 Manufacturing Process

Two kinds of manufacturing processes are used here. One process was used for the fabrication of the "air-filled cell 2" lines, and another for "low-loss-substrate cell" lines. In the two process, we met different issues and we will introduce and discuss them

separately. In both cases, 4-, 5-, and 6-cell truncated lines have been fabricated, due to the size limitation of the substrates which can be treated by the laser etching machine and the drilling machine used.

3.5.1.1 Fabrication of "air-filled cell 2" lines

The "air-filled cell 2" lines consist of three layers. The top and bottom layers are used as copper planes, the middle layer is air-filled and consists of metallic vias. A LPKF S4 machine was used to drill the vias by laser; the fabricated FR-4 board after this step is shown in Fig. 3.41(a). Then, after the vias were drilled, we used LPKF contact S4 machine to metallize the vias as shown in Fig. 3.41(b). After the metallization, we cut the substrate of the middle layer to make it air-filled, and then drilled side holes for the assembly screws using the laser. The top and bottom layers are fabricated using a similar process and all three fabricated layers are shown in Fig. 3.41(c). At last, we assembled them together using the screws, soldered the copper pillars which act as internal metallic vias inside the air region, and soldered the SMA connectors as shown in Fig. 3.41(d).

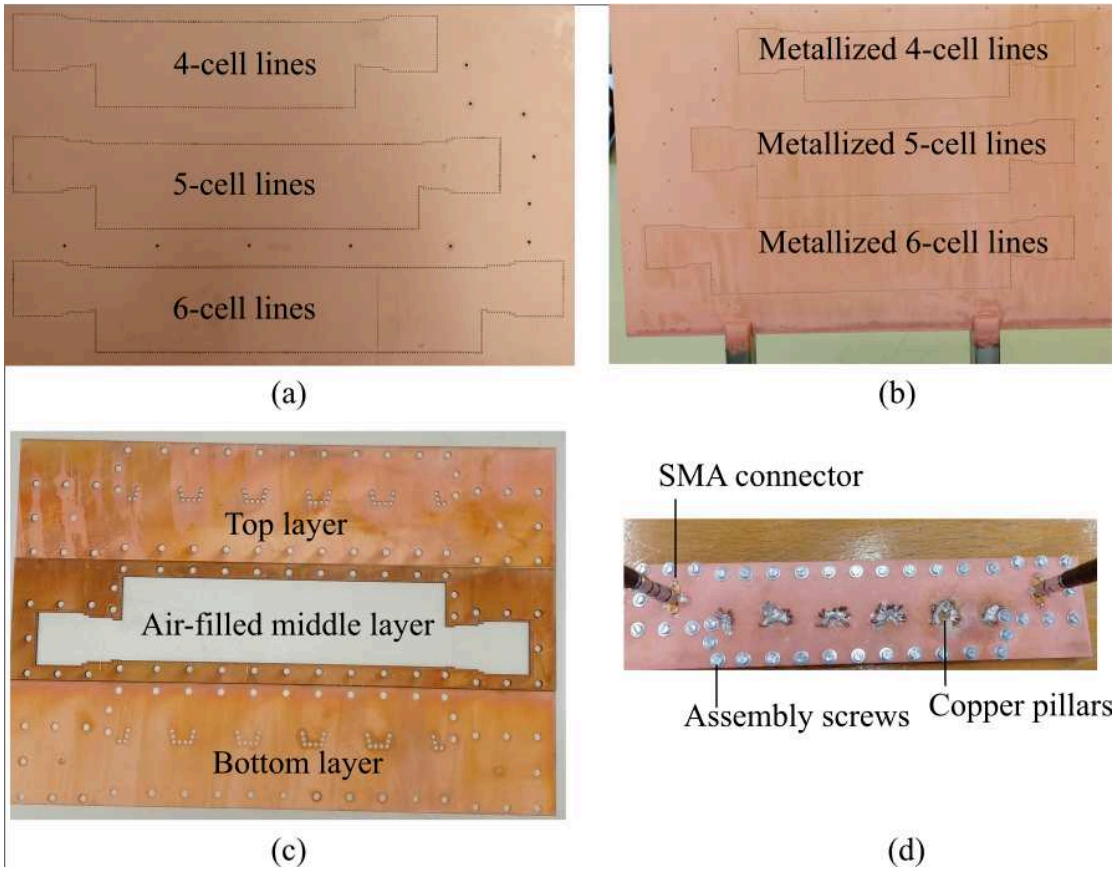

Fig. 3.41 The fabrication of "air-filled cell 2" SIWs lines. (a) Drilling of different length truncated "air-filled cell 2" lines. (b) Metallization of "air-filled cell 2" lines. (c) Top, bottom and air-filled middle layer of the 5-cell line. (d) Assembling of the 5-cell line.

The specifications of the "air-filled cell 2" prototypes are summarized here:

- **substrate**: 0.8 mm FR-4 for top and bottom layers. 1.6 mm FR-4 for middle layer. The ϵ_r is 4.4, the loss tangent is 0.02. The real dielectric constant was independently measured for the transmission coefficient in an SIW waveguide of known length.
- **Dimensions (including transitions)**: 52 mm $\times$200 mm (4 cells); 52 mm$\times$230 mm (5 cells); 52mm $\times$ 260 mm (6 cells).

3.5.1.2 Fabrication of low-loss-substrate SIWs-DBE lines

We used the Neltec NY9208 as the low-loss substrate, which is made by PTFE material. The substrate cannot be drilled with the laser of LPKF S4 machine, and does not activate during the galvanic metallization process. We have used therefore different drilling and metallization methods. We have used a mechanical milling machine (LPKF ProtoMat S64) to drill the vias (Fig. 3.42(a)). The vias were metallized with an LPKF metallization paste (a rubber scraper was used to push the paste inside the vias and the board was heated in an oven to solidify the paste, see Fig. 3.42(b)). At last, the SMA connectors were soldered and the final prototypes are shown in Fig. 3.42(c).

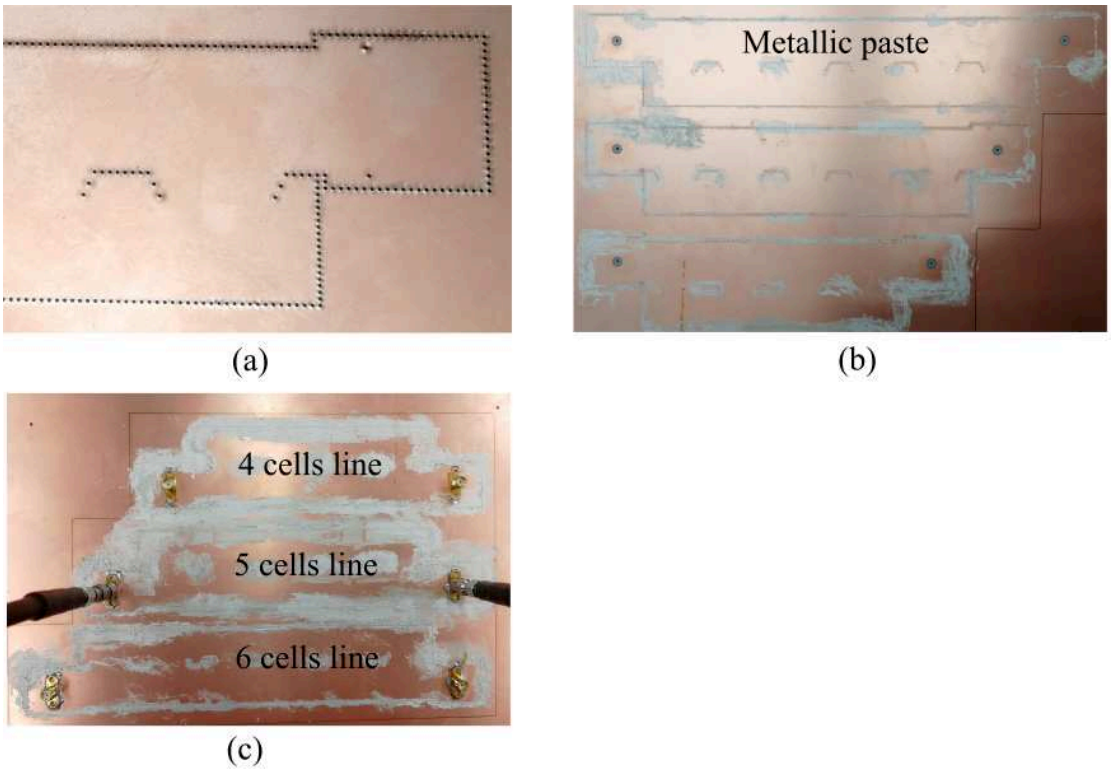

Fig. 3.42 The fabrication of "low-loss-substrate cell" SIWs lines. (a) Drilling details. (b) Metallic paste for the vias. (c) Final prototypes of 4-cell, 5-cell and 6-cell "low-loss-substrate cell" SIWs lines.

The specifications of the "low-loss-substrate cell" prototypes are resumed here:

- **substrate**: 1.524 mm Neltec NY9208, whose ϵ_r is 2.08, loss tangent is 6×10^{-4}. The real dielectric constant was independently estimated by measurements of the phase of the transmission coefficient in an SIW waveguide of known length.
- **Dimension (including transitions)**: 52 mm$\times$190 mm (4 cells); 52 mm$\times$220 mm (5 cells); 52 mm$\times$250 mm (6 cells).

3.5.2 Measurement Results

In this section, we present the measurement results of "air-filled cell 2" lines and "low-loss-substrate cell" lines.
In Fig. 3.43, the S parameters of 4-, 5-, 6- "low-loss-substrate cell" SIWs lines are presented. The measurement results are compared with the lossy models simulated with HFSS, complete with transitions and SMA connectors. The measured curves fit the simulation results well, confirming the existence of the resonance and their approaching to the ideal DBE frequency as the number of cells increases. Since the comparisons are most interesting around the DBE resonance peaks, relevant data are resumed in Table 3.2. From the data in the table, we can see that there is a slight frequency shift going from 0.01 GHz to 0.018 GHz between the measurements and the simulation results. This frequency shift may be caused by the fabrication tolerances and the transition imperfections. The 4 cells measurement results fit very well with the simulation results with only a difference of 0.89 dB for $|S_{11}|$ and 1.15 dB for S_{21}. With the increase of the number of cells, small differences of the minimal peak values of $|S_{11}|$ appear (for 5 cells -7 dB are measured instead of -12 dB, and for 6 cells -6 dB are measured instead of -9 dB). This can be related to an imperfect metallization of the vias holes with the metallic paste. Based on the S parameters measurements, we obtain the Q-factors in Fig. 3.44a. The Q-factor of the measurement are slightly below the Q-factor of simulation of lossy DBE lines with transitions, indicating that real losses are higher than simulated results as fabrication error can influence the fabricated DBE structures. Still, the Q factor increases as expected following the same trend as in the simulated results, thus confirming the excitation of DBE resonances.
The measured S parameters of "air-filled cell 2" lines are shown in Fig. 3.45. The frequency shift for 4-cell line is negligible, while the frequency shift of 5-cell line and 6-cell line are more visible but still low (around 1-5%, magnified by the narrow bandwidth shown in the figures). This can be explained with imperfections in the transitions and in the copper-pillar soldering. The details of the S parameters at the DBE resonance frequency is shown in Table. 3.3. The measured S_{11} is decreasing with the number of cell and we can see that the resonance for the 6-cell line is already weaker than expected,

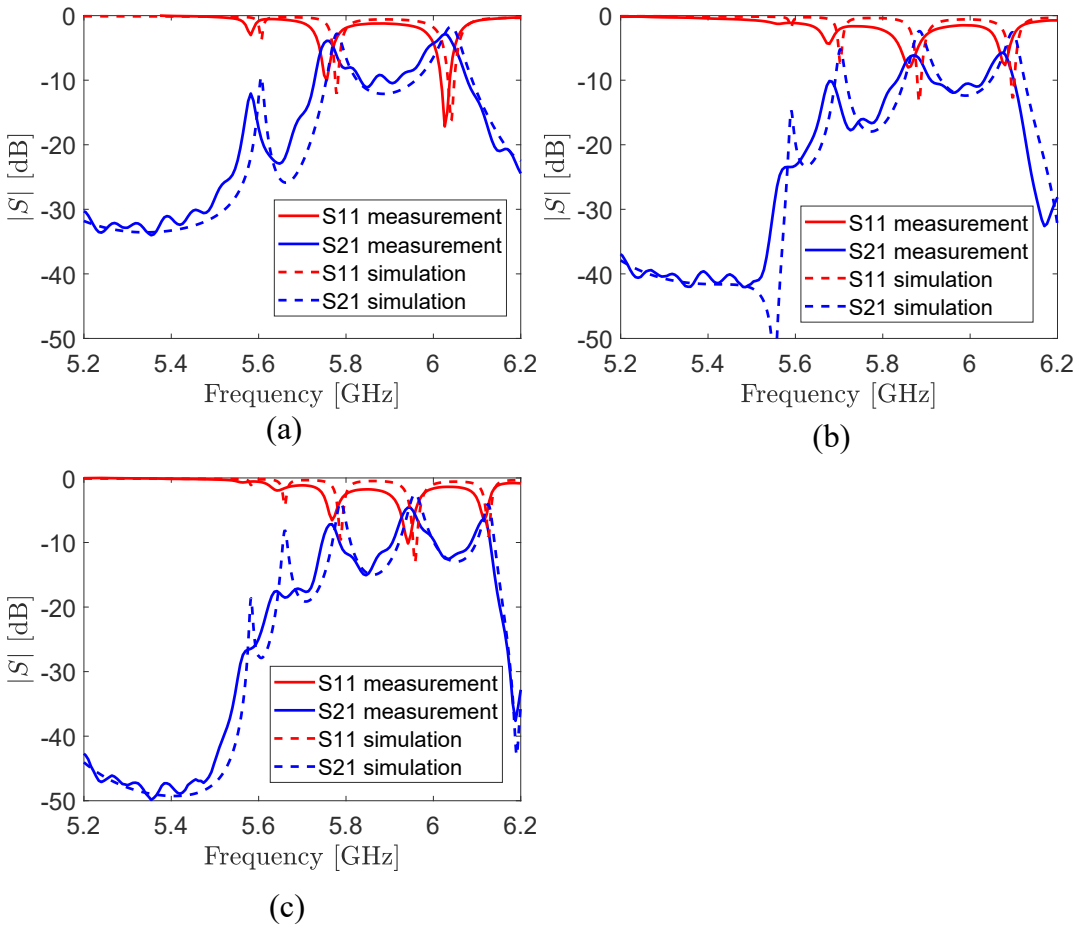

Fig. 3.43 S parameters measurements of "low-loss-substrate cell" SIWs lines. (a) 4-cell truncated line. (b) 5-cell truncated line. (c) 6-cell truncated line.

which confirms that the fabrication of the air-filled SIW can be subject to imperfections, mainly related to the substrate stacking and the vias soldering. The Q-factor of the "air-filled cell 2" are shown in Fig. 3.44b. Its values follow well the simulated ones, apart from the last 6-cell case, where the resonance becomes too weak to measure the factor. In conclusion, the S parameters measurement results of the fabricated "air-filled cell 2" and of the "low-loss-substrate cell" SIWs have been presented. All the measured S parameters fit very well with the simulated ones, with negligible frequency shifts in the resonances, which approach the ideal DBE frequency of the infinite line as expected. The shape of the resonance is also the same. A weak resonance has been measured in the 6-cell "air-filled cell 2", probably due to the difficult fabrication process required to embed the vias inside the air-filled region and to close the full structure. The Q-factor of "low-loss-substrate cell" and "air-filled cell 2" SIWs lines shows the fast increasing trend as the simulation results.

Table 3.2 Comparison between measured and simulated S parameters of "low-loss-substrate cell" SIWs lines at the DBE resonance peak

Type			DBE Resonance Frequency (GHz)	Magnitude (dB)
4 cells	Simulated	S_{11}	6.04	-16.28
		S_{21}	6.04	-1.71
	Measured	S_{11}	6.026	-17.17
		S_{21}	6.026	-2.86
5 cells	Simulated	S_{11}	6.098	-12.78
		S_{21}	6.098	-2,58
	Measured	S_{11}	6.08	-7.67
		S_{21}	6.08	-5.72
6 cells	Simulated	S_{11}	6.126	-9.07
		S_{21}	6.126	-4.07
	Measured	S_{11}	6.116	-6.12
		S_{21}	6.116	-6.34

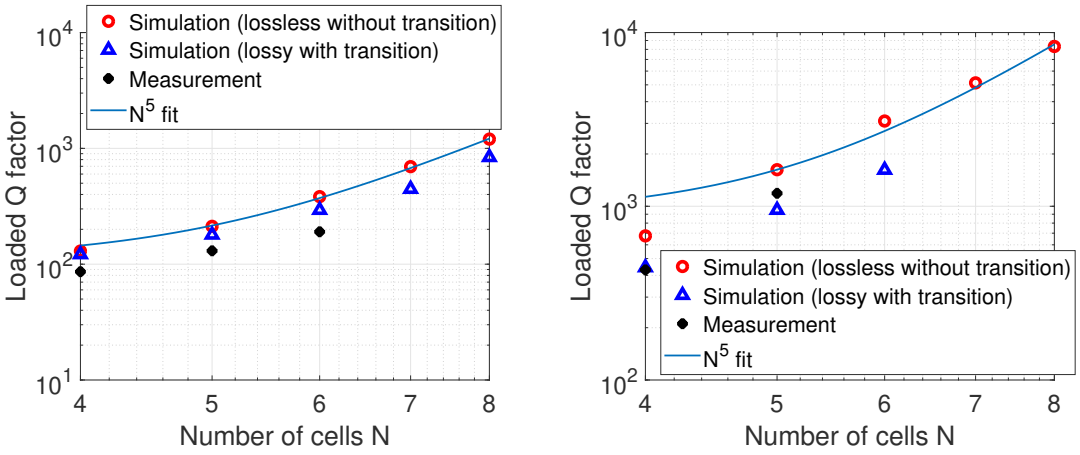

Fig. 3.44 Measurement of Q factor. (a) Q-factors of "low-loss-substrate cell" lines. (b) Q-factors of "air-filled cell 2" lines.

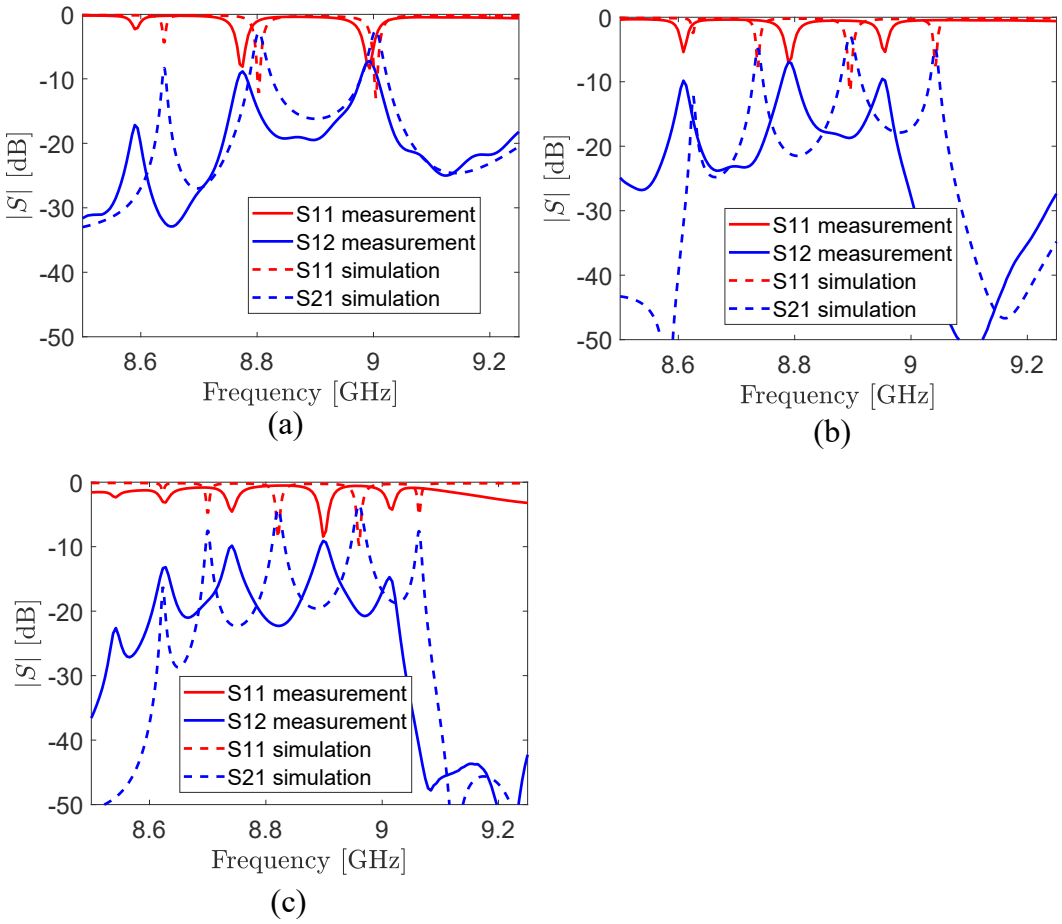

Fig. 3.45 S parameters of measurements of "air-filled cell 2" lines. (a) 4-cell truncated line. (b) 5-cell truncated line. (c) 6-cell truncated line.

Table 3.3 Comparison between measurement and simulation S parameters of "air-filled cell 2" lines at the DBE resonance peak

Type			DBE Resonance Frequency (GHz)	Magnitude (dB)
4 cells	Simulated	S_{11}	9.004	-12.99
		S_{21}	9.004	-2.47
	Measured	S_{11}	8.993	-8.39
		S_{21}	8.993	-7.23
5 cells	Simulated	S_{11}	9.041	-7.56
		S_{21}	9.041	-4.91
	Measured	S_{11}	8.956	-5.38
		S_{21}	8.956	-9.54
6 cells	Simulated	S_{11}	9.064	-5.18
		S_{21}	9.064	-7.59
	Measured	S_{11}	9.017	-4.26
		S_{21}	9.017	-14.72

3.6 Conclusions

In this chapter, we studied the resonant behavior of different truncated SIWs-DBE lines by full-wave simulations. For the "long cell", "double-oblique-line cell", "single-oblique-line cell", and "corner cell" designs, the truncated lines support strong DBE resonances in the absence of losses, as confirmed by their simulated S parameters and computed Q factors, group delays, and field amplitude distribution. However, in the lossy cases, the DBE resonances are strongly affected, which confirms the importance of minimizing losses when designing practical SIWs-DBE structures. Interestingly, the "corner cell" design share the same substrate and similar size with "double-oblique-line cell" and "single-oblique-line cell", but it is more robust to losses, which confirms it as a good topology to design SIWs-DBE structures. The low-loss designs of "low-loss-substrate cell", "air-filled cell 1", and "air-filled cell 2" present DBE resonances which are reasonably robust to the presence of losses ("low-loss-substrate cell" design until 8 cells, "air-filled cell 1" design until 7 cells, "air-filled cell 2" design until 6 cells). Although the DBE resonances are weakly influenced by losses, the Q factor still shows the typical trend with respect to the number of cells N.

Secondly, we proposed two designs of feeding transitions (a CBCPW transition and an SMA-SIW transition) for the truncated SIWs-DBE or AFSIWs-DBE lines. The CBCPW-SIW-AFSIW transition provides a good matching for the "air-filled" SIWs truncated lines near DBE frequency, but suffer from substrate losses ($|S_{11}| < -20$ dB and $|S_{21}| = -1.1$ dB). The SMA-SIW transition provides good matching both for the "low-loss-substrate" SIWs lines and the "air-filled" SIWs lines ($|S_{11}| < -20$ dB and $|S_{21}| < -0.7$ dB).

At last, fabrication and measurement of the "low-loss-substrate cell" and the "air-filled cell 2" designs are discussed. The measured S parameters of both designs fit well with the simulation results with negligible frequency shifts and their Q factors show the fast increasing trend as the simulation results. A weaker resonance than expected in one of the prototypes (the 6-cell "air-filled cell 2") maybe caused by the fabrication tolerance of the air-filled region.

These results show good solutions (in term of materials and geometry) for the realization of DBE condition in SIW technology. They confirm that this condition can be observed with prototype realized with standard fabrication procedures usually available in microwave labs, despite the expected sensitivity to losses and geometric parameters of this resonant phenomenon. This is partly due to the properties of the selected cell, which 1) keeps a DBE point even if the angle of its oblique lines is varied within a fairly large range of values, 2) is less sensitive to losses with respect to the other geometries proposed here. Another major issue is of course evident from the comparison of the different truncated lines: the minimization of dielectric losses, which prevent the ob-

servation of DBE resonances with a large number of cells. This was achieved in one case by replacing the Rogers RO3010 (loss tangent 5×10^{-3}) with the Neltec NY9208 substrate (loss tangent 6×10^{-4}) and in the other cases by designing air-filled SIW.

CHAPTER 4

Conclusions and Future Works

In this final Chapter we draw some conclusions on the analyses presented in this thesis in Section 4.1. In Section 4.2 we present some preliminary analyses to show how the results obtained in the previous chapters can be easily used to implement DBE points in different millimeter-wave technologies, such as gap waveguides and multilayer waveguides. Finally, in Section 4.3, we present some possible future research topics to use the results presented in the thesis for the development of novel integrated microwave devices and antennas at millimeter waves.

4.1 Conclusions

In this thesis, a design method to introduce degenerate band edge conditions into periodic SIW lines has been presented. We proposed a multimodal transfer-matrix method to perform a Bloch analysis of the 4-port unit cell including both phase and attenuation constants. This leads to the computation of a hyperdistance among the four Bloch eigenvectors who coalesce at DBE points.

This makes it possible to study and design DBE unit cells in SIW. Simple models for the unit cell have been studied in order to understand which kind of couplers can develop a DBE. Different kinds of couplers have been studied based on the form of their scattering matrix. The results show that sufficient conditions to achieve a DBE can be recognized: *i)* different reflections at the four ports of the unit cell, and high reflection at some of the ports; *ii)* a privileged propagation path between at least two of the four ports. According to these rules, we successfully synthesised the DBE in different SIW designs. By studying the dispersion relation and hyperdistance near DBE, we studied the sensitiveness of the DBE condition to geometrical parameters and to losses. We remark that a condition to minimize the impact of losses and truncation effects is the absence of higher-order passbands in the proximity of DBE points. Considering these results, the most robust cell design was selected for lower-loss lines, characterized by either a low-loss substrate or air-filled SIW structure, thus successfully minimizing losses. It is important to stress, after these analyses, that despite the large number of unit-cell configurations proposed here capable to achieve a DBE condition, the design

of a topology suitable for this task is not at all a simple task. This can be understood for example by looking at the results in 2.3.3, where only a suitable rotation of one of the two sub-couplers gives the required DBE. Also, this is clear by considering the parametric full-wave analyses of the unit cells in Chapter 2. The variation of geometrical parameters (such as the φ angles defining the orientation of the oblique lines) the DBE condition is lost on the entire frequency band of observation. This sensitivity makes it particularly difficult to find unit cells assuring DBE conditions, and makes even more useful both the guidelines developed on the basis of the unit-cell scattering parameters and the unit cells proposed. Furthermore, an important result of our analyses is that this sensitivity is strongly reduced in one of the proposed geometries (the "corner cell" one), where the modification of some geometrical parameters move the DBE in frequency but do not suppress it. This cell was subsequently used for experiments.

Following the analysis of the unit cells, we studied the resonant behavior of truncated SIW lines by full-wave simulations. The S parameters, Q factors and group delays were presented for different length SIW lines with and without losses. The typical characteristics of DBE resonance were observed for all the lossless designs. With losses, the three low-loss designs present observable DBE resonances, while the other designs are strongly affected by dielectric losses. Two transitions were designed in order to feed the truncated structures, and one of the them (minimizing dielectric losses) has been selected for the realization of the prototypes. Considering all the influence of losses, truncation and transitions, we fabricated 4-, 5-, and 6-cell SIWs lines, one using a low-loss substrate and the other realized as an air-filled SIW. For both of the designs, the measured S parameters fit well with the simulation results. The same design rules used for the SIW designs were successfully used also for the design of a DBE point in an air-filled multilayer waveguide, a recent dielectric-less technology based on glide-symmetric holey metasurfaces, suitable for application at millimeter-waves.

In summary, as proposed in Chapter 1, we have (1) developed a mathematical model to find design rules based on the S matrix of unit cells capable to achieve DBE points; (2) designed several unit cells of SIWs-DBE periodic structures and studied their performance considering the losses, robustness to geometrical perturbations, cost, and fabrication aspects; (3) studied the influence of truncation on DBE resonances, fabricated and measured two prototypes after designing proper transitions. In the next section we propose a unit-cell achieving a DBE condition in a different technology, recently developed for low-cost and low-loss millimeter-wave integrated devices: the air-filled multilayer waveguide (MLW).

4.2 DBE Point in a Multilayer Waveguide with Glide-Symmetric EBG

The modelling tools and the guidelines for the S matrix design proposed in Chapter 2 can be extended to achieve the DBE in other 1-D periodic structures whose unit cell consists of a combination of coupled transmission lines. In order to limit the loss influence to DBE, especially if the design is done at higher frequencies (for example at millimeter-wave frequencies), the best candidate for an alternative technology would be a metallic-like waveguide having a low profile and compact size, and being easy to integrate as a SIW. One of the potential structure is the recently proposed air-filled multilayer waveguide (MLW) [15], whose schematic is shown in Fig. 4.1. It is a metallic waveguide whose side walls are composed of a stack of thin metallic plates suitably etched to host a groove where wave propagation occur. The plates are stacked one on top of the others. This leaves air gaps between the plates, which would be responsible for a very strong lateral leakage (see Fig. 4.1a). The leakage is avoided by etching a glide symmetric arrangement of holes acting as lateral EBG to confine the wave inside the groove. While simple periodic holes do not create a stopband sufficiently strong to confine the field, their alternating distribution increases the confinement and make a suitable EBG for this kind of application. Also, the use of holes instead of other structures (e.g., pins as in gap waveguides) make the fabrication process particularly interesting for its simplicity.

The effectiveness of a glide symmetric arrangement of holes to create a robust EBG effect is a surprising result which was only recently reported [118], and deserves a short discussion. Glide symmetry is a kind of higher symmetries in periodic structure. Its definition [16] indicates that a glide-symmetric periodic structure is invariant after a translation of half period and a mirroring with respect to a plane. A normal 1-D periodic structure and a glide-symmetric periodic structure are shown in Fig. 4.2. Based on the Cartesian coordinates shown in Fig. 4.2, the mathematical definition of 1-D glide-symmetric operator G_p is [16]

$$\begin{aligned} x &\rightarrow x + d/2 \\ y &\rightarrow y \\ z &\rightarrow -z \end{aligned} \tag{4.1}$$

where d is the length of period. Note that in the case of the 2-D glide-symmetric holes in the MLW, the translation of half a period occurs both along the x and y directions.

Glide symmetry often brings special propagation characteristics to periodic structures, such as a low-dispersive response for the first propagating mode [119] and the disappearance of the first bandgap between first and second mode [120]. These features are interesting to design ultra-wideband metasurface graded-index lenses: the refrac-

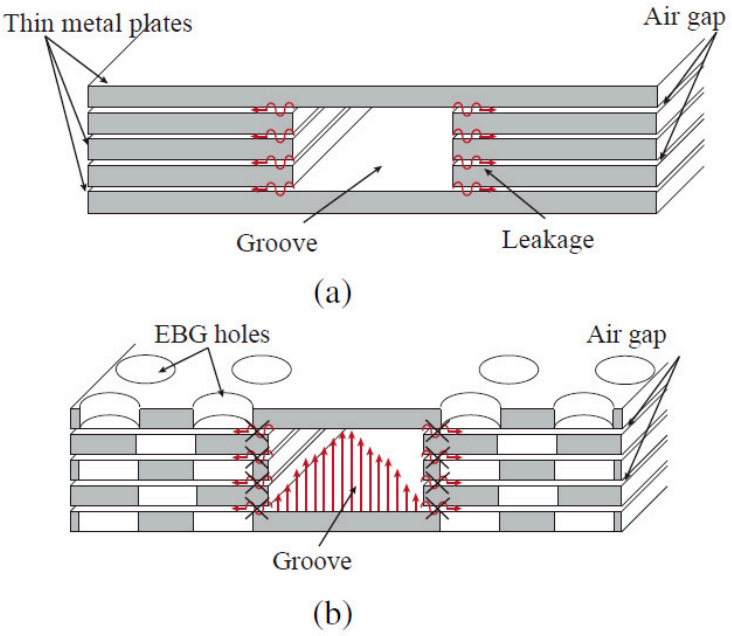

Fig. 4.1 Schematic of the air-filled multilayer waveguide [15]. (a) Cross section view. (b) The contribution of glide symmetric holes for field-leakage suppression.

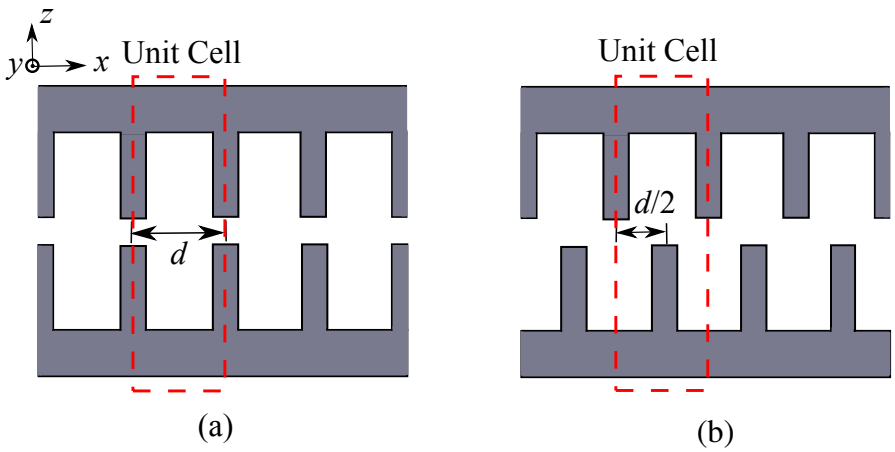

Fig. 4.2 Geometry comparison between normal periodic structures and glide-symmetric periodic structures [16], where d is the period length. (a) Normal periodic structures. (b) Glide-symmetric periodic structures.

tive index can be modified with an adiabatic variation of geometrical parameters along the metasurface, as done e.g. in [121], while a local glide-symmetric configuration decreases the frequency dispersion of the effective index [122]. Furthermore, glide symmetry also leads to a wider stopband at higher frequency with respect to the simpler non-glide structure. This has a large range of applications in high-frequency EBG structures [118]. In our case, compared to an air-filled SIW, the fabrication process of glide-symmetric holes in MLW is much easier because it does not require contact between different layers or the use of dielectric. This technology is also easier to implement than standard gap waveguide, since it does not require the realization of pins by means of a precise milling process.

Based on this MLW structure, we show with some preliminary result that a DBE can be achieved with this technology by using the results discussed in the previous section. According to the EBG done with glide-symmetric holes proposed in [15], we designed the unit cell of glide-symmetric holes whose wide stop-band is from 50 GHz to 100 GHz. These results have been obtained with the HFSS eigensolver, where the unit cell in Fig. Fig. 4.3(a) is simulated with periodic lateral boundary conditions. Five metallic plates are staked. The period d is 3.72 mm, the diameter of the holes d_h is 2 mm, the thickness of each plate h is 0.2 mm, the thickness of the gaps is 0.01 mm. The dispersion diagram is shown in Fig. 4.3(b) and confirms the presence of the stop-band.

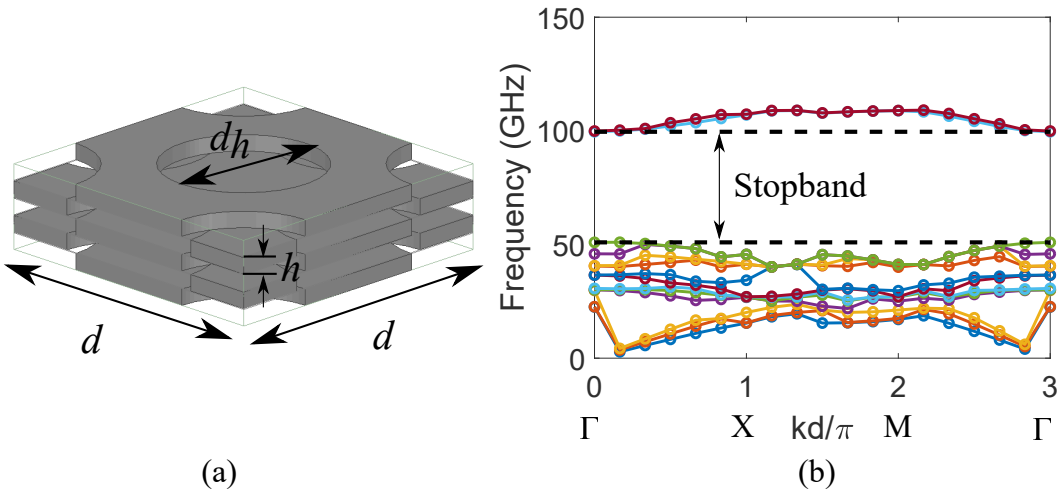

Fig. 4.3 EBG design of glide-symmetric holes. (a) Geometry of the unit cell. (b) Dispersion diagram. The stop-band is from 50 GHz to 100 GHz.

Following the guidelines given in Section 2.3.3.1 regarding the types of couplers, we propose a unit cell design to achieve the DBE in Fig. 4.4. The periodic corrugations along the edges of the waveguides are used to avoid the wave coupling in the gap between different layers [118]. In order to increase reflections at some ports only, and at the same time to introduce an asymmetry in the coupled lines, we put an extra hole acting as a partial blockage in waveguide 1 as shown in the red square in Fig. 4.4. The

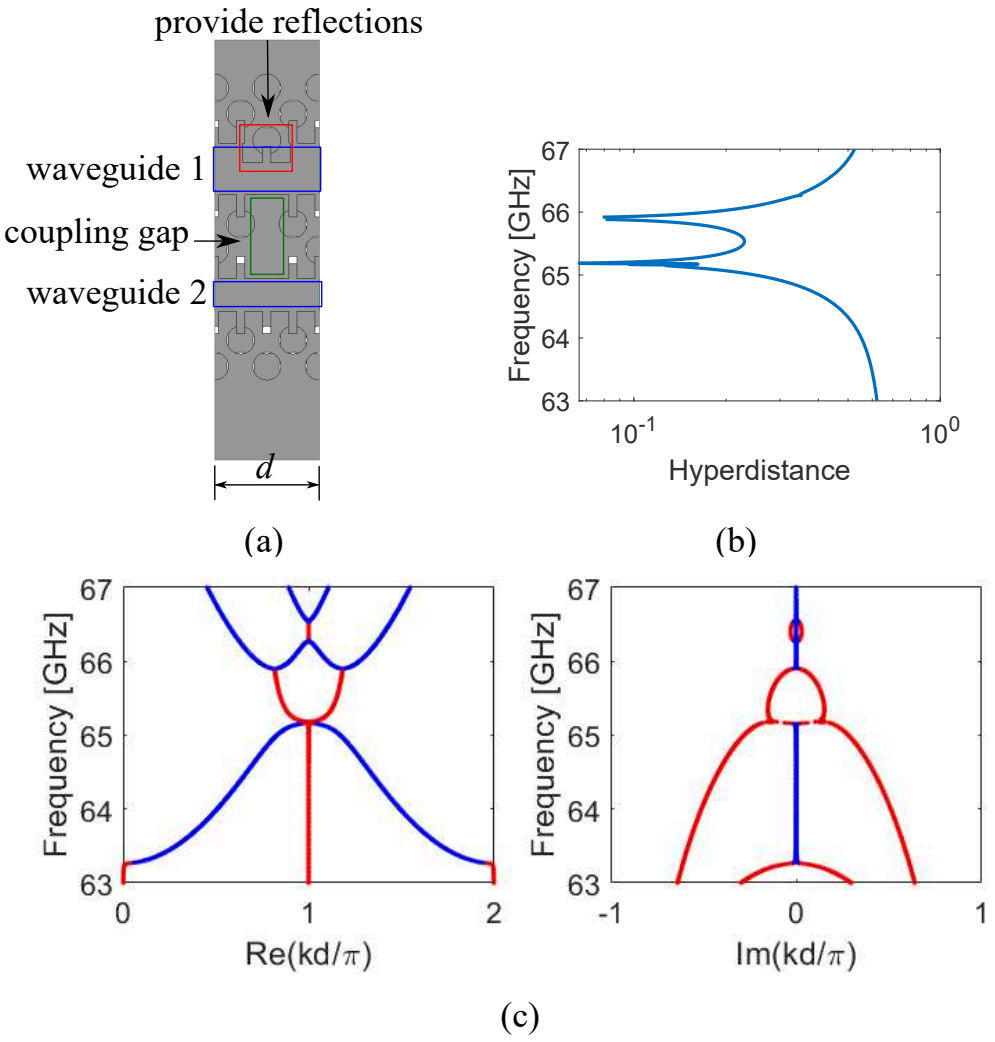

Fig. 4.4 Multilayer glide-symmetric unit cell with DBE. (a) Geometry of the unit cell. (b) Hyperdistance. (c) Dispersion diagram: propagating modes (blue lines), evanescent modes (red lines). The DBE frequency locates at 65.19 GHz.

coupling between two waveguides is provided by removing part of the glide-symmetric EBG holes between two waveguides, so the wave can propagate through this path. The lossless dispersion diagram in Fig. 4.4(c) shows a DBE at 65.19 GHz, confirmed by the the null hyperdistance among the four eigenvectors at that frequency (Fig. 4.4(b)).
Although the DBE in the MLW is achieved as desired, this unit cell is not a fully optimized design. Its DBE is too near to the higher-frequency passbands at 66 GHz, which will affect the DBE resonances once the periodic lines are truncated. Further optimization of the topology of unit cell, and the study of loss impact on truncated lines will be the subject of future work.

4.3 Future work

The analysis on the presence of a DBE conditions in coupled transmission lines has been validated by simulations and experimental results of SIWs-DBE structures. This method can be extended to other type of structures particularly suitable for millimeter-wave applications. Among the potential structures, two low-loss candidates are the gap waveguide and the air-filled multilayer waveguide. The last one, shown in the previous section, can easily grant low-loss DBE due to the absence of dielectrics, similarly to what has been shown in the air-filled SIW.
The development of more solutions for DBE excitation in microwave and millimeter-wave devices will open the way to the design of strongly coupled resonators and antennas. As in [41], a negative resistance can compensate the losses in DBE unit cells, which is an interesting solution to eliminate the losses influence on DBE resonances. This can be implemented on the unit cells presented in this thesis, and will allow the realization of integrated oscillators with high spectral purity and performance largely independent on external loads.
Another potential application is the development of an antenna array, based on the idea developed in [123] where coupled microstrip lines with RBE are used, and radiation losses are balanced with distributed gain as in the previously discussed oscillator. This is a radiating array with stable radiation frequency at millimeter-waves which can be very suitably extended to SIWs-DBE circuits thanks to our work. In order to make our truncated device radiate, slots should be etched in its top metallic plate. This is particularly simple in our "corner-cell" topology, since a large part of the unit cell is free of pins, which leaves flexibility for the choice of the position, shape, and number of slots in each cell. The same would not be true for the other unit cells proposed, where the oblique lines of vias cover a large part of their footprint.
The independence on loading and the power efficiency suggest these devices as promising for applications to integrated circuits, front-end, active antennas for next-generation communicating devices.

REFERENCES

[1] B. E. A. Saleh and M. C. Teich, *Fundamentals of photonics; 2nd ed.*, ser. Wiley series in pure and applied optics. New York, NY: Wiley, 2007.

[2] A. Figotin and I. Vitebskiy, "Gigantic transmission band-edge resonance in periodic stacks of anisotropic layers," *Physical Review E*, vol. 72, no. 3, Sep. 2005.

[3] J. T. Sloan, M. A. K. Othman, and F. Capolino, "Theory of Double Ladder Lumped Circuits With Degenerate Band Edge," *IEEE Transactions on Circuits and Systems I: Regular Papers*, vol. 65, no. 1, pp. 3–13, Jan. 2018.

[4] V. Laude, J. M. Escalante, and A. Martínez, "Effect of loss on the dispersion relation of photonic and phononic crystals," *Physical Review B*, vol. 88, no. 22, p. 224302, Dec. 2013.

[5] A. F. Abdelshafy, M. A. K. Othman, D. Oshmarin, A. T. Almutawa, and F. Capolino, "Exceptional Points of Degeneracy in Periodic Coupled Waveguides and the Interplay of Gain and Radiation Loss: Theoretical and Experimental Demonstration," *IEEE Transactions on Antennas and Propagation*, pp. 1–1, 2019.

[6] M. A. K. Othman and F. Capolino, "Demonstration of a Degenerate Band Edge in Periodically-Loaded Circular Waveguides," *IEEE Microwave and Wireless Components Letters*, vol. 25, no. 11, pp. 700–702, Nov. 2015.

[7] G. Mumcu, K. Sertel, and J. L. Volakis, "Miniature Antenna Using Printed Coupled Lines Emulating Degenerate Band Edge Crystals," *IEEE Transactions on Antennas and Propagation*, vol. 57, no. 6, pp. 1618–1624, Jun. 2009.

[8] S. Yarga, K. Sertel, and J. Volakis, "Highly directive dielectric resonator antennas operating at higher order degenerate band edge modes," in *2008 IEEE Antennas and Propagation Society International Symposium*. San Diego, CA: IEEE, Jul. 2008, pp. 1–4.

[9] G. Méndez-Jerónimo, S. C. Sejas-García, and R. Torres-Torres, "Modeling and Parameter Extraction for the Metal Surface Roughness Loss Effect on Substrate

Integrated Waveguides From S-Parameters," *IEEE Transactions on Microwave Theory and Techniques*, 2018.

[10] D. Deslandes, "Design equations for tapered microstrip-to-Substrate Integrated Waveguide transitions," in *2010 IEEE MTT-S International Microwave Symposium*, May 2010, pp. 704–707.

[11] X. Chen and K. Wu, "Low-loss ultra-wideband transition between conductor-backed coplanar waveguide and substrate integrated waveguide," in *2009 IEEE MTT-S International Microwave Symposium Digest*, Jun. 2009.

[12] A. Morini, M. Farina, C. Cellini, T. Rozzi, and G. Venanzoni, "Design of Low-Cost non-radiative SMA-SIW Launchers," in *2006 European Microwave Conference*, Sep. 2006, pp. 526–529.

[13] F. Parment, A. Ghiotto, T. Vuong, J. Duchamp, and K. Wu, "Air-Filled Substrate Integrated Waveguide for Low-Loss and High Power-Handling Millimeter-Wave Substrate Integrated Circuits," *IEEE Transactions on Microwave Theory and Techniques*, vol. 63, no. 4, pp. 1228–1238, Apr. 2015.

[14] D. M. Pozar, *Microwave engineering*, 4th ed. Hoboken, NJ, USA: Wiley, 2012.

[15] A. Vosoogh, H. Zirath, and Z. S. He, "Novel air-filled waveguide transmission line based on multilayer thin metal plates," *IEEE Transactions on Terahertz Science and Technology*, vol. 9, no. 3, pp. 282–290, 2019.

[16] A. Hessel, M. H. Chen, R. Li, and A. Oliner, "Propagation in periodically loaded waveguides with higher symmetries," *Proceedings of the IEEE*, vol. 61, no. 2, Feb. 1973.

[17] E. Yablonovitch, "Inhibited Spontaneous Emission in Solid-State Physics and Electronics," *Physical Review Letters*, vol. 58, no. 20, pp. 2059–2062, May 1987.

[18] Y. Qian and T. Itoh, "Microwave applications of photonic band-gap (PBG) structures," in *1999 Asia Pacific Microwave Conference. APMC'99. Microwaves Enter the 21st Century. Conference Proceedings (Cat. No.99TH8473)*, vol. 2, Nov. 1999, pp. 315–318 vol.2.

[19] T. Lopetegi, M. Laso, J. Hernandez, M. Bacaicoa, D. Benito, M. Garde, M. Sorolla, and M. Guglielmi, "New microstrip "Wiggly-Line" filters with spurious passband suppression," *IEEE Transactions on Microwave Theory and Techniques*, vol. 49, no. 9, pp. 1593–1598, Sep. 2001.

[20] F. Martin, F. Falcone, J. Bonache, T. Lopetegi, M. Laso, and M. Sorolla, "Dual electromagnetic bandgap CPW structures for filter applications," *IEEE Microwave and Wireless Components Letters*, vol. 13, no. 9, pp. 393–395, Sep. 2003.

[21] W. Chappell and X. Gong, "Wide bandgap composite EBG substrates," *IEEE Transactions on Antennas and Propagation*, vol. 51, no. 10, pp. 2744–2750, Oct. 2003.

[22] F.-R. Yang, K.-P. Ma, Y. Qian, and T. Itoh, "A novel TEM waveguide using uniplanar compact photonic-bandgap (UC-PBG) structure," *IEEE Transactions on Microwave Theory and Techniques*, vol. 47, no. 11, pp. 2092–2098, Nov. 1999.

[23] R. Coccioli, F.-R. Yang, K.-P. Ma, and T. Itoh, "Aperture-coupled patch antenna on UC-PBG substrate," *IEEE Transactions on Microwave Theory and Techniques*, vol. 47, no. 11, pp. 2123–2130, Nov. 1999.

[24] M. Y. Nada, M. A. K. Othman, O. Boyraz, and F. Capolino, "Giant Resonance and Anomalous Quality Factor Scaling in Degenerate Band Edge Coupled Resonator Optical Waveguides," *Journal of Lightwave Technology*, vol. 36, no. 14, pp. 3030–3039, Jul. 2018.

[25] J. Volakis, K. Sertel, G. Mumcu, and S. Yarga, "Frozen modes in bounded photonic crystals for high gain antennas," in *2006 IEEE Antennas and Propagation Society International Symposium*. Albuquerque, NM, USA: IEEE, 2006, pp. 414–417.

[26] T. Kato, *Perturbation theory for linear operators*, ser. Grundlehren der mathematischen Wissenschaften. Berlin Heidelberg: Springer-Verlag, 1966.

[27] W. D. Heiss, "Exceptional points of non-Hermitian operators," *Journal of Physics A: Mathematical and General*, vol. 37, no. 6, pp. 2455–2464, Jan. 2004.

[28] W. Heiss, "Exceptional Points – Their Universal Occurrence and Their Physical Significance," *Czechoslovak Journal of Physics*, vol. 54, no. 10, pp. 1091–1099, Oct. 2004.

[29] C. Dembowski, H.-D. Gräf, H. L. Harney, A. Heine, W. D. Heiss, H. Rehfeld, and A. Richter, "Experimental Observation of the Topological Structure of Exceptional Points," *Physical Review Letters*, vol. 86, no. 5, pp. 787–790, Jan. 2001.

[30] E.-M. Graefe and H. F. Jones, "Pt-symmetric sinusoidal optical lattices at the symmetry-breaking threshold," *Physical Review A*, vol. 84, no. 1, Jul. 2011.

[31] M.-A. Miri and A. Alù, "Exceptional points in optics and photonics," *Science*, vol. 363, no. 6422, p. eaar7709, Jan. 2019.

[32] W. D. Heiss, F. G. Scholtz, and H. B. Geyer, "The large N behaviour of the Lipkin model and exceptional points," *Journal of Physics A: Mathematical and General*, vol. 38, no. 9, Feb. 2005.

[33] A. Figotin and I. Vitebskiy, "Slow light in photonic crystals," *Waves in Random and Complex Media*, vol. 16, no. 3, pp. 293–382, Aug. 2006.

[34] E. Hecht, *Optics*. Pearson Education, Incorporated, 2017.

[35] C. Locker, K. Sertel, and J. L. Volakis, "Emulation of Propagation in Layered Anisotropic Media With Equivalent Coupled Microstrip Lines," *IEEE Microwave and Wireless Components Letters*, vol. 16, no. 12, pp. 642–644, Dec. 2006.

[36] D. Oshmarin, F. Yazdi, M. A. K. Othman, J. Sloan, M. Radfar, M. M. Green, and F. Capolino, "Oscillator Based on Lumped Double Ladder Circuit with Band Edge Degeneracy," *arXiv:1610.00415 [physics]*, Oct. 2016.

[37] G. W. Hanson, A. B. Yakovlev, M. Othman, and F. Capolino, "Exceptional points of degeneracy and branch points for transmission-line problems - linear algebra and bifurcation theory perspectives," 2018.

[38] T. Mealy and F. Capolino, "General Conditions to Realize Exceptional Points of Degeneracy in Two Uniform Coupled Transmission Lines," *arXiv:2003.04215 [physics]*, Mar. 2020.

[39] N. Gutman, C. Martijn de Sterke, A. A. Sukhorukov, and L. C. Botten, "Slow and frozen light in optical waveguides with multiple gratings: Degenerate band edges and stationary inflection points," *Physical Review A*, vol. 85, no. 3, p. 033804, Mar. 2012.

[40] A. Figotin and I. Vitebskiy, "Slow wave phenomena in photonic crystals," *Laser and Photonics Reviews*, vol. 5, no. 2, pp. 201–213, Mar. 2011.

[41] A. F. Abdelshafy, D. Oshmarin, M. A. K. Othman, M. M. Green, and F. Capolino, "Distributed degenerate band edge oscillator," *IEEE Transactions on Antennas and Propagation*, pp. 1–1, 2020.

[42] M. A. K. Othman, X. Pan, G. Atmatzakis, C. G. Christodoulou, and F. Capolino, "Experimental Demonstration of Degenerate Band Edge in Metallic Periodically Loaded Circular Waveguide," *IEEE Transactions on Microwave Theory and Techniques*, vol. 65, no. 11, pp. 4037–4045, Nov. 2017.

[43] J. G. Pedersen, S. Xiao, and N. A. Mortensen, "Limits of slow light in photonic crystals," *Physical Review B*, vol. 78, no. 15, Oct. 2008.

[44] K. Scharnhorst, "Angles in Complex Vector Spaces," *Acta Applicandae Mathematica*, vol. 69, no. 1, pp. 95–103, Oct. 2001.

[45] D. Oshmarin, F. Yazdi, M. Othman, J. Sloan, M. Radfar, M. Green, and F. Capolino, "A New Oscillator Concept Based on Band Edge Degeneracy in Lumped Double-Ladder Circuits," *IET Circuits, Devices andamp; Systems*, Feb. 2019.

[46] N. Apaydin, L. Zhang, K. Sertel, and J. L. Volakis, "Experimental Validation of Frozen Modes Guided on Printed Coupled Transmission Lines," *IEEE Transactions on Microwave Theory and Techniques*, vol. 60, no. 6, pp. 1513–1519, Jun. 2012.

[47] E. Irci, K. Sertel, and J. Volakis, "Unidirectional transmission characteristics of printed magnetic photonic crystals," in *2008 IEEE Antennas and Propagation Society International Symposium*. San Diego, CA: IEEE, Jul. 2008, pp. 1–4.

[48] M. B. Stephanson, K. Sertel, and J. L. Volakis, "Frozen Modes in Coupled Microstrip Lines Printed on Ferromagnetic Substrates," *IEEE Microwave and Wireless Components Letters*, vol. 18, no. 5, pp. 305–307, May 2008.

[49] F. Yazdi, D. Oshmarin, A. T. Almutawa, and F. Capolino, "Experimental Demonstration of Sixth Order Degenerate Band Edge in Coupled Microstrip Waveguides," *arXiv:1906.03331 [physics]*, Jun. 2019.

[50] A. M. Zuboraj, B. K. Sertel, and C. J. L. Volakis, "Propagation of Degenerate Band-Edge Modes Using Dual Nonidentical Coupled Transmission Lines," *Physical Review Applied*, vol. 7, no. 6, Jun. 2017.

[51] M. G. Wood, J. R. Burr, and R. M. Reano, "Degenerate band edge resonances in periodic silicon ridge waveguides," *Optics Letters*, vol. 40, no. 11, p. 2493, Jun. 2015.

[52] J. R. Burr and R. M. Reano, "Zero-coupling-gap degenerate band edge resonators in silicon photonics," *Optics Express*, vol. 23, no. 24, p. 30933, Nov. 2015.

[53] M. Y. Nada, M. A. K. Othman, and F. Capolino, "Theory of coupled resonator optical waveguides exhibiting high-order exceptional points of degeneracy," *Physical Review B*, vol. 96, no. 18, Nov. 2017.

[54] R. A. Chilton, K.-Y. Jung, R. Lee, and F. L. Teixeira, "Frozen Modes in Parallel-Plate Waveguides Loaded With Magnetic Photonic Crystals," *IEEE Transactions on Microwave Theory and Techniques*, vol. 55, no. 12, pp. 2631–2641, Dec. 2007.

[55] A. I. Ignatov, A. M. Merzlikin, M. Levy, and A. P. Vinogradov, "Formation of Degenerate Band Gaps in Layered Systems," *Materials*, vol. 5, no. 12, pp. 1055–1083, Jun. 2012.

[56] S. Yarga, K. Sertel, and J. L. Volakis, "Finite degenerate band edge crystals using barium titanate-alumina layers emulating uniaxial media for directive planar antennas," in *2007 IEEE Antennas and Propagation International Symposium*. Honolulu, HI, USA: IEEE, Jun. 2007, pp. 1317–1320.

[57] G. Mumcu, K. Sertel, and J. L. Volakis, "Miniature Antennas and Arrays Embedded Within Magnetic Photonic Crystals," *IEEE Antennas and Wireless Propagation Letters*, vol. 5, pp. 168–171, 2006.

[58] J. L. Volakis and K. Sertel, "Narrowband and Wideband Metamaterial Antennas Based on Degenerate Band Edge and Magnetic Photonic Crystals," *Proceedings of the IEEE*, vol. 99, no. 10, pp. 1732–1745, Oct. 2011.

[59] Lanlin Zhang, K. Sertel, and J. L. Volakis, "Self-biased magnetic photonic crystals for unidirectional antennas," in *2011 IEEE International Symposium on Antennas and Propagation (APSURSI)*. Spokane, WA: IEEE, Jul. 2011, pp. 677–679.

[60] S. Yarga, K. Sertel, and J. Volakis, "Degenerate Band Edge Crystals and Periodic Assemblies for High Gain Antennas," in *2006 IEEE Antennas and Propagation Society International Symposium*. Albuquerque, NM, USA: IEEE, 2006, pp. 7–10.

[61] S. Yarga, K. Sertel, and J. L. Volakis, "Degenerate Band Edge Crystals for Directive Antennas," *IEEE Transactions on Antennas and Propagation*, vol. 56, no. 1, pp. 119–126, Jan. 2008.

[62] ——, "A Directive Resonator Antenna Using Degenerate Band Edge Crystals," *IEEE Transactions on Antennas and Propagation*, vol. 57, no. 3, pp. 799–803, Mar. 2009.

[63] M. A. K. Othman and F. Capolino, "Coupled transmission line array antennas with exceptional points of degeneracy," in *2017 IEEE International Symposium*

on Antennas and Propagation USNC/URSI National Radio Science Meeting, Jul. 2017, pp. 57–58.

[64] M. A. K. Othman, M. Veysi, A. Figotin, and F. Capolino, "Low Starting Electron Beam Current in Degenerate Band Edge Oscillators," *IEEE Transactions on Plasma Science*, vol. 44, no. 6, pp. 918–929, Jun. 2016.

[65] A. F. Abdelshafy, M. A. K. Othman, F. Yazdi, M. Veysi, A. Figotin, and F. Capolino, "Electron-Beam-Driven Devices With Synchronous Multiple Degenerate Eigenmodes," *IEEE Transactions on Plasma Science*, vol. 46, no. 8, pp. 3126–3138, Aug. 2018.

[66] T. Mealy, A. F. Abdelshafy, and F. Capolino, "Exceptional Point of Degeneracy in Backward-Wave Oscillator with Distributed Power Extraction," *arXiv:1904.12946 [physics]*, Apr. 2019.

[67] M. A. K. Othman, V. Ananth Tamma, and F. Capolino, "Theory and New Amplification Regime in Periodic Multimodal Slow Wave Structures With Degeneracy Interacting With an Electron Beam," *IEEE Transactions on Plasma Science*, vol. 44, no. 4, pp. 594–611, Apr. 2016.

[68] M. A. K. Othman, M. Veysi, A. Figotin, and F. Capolino, "Giant Amplification in Degenerate Band Edge Slow-Wave Structures Interacting with an Electron Beam," *Physics of Plasmas*, vol. 23, no. 3, Mar. 2016.

[69] F. Yazdi, M. A. K. Othman, M. Veysi, A. Figotin, and F. Capolino, "A New Amplification Regime for Traveling Wave Tubes With Third-Order Modal Degeneracy," *IEEE Transactions on Plasma Science*, vol. 46, no. 1, pp. 43–56, Jan. 2018.

[70] V. A. Tamma, A. Figotin, and F. Capolino, "Concept for Pulse Compression Device Using Structured Spatial Energy Distribution," *IEEE Transactions on Microwave Theory and Techniques*, pp. 1–14, 2016.

[71] N. Gutman, A. A. Sukhorukov, F. Eilenberger, and C. M. de Sterke, "Bistability suppression and low threshold switching using frozen light at a degenerate band edge waveguide," *Optics Express*, vol. 20, no. 24, p. 27363, Nov. 2012.

[72] M. Veysi, M. A. K. Othman, A. Figotin, and F. Capolino, "Degenerate band edge laser," *Physical Review B*, vol. 97, no. 19, May 2018.

[73] M. A. K. Othman, F. Yazdi, A. Figotin, and F. Capolino, "Giant gain enhancement in photonic crystals with a degenerate band edge," *Physical Review B*, vol. 93, no. 2, Jan. 2016.

[74] Ke Wu, D. Desiandes, and Y. Cassivi, "The substrate integrated circuits - a new concept for high-frequency electronics and optoelectronics," in *6th International Conference on Telecommunications in Modern Satellite, Cable and Broadcasting Service, 2003. TELSIKS 2003.*, vol. 1. Serbia, Montenegro, Nis: IEEE, 2003, pp. P–III–P–X.

[75] Y. Cassivi, L. Perregrini, P. Arcioni, M. Bressan, K. Wu, and G. Conciauro, "Dispersion characteristics of substrate integrated rectangular waveguide," *IEEE Microwave and Wireless Components Letters*, vol. 12, no. 9, pp. 333–335, Sep. 2002.

[76] D. Deslandes and Ke Wu, "Accurate modeling, wave mechanisms, and design considerations of a substrate integrated waveguide," *IEEE Transactions on Microwave Theory and Techniques*, vol. 54, no. 6, pp. 2516–2526, Jun. 2006.

[77] M. M. Honari, R. Mirzavand, H. Saghlatoon, and P. Mousavi, "Two-Layered Substrate Integrated Waveguide Filter for UWB Applications," *IEEE Microwave and Wireless Components Letters*, vol. 27, no. 7, pp. 633–635, Jul. 2017.

[78] E. Massoni, N. Delmonte, G. Macchiarella, L. Perregrini, and M. Bozzi, "Half-mode SIW Filters with Resonant Couplings Implementing Transmission Zeros," in *2018 IEEE/MTT-S International Microwave Symposium - IMS*, Jun. 2018.

[79] Y. D. Dong, T. Yang, and T. Itoh, "Substrate Integrated Waveguide Loaded by Complementary Split-Ring Resonators and Its Applications to Miniaturized Waveguide Filters," *IEEE Transactions on Microwave Theory and Techniques*, vol. 57, no. 9, pp. 2211–2223, Sep. 2009.

[80] X.-P. Chen and K. Wu, "Self-equalised pseudo-elliptical filter made of substrate integrated waveguide," *Electronics Letters*, vol. 45, no. 2, Jan. 2009.

[81] B. Potelon, J.-F. Favennec, C. Quendo, E. Rius, C. Person, and J.-C. Bohorquez, "Design of a Substrate Integrated Waveguide (SIW) Filter Using a Novel Topology of Coupling," *IEEE Microwave and Wireless Components Letters*, vol. 18, no. 9, Sep. 2008.

[82] W. Shen, L.-S. Wu, X.-W. Sun, W.-Y. Yin, and J.-F. Mao, "Novel Substrate Integrated Waveguide Filters With Mixed Cross Coupling (MCC)," *IEEE Microwave and Wireless Components Letters*, vol. 19, no. 11, Nov. 2009.

[83] U. Rosenberg, "New 'Planar' waveguide cavity elliptic function filters," in *1995 25th European Microwave Conference*, vol. 1, Sep. 1995, pp. 524–527.

[84] E. Ofli, R. Vahldieck, and S. Amari, "Novel E-plane filters and diplexers with elliptic response for millimeter-wave applications," *IEEE Transactions on Microwave Theory and Techniques*, vol. 53, no. 3, Mar. 2005.

[85] X. Chen, W. Hong, J. Chen, and K. Wu, "Substrate integrated waveguide elliptic filter with high mode," in *2005 Asia-Pacific Microwave Conference Proceedings*, vol. 1, Dec. 2005.

[86] X.-P. Chen and K. Wu, "Substrate Integrated Waveguide Filters: Design Techniques and Structure Innovations," *IEEE Microwave Magazine*, vol. 15, no. 6, pp. 121–133, Sep. 2014.

[87] C. T. Bui, P. Lorenz, M. Saglam, W. Kraemer, and R. H. Jansen, "Investigation of Symmetry Influence in Substrate Integrated Waveguide (SIW) Band-Pass Filters using Symmetric Inductive Posts," in *2008 38th European Microwave Conference*, Oct. 2008, pp. 492–495.

[88] T.-S. Yun, H. Nam, K.-B. Kim, and J.-C. Lee, "Iris waveguide bandpass filter using substrate integrated waveguide (SIW) for satellite communication," in *2005 Asia-Pacific Microwave Conference Proceedings*, vol. 1, Dec. 2005.

[89] J. Rhodes and R. Cameron, "General Extracted Pole Synthesis Technique with Applications to Low-Loss TE/sub011/ Mode Filters," *IEEE Transactions on Microwave Theory and Techniques*, vol. 28, no. 9, Sep. 1980.

[90] S. Amari and U. Rosenberg, "Characteristics of cross (bypass) coupling through higher/lower order modes and their applications in elliptic filter design," *IEEE Transactions on Microwave Theory and Techniques*, vol. 53, no. 10, Oct. 2005.

[91] D. Deslandes and K. Wu, "Substrate integrated waveguide dual-mode filters for broadband wireless systems," in *Radio and Wireless Conference, 2003. RAWCON '03. Proceedings*, Aug. 2003, pp. 385–388.

[92] H. Tang, W. Hong, Z. Hao, J. Chen, and K. Wu, "Optimal design of compact millimetre-wave SIW circular cavity filters," *Electronics Letters*, vol. 41, no. 19, Sep. 2005.

[93] H. M. Hizan, I. C. Hunter, and A. I. Abunjaileh, "Integrated Dual-Band Radiating Bandpass Filter Using Dual-Mode Circular Cavities," *IEEE Microwave and Wireless Components Letters*, vol. 21, no. 5, May 2011.

[94] H. J. Tang, W. Hong, J.-X. Chen, G. Q. Luo, and K. Wu, "Development of Millimeter-Wave Planar Diplexers Based on Complementary Characters of Dual-

Mode Substrate Integrated Waveguide Filters With Circular and Elliptic Cavities," *IEEE Transactions on Microwave Theory and Techniques*, vol. 55, no. 4, Apr. 2007.

[95] F. Mira, J. Mateu, S. Cogollos, and V. E. Boria, "Design of Ultra-Wideband Substrate Integrated Waveguide (SIW) Filters in Zigzag Topology," *IEEE Microwave and Wireless Components Letters*, vol. 19, no. 5, pp. 281–283, May 2009.

[96] Z.-C. Hao, W. Hong, J.-X. Chen, X.-P. Chen, and K. Wu, "Compact super-wide bandpass substrate integrated waveguide (SIW) filters," *IEEE Transactions on Microwave Theory and Techniques*, vol. 53, no. 9, Sep. 2005.

[97] W. Qin, W. Hong, H. J. Tang, and J. Wang, "Design and implementation of UWB bandpass filter with a frequency notch for choking back the interference from narrow band wireless communication systems," in *2009 IEEE International Conference on Ultra-Wideband*, Sep. 2009.

[98] X.-P. Chen, K. Wu, and Z.-L. Li, "Dual-Band and Triple-Band Substrate Integrated Waveguide Filters With Chebyshev and Quasi-Elliptic Responses," *IEEE Transactions on Microwave Theory and Techniques*, vol. 55, no. 12, Dec. 2007.

[99] H. Di, B. Wu, X. Lai, and C.-H. Liang, "Synthesis and realization of novel triple-passband filter based on frequency transformation," in *2009 Asia Pacific Microwave Conference*, Dec. 2009.

[100] ——, "Synthesis of Cross-Coupled Triple-Passband Filters Based on Frequency Transformation," *IEEE Microwave and Wireless Components Letters*, vol. 20, no. 8, Aug. 2010.

[101] B.-J. Chen, T.-M. Shen, and R.-B. Wu, "Dual-Band Vertically Stacked Laminated Waveguide Filter Design in LTCC Technology," *IEEE Transactions on Microwave Theory and Techniques*, vol. 57, no. 6, Jun. 2009.

[102] W.-L. Tsai and R.-B. Wu, "Tri-band filter design using substrate integrated waveguide resonators in LTCC," in *2010 IEEE MTT-S International Microwave Symposium*, May 2010.

[103] J. C. Bohorquez, B. Potelon, C. Person, E. Rius, C. Quendo, G. Tanne, and E. Fourn, "Reconfigurable Planar SIW Cavity Resonator and Filter," in *2006 IEEE MTT-S International Microwave Symposium Digest*, Jun. 2006.

[104] V. Sekar, M. Armendariz, and K. Entesari, "A 1.2–1.6-GHz Substrate-Integrated-Waveguide RF MEMS Tunable Filter," *IEEE Transactions on Microwave Theory and Techniques*, vol. 59, no. 4, Apr. 2011.

[105] M. Bozzi, M. Pasian, and L. Perregrini, "Modeling of losses in substrate integrated waveguide components," in *2014 International Conference on Numerical Electromagnetic Modeling and Optimization for RF, Microwave, and Terahertz Applications (NEMO)*, May 2014, pp. 1–4.

[106] T. Martin, A. Ghiotto, A. Marque, T.-P. Vuong, F. Lotz, P. Monteil, and L. Carpentier, "Broadband air-filled SIW to waveguide transition for interconnect, instrumentation and measurement applications," in *2017 IEEE MTT-S International Microwave Workshop Series on Advanced Materials and Processes for RF and THz Applications (IMWS-AMP)*. Pavia: IEEE, Sep. 2017, pp. 1–3.

[107] J. L. Cano, A. Mediavilla, and A. R. Perez, "Full-Band Air-Filled Waveguide-to-Substrate Integrated Waveguide (SIW) Direct Transition," *IEEE Microwave and Wireless Components Letters*, vol. 25, no. 2, pp. 79–81, Feb. 2015.

[108] N. H. Nguyen, F. Parment, A. Ghiotto, K. Wu, and T. P. Vuong, "A fifth-order air-filled SIW filter for future 5G applications," in *2017 IEEE MTT-S International Microwave Workshop Series on Advanced Materials and Processes for RF and THz Applications (IMWS-AMP)*, Sep. 2017, pp. 1–3.

[109] C. Tomassoni, L. Silvestri, M. Bozzi, L. Perregrini, and A. Ghiotto, "A novel filter based on a dual-mode air-filled substrate integrated waveguide cavity resonator," in *2017 IEEE MTT-S International Conference on Numerical Electromagnetic and Multiphysics Modeling and Optimization for RF, Microwave, and Terahertz Applications (NEMO)*, May 2017, pp. 290–292.

[110] L. Silvestri, A. Ghiotto, C. Tomassoni, M. Boziz, and L. Perregrini, "Partially Air-Filled Substrate Integrated Waveguide Filters With Full Control of Transmission Zeros," *IEEE Transactions on Microwave Theory and Techniques*, vol. 67, no. 9, Sep. 2019.

[111] M. Zuboraj and J. L. Volakis, "Dispersion engineering and mode control using multiple pairs of non-identical coupled transmission lines," in *2017 IEEE International Symposium on Antennas and Propagation and USNC/URSI National Radio Science Meeting*. San Diego, CA, USA: IEEE, Jul. 2017, pp. 449–450.

[112] B. Gralak, S. Enoch, and G. Tayeb, "Anomalous refractive properties of photonic crystals," *J. Opt. Soc. Am. A*, vol. 17, no. 6, pp. 1012–1020, Jun 2000. [Online]. Available: http://josaa.osa.org/abstract.cfm?URI=josaa-17-6-1012

[113] F. Mesa, G. Valerio, R. Rodríguez-Berral, and O. Quevedo-Teruel, "Simulation-assisted efficient computation of the dispersion diagram of periodic structures," *IEEE Antennas and Propagation Magazine, in press*, 2020.

[114] M. Bagheriasl and G. Valerio, "Bloch Analysis of Electromagnetic Waves in Twist-Symmetric Lines," *Symmetry*, vol. 11, no. 5, May 2019.

[115] L. Silvestri, E. Massoni, M. Bozzi, L. Perregrini, C. Tomassoni, and A. Coves, "A new class of SIW filters based on periodically perforated dielectric substrate," in *2016 46th European Microwave Conference (EuMC)*. London, United Kingdom: IEEE, Oct. 2016, pp. 775–778.

[116] A. F. Abdelshafy, M. A. K. Othman, D. Oshmarin, A. Al-Mutawa, and F. Capolino, "Exceptional Points of Degeneracy in Periodically-Coupled Waveguides and the Interplay of Gain and Radiation Loss: Theoretical and Experimental Demonstration," *arXiv:1809.05256 [physics]*, Sep. 2018.

[117] "ANSYS HFSS: High Frequency Electromagnetic Field Simulation Software." [Online]. Available: https://www.ansys.com/products/electronics/ansys-hfss

[118] M. Ebrahimpouri, E. Rajo-Iglesias, Z. Sipus, and O. Quevedo-Teruel, "Cost-Effective Gap Waveguide Technology Based on Glide-Symmetric Holey EBG Structures," *IEEE Transactions on Microwave Theory and Techniques*, vol. 66, no. 2, Feb. 2018.

[119] O. Quevedo-Teruel, M. Ebrahimpouri, and M. Ng Mou Kehn, "Ultrawideband Metasurface Lenses Based on Off-Shifted Opposite Layers," *IEEE Antennas and Wireless Propagation Letters*, vol. 15, Dec. 2016.

[120] G. Valerio, Z. Sipus, A. Grbic, and O. Quevedo-Teruel, "Accurate Equivalent-Circuit Descriptions of Thin Glide-Symmetric Corrugated Metasurfaces," *IEEE Transactions on Antennas and Propagation*, vol. 65, no. 5, May 2017.

[121] A. Dhouibi, S. Nawaz Burokur, A. de Lustrac, and A. Priou, "Metamaterial-based half maxwell fish-eye lens for broadband directive emissions," *Applied Physics Letters*, vol. 102, no. 2, p. 024102, 2013.

[122] O. Quevedo-Teruel, J. Miao, M. Mattsson, A. Algaba-Brazalez, M. Johansson, and L. Manholm, "Glide-symmetric fully metallic luneburg lens for 5g communications at ka-band," *IEEE Antennas and Wireless Propagation Letters*, vol. 17, no. 9, pp. 1588–1592, 2018.

[123] M. A. K. Othman and F. Capolino, "Coupled transmission line array antennas with exceptional points of degeneracy," in *2017 IEEE International Symposium on Antennas and Propagation USNC/URSI National Radio Science Meeting*, 2017, pp. 57–58.

LIST OF PUBLICATIONS

Conference Proceedings

1. H. Mohamad, **T. Zheng**, M. Casaletti, Z. Ren, A. F. Abdelshafy, F. Capolino, and G. Valerio,"Degenerate band edge condition in substrate-integrated waveguides," ***APS/URSI 2018***.

2. **T. Zheng**, H. Mohamad, M. Casaletti, A. F. Abdelshafy, F. Capolino, G. Valerio, and Z. Ren,"Achieving a degenerate band edge resonance in substrate integrated waveguides," ***CEFC 2018, Poster presentation***.

3. **T. Zheng**, M. Casaletti, A. F. Abdelshafy, F. Capolino, Z. Ren, and G. Valerio, "Loss analysis for the degenerate band edge resonance in substrate integrated waveguides," ***EuCAP 2019, Oral presentation***.

4. **T. Zheng**, M. Casaletti, A. F. Abdelshafy, F. Capolino, Z. Ren, and G. Valerio, "Résonances géantes en substrate integrated waveguides," ***JNM 2019, Poster presentation***.

5. **T. Zheng**, M. Casaletti, A. F. Abdelshafy, F. Capolino, Z. Ren, and G. Valerio, "Bloch analysis for the study of degenerate band edge modes in periodic substrate-integrated waveguides," ***COMPUMAG 2019, Poster presentation***.

6. **T. Zheng**, M. Casaletti, Z. Ren, A. F. Abdelshafy, F. Capolino and G. Valerio, "High-Q substrate-integrated-waveguide resonator with degenerate band edge," ***ICEAA 2019***.

7. **T. Zheng**, M. Casaletti, A. F. Abdelshafy, F. Capolino, Z. Ren and G. Valerio, "Degenerate band edge resonances in air-filled substrate integrated waveguide," ***EuCAP 2020, Poster presentation***.

Publications in Journals

1. **T. Zheng**, M. Casaletti, A. F. Abdelshafy, F. Capolino, Z. Ren and G. Valerio, "Synthesis of DBE degeneracies in substrate-integrated waveguides," *IEEE Transactions on Microwave Theory and Techniques*, *to be submitted*.

Appendix
Conversion formulas from the scattering matrix to the transmission matrix

According to (2.19)-(2.22), we have the following expressions:

$$\begin{aligned}
\underline{\mathbf{T}}_{oo} - \underline{\mathbf{T}}_{io}\underline{\mathbf{Z}}_o^{-1} &= \frac{1}{2}\left[(\underline{\mathbf{I}} + \underline{\mathbf{S}}_{ii}) \cdot \underline{\mathbf{S}}_{oi}^{-1} \cdot (\underline{\mathbf{I}} - \underline{\mathbf{S}}_{oo}) + \underline{\mathbf{S}}_{io}\right] \\
&\quad + \frac{1}{2}\left[(\underline{\mathbf{I}} + \underline{\mathbf{S}}_{ii}) \cdot \underline{\mathbf{S}}_{oi}^{-1} \cdot (\underline{\mathbf{I}} + \underline{\mathbf{S}}_{oo}) - \underline{\mathbf{S}}_{io}\right] \\
&= (\underline{\mathbf{I}} + \underline{\mathbf{S}}_{ii})\underline{\mathbf{S}}_{oi}^{-1} \qquad \text{(A.1)} \\
-\underline{\mathbf{Z}}_i\underline{\mathbf{T}}_{oi} + \underline{\mathbf{Z}}_i\underline{\mathbf{T}}_{ii}\underline{\mathbf{Z}}_o^{-1} &= \frac{1}{2}\left[(\underline{\mathbf{I}} - \underline{\mathbf{S}}_{ii}) \cdot \underline{\mathbf{S}}_{oi}^{-1} \cdot (\underline{\mathbf{I}} - \underline{\mathbf{S}}_{oo}) - \underline{\mathbf{S}}_{io}\right] \\
&\quad + \frac{1}{2}\left[(\underline{\mathbf{I}} - \underline{\mathbf{S}}_{ii}) \cdot \underline{\mathbf{S}}_{oi}^{-1} \cdot (\underline{\mathbf{I}} + \underline{\mathbf{S}}_{oo}) + \underline{\mathbf{S}}_{io}\right] \\
&= (\underline{\mathbf{I}} - \underline{\mathbf{S}}_{ii})\underline{\mathbf{S}}_{oi}^{-1} \qquad \text{(A.2)} \\
-\underline{\mathbf{T}}_{oo} + \underline{\mathbf{Z}}_i^{-1}\underline{\mathbf{T}}_{oi} &= -\frac{1}{2}\left[(\underline{\mathbf{I}} + \underline{\mathbf{S}}_{ii}) \cdot \underline{\mathbf{S}}_{oi}^{-1} \cdot (\underline{\mathbf{I}} - \underline{\mathbf{S}}_{oo}) + \underline{\mathbf{S}}_{io}\right] \\
&\quad - \frac{1}{2}\left[(\underline{\mathbf{I}} - \underline{\mathbf{S}}_{ii}) \cdot \underline{\mathbf{S}}_{oi}^{-1} \cdot (\underline{\mathbf{I}} - \underline{\mathbf{S}}_{oo}) - \underline{\mathbf{S}}_{io}\right] \\
&= \underline{\mathbf{S}}_{oi}^{-1}(\underline{\mathbf{S}}_{oo} - \underline{\mathbf{I}}) \qquad \text{(A.3)} \\
-\underline{\mathbf{T}}_{io}\underline{\mathbf{Z}}_o^{-1} + \underline{\mathbf{Z}}_i^{-1}\underline{\mathbf{T}}_{ii}\underline{\mathbf{Z}}_o^{-1} &= \frac{1}{2}\left[(\underline{\mathbf{I}} + \underline{\mathbf{S}}_{ii}) \cdot \underline{\mathbf{S}}_{oi}^{-1} \cdot (\underline{\mathbf{I}} + \underline{\mathbf{S}}_{oo}) - \underline{\mathbf{S}}_{io}\right] \\
&\quad + \frac{1}{2}\left[(\underline{\mathbf{I}} - \underline{\mathbf{S}}_{ii}) \cdot \underline{\mathbf{S}}_{oi}^{-1} \cdot (\underline{\mathbf{I}} + \underline{\mathbf{S}}_{oo}) + \underline{\mathbf{S}}_{io}\right] \\
&= \underline{\mathbf{S}}_{oi}^{-1}(\underline{\mathbf{S}}_{oo} + \underline{\mathbf{I}}) \qquad \text{(A.4)}
\end{aligned}$$

Solving (A.1) and (A.2) together, we get

$$\begin{aligned}
\underline{\mathbf{S}}_{ii} &= (-\underline{\mathbf{Z}}_i\underline{\mathbf{T}}_{ii}\underline{\mathbf{Z}}_o^{-1} - \underline{\mathbf{T}}_{io}\underline{\mathbf{Z}}_o^{-1} + \underline{\mathbf{Z}}_i\underline{\mathbf{T}}_{oi} + \underline{\mathbf{T}}_{oo}) \\
&\quad \cdot (\underline{\mathbf{Z}}_i\underline{\mathbf{T}}_{ii}\underline{\mathbf{Z}}_o^{-1} - \underline{\mathbf{T}}_{io}\underline{\mathbf{Z}}_o^{-1} - \underline{\mathbf{Z}}_i\underline{\mathbf{T}}_{oi} + \underline{\mathbf{T}}_{oo})^{-1} \qquad \text{(A.5)} \\
\underline{\mathbf{S}}_{oi} &= 2(\underline{\mathbf{Z}}_i\underline{\mathbf{T}}_{oo}\underline{\mathbf{Z}}_o^{-1} - \underline{\mathbf{T}}_{io}\underline{\mathbf{Z}}_o^{-1} - \underline{\mathbf{Z}}_i\underline{\mathbf{T}}_{oi} + \underline{\mathbf{T}}_{oo})^{-1} \qquad \text{(A.6)}
\end{aligned}$$

Solving (A.3) and (A.4) together, we get

$$\begin{aligned}\underline{\mathbf{S}}_{oo} = &(\underline{\mathbf{Z}}_i\underline{\mathbf{T}}_{ii}\underline{\mathbf{Z}}_o^{-1} - \underline{\mathbf{T}}_{io}\underline{\mathbf{Z}}_o^{-1} + \underline{\mathbf{Z}}_i\underline{\mathbf{T}}_{oi} - \underline{\mathbf{T}}_{oo}) \\ &\cdot (\underline{\mathbf{Z}}_i\underline{\mathbf{T}}_{ii}\underline{\mathbf{Z}}_o^{-1} - \underline{\mathbf{T}}_{io}\underline{\mathbf{Z}}_o^{-1} - \underline{\mathbf{Z}}_i\underline{\mathbf{T}}_{oi} + \underline{\mathbf{T}}_{oo})^{-1}\end{aligned} \tag{A.7}$$

Substituting $\underline{\mathbf{S}}_{ii}$, $\underline{\mathbf{S}}_{oo}$, and $\underline{\mathbf{S}}_{oi}$ into (2.22), we obtain the expression of $\underline{\mathbf{S}}_{io}$

$$\underline{\mathbf{S}}_{io} = 2\underline{\mathbf{T}}_{oo} - (\underline{\mathbf{I}} + \underline{\mathbf{S}}_{ii})\underline{\mathbf{S}}_{oi}^{-1}(\underline{\mathbf{I}} - \underline{\mathbf{S}}_{oo}) \tag{A.8}$$